SUPRAMOLECULAR CONTROL OF SYNTHESIS AND ELECTRONIC STRUCTURE OF PORPHYRIN OLIGOMERS

A thesis submitted to the board of the faculty of Physical Sciences in partial
fulfillment of the requirements for the degree of

Doctor of Philosophy of the University of Oxford

By

Johannes Klaus Sprafke

The Chemistry Research Laboratory and Keble College, Oxford
Trinity Term 2011

SUPRAMOLECULAR CONTROL OF SYNTHESIS AND ELECTRONIC STRUCTURE OF PORPHYRIN OLIGOMERS

Abstract

Johannes Klaus Sprafke, Keble College, University of Oxford

D.Phil Thesis, Trinity Term 2011

The work described in this thesis demonstrates the use of supramolecular chemistry in the template-directed synthesis of porphyrin nanorings and as a tool to control conformation and topology of π-conjugated porphyrin oligomers. Particular emphasis is placed on changes to the electronic structure of these oligomers depending on their conformation.

Chapter 1 gives an overview of π-conjugated porphyrin oligomers and conjugated macrocycles in general, followed by an introduction into supramolecular cooperativity and small angle X-ray scattering in solution.

Chapter 2 describes advances in the synthesis, solution structure elucidation and optoelectronic properties of a fully conjugated cyclic porphyrin hexamer. The high rigidity and symmetry of this nanoring as well as its bent π-system lead to a significant decrease in its HOMO-LUMO gap. The resulting near-infrared emission was exploited in the fabrication of light emitting diodes, demonstrating the use of a bent topology for minimizing aggregation in thin films.

The synthesis of a [12]porphyrin nanoring using a hexadentate template is presented in *Chapter 3*. The concept of Vernier templating is introduced as a general strategy for the synthesis of large monodisperse macrocycles. The nanoring is characterized and its cooperative binding to two template molecules is studied. In *Chapter 4* a bidentate ligand is used in the cooperative formation of a sandwich complex beween two nanorings.

Chapter 5 provides an analysis of the rigidity of the butadiyne linked porphyrin oligomers used throughout this thesis. A linear chain is significantly more flexible in solution than on a surface where it is confined within two dimensions. Analysis of the persistence length indicates that a porphyrin nanoring with more than around 20 units would not be significantly strained.

The supramolecular binding of linear porphyrin oligomers to carbon nanotubes is analyzed in *Chapter 6*. The binding strength increases sharply with oligomer length and binding is strongest with (8,6) and (7,5) tubes. The energy level alignment in these porphyrin CNT complexes appears to be favorable for an application in photovoltaics.

In *Chapter 7* bisamidine-carboxylate salt bridges together with zinc-nitrogen coordination chemistry are used to access a variety of topologies in assemblies based on carboxylic acid functionalized porphyrin dimers.

Acknowledgements

First of all I would like to thank Harry for his great support and guidance throughout my time as a DPhil student and for giving me the freedom to explore so many quite different areas in my research.

It would not have been possible to obtain many of the results presented in this thesis without the tremendous contributions of numerous collaborators who either showed me how to use their instrumentation or did the experiments for me: Mike Wykes and Dr David Beljonne (University of Mons, molecular dynamics simulations and electronic structure calculations plus great hosts for my three week secondment); Sam Stranks and Prof Robin Nicholas (Oxford Physics, carbon nanotube experiments); Dr Alex Saywell and Prof Peter Beton (University of Nottingham, STM); Dr Olly Fenwick and Professor Franco Cacialli (University College London, fabrication of OLEDs); Rokas Drevinskas, Dr Ramunas Augulis and Prof Donatas Zigmantas (University of Lund, low temperature emission and 2D electronic spectroscopy); Dr Marc Malfois (Diamond Light Source, help with SAXS experiments); Dr Jamie Warner (Oxford Materials, TEM); and Dr Barbara Odell and Dr Tim Claridge (Oxford NMR). A big thank you to all of you! Your efforts increased the quality of my research and you also gave me interesting insights into numerous research areas and experimental techniques.

Thank you to Dr Frank Bock, Prof Wei Zhang and Dr Markus Hofmann, my labsupervisors at different stages as an undergraduate or new DPhil student, who introduced me into everything required to work in the lab.

It was a great pleasure to carry out this work within THREADMILL; the enriching discussions with all members are highly appreciated and additionally it was always great fun to meet all of you in so many nice places all across Europe.

Thanks to all members of the Anderson group who made my time as a summer student, DPhil student and short-term postdoc extremely enjoyable. To name only a few: Markus H., Emma, Katsutoshi, Louisa, Rienk, Hannah, Nicola, Karl, Marie, Atsuomi, Sally, Markus D., Guzman, Dima, Jon, Jan, Phil, Ismael and Georg. Particular thanks to Prof Mitsuhiko Morisue for leaving the NMR tube in my door. Another big thanks to Giuseppe for sharing houses, rooms and beds with me over three years.

Thanks to all my good friends outside of the lab for keeping me in touch with the real world: Thomas D., Martin, Andreas, Frank, Thomas K., Jens, Achim, Uli, Flo, Anu, Kathi and Craig.

Liebe Eltern, Katharina und Tobias: Vielen Dank für eure Hilfe und Unterstützung aus der Ferne, auch schon während des Studiums. Danke auch für das Ertragen meines Vagabundendaseins in den letzten 5 Jahren. Thanks to Hazel for maintaining and feeding me over the last months, for proof-reading my whole thesis and for always being there for me.

Best of luck to Dima, Georg and any other future bearer of the burden!

Contents

Abbreviations

AFM	Atomic force microscopy
AM1	Austin model 1
aq	Aqueous
Ar	Aryl
ATP	Adenosine triphosphate
B band	Soret band, porphyrin S_0-S_2 absorption band
B3LYP	Becke, three parameter, Lee-Yang-Parr
BHLYP	Becke, half and half-exchange, Lee-Yang-Parr
BChl	Bacteriochlorophyll
Bipy	4,4'-bipyridine
CoMoCat	Cobalt molybdenum catalyst
CNT	Carbon nanotube
COSY	Correlation spectroscopy
c-PPA	Cyclic *para*-phenylacetylene
c-PP	Cyclic *para*-phenylene
d	Doublet
Da	Dalton
DABCO	1,4-Diazabicyclo[2.2.2]-octane
dba	Dibenzylideneacetone
DCB	*ortho*-Dichlorobenzene
DCC	*N,N'*-Dicyclohexyl-carbodiimide
DDQ	2,3-Dichloro-5,6-dicyano-*p*-benzoquinone
DEER	Double electron-electron resonance
DFT	Density functional theory
DMAP	4-(Dimethylamino)pyridine
DNA	Desoxyribonucleic acid
DOS	Density of states
DOSY	Diffusion-ordered spectroscopy
EL	Electroluminescence
EM	Effective molarity
EPR	Electronic paramagnetic resonance
EQE	External quantum efficiency
ESI	Electrospray ionization
Et	Ethyl
F8BT	Poly(9,9'-dioctylfluorene)-*alt*-benzothiadiazole

FRET	Förster resonance energy transfer
FWHM	Full width at half maximum
GPC	Gel permeation chromatography
HiPCO	High pressure carbon monoxide
HOMO	Highest occupied molecular orbital
HOPG	Highly oriented pyrolitic graphite
HR	High resolution
HT	Herzberg-Teller
INDO	Intermediate neglect of differential overlap
IQE	Internal quantum efficiency
IR	Infrared
i	Iso carbon
ITO	Indium-tin-oxide
LH	Light harvesting system
LUMO	Lowest unoccupied molecular orbital
m	Meta
m	Multiplet
MALDI	Matrix-assisted laser desorption ionization
MD	Molecular dynamics
Me	Methyl
MEH-PPV	Poly(2-methoxy-5-(2-ethylhexyloxy)-1,4-phenylenevinylene
MM	Molecular mechanics
MS	Mass spectrometry
MW	Molecular weight
MWCNT	Multi-walled carbon nanotube
NBS	*N*-Bromosuccinimide
NICS	Nucleus independent chemical shift
NIR	Near-infrared
NMR	Nuclear magnetic resonance
NOE	Nuclear Overhauser effect
NOESY	Nuclear Overhauser effect spectroscopy
o	Ortho
OLED	Organic light emitting diode
p	Para
P3HT	Poly(3-hexylthiophene)
PE 40-60	Petrol ether boiling between 40 and 60 °C
Ph	Phenyl

PM3	Parametrized model number three
PL	Photoluminescence
PLE	Photoluminescence excitation
PDF	Pair distribution function
PEDOT	Poly(3,4-ethylenedioxythiophene)
PSS	Poly(styrenesulfonate)
PV	Photovoltaics
Q band	Porphyrin S_0-S_1 absorption band
RC	Reaction center
RT	Room temperature
SAXS	Small angle X-ray scattering
SCF	Self-consistent field
SCI	Single configuration interaction
SDBS	Sodium dodecylbenzene sulfonate
SEC	Size exclusion chromatography
SWCNT	Single-walled carbon nanotube
STM	Scanning tunneling microscopy
t	Triplet
t	tertiary carbon
TBAF	Tetra-*n*-butylammonium fluoride
TD	Time dependent
TEG	Triethylene glycol
TEM	Transmission electron microscopy
TFA	Trifluoroacetic acid
THF	Tetrahydrofuran
THS	Trihexylsilyl
TIPS	Tri*iso*propysilyl
TLC	Thin layer chromatography
TMEDA	Tetramethylethyenediamine
TOF	Time of flight
UHV	Ultrahigh vacuum
UV	Ultra-violet
Vis	Visible
WLC	Worm-like chain

Chapter 1

Introduction

This chapter begins with a brief introduction on porphyrins as nature's colorants and their crucial role in natural light harvesting systems. Different ways of linking porphyrin macrocycles with conjugated bridges are introduced, followed by a deeper discussion on the electronic structure and synthesis of butadiyne-linked porphyrin oligomers. In the next section, concepts for the synthesis of fully π-conjugated nanorings are introduced and illustrated by examples. These examples also highlight the unique properties of conjugated nanorings. The supramolecular chemistry and multicomponent assemblies of porphyrin oligomers are a central theme in this thesis and a short introduction to this topic and the important concept of cooperativity in self-assembly is given. The chapter closes with an introduction into small angle X-ray scattering as a technique for the structural characterization of nanoscale assemblies in solution.

1.1 Porphyrins and Their Role in Natural Light Harvesting Systems

Porphyrins are aromatic tetrapyrrolic macrocycles with methine bridges linking the pyrrole units at their α-positions. The eight β-pyrrole carbon atoms and the four methine bridges, termed *meso* carbons, allow structural modification of the porphyrin core by substitution of the hydrogens present in porphin, the simplest porphyrin (Figure 1.1a). In neutral free-base porphyrins two of the inner nitrogens bear hydrogen atoms that can be displaced by a metal cation: the rigid scaffold and the four inward-pointing nitrogen donors make the dianionic porphyrins excellent chelating ligands for a variety of metals, thereby providing further structural diversity (Figure 1.1b). Porphyrins are Hückel aromatics as 18 out of the 26 π-electrons provide a cyclic conjugation path. The aromatic ring current causes de-shielding of the outer protons and strong shielding of the NH-protons manifested in unusual chemical shifts observed by ^{1}H NMR (Figure 1.1c).

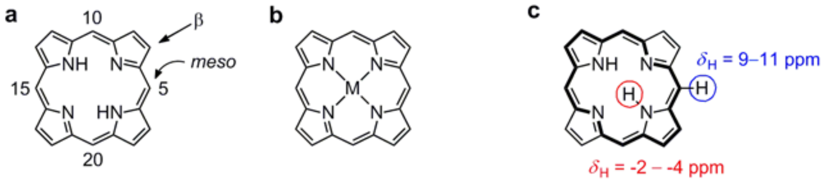

Figure 1.1. *(a) Structure of free base porphin illustrating the numbering system for carbon atoms and arrows indicating meso and β-positions; (b) metalloporphyrin; (c) aromaticity in porphyrins: the bonds in bold mark the 18 π-electron pathway and the resulting chemical shifts of inner (red) and outer (blue) protons.*

Porphyrin derivatives can be found in many biological systems performing various functions. Hemes are iron porphyrins that are important co-factors for enzymes (for example in cytochrome P450) and oxygen transporters (in hemoglobin). Vitamin B12 is a cobalt porphyrinoid that plays a critical role in the nervous system and magnesium porphyrins (chlorophylls) are important pigments in light harvesting. A common property of all naturally occurring and synthetic porphyrins is their strong color, resulting from their extended π-systems. The two lowest electronic transitions of simple porphyrins are both in the visible region with the intense Soret (or B) band between 400 and 450 nm and the weaker Q band around 550 nm. The four orbital model proposed by Gouterman explains the origin of these two transitions using the frontier orbitals (Figure 1.2).[1,2] The two lowest unoccupied molecular orbitals in D_{4h} symmetric porphyrins are degenerate ($e_{g\,x}$ and $e_{g\,y}$ symmetry), whereas the two highest occupied molecular orbitals, with a_{2u} (HOMO-1) and a_{1u} (HOMO) symmetry, have different energies. Transitions from HOMO and HOMO-1 to the degenerate LUMOs results in two excited states, but through configuration interaction these two states split resulting in a higher energy transition (Soret or B band, S_0-S_2) with large oscillator strength, and a lower energy transition (Q band, S_0-S_1) with smaller oscillator strength.

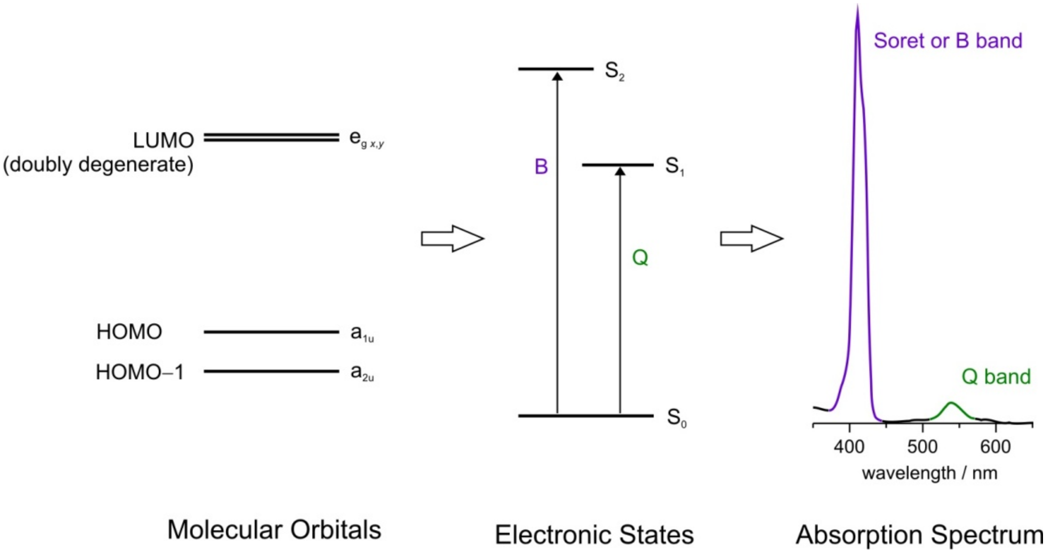

Figure 1.2. *Explanation of the absorption spectra of porphyrins using the Gouterman four orbital model. Figure adapted from ref. 3.*

Structural modification of the porphyrin core or exchange of the coordinated metal can significantly influence the optical properties of porphyrins due to electronic coupling, deformation of the macrocycle or changes in symmetry. Besides the effect of macrocycle structure, the optical properties of porphyrins also strongly depend on their environment because through-space electronic coupling can severely influence transition energies, for example in aggregates.[4] This factor is of major importance in biological light harvesting systems such as the well studied photosystem of purple bacteria.[5,6] The photosystem is a gigantic trans-membrane complex consisting of the two circular light harvesting (LH) complexes LH1 and LH2 and the reaction center (RC) which is bound inside LH2 (Figure 1.3e). Bacteriochlophyll *a* (BChl *a*, Figure 1.3a) molecules, which are magnesium porphyrins, serve as the predominant light absorbing pigments in LH1 and LH2. A protein matrix holds the BChl *a* units precisely in three different environments: the B875 ring that is integrated in LH1 and the B850 and B800 rings, both in LH2 (Figure 1.3c). The distances and orientations between the porphyrin units are specific to each ring, resulting in different degrees of electronic coupling. In B800 (absorption maximum around 800 nm) the distance between two porphyrin units is large (21 Å) and thus there is little electronic coupling. In B850 the distance is significantly smaller (9 Å) and strong J-type coupling[4] exists between the porphyrins. The absorption maximum is therefore red-shifted to 850 nm and if a photon is absorbed by one of the 16 BChl *a* units the exciton delocalizes over the whole ring within 100 fs. In B800 the exciton remains localized but after 1–2 ps the excited state energy is transferred ‘downhill’ to B850 which serves as a ‘storage ring’ due to its long excited state lifetime of about 1 ns. The electronic coupling is greatest in the B875 ring of LH1 which absorbs at around 875 nm. This low lying excited state funnels excitation energy from the surrounding LH2 complexes to LH1 from where it is transferred to the reaction center. Here charge separation occurs and, over several redox steps, the energy is finally stored as chemical energy in the form of ATP.

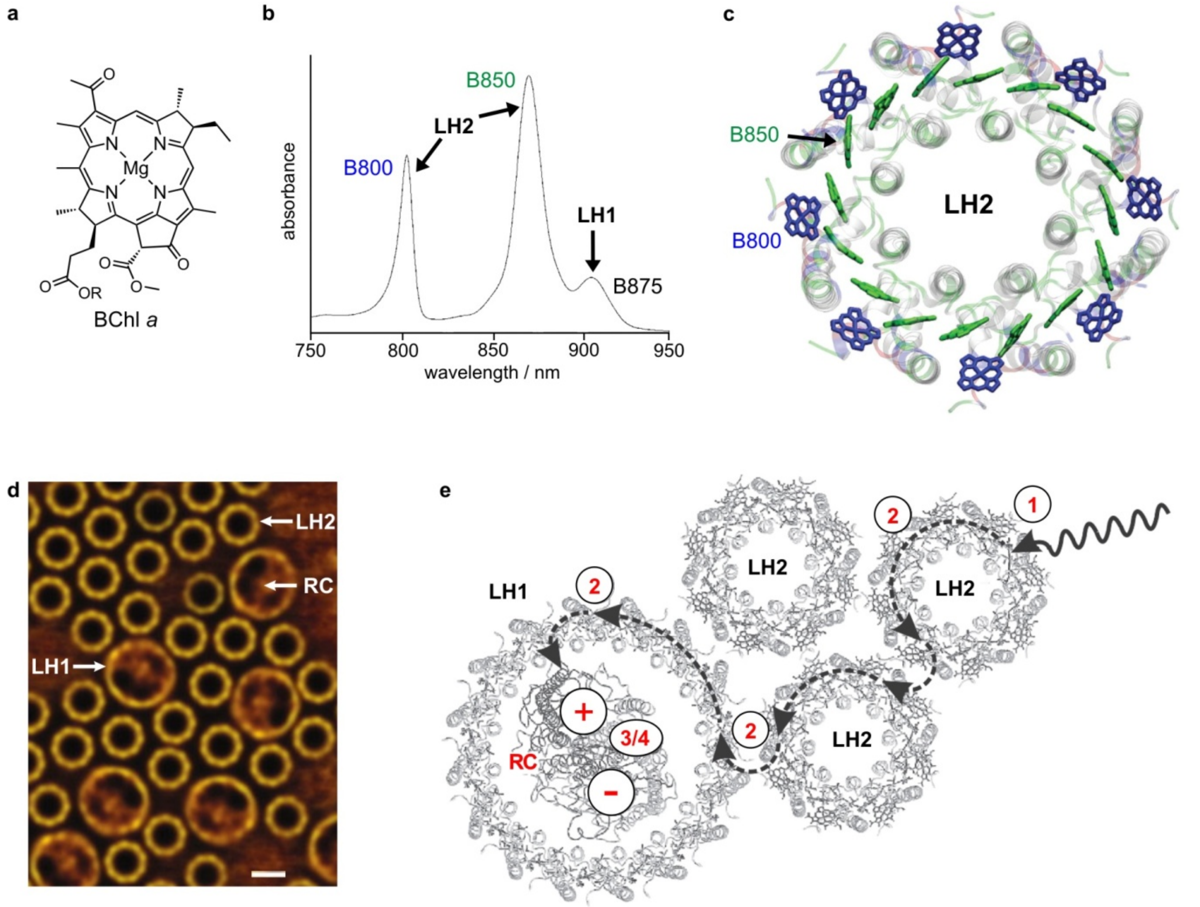

Figure 1.3. Light harvesting systems of purple bacteria. (a) Structure of Bacteriochlorophyll a; (b) low temperature (10 K) absorption spectrum of membrane fragments of Rhodopseudomanas (Rs.) acidophilia;[7] *(c) crystal structure of LH2 from Rs. molischianum, reprinted from ref. 6; (d) fitted AFM image of a native membrane of Rs. photometricum (scale bar = 5 nm), adapted from ref. 8; (e) photosystem of the Rhodobacter sphaeroides with black arrows indicating the flow of energy from 1) absorption, 2) transfer, 3) charge separation and 4) redox processes, reprinted from ref. 7.*

The natural light harvesting complexes are a fascinating example of how supramolecular organization can influence the electronic structure of chromophores. It is the great structural control exerted by the protein matrix that keeps each chromophore at exactly the right position in order to optimize light absorption and energy flow. The complexity and elegance of the natural photosystems serve as a great motivation for the creation of increasingly sophisticated artificial light harvesting arrays.[9,10]

1.2 Conjugated Porphyrin Oligomers

Models for natural light harvesting systems can be seen in the broader context of organic electronic materials. In order to achieve structural definition and strong electronic coupling similar to that in the natural light harvesting complexes, synthetic chemists can link chromophores covalently, either directly or by conjugated bridges, leading to the concept of π-conjugated oligomers[11,12] and polymers.[13] In these compounds, excited states are delocalized[14] and charges are transported efficiently along the molecular backbone or through molecular crystals.[15,16] These properties have raised significant academic and commercial interest and led to the development of the field of organic (or plastic) electronics with applications in light emitting diodes,[17,18] field effect transistors,[19] sensors[20] and photovoltaics.[21,22]

1.2.1 Electronic Structure

Porphyrins can be linked covalently either at the *meso* or β-positions. It has been shown that electronic coupling through β-β and β-meso linkages is much less efficient than through *meso*-*meso* connections, probably because of the relatively small frontier orbital coefficients at the β-positions.[3] The electronic coupling through direct *meso*-*meso* bonds[23] or *para*-phenylene bridges[24,25] is weak because the steric interactions between the aryl *ortho*-hydrogens and the porphyrin β-hydrogens result in large dihedral angles and thus minimal π-overlap. The use of sterically less demanding linkers such as ethyne or butadiyne, as introduced by Arnold,[26] Anderson[27] and Therien,[28] leads to strong electronic coupling as indicated by the red-shift of the longest wavelength absorption maxima $\lambda_{\max}$ (Figure 1.4). Even stronger red-shifts were achieved by Anderson and Therien by applying strategies that are known to result in strong electronic delocalization, i.e. the use of linkers incorporating groups that stabilize quinoidal resonance structures, such as anthracene,[29] pentacene[30] or benzo-bis(thiadiazoles)[30] (Figure 1.4), as well as the formation of a cyanine-like structure by incorporating a cationic linker.[31,32] A highly efficient way of linking porphyrins has also been developed by Osuka, by doubly or triply fusing the macrocycles, resulting in the formation of a highly delocalized π-system (Figure 1.4).[33,34]

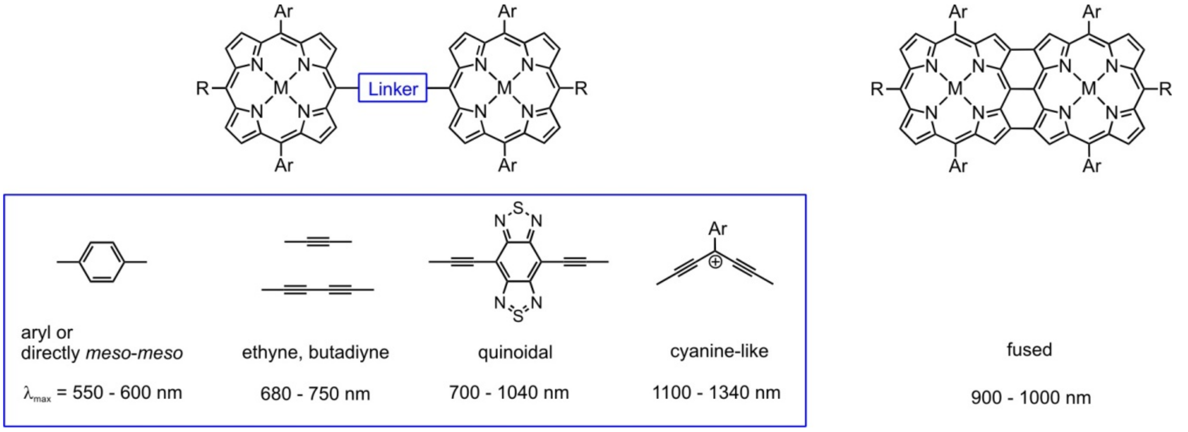

Figure 1.4. *Selected porphyrin dimer linkers and their influence on the energy gap expressed as the longest wavelength transition in the absorption spectra* λ_{max}.

The increased electronic coupling (by choice of a suitable linker unit) suggested by the absorption spectra was confirmed by several computational studies on semi-empirical[30,35,36] and density functional theory (DFT)[32,37,38] levels of theory. As shown in Figure 1.5 for the HOMO and LUMO of a butadiyne-linked porphyrin dimer,[38] the frontier orbitals tend to extend over the whole molecule and the calculated energy gaps are significantly reduced compared to the monomer.

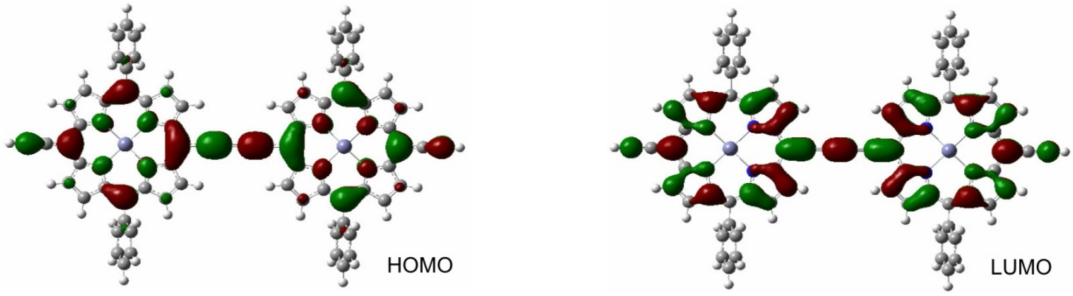

***Figure 1.5.** HOMO and LUMO of a butadiyne-linked porphyrin dimer calculated by time-dependent DFT.*[38]

The Soret absorption band of a butadiyne-linked porphyrin dimer is split into two components, whilst there is only one band in the spectrum of a D_{4h} symmetric monomer. This splitting results from the reduced symmetry of the porphyrins and the coupling between the two porphyrin units.[27] The Soret band consists of a B_x and a B_y component that are degenerate in a D_{4h} monomer, but this degeneracy is lifted the for porphyrin dimer due to its lower D_{2h} symmetry (Figure 1.6a,b). The transition dipoles of the B_x components (along the linker axis) are arranged in a head-to-tail fashion, whereas the B_y components are parallel. Therefore the excited state splits when each of the two pairs couple, resulting in a red-shifted B_x component and a blue-shifted B_y component as confirmed by polarized spectroscopy.[39] For the Q band, theory predicts only a vanishingly small contribution from the Q_y component and most of the absorption is polarized along the linker axis.[35,38] Thus the Q band is dominated by the electronic coupling through the bridge (along the x-axis) which is the reason for the strong red-shifts observed in the Q bands of dimers compared to analogous monomers.

A second effect that has to be taken into account when explaining the absorption spectrum of a butadiyne-linked porphyrin dimer is the influence of the dihedral angle between the two chromophores. Figure 1.6c shows calculated absorption spectra for a co-planar (in blue) and a perpendicular conformation (in red). Whilst the spectrum of the perpendicular conformation resembles that of a simple monomer with only one Soret and one Q band, the spectrum of the co-planar dimer has a split Soret band and a single Q band that is red-shifted by about 100 nm compared to the perpendicular conformation. The Q band of the experimental absorption spectrum contains contributions from both conformations suggesting a wide distribution of dihedral angles at room temperature (Figure 1.6b). According to DFT calculations, the co-planar conformation is lowest in energy due to efficient interporphyrin conjugation, but the rotational barrier around the bridge is low (0.67 kcal/mol) explaining the variety of conformations in the experimental spectrum at room temperature ($RT = 0.59$ kcal/mol).[38]

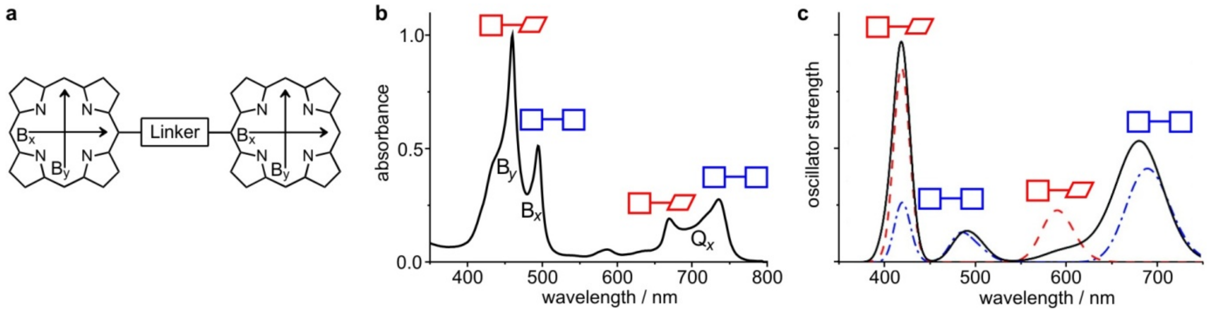

Figure 1.6. Absorption spectrum of a butadiyne-linked porphyrin dimer. (a) Transition dipole moments of Soret band transitions that are exciton coupled; (b) absorption spectrum of porphyrin dimer in $CHCl_3$ /1%pyridine with contributions from different conformations and exciton coupling; (c) Gaussian broadened calculated absorption spectra of co-planar conformation (blue), perpendicular conformation (red) and Boltzmann weighted spectrum over all dihedral angles (black), spectra from ref. 38.

In contrast to the wide distribution of dihedral angles in the dimer ground state structure, the rotational barrier in the first excited state S_1 was calculated to be significantly higher (3.9 kcal/mol) suggesting a predominantly planar conformation. Fluorescence excitation experiments support this prediction since emission was found to come mostly from a planarized first excited state.[38] Ultrafast polarized pump-probe spectroscopy[40] and fluorescence anisotropy[41] studies of ethyne and butadiyne-linked porphyrin oligomers produced a more detailed picture of the excited state dynamics. After excitation of the Soret band internal conversion from S_2 to S_1 occurs on the time scale of one picosecond[40] and within further 100 ps the first excited state relaxes into the planar emissive state, which decays to the ground state S_0 in about one nanosecond.[38,40,41]

In summary, the absorption spectrum of butadiyne-linked porphyrin dimers consist of transitions from S_0 to both S_1 (Q band) and S_2 (Soret band) within a wide range of dihedral conformations, whereas (in low viscosity solvents) the emission spectrum is dominated by the S_1-S_0 transition from a single, planar conformation.

While the coupling of porphyrins using quinoidal and cationic bridges has so far been limited to dimers, probably because of synthetic difficulties, less complex linkers such as ethyne[42] and butadiyne,[43,44] but also fused porphyrins,[34] have been extended to longer oligomers and even polymers. Figure 1.7b shows the absorption spectra of a series of butadiyne-linked porphyrin oligomers ***l*-P*N*$_{\mathbf{C8}}$** up to the octamer (N = 8). The Soret bands do not change significantly with increasing oligomer length, but the low energy Q bands are progessively intensified and red-shifted, indicating efficient electronic coupling along the backbone. The decrease in HOMO-LUMO gap has been confirmed by electrochemically determined HOMO and LUMO energies (Figure 1.7c).[45,46]

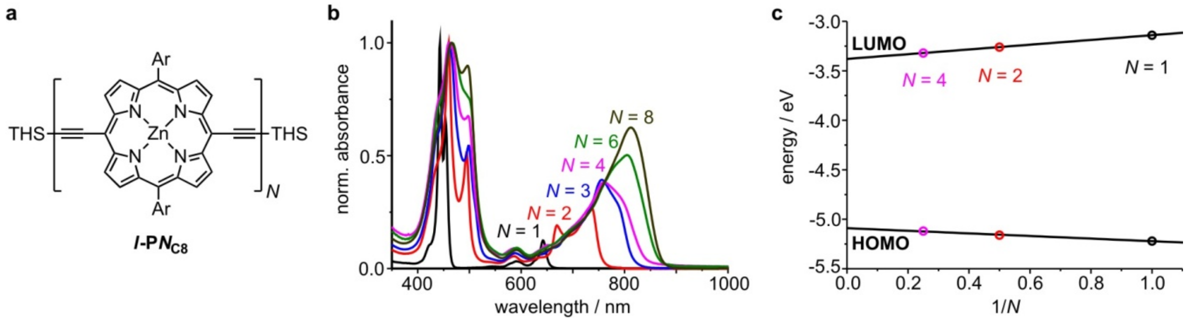

Figure 1.7. *Energy gap of butadiyne-linked porphyrin oligomers. (a) General structure of the series* ***l-PN$_{C8}$****; (b) absorption spectra in $CHCl_3$ /1% pyridine normalized at the Soret band; (c) electrochemically determined HOMO and LUMO energies for N= 1, 2 and 4, with the black lines linearly extrapolating to the polymer limit.*

The highly delocalized π-system and the rigid shape with lengths up to 10 nm (***l*****-P8$_{C8}$**) make butadiyne-linked porphyrin oligomers promising candidates for long range charge transport. The excellent conductance through these molecular wires has been demonstrated using various approaches such as charge recombination rates in donor-acceptor systems,[45] STM single molecule break junctions[47] and microwave conductivity.[48]

1.2.2 Synthesis of Butadiyne-linked Porphyrin Oligomers

Besides modification of the electronic properties, the main reason to synthesize a wide variety of butadiyne-linked porphyrin oligomers has been to gain control over their solubility and self-assembly or aggregation behavior. The first butadiyne-linked porphyrin dimers synthesized by Arnold[26] and Anderson[27] were substituted with β-alkyl solubilizing groups in order to achieve good solubility. However, strongly bound dimeric aggregates formed in the absence of an axially coordinating ligand such as pyridine. In the next generation of these dimers, Anderson introduced *meso*-aryl side groups that lie nearly perpendicular to the porphyrin plane and significantly reduce aggregation. The complete series from monomer ***l*****-P1** to hexamer ***l*****-P6** was synthesized using 3,5-bis-*tert*-butyl phenyl side groups,[43] but longer oligomers were too insoluble to extend this series further. Improved solubility was attained by replacing the rigid *tert*-butyl groups with various long and flexible alkyl chains, enabling the synthesis of a range of oligomers[49] and polymers.[44,48]

The synthetic approach to a series of these porphyrin oligomers usually consists of a sequence of deprotection and acetylene homo-coupling steps, irrespective of the aryl substituents.[49,50] The synthesis of oligomer series with 3,5-bis-*tert*-butyl phenyl side groups ***l*****-P*N*** and with 3,5-bis-octyloxy phenyl side groups ***l*****-P*N*$_{C8}$** is detailed here as these derivatives were used throughout this thesis.

A convenient synthesis of porphyrins with identical substituents on opposite meso positions was introduced by Lindsey, and is based on the condensation of an aldehyde with dipyrromethane **1** to initially form a porphyrinogen that is subsequently oxidized to a porphyrin (Scheme 1.1).[51] Dipyrromethane **1**[52] and benzaldehyde derivatives **2a**[49] and **2b**[53] are accessible on a multigram scale and porphyrin synthesis proceeds in both cases in nearly 50% yield. Free base porphyrins **3a**/**b** are quantitatively converted to zinc porphyrins **4a**/**b** using $Zn(OAc)_2$. The significantly larger HOMO coefficients at the *meso* compared to the β-positions (Section 1.2.1 and ref. 3) allows selective electrophilic *meso*-bromination with *N*-bromosuccinimide (NBS) in excellent yields. Dibromoporphyrins **5a**/**b** can then undergo Sonogashira coupling with trihexylsilyl-protected acetylene[54] to give porphyrin monomers ***l*-P1**/***l*-P1$_{C8}$**. Besides protection of the terminal acetylene, the trihexylsilyl (THS) group also serves as an additional solubilizing group and can ease separation in the subsequent statistical deprotection steps.

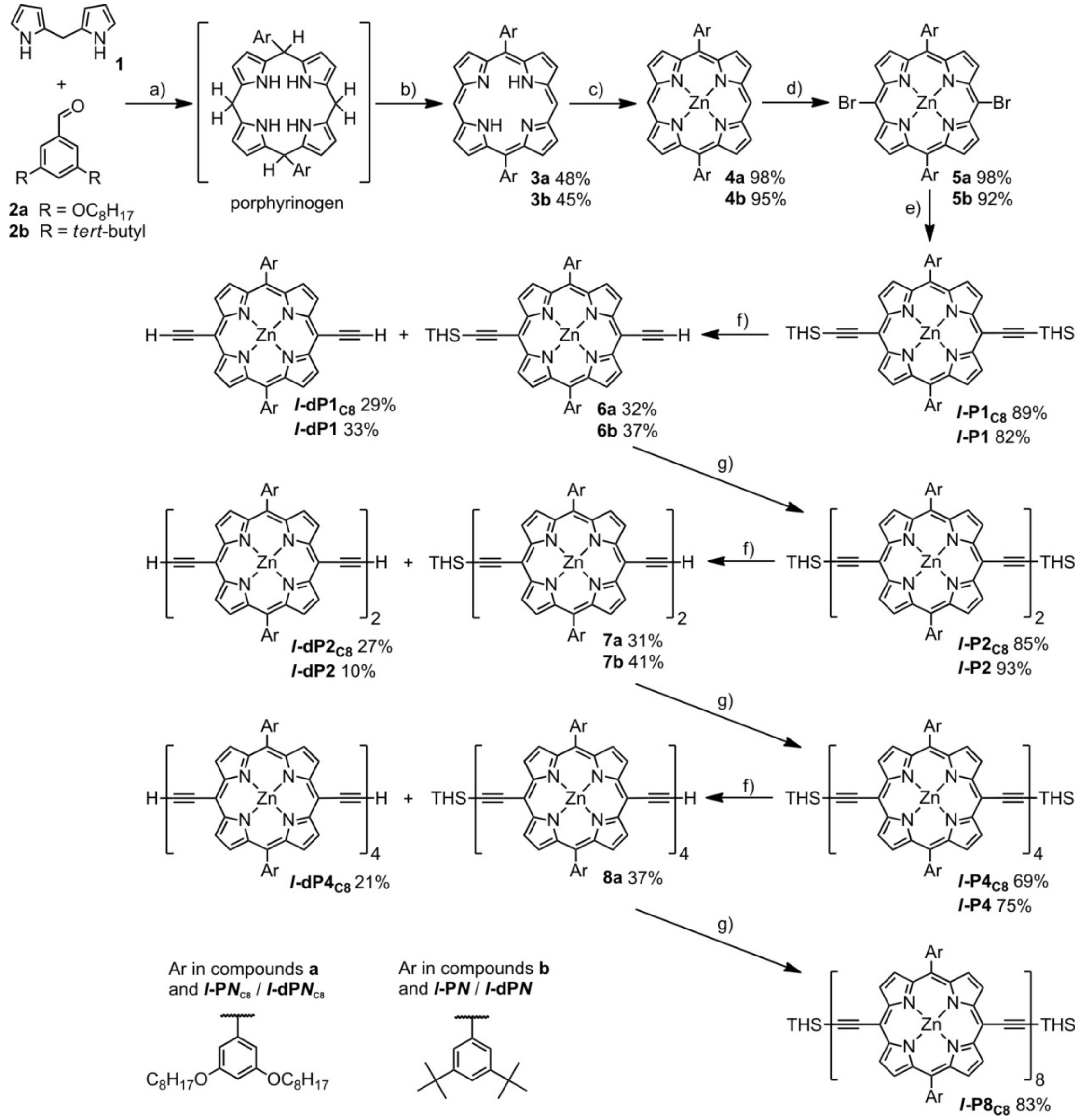

Scheme 1.1. *Synthesis of butadiyne-linked porphyrin oligomers. THS stands for trihexylsilyl. Reagents and conditions: a) TFA; b) DDQ; c) $Zn(OAc)_2$; d) NBS; e) (trihexylsilyl)acetylene,[54] $Pd(OAc)_2$, PPh_3, CuI, NEt_3; f) TBAF; g) CuCl, TMEDA.*

The conversion of monomers ***l*-P1**/***l*-P1**$_{\mathbf{C8}}$ to dimers ***l*-P2**/***l*-P2**$_{\mathbf{C8}}$ requires a statistical deprotection step to break the symmetry of ***l*-P1**/***l*-P1**$_{\mathbf{C8}}$. Silyl deprotection with tetra *n*-butylammonium fluoride (TBAF) produces a statistical mixture of fully deprotected monomers ***l*-dP1**/***l*-dP1**$_{\mathbf{C8}}$, the desired mono-deprotected products **6a**/**b** and remaining starting material. Glaser coupling of monomers **6a**/**b** gives dimers ***l*-P2**/***l*-P2**$_{\mathbf{C8}}$ in good yields. Tetramers ***l*-P4**/***l*-P4**$_{\mathbf{C8}}$ and octamer ***l*-P8**$_{\mathbf{C8}}$ are synthesized iteratively by the same mono-deprotection acetylene homo-coupling steps. At the level of octamer ***l*-P8**$_{\mathbf{C8}}$ it is not possible to separate fully and mono-deprotected porphyrins, thus preventing controlled synthesis of a 16-mer.[49]

The syntheses of oligomers that cannot be reached simply by doubling the number of porphyrin units require an additional low yielding statistical step (Scheme 1.2a). Trimers ***l*-P3**/***l*-P3**$_{\mathbf{C8}}$ can be synthesized by Glaser coupling of mono-deprotected monomers **6a**/**b** with mono-deprotected dimers **7a**/**b**. The resulting mixture of dimer, trimer and tetramer can be separated by size-exclusion chromatography (SEC) to give ***l*-P3**/***l*-P3**$_{\mathbf{C8}}$ in 40% yield. In order to obtain hexamers ***l*-P6**/***l*-P6**$_{\mathbf{C8}}$ the trimer can be statistically deprotected and coupled. In a similar way to trimer, the pentamer has been synthesized from mono-deprotected dimer and mono-deprotected trimer with separation of the oligomeric by-products.[50]

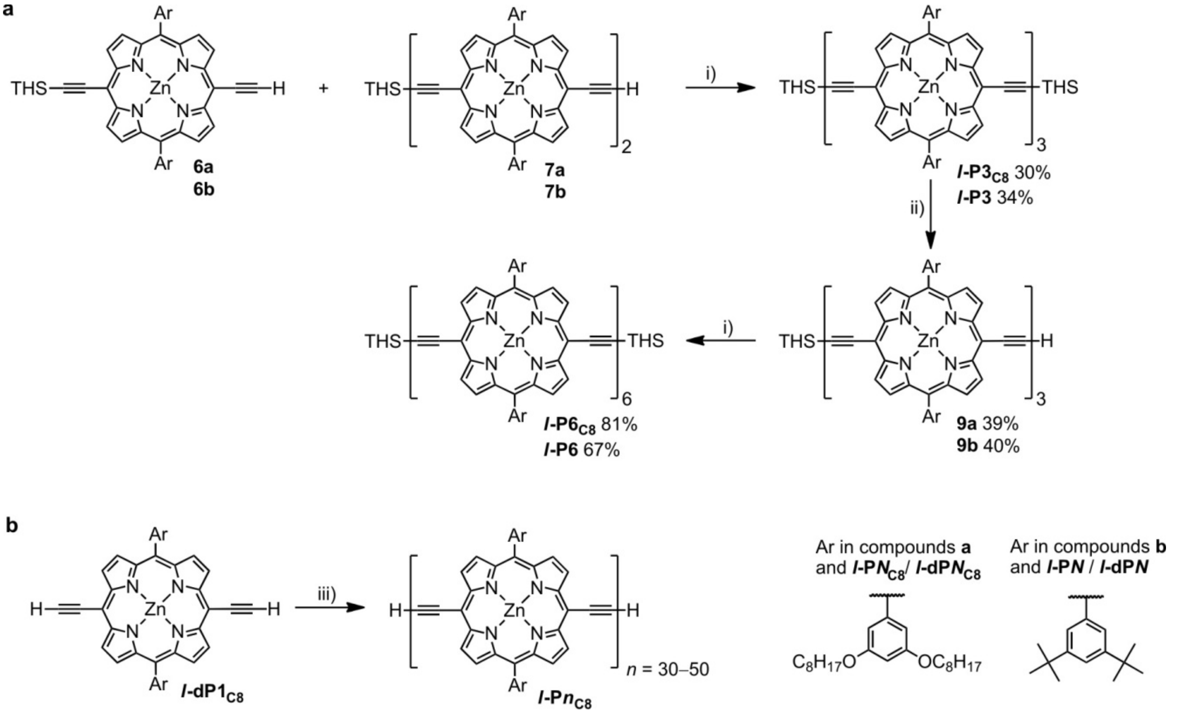

Scheme 1.2. *Synthesis of (a) porphyrin trimer and hexamer and (b) a porphyrin polymer; THS stands for trihexylsilyl. Reagents and conditions: i) CuCl, TMEDA; iii) TBAF; iii)* $PdCl_2(PPh_3)_2$*, CuI, 1,4-benzoquinone, i-*Pr_2NH*.*

The synthesis of porphyrin polymers from fully deprotected monomers using Glaser coupling conditions produced polymers with low molecular weights and about 10–15 repeat units.[44,55] For the synthesis of polymer ***l*-P*n***$_{\mathrm{C8}}$ from fully deprotected monomer ***l*-dP1**$_{\mathrm{C8}}$, palladium catalyzed oxidative acetylene homo-coupling was used to give significantly longer polymers that were only limited by their solubility (Scheme 1.2b). Some of the properties of polymer ***l*-P*n***$_{\mathrm{C8}}$ (n = 30–50) will be described in the following chapters.

1.3 Synthesis of Conjugated Nanorings

The conversion of linear π-conjugated oligomers into their cyclic analogues is not only a synthetic challenge. The study of these cyclic oligomers is expected to provide new insights into electronic delocalization. For example, the highly efficient energy transfer in natural light harvesting complexes is, at least in part, due to the highly symmetric circular arrangement of chromophores.[7] Fully π-conjugated nanorings are also intriguing compounds because they combine an “end-free” π-electron system with well defined size and shape. The lack of end-group effects, change in symmetry and in some cases the presence of ring strain, often result in surprisingly different linear as well as non-linear optical properties compared to their acyclic analogues. Furthermore, the rigidity of conjugated macrocycles has been exploited in host-guest systems in solution and on surfaces. Despite these promising properties, the synthesis of such nanorings remains challenging: many approaches either rely on statistical oligomerizations that lead to a mixture of ring sizes or apply a lengthy stepwise synthesis. The synthesis of belt-like conjugated macrocycles with radially aligned p-orbitals (as in carbon nanotubes) is particularly difficult because these compounds are often strained.

1.3.1 Synthesis of Unstrained Nanorings

Three general strategies exist for the synthesis of large π-conjugated nanorings: 1) intramolecular ring-closure of either a flexible or already bent linear precursor, 2) cyclo-oligomerization of small bent building blocks, which usually results in a mixture of different ring sizes and 3) covalent or non-covalent template-directed cyclization. While linear polymers are the major by-products in all these strategies, it is particularly important to perform intramolecular cyclizations under high-dilution conditions to avoid intermolecular coupling. An impressive example of this strategy is Mayor’s synthesis of the giant molecular ring **10** with a diameter of 12 nm (Scheme 1.3).[56] The ring consists of linear *para*-phenylethynylenes with thiophene corner units in order to allow cyclization without inducing strain. The linear hexadecamer ***l*-10** synthesized in a stepwise procedure was cyclized under high dilution conditions (8×10^{-6} M) using copper(II) acetate mediated oxidative acetylene coupling to give the nanoring in 38% yield.

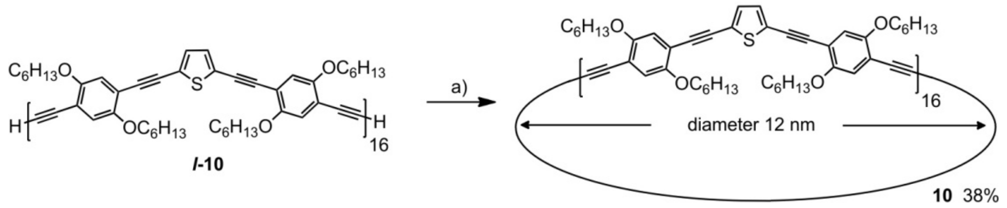

Scheme 1.3. *Mayor's giant nanoring as an example of intramolecular cyclization. Reagents: a) Cu(OAc)$_2$.*

A cyclo-oligomerization approach was chosen by Iyoda for the synthesis of a series of oligothiophene ethynylene macrocycles **12**–**16** (Scheme 1.4).[57] The pentathiophene precursor **11** with terminal aldehyde groups was cyclized using McMurry coupling to give a statistical mixture of various ring-sizes with 10, 15, 20, 25 or 30 thiophene units, which could be separated using gel permeation chromatography. The two-photon absorption in the macrocycles is almost one order of magnitude higher than in linear oligo or polythiophene derivatives, which the authors attribute to efficient electronic delocalization in the nanorings.[58] It was found that the electronic delocalization reaches a limit at 18 thiophene units: the excited state is delocalized over this length and the two-photon cross-section per thiophene unit does not increase above this ring size.[59]

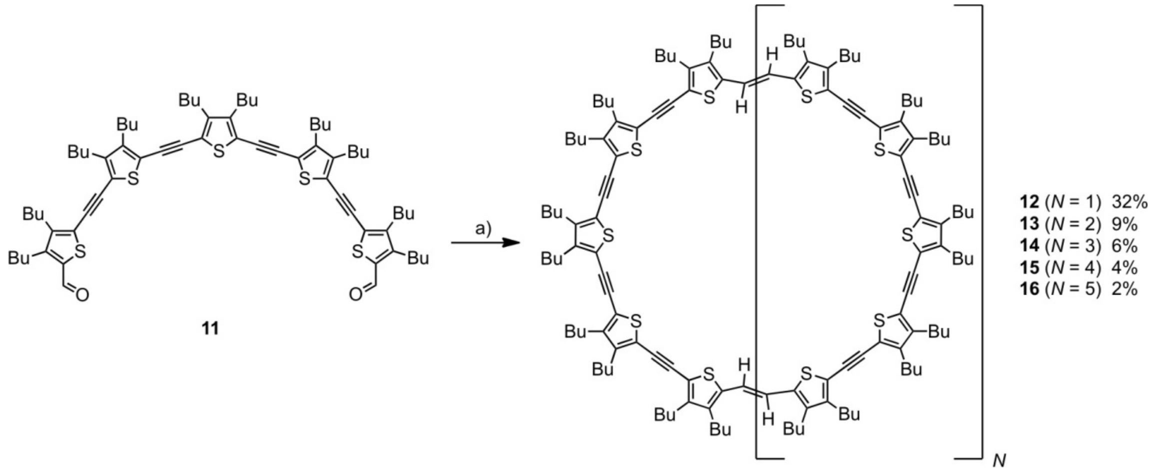

Scheme 1.4. *Cyclo-oligomerization approach for the synthesis of thiophene ethynylene macrocycles by Iyoda. Reagents: a) TiCl$_4$, Zn, pyridine.*

The group of Bäuerle has developed a number of routes to different cyclic oligothiophenes.[60-62] Their elegant cyclo-oligomerization route is shown in Scheme 1.5 and involves the formation of a statistical mixture of multinuclear dithienyl platinum complexes **18** that are converted into oligothiophenes **19**–**24** by reductive elimination. The 57% overall yield of cyclic species demonstrates the efficiency of this step-wise approach. The optical gap and the oxidation potential of these nanorings is significantly reduced compared to their linear analogues, which has been attributed to a more planar geometry in the rings.[62]

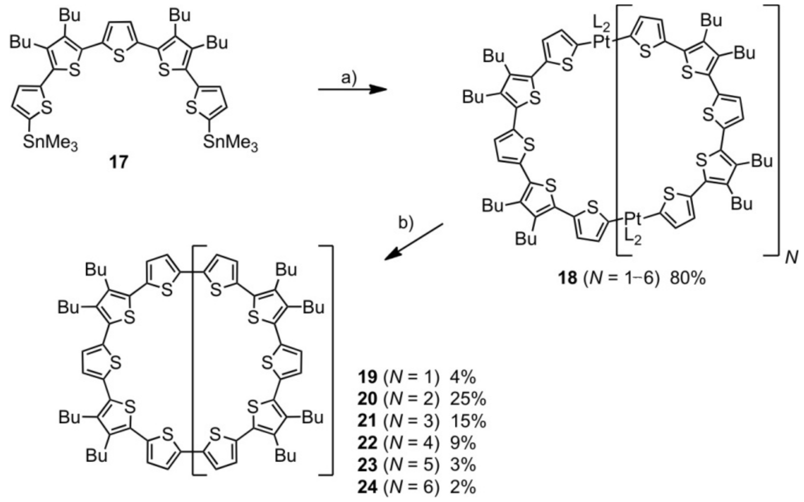

Scheme 1.5. *Bäuerle's synthesis of a cyclic oligothiophene. Reagents: a) Pt(cod)Cl_2; b) dppf, then 140 °C. L_2 = cod = 1,5-cyclooctadiene; dppf = 1,1'-bis(diphenylphosphino)ferrocene.*

An oligocyclization route has also been applied in the synthesis of fully conjugated porphyrin macrocycles. Sugiura and Sakata reported a porphyrin square tetramer (in 22% yield)[63] and dodecamer **25** (in 9% yield, Figure 1.8a)[64] from Glaser coupling of four corner units consisting of one and three porphyrin units, respectively. Besides simple NMR spectra due to the high symmetry of the compounds, the formation of squares was also confirmed by scanning tunneling microscopy (Figure 1.8b,c).

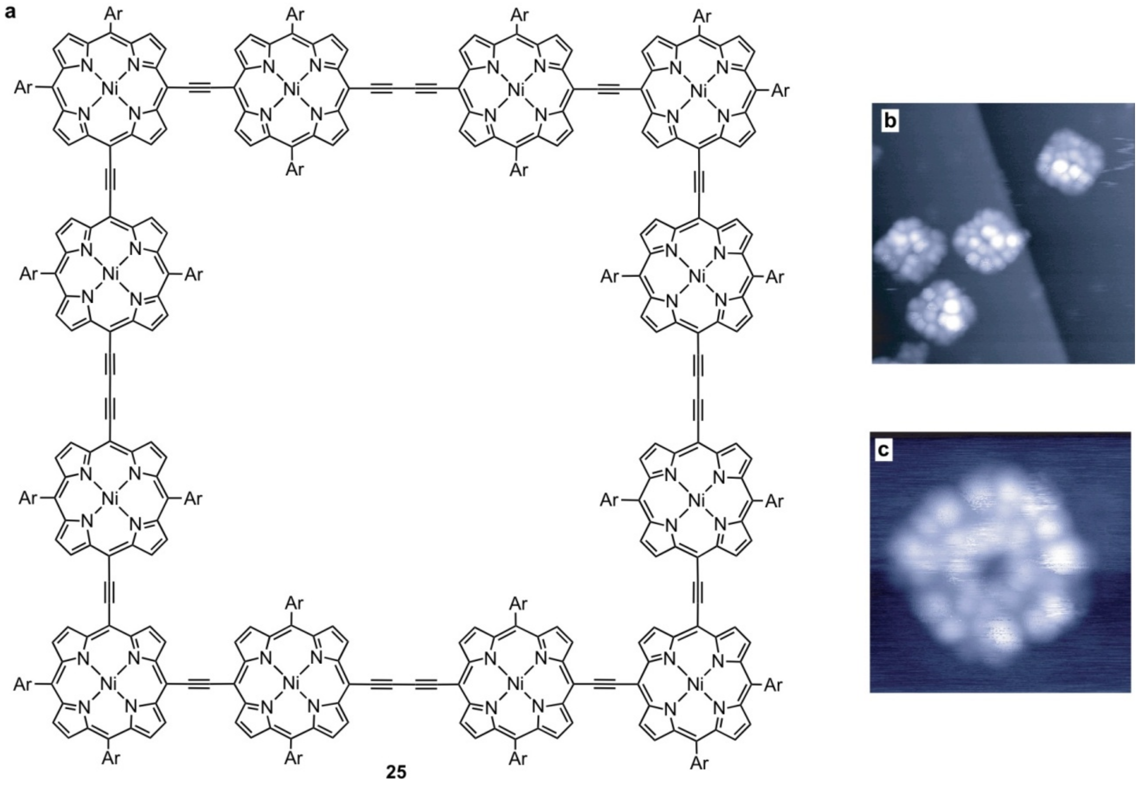

Figure 1.8. *(a) Sugiura's porphyrin dodecamer square* ***25****; (b) UHV-STM image of* ***25*** *deposited on a Cu(111) surface; (c) enlarged view of one macrocycle. STM images reprinted from ref. 64.*

A crucial improvement in the oligocyclization strategy was reported by Zhang and Moore.[63,64] Arylene ethynylene macrocycles such as **27** were synthesized in good yields (61–81%) using a highly reactive alkyne metathesis catalyst[65] (Scheme 1.6). The reaction is driven by the appropriate choice of R' groups: when R' is a methyl group the by-product (2-butyne) evaporates, while precipitation occurs when choosing R' to result in a sufficiently insoluble by-product. The precipitation driven reaction allows the large scale synthesis (~6 g) of macrocycle **27**. The metathesis approach takes advantage of the reversibility of the coupling reaction, resulting in formation of the thermodynamic product: a cyclic product is preferred to a linear chain for entropic reasons and the hexagonal macrocycle **27** is the enthalpically favored cyclic product due to its minimal strain. Although *meta*-phenylene based macrocycles, such as **27**, are cross-conjugated, this strategy appears to be highly promising for the synthesis of fully conjugated macrocycles.

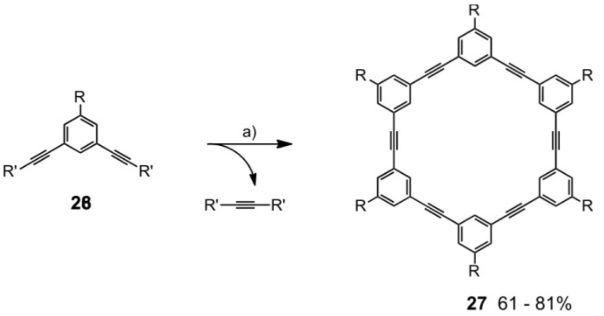

Scheme 1.6. *Precipitation-driven synthesis of arylene ethynylene macrocycles* ***27*** *by alkyne metathesis. Reagents: a) EtC≡Mo[NAr(tBu)]$_3$; R = OTEG, CO$_2$TEG; R' = Me, benzoylbiphenyl.*

Template-directed approaches to the synthesis of unstrained conjugated macrocycles include Höger’s spoked wheels,[66] and the cyclic oligocarbazole **29** (Scheme 1.7)[67] and oligofluorene[68] synthesized by Müllen’s group. Four tricarbazole units, covalently linked to the *meso*-positions of a porphyrin template, were coupled using Yamamoto conditions to afford the template bound oligocarbazole macrocycle. The template was removed by hydrolysis of the esters linking the porphyrin to the nanoring. Although the cyclization was carried out at low concentrations (8×10^{-5} M) to avoid intermolecular reactions, it proceeds in a significantly lower yield (9%) than in the case of Höger’s wheels (60%). The reason may be the high flexibility of the alkyl linkers between the template and the carbazole units. In a later study, a closely related conjugated carbazole nanoring was used to bind hexabenzocoronene on a highly oriented pyrolitic graphite (HOPG) surface.[69]

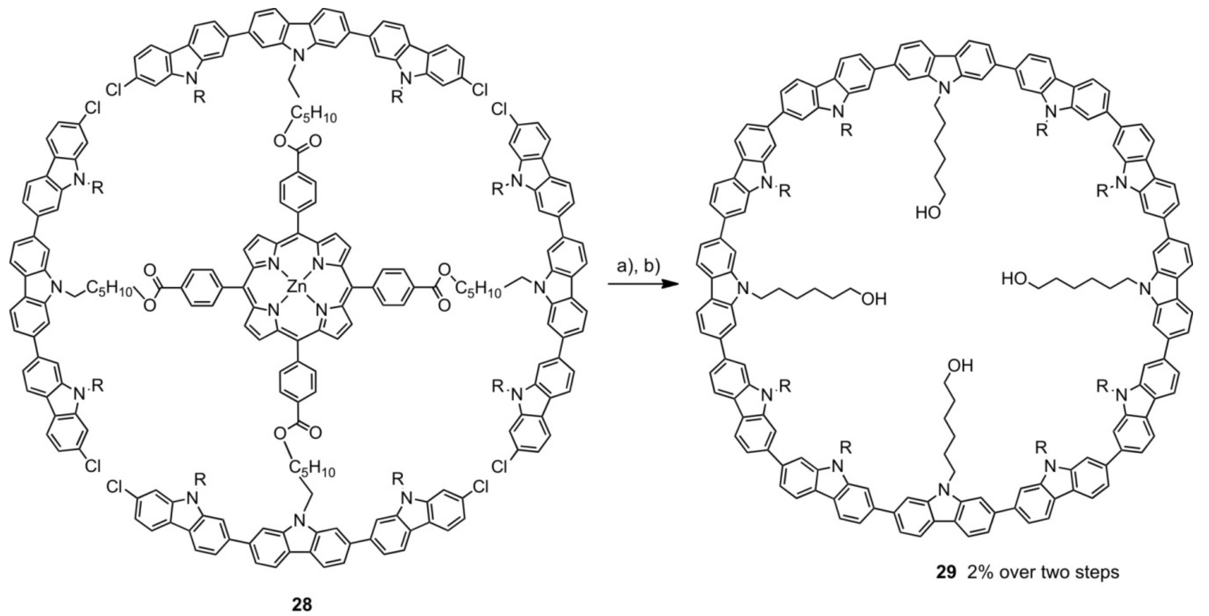

Scheme 1.7. Synthesis of Müllen's oligocarbazole macrocycle. Reagents and yields: a) Ni(cod)$_2$, 2,2'-bipyridine, 1,5-cyclooctadiene, 9%; b) KOH, 18%; R = 2-hexyldecyl.

1.3.2 Synthesis of Strained Nanorings

In general the synthesis of strained nanorings faces the same challenges as for unstrained rings and the same strategies as described above can be applied. However the presence of strain in the target nanorings provides an additional difficulty because formation of the cyclic product is enthalpically disfavored compared to an unstrained linear product. A common strategy to mitigate this problem is the synthesis of a partially unsaturated cyclic precursor followed by an efficient reaction that leads to formation of the strained conjugated nanoring. Oda and Kawase have synthesized a series of cyclic *para*-phenylacetylenes (*c*-PPA) **34–37** following this approach (Scheme 1.8a).[70,71] The unstrained precursors **30–33** were made by an oligocyclization of 4,4'-diformyl-(*Z*)-stilbene using McMurry conditions. Bromination of the double bonds followed by elimination using potassium *tert*-butoxide afforded *c*-PPAs **34–37** in varying yields. The high strain energy in the smallest nanoring **34** results in its explosive decomposition upon heating to 80° C under air and a general sensitivity towards oxygen. The larger, less strained rings are more stable but all *c*-PPAs have to be stored under an inert atmosphere. The *c*-PPAs are classified as molecular belts[72] because unlike the nanorings described so far, their p-orbitals are radially oriented, with the lobes pointing towards the center of the ring. This arrangement leads to the ability to bind other molecules that have a curved π-surface such as fullerenes ($K_a = 10^4$–10^6 M^{-1}),[73] and also allows the formation of 'onion complexes' between larger and smaller rings.[74,75]

Cycloparaphenylenes (*c*-PPs) were a long sought target for synthesis but only in the past few years three goups independently achieved their synthesis (Scheme 1.8b). Yamago[76] used a protocol similar to Bäuerle's cyclic oligothiophene synthesis, involving the formation of tetraplatinum square **38** followed by bromine induced reductive elimination giving [8]cycloparaphenylene **46** in 49% yield.

The *c*-PP syntheses reported by Bertozzi[77] and Itami[78,79,80] are both based on a final elimination step driven by aromatization in the formation of benzene. Bertozzi synthesized a statistical mixture of precursors **39**–**41**, containing angled 3,6-*syn*-dimethoxy-cyclohexa-1,4-diene units, by an oligocyclization Suzuki reaction. Lithium naphthalenide was found to be an efficient one electron donor to induce elimination of methoxy groups leading to the formation of [9]cycloparaphenylene **47**, [12]cycloparaphenylene **48** and [18]cycloparaphenylene **52**. The precursor chosen by Itami is nearly unstrained, allowing a controlled sequential synthesis without the need for a statistical oligomerization step. Square **42** was synthesized by stepwise Suzuki couplings linking the *cis*-1,4-diphenylcyclohexane corner groups. Insertion of additional phenyl units allows directed synthesis of precursors **43**–**45**. The unstrained precursors can then be converted to the corresponding cycloparaphenylenes **48**–**51** by heating with either acid or base.

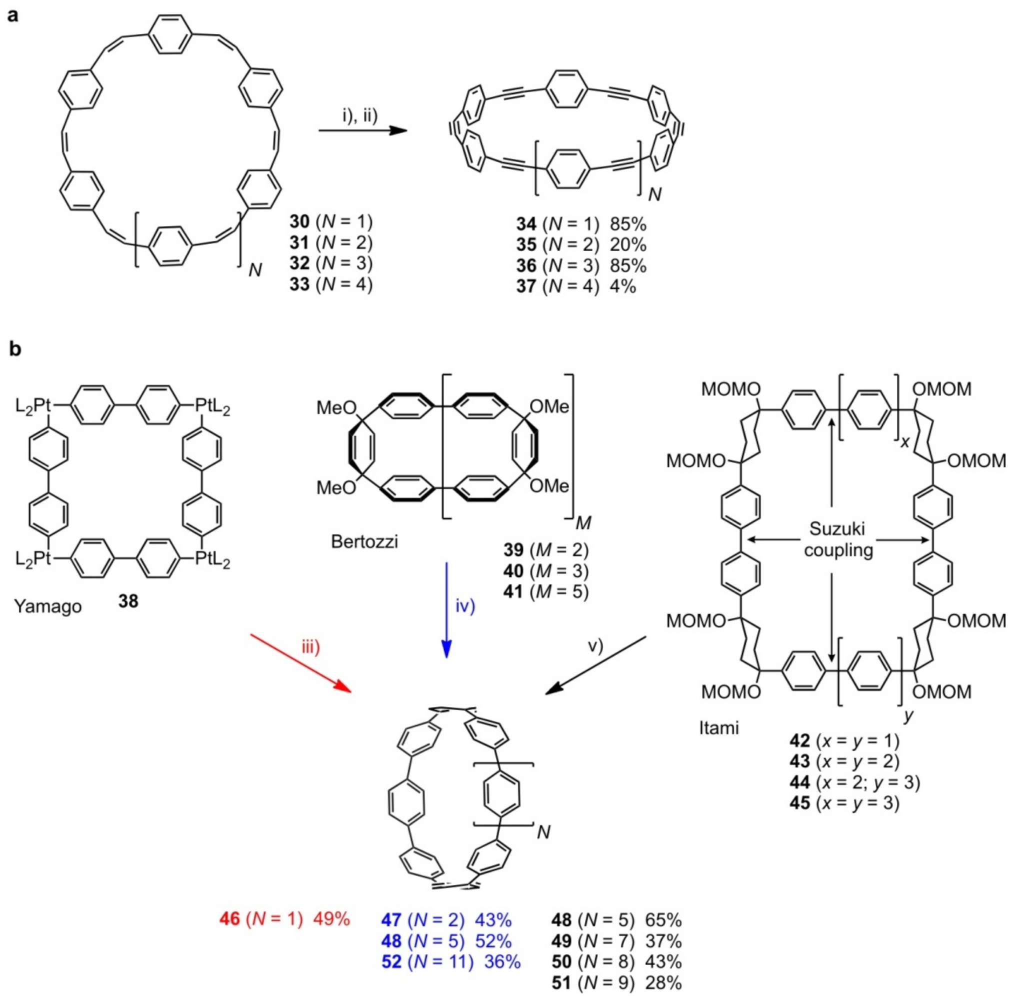

Scheme 1.8. *Synthesis of strained cyclic (a) para-phenylacetylenes and (b) para-phenylenes. Reagents: i) Br_2; ii) t-BuOK; iii) Br_2; iv) lithium naphthalenide; v) N = 5: p-TsOH, microwaves; N = 7,8,9: $NaHSO_4{\cdot}H_2O$. L_2 = dppf; p-TsOH = para-toluenesulfonic acid; MOM = methoxymethyl.*

It was found that the smallest *c*-PPs have extremely large Stokes-shifts, but apart from some theoretical studies, no in-depth analysis has been carried out to investigate the electronic structure of these nanorings. An important motivation for the synthesis of *c*-PPs is their use as templates for the controlled synthesis of carbon nanotubes with defined diameter, but to date no results have been published on this aspect.

Templates have been used with great success in the synthesis of macrocycles and in particular for porphyrin based systems.[81-84] Through the synthesis of a cyclic porphyrin octamer, Anderson's group demonstrated that by choice of an appropriate template, cyclization and induction of strain can be achieved in a single reaction (Scheme 1.9).[85] The crucial step was the design and synthesis of a complementary template that would allow efficient cyclization of deprotected linear octamer ***l*-dP8$_{C8}$**. The template **T8** forms a strong 1:1 complex with ***l*-dP8$_{C8}$** and subsequent Pd-catalyzed acetylene homo-coupling affords the nanoring template complex ***c*-P8$_{C8}$·T8** in 14% yield. In the final step the template was removed by addition of an excess of the competing ligand pyridine. Ultrafast fluorescence anisotropy measurements on the linear octamer template complex ***l*-dP8$_{C8}$·T8** showed that the excited state is delocalized around the whole circle.[86]

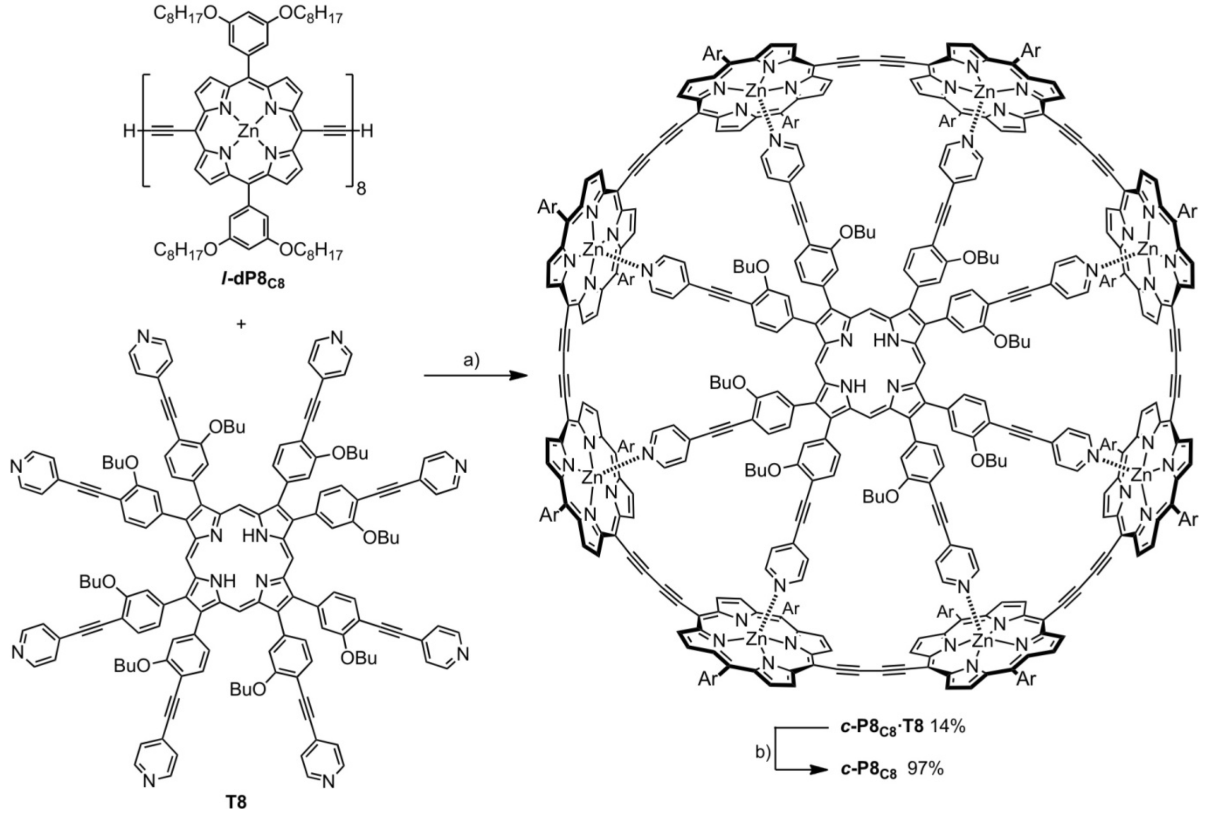

Scheme 1.9. *Template-directed synthesis of cyclic porphyrin octamer* ***c-P8$_{C8}$****. Reagents: a) PdCl$_2$(PPh$_3$)$_2$, CuI, I$_2$, i-Pr$_2$NH; b) pyridine.*

Following on from the synthesis of the cyclic octamer, Hoffmann and Anderson reported the template-directed synthesis of the even more strained cyclic hexamers ***c*-P6**/***c*-P6$_{C8}$**.[87] The cyclization was developed from an intramolecular ring-closure to a cyclo-oligomerization of three porphyrin dimers ***l*-P2**/***l*-P2$_{C8}$** coordinating to hexadentate template **T6** (Scheme 1.10). The synthesis of cyclic hexamer is significantly more convenient than that of cyclic octamer: porphyrin dimer is readily available, the template **T6** can be synthesized in two steps from commercial starting materials and the cyclization step is significantly more efficient (33–44% yield). The affinity of the template **T6** for the nanoring ***c*-P6** is extremely high ($K_a = 7 \times 10^{38}$ M^{-1}) due to the excellent geometric fit and the presence of chelate cooperativity between the 'arms' of the template. From binding titrations the Gibbs free energy required to bend the linear hexamer ***l*-P6** into the cyclic conformation was determined to be 101 kJ mol^{-1}. Steady-state absorption and emission spectra in combination with basic DFT calculations indicate a decrease of the HOMO-LUMO gap in the nanoring compared to the linear hexamer and was interpreted as a sign of more efficient conjugation in the cyclic species.

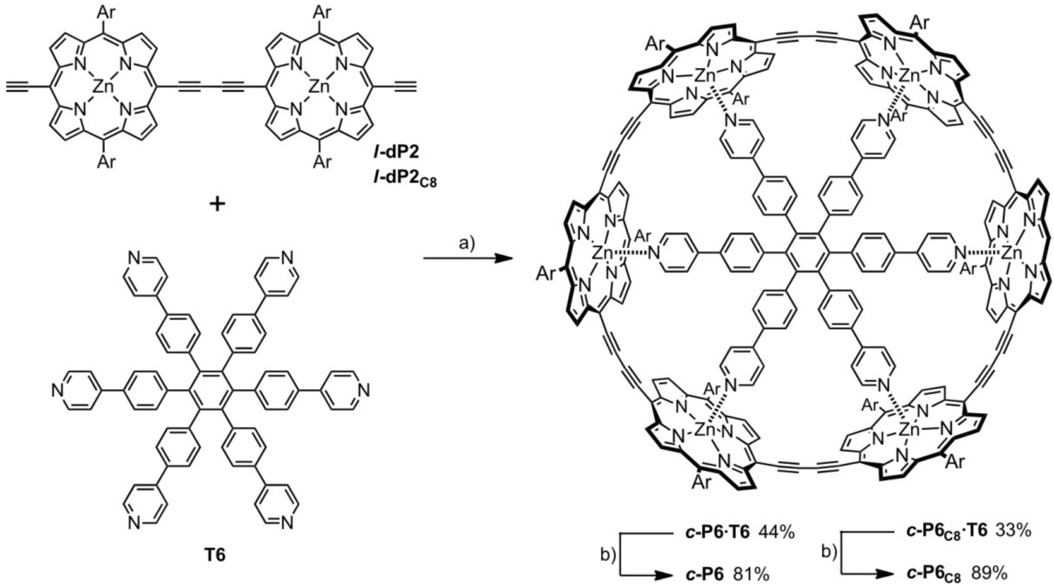

Scheme 1.10. *Template-directed synthesis of cyclic porphyrin hexamers* ***c-P6/c-P6$_{C8}$****. Reagents: a) $PdCl_2(PPh_3)_2$, CuI, I_2, i-Pr_2NH; b) DABCO. For* ***PN****, Ar = 3,5-bis-tert-butyl phenyl; for* ***PN$_{C8}$****, Ar = 3,5-bis-octyloxy phenyl.*

1.4 Cooperativity in Supramolecular Porphyrin Assemblies

In a zinc porphyrin the tetradentate porphyrin ligand and the Zn center form a square-planar complex. In this complex the coordination sphere of Zn^{2+} is not saturated and addition of a monovalent nitrogen containing ligand results in formation of a pentacoordinated square-pyramidal complex. Binding of this exocyclic axial ligand in solution is weak and reversible, and due to its directionality this binding motif has been widely exploited in the formation of supramolecular porphyrin assemblies and in template-directed synthesis (as shown above).[88,89] Coordination of a sixth ligand to form an octahedral complex is extremely weak but is often observed in the solid state.[90]

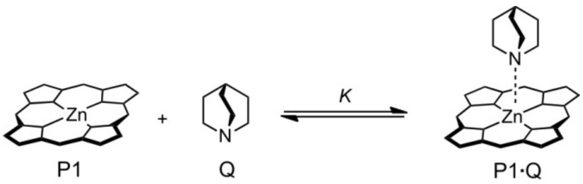

Scheme 1.11. *Binding of quinuclidine (Q) to zinc porphyrin monomer (P1). For clarity nitrogen atoms and double bonds are removed in the porphyrin structure.*

Scheme 1.11 shows the equilibrium that governs the formation of the complex P1•Q from binding of a quinuclidine ligand Q to a zinc porphyrin monomer P1. This equilibrium is described quantitatively by the binding constant *K*, described by Equation (1.1).

$$K = \frac{[\mathrm{P1} \cdot \mathrm{Q}]}{[\mathrm{P1}][\mathrm{Q}]} \tag{1.1}$$

The binding constant depends on electronic and steric parameters of both binding partners as well as the solvent and the temperature. Room temperature binding constants for the interaction of ligands such as pyridine or quinuclidine with zinc porphyrins in non-competitive solvents (e.g. toluene, $CHCl_3$) are in the range of 10^3–10^6 M^{-1}. This binding strength implies that a 1:1 mixture of the two components forms the complex nearly quantitatively at common NMR concentrations (~10^{-3} M). At concentrations typical for a UV/vis absorption or fluorescence experiments (~10^{-6} M), complex formation is incomplete and an excess of ligand has to be added to saturate the zinc binding site. The determination of binding constants by supramolecular titrations requires a quantifiable amount of all species in solution. Thus the upper limit for direct measurement of binding constants is about 10^4 M^{-1} for NMR titrations, 10^7 M^{-1} for UV/vis absorption and 10^8 M^{-1} for fluorescence titrations. Larger binding constants can be determined by means of competitive "break-up" or "denaturation" experiments where a weaker binding ligand, of known binding strength, is added in excess to a complex until the original ligand is displaced.[50]

If more than two binding partners are involved in a supramolecular binding process, cooperativity between the components has to be taken into account: binding of one ligand can influence the binding strength of another ligand.[91] If the presence of the first ligand increases the binding strength of the second ligand the process shows positive cooperativity, if the second binding event is disfavored by the first one, there is negative cooperativity. In the extreme case of positive cooperativity we observe all-or-nothing behavior, where the only two species in significant concentrations are the free, unbound receptor and the receptor with both ligands bound. Cooperative processes also tend to be "all-or-nothing" in the macroscopic sense that the system moves from fully unbound to fully bound in response to a small change in ligand concentration.

1.4.1 Allosteric Cooperativity

Hemoglobin, the oxygen transporter in our blood, can bind four molecules of oxygen. Binding of oxygen at one site increases the affinity of the other sites for oxygen which results in a very narrow switching window from free to oxygen-saturated hemoglobin. This behavior is called positive allosteric cooperativity: several molecules of a monodentate ligand bind to a receptor with multiple binding sites that are covalently linked. Another potential example for allosteric cooperativity is the binding of quinuclidine Q to a porphyrin dimer P2 (Scheme 1.12). The binding constants for this two-step process are given by Equations (1.2) and (1.3).

$$K_1 = 2K \tag{1.2}$$

$$K_2 = 0.5\alpha K \tag{1.3}$$

The factors 2 and 0.5 are statistical factors[92] that reflect the degeneracy of the intermediate complex P2•Q and link the binding constants K_1 and K_2 to the microscopic binding constant K. In the first step there are two possible ways to bind the ligand, but only one way to release it. In the second step there is only one quinuclidine receptor but two sites from which it can be released.

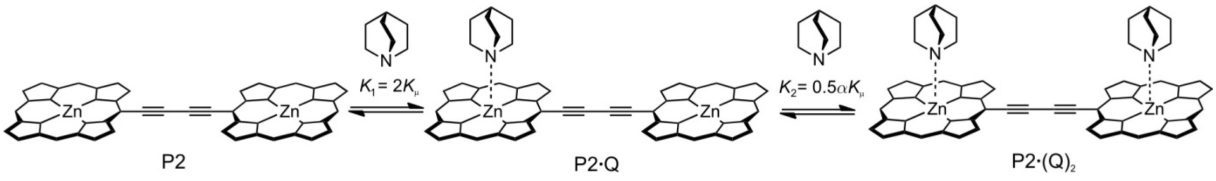

Scheme 1.12. Binding of quinuclidine (Q) to porphyrin dimer (P2). For clarity nitrogen atoms and double bonds are removed for in the porphyrin structure.

The allosteric cooperativity between the ligands is quantified by the interaction parameter α. In the case of positive cooperativity, where the second molecule of quinuclidine binds stronger than the first one, then $\alpha > 1$. If the second molecule binds weaker, for example due to steric interactions with the first ligand, then $\alpha < 1$, and in the absence of cooperativity $\alpha = 1$. Experimentally it was found that there is no cooperativity between the two molecules of quinuclidine binding a porphyrin dimer ($\alpha = 1.1 \pm 0.4$ in toluene).[50]

The determination of α can be difficult, particularly in larger, more complex systems. An alternative way of describing allosteric cooperativity is the Hill coefficient n_h that can be directly obtained from a binding isotherm and does not even require knowledge of the stoichiometry of a complex.[93] In a Hill plot log $(\theta/(1-\theta))$ is plotted against log [Q], where θ is the binding site-occupancy and [Q] is the ligand concentration. The slope of this plot in the central region ($\theta = 0.5$) is the Hill coefficient. Positive cooperativity results in a slope greater than 1, negative cooperativity leads to a slope of less than one. The steepness of the Hill plot is a measure of how quickly the system switches from an unbound to a bound state upon increasing ligand concentration. A system with large positive allosteric cooperativity will express all-or-nothing behavior and switch in a very narrow concentration window.

1.4.2 Chelate Cooperativity

Double-strand formation of DNA is a highly cooperative process where two strands, each with multiple covalently linked binding sites, form a complex. Since the binding sites of both the host and the guest are each covalently linked, the cooperativity is now intramolecular (compared to the intermolecular allosteric cooperativity) and is termed chelate cooperativity.

The addition of a bidentate ligand such as 1,4-diazabicyclo[2.2.2]octane (DABCO) D to porphyrin dimer P2 results in the formation of the double strand complex $(P2)_2{\cdot}(D)_2$.[27,50] Scheme 1.13 shows the last two steps of double-strand formation. In the first step a molecule of DABCO binds to the outside of the sandwich complex $(P2)_2{\cdot}D$ followed by the intramolecular ring-closure. The chelate effect, which favors this cyclization event over the first intermolecular process, is quantified by the effective molarity *EM* as defined by Equation (1.4).

$$EM = \frac{K_{\text{intra}}}{K_{\text{inter}}} \tag{1.4}$$

The effective molarity corresponds to the concentration threshold from which an intermolecular binding process would be preferred over the intramolecular ring closing event. At high concentrations this will eventually lead to the formation of a supramolecular polymer, explaining why many multicomponent chelate complexes do not exist in the solid state.

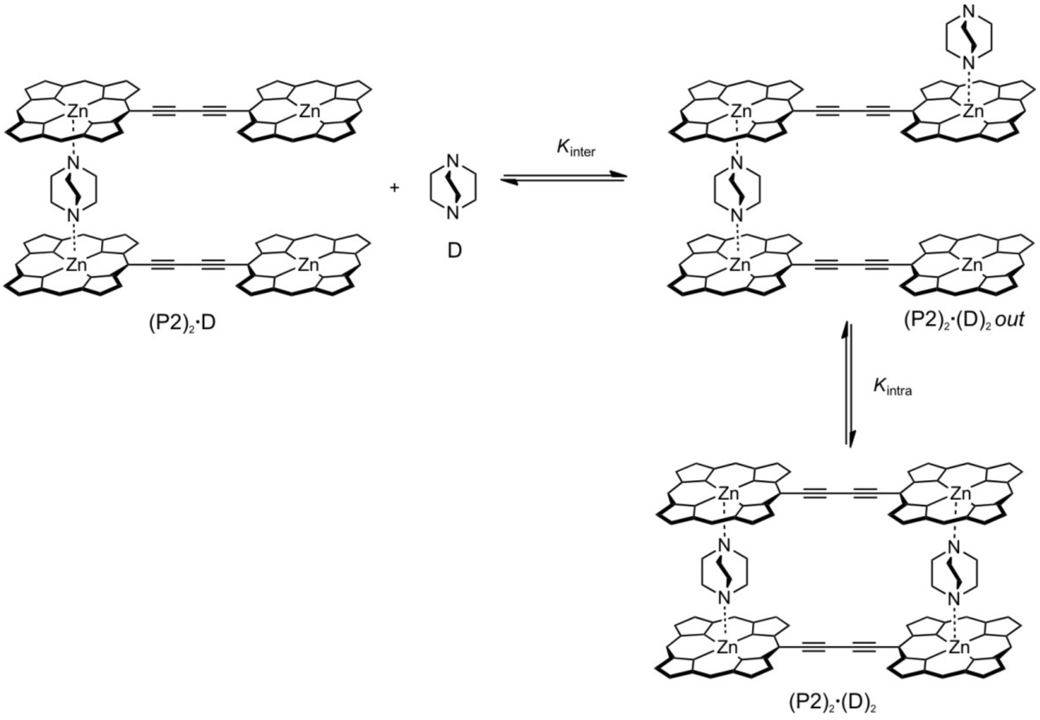

Scheme 1.13. *Ladder formation between porphyrin dimer (P2) and DABCO (D). For clarity nitrogen atoms and double bonds are removed for in the porphyrin structure. For simplicity statistical factors are not used here. As described above and in ref. 50, the interaction parameters α in this process are all 1 and so they were not considered for this equilibrium.*

For a double-strand complex from linear oligomers ***l*-P*N*$_{C8}$** and DABCO, effective molarities between 2 and 5 M have been measured (depending on oligomer length), indicating strong chelate cooperativity in these complexes.[94] Binding titrations also showed that double-strand formation is an all-or-nothing process with negligible populations of intermediate structures.

In the double-strand complexes the porphyrin oligomers are held in a co-planar conformation, resulting in increased intensity of the most red-shifted part of the Q absorption band[27] and more efficient charge transport along the backbone.[48] This example illustrates how Zn-N interactions can be used to control the electronic structure of butadiyne-linked porphyrin oligomers.

1.5 Introduction to Small Angle X-ray Scattering (SAXS) in Solution

Some of the molecules or assemblies presented in this thesis reach molecular weights of more than 10 kDa and extend over nearly 10 nm. To obtain detailed structural information on such macromolecules other techniques are required in addition to the classical methods used for small molecules. Information on the three-dimensional structure of small molecules can be obtained from crystallography or NMR techniques such as NOESY or DOSY. However, with increasing molecular weight it becomes difficult to obtain crystals suitable for X-ray diffraction and NOE signals can usually only be observed at distances smaller than 0.6 nm. DOSY is a useful technique to estimate molecular volumes but does not allow more detailed structural information to be extracted. Synthetic monodisperse macromolecules of comparable dimension to the porphyrin oligomers are rare, but biological macromolecules such as proteins usually have similarly well-defined structures. The molecular weights of proteins can be significantly higher than that of the porphyrin oligomers studied here, but due to their tight folding they often have comparable volumes. The comparison between the calculated structures of linear and cyclic porphyrin oligomers ($MW = 6$ kDa) with the crystal structure of the green fluorescent protein[95] ($MW = 30$ kDa) demonstrates this tendency (Figure 1.9). Small angle X-ray scattering (SAXS) in solution has emerged as an important technique to study proteins in solution due to relatively simple sample preparation and its complementarity with crystallography.[96-98] In recent years Tiede and Wasielewski pioneered the use of this technique in the analysis of synthetic supramolecular assemblies and demonstrated its great potential in this area.[9,99,100]

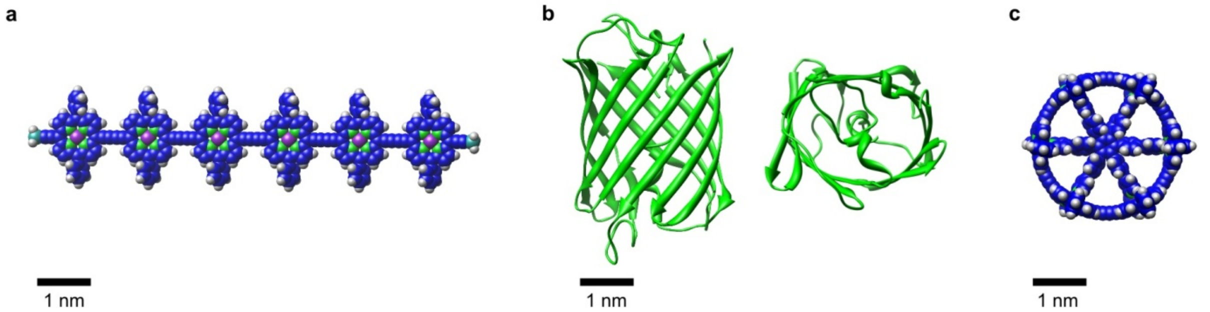

Figure 1.9. *Comparison of the dimensions of some molecules synthesized for this thesis (a) linear porphyrin hexamer **l-P6** and (c) cyclic porphyrin hexamer **c-P6·T6** with (b) the green fluorescent protein (GFP) viewed from the side (left) and from top (right). Structures of porphyrin oligomers were calculated using the MM+ force field implemented in HyperChem^{TM}, the coordinates of the crystal structure of GFP (resolution 1.9 Å) are from ref. 95 and the image was prepared using the program Chimera.*

1.5.1 Background on SAXS

In a SAXS experiment a sample (dissolved in water or an organic solvent) is irradiated with a collimated beam of high intensity X-rays typically produced by a synchrotron. Most of the incident X-rays (λ = 0.8–1.5 Å) pass through the sample but some of the light is elastically scattered by the electrons in the sample at the angle 2θ. The origin of the scattering lies in oscillations of the electrons under the influence of the electric field of the X-rays. This makes each electron the source of new spherical waves with the same wavelength as the incident X-rays. The spherical waves from different electrons in the molecule, at distance r, interfere and create a scattering pattern on the detector (Figure 1.10). The scattering angle 2θ is typically expressed as the momentum transfer vector q and the two values are related by Equation (1.5) with λ being the wavelength of the incident X-rays.[96]

$$q = \frac{4\pi \sin\theta}{\lambda} \tag{1.5}$$

The momentum transfer vector q (‘reciprocal space’, in Å^{-1}) can be converted to the distance between two electrons r (‘real space’, in Å) by Equation (1.6).[97]

$$r = \frac{2\pi}{q} \tag{1.6}$$

From this equation one can easily access the maximum resolution (defined as r_{min}) of a SAXS experiment, because it only depends on the maximum measured q-value (e.g. the widest angle) and is in theory only limited by the X-ray wavelength λ. However, the fact that SAXS is a contrast technique often further limits the maximum resolution: most of the scattering in a sample is not from the solute but from solvent molecules, and the scattering spectrum is obtained by subtracting the solvent background spectrum from the sample spectrum. Usually the solvent molecules are in the size range of several angstroms (the diameter of toluene is 5.5 Å), resulting in very strong solvent scattering at wide angles (for toluene approximately q > 1.1 Å^{-1}). At these wide angles, the intensity of the sample scattering can be lower than 1% of the solvent scattering which makes background subtraction challenging.[99] Usually resolutions up to 5 Å can be achieved, but with careful background subtraction values as low as 1 Å have been reported.[101]

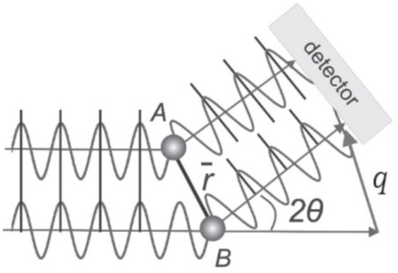

Figure 1.10. *Definition of the angle 2θ and the momentum transfer vector q from scattering of two electrons A and B at distance r. Figure reprinted from ref. 98.*

The principles of SAXS in solution and X-ray diffraction from single crystals are identical, but there is an important difference: in a single crystal the molecules are highly organized, whereas in solution the molecules have random orientations in relation to each other and to the detector. The resulting scattering pattern is therefore continuous and radially symmetric compared to the familiar diffraction pattern arising from a single crystal (Figure 1.11). As the SAXS spectrum is radially symmetric, it is essentially a one-dimensional spectrum that contains less information compared to the two-dimensional diffraction pattern from a crystal. A diffraction pattern contains information on the distance and orientation between two electrons and can be used to calculate a molecular structure with atomic resolution. Since molecules lose their relative orientation in solution, the SAXS curve gives only information about the distances between electrons which can be obtained as the Fourier transform of the scattering spectrum. The resulting curve is the electronic pair-distribution function (PDF) which is the normalized probability of a pair of electron densities at distance r (Figure 1.11). Structural information such as the largest distance in the molecule $r_{\max}$ is directly accessible from the PDF. Peaks in the PDF can often be assigned to distances between parts of the molecule with high electron densities (e.g. metal atoms).

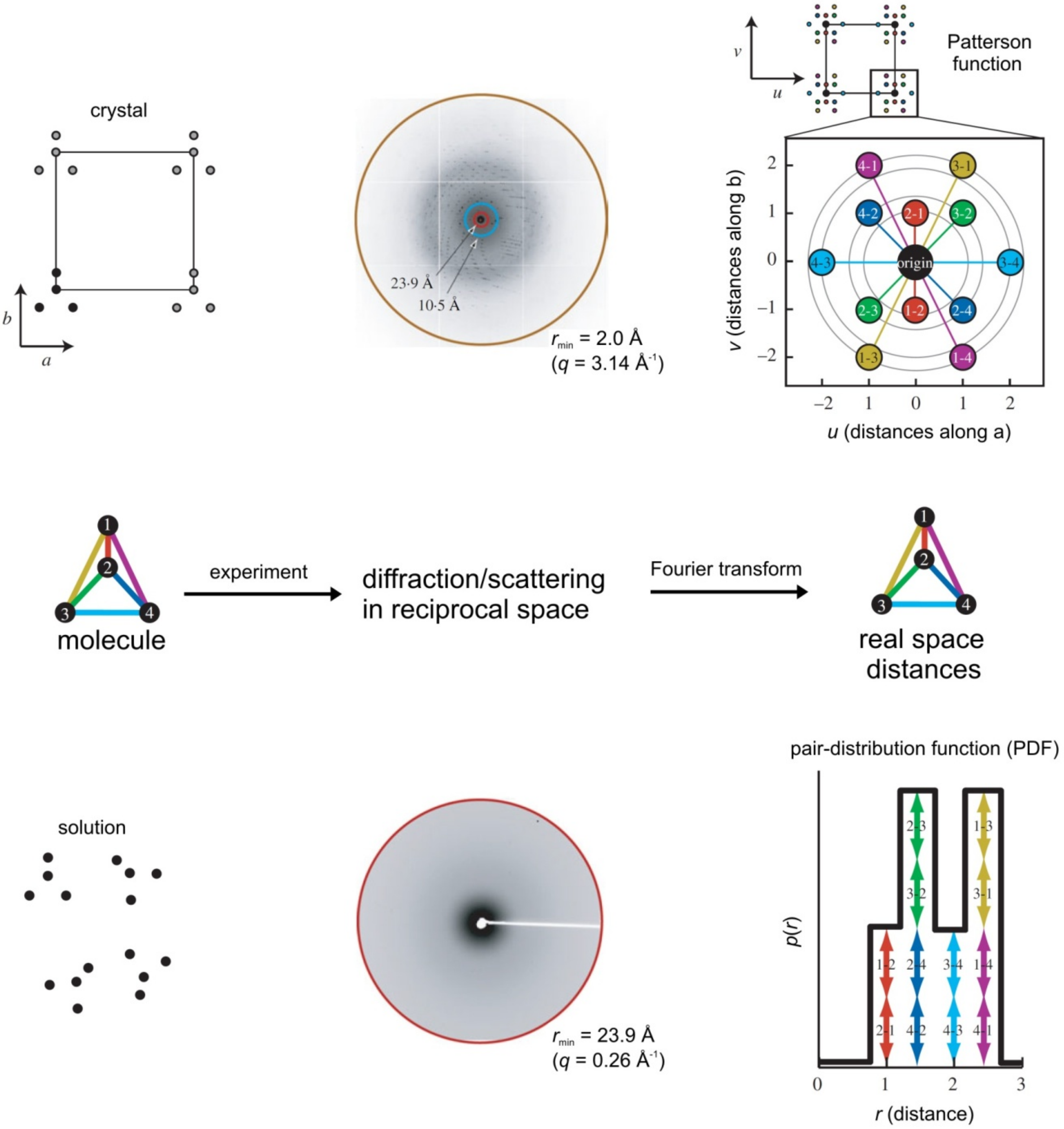

Figure 1.11. *Comparison of X-ray diffraction (top row) with SAXS (bottom row). The scheme in the middle shows the steps (data acquisition and Fourier transform) that are carried out in both experiments. The diffraction pattern (top middle) is from a superoxide dismutase crystal and the blue circle shows the maximum resolution (2.0 Å).The red circle in the diffraction pattern illustrates the comparably lower resolution of the SAXS pattern (bottom middle) of 23.9 Å. All figures reproduced with permission from ref. 97.*

Although less structural data is obtained directly, and the resolution tends to be lower than in X-ray diffraction, SAXS can be advantageous. The growing of single crystals which is a great challenge when working with macromolecules can be avoided and any sample that is sufficiently soluble can be analyzed. Additionally SAXS can capture structural dynamics in solution, whereas crystal structures only give one conformation. This is particularly important in the analysis of proteins that are naturally situated in aqueous environments where conformational effects can have a large influence on their function.[97]

Unlike in crystallography where diffraction data can be solved by direct methods to give the coordinates of the unit cell, in SAXS a number of different parameters needs to be used to gain information on the structure. The extrapolated scattering intensity at zero angle $I(0)$ is proportional to the concentration of electrons in the sample. If the mass concentration c of the sample (X) is known, the molecular weight MW can be calculated from $I(0)$ using a calibration standard (ST) with known mass concentration and molecular weight using Equation (1.7).[102]

$$MW_{\mathrm{X}} = \frac{I(0)_{\mathrm{X}}}{c_{\mathrm{X}}} \times \frac{c_{\mathrm{ST}}}{I(0)_{\mathrm{ST}}} MW_{\mathrm{ST}} \tag{1.7}$$

The radius of gyration R_g is the root mean square distance of all electrons in a molecule from its center of gravity and gives a measure of molecular size. R_g can be determined directly from the scattering data at very small angles ($q \times R_g < 1.3$) by fitting to the Guinier equation (1.8).[103]

$$I(q) = I(0)\exp(\frac{-R_g^2 q^2}{3}) \tag{1.8}$$

A plot of ln $I(q)$ against q^2 gives R_g from the gradient and $I(0)$, required for calculation of the molecular weight, as the intercept. Fourier transforms of the scattering data are only reliable if the sample is monodisperse. Polydispersity, either due to an impurity, aggregation or the presence of a mixture of conformations, usually results in a non-linear Guinier plot, which is a good indicator of data quality and gives a means to decide whether further processing is appropriate.

Ideally a Fourier transform of the scattering data should be carried out over the entire q-range, but since this is experimentally impossible, indirect Fourier transform methods for finite q-ranges have been developed.[105] The program GNOM[105] developed by Svergun is widely used for this purpose although others exist as well.[106,107] Besides the PDF, GNOM also gives R_g and $I(0)$ values that are evaluated over the whole q-range and not only in the Guinier region at very small angles. This usually makes the values determined by GNOM more reliable than a Guinier fit.[97]

The most detailed structural information can be obtained by comparing the experimental scattering data, the radius of gyration and the pair-distribution function with data simulated from a molecular model. The simulation of a scattering curve is not trivial because of the influence of the solvation shell that surrounds the solute. For all the work in this thesis the program CRYSOL[108] was used to generate scattering curves from molecular models. The program uses the atomic coordinates and the electron density of the solvent (e.g. toluene 0.283 e/Å^3)[109] to simulate a scattering curve by fitting to the experimental scattering curve. A curve can also be obtained without fitting to the experimental data, however since the program was written for analysis of proteins, parameters such as the thickness and the contrast of the solvation shell are all parameterized for aqueous solutions. From the simulated scattering curve the radius of gyration can be obtained from a Guinier fit and the program GNOM can be used to create a PDF (and give R_g). The agreement between experimental and simulated scattering curves and PDFs is the most important criterion for the evaluation of a structure. If the quality of the fits deviates between the scattering data and the PDF it is advisable to rely more on the agreement in the scattering data because artifacts from the Fourier transform can influence the shape of the PDF.[98]

A difficulty in analyzing SAXS data from large molecules in solution is to capture structural dynamics due to conformational changes. Since this information is not contained in a single rigid molecular model, the simulated SAXS data can significantly deviate when analyzing a conformationally flexible molecule or assembly. It has been shown that Monte Carlo or molecular dynamics (MD) methods can be used to adequately simulate SAXS data in such cases.[110,111] This approach not only allows verification of SAXS data, but can also be used in reverse to validate the parameterization of force fields used for MD simulations on macromolecules.

A further computational method to obtain three dimensional structures from experimental scattering curves is the so called *ab-initio* calculation.[96,97] Programs such as DAMMIN[112] can calculate coarse bead (or dummy atom) models directly from the scattering curve without the requirement of a molecular model. The program assumes a starting shape and calculates its scattering curve that is then compared to the experimental scattering data. By iteratively minimizing the discrepancy between the two curves a low resolution structure can be obtained. Often these structures are crude and give only the rough shape of an object, but they are useful to validate molecular models.[97]

1.5.2 Example for SAXS-Analysis: A Triphenylamine Functionalized β-Cyclodextrin

In order to provide a practical example for the reader, the SAXS analysis of a functionalized β-cyclodextrin is presented in the following. β-Cyclodextrin is a commonly used macrocycle in the synthesis of conjugated polyrotaxanes. Dr. Giuseppe Sforazzini functionalized all 21 hydroxyl groups with triphenyl amine (TPA) groups. This TPA functionalized cyclodextrin monomer is a model compound for polyrotaxane insulated molecular wires also prepared by Sforazzini. SAXS analysis was carried out to acquire information on the solution structure of the macrocycle, particularly to determine its diameter. This parameter could then be used to determine the structure of the polyrotaxane using SAXS.

I acquired SAXS data for this sample at beamline I-22 at the Diamond Light Source. The experimental scattering data shown in Figure 1.12a were obtained from the two dimensional SAXS pattern by sector integration using the program DREAM written by Dr. Marc Malfois at Diamond. Mike Wykes (University of Mons, Belgium) performed MD simulations on the compound which gave 10,000 structures, for each of which a scattering curve was simulated using CRYSOL. The average of these curves gives an excellent fit to the experimental scattering data. The radius of gyration for both the experimental and the simulated data, obtained using the program GNOM, match closely and identical values were found from Guinier fits (Figure 1.12b). GNOM was used to perform a Fourier transform of both data sets and the resulting PDFs are shown in Figure 1.12d. Excellent agreement between the two curves was found and the longest distance between two electrons in the molecule $r_{\max}$

determined from the PDF matches the value measured in the model. In summary, good agreement between experimental and simulated data was found for all three criteria under investigation, thus confirming the accuracy of the proposed molecular model.

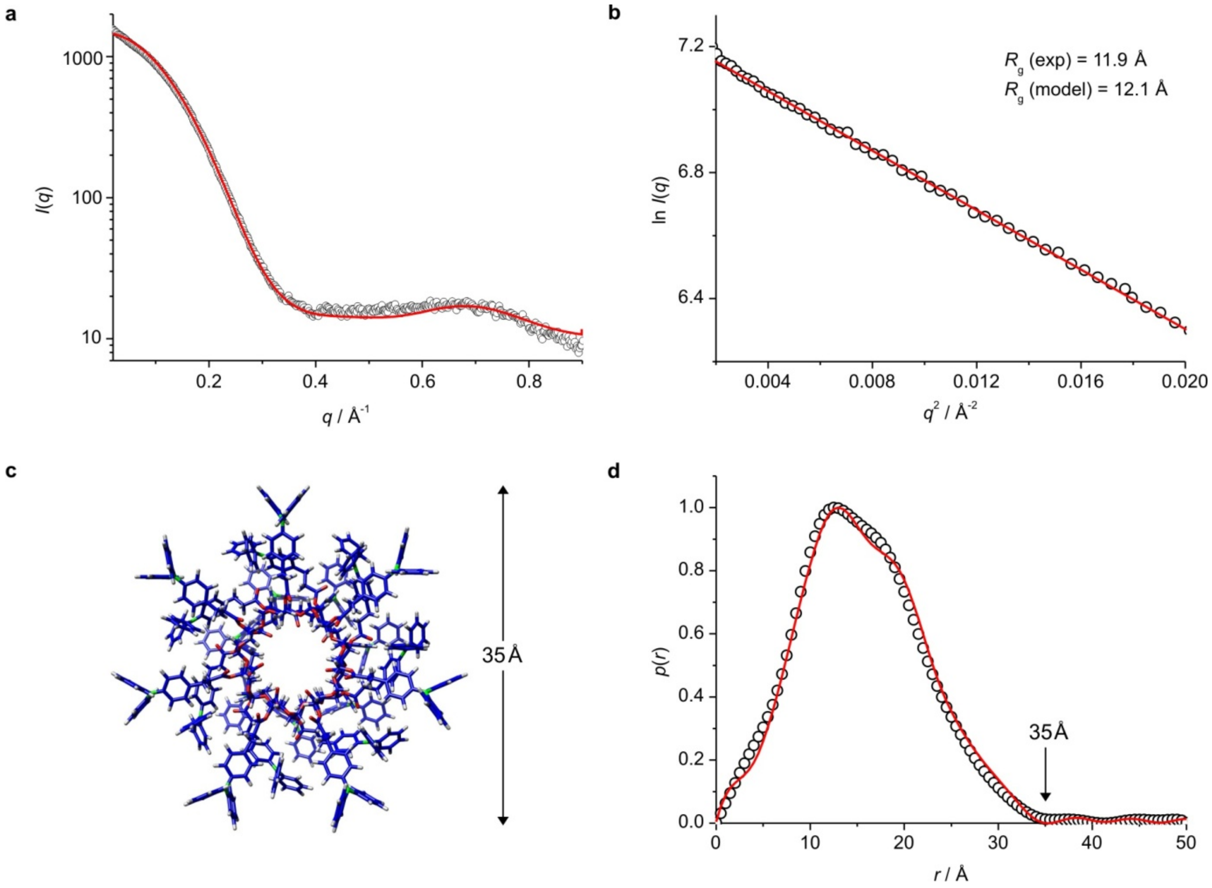

Figure 1.12. *SAXS analysis of triphenylamine functionalized β-cyclodextrin in toluene at 295 K collected at Diamond Light Source, UK. (a) Experimental (black circles) and simulated (red line) scattering curves; (b) Guinier plot with experimental scattering (black circles) and Guinier fit (red line); (c) molecular model minimized with the MM+ force field implemented in HyperChem^{TM}; (d) pair-distribution function from experimental data (black circles) and from simulated scattering data (red line).*

1.6 References

[1] M. Gouterman, *J. Mol. Spec.* **1961**, *6*, 138–163.
[2] M. Gouterman, G. H. Wagnière, L. C. Snyder, *J. Mol. Spec.* **1964**, *11*, 108–127.
[3] H. L. Anderson, *Chem. Commun.* **1999**, 2323–2330.
[4] F. Würthner, T. E. Kaiser, C. R. Saha-Möller, *Angew. Chem. Int. Ed.* **2011**, *50*, 3376–3410.
[5] T. Pullerits, V. Sundström, *Acc. Chem. Res.* **1996**, *29*, 3811–389.
[6] *Biophysical Techniques in Photosynthesis*, Vol. 2 (Eds. T. J. Aartsma, J. Martysik), Springer, **2008**.
[7] T. J. Aartsma, J. Köhler, in *Biophysical Techniques in Photosynthesis*, Vol. 2 (Eds. T. J. Aartsma, J. Martysik), Springer, **2008**, pp. 241–266.
[8] S. Scheuring, J. N. Sturgis, V. Prima, A. Bernadac, D. Lévy, J.-L. Rigaud, *Proc. Natl. Acad. Sci. U.S.A.* **2004**, *101*, 11293–11297.
[9] M. R. Wasielewski, *Acc. Chem. Res.* **2009**, *42*, 1910–1921.
[10] Y. Nakamura, N. Aratani, A. Osuka, *Chem. Soc. Rev.* **2007**, *36*, 831–845.

[11] J. M. Tour, *Chem. Rev.* **1996**, *96*, 537–553.
[12] R. E. Martin, F. Diederich, *Angew. Chem. Int. Ed.* **1999**, *38*, 1350–1377.
[13] H. Shirakawa, *Angew. Chem. Int. Ed.* **2001**, *40*, 2574–2580.
[14] E. Collini, G. D. Scholes, *Science* **2009**, *323*, 369–373.
[15] J.-L. Brédas, D. Beljonne, V. Coropceanu, J. Cornil, *Chem. Rev.* **2004**, *104*, 4971–5003.
[16] Y. Coropceanu, J. Cornil, D. A. da Silva Filho, Y. Olivier, R. Silbey, J.-L. Brédas, *Chem. Rev.* **2007**, *107*, 926–952.
[17] R. H. Friend, R. W. Gymer, A. B. Holmes, J. H. Burroughes, R. N. Marks, C. Taliani, D. D. C. Bradley, D. A. Dos Santos, J.-L. Brédas, M. Lögdlund, W. R. Salaneck, *Nature* **1999**, *297*, 121–128.
[18] A. Kraft, A. C. Grimsdale, A. B. Holmes, *Angew. Chem. Int. Ed.* **1998**, *37*, 402–428.
[19] S. Allard, M. Forster, B. Souharce, H. Thiem, U. Scherf, *Angew. Chem. Int. Ed.* **2008**, *47*, 4070–4098.
[20] S. W. Thomas III, G. D. Joly, T. M. Swager, *Chem. Rev.* **2007**, *107*, 1339–1386.
[21] S. Günes, H. Neugebauer, N. S. Sariciftci, *Chem. Rev.* **2007**, *107*, 1324–1338.
[22] A. Hagfeldt, G. Boschloo, L. Sun, L. Kloo, H. Petterson, *Chem. Rev.* **2010**, *110*, 6595–6663.
[23] A. Osuka, A. Shimidzu, *Angew. Chem. Int. Ed.* **1997**, *36*, 135–137.
[24] A. Nakano, A. Osuka, I. Yamazaki, Y. Yamazaki, Y. Nishimura, *Angew. Chem. Int. Ed.* **1998**, *37*, 3023–3027.
[25] R. W. Wagner, T. E. Johnson, J. S. Lindsey, *J. Am. Chem. Soc.* **1996**, *118*, 11166–11180.
[26] D. P. Arnold, A. W. Johnson, M. Mahendran, *J. Chem. Soc., Perkin Trans. 1* **1978**, 366–370.
[27] H. L. Anderson, *Inorg. Chem.* **1994**, *33*, 972–981.
[28] V. S.-Y. Lin, S. G. DiMagno, M. J. Therien, *Science* **1994**, *264*, 1105–1111.
[29] P. N. Taylor, A. P. Wylie, J. Huuskonen, H. L. Anderson, *Angew. Chem. Int. Ed.* **1998**, *37*, 986–989.
[30] K. Susumu, T. V. Duncan, M. J. Therien, *J. Am. Chem. Soc.* **2005**, *127*, 5186–5195.
[31] K. J. Thorley, J. M. Hales, H. L. Anderson, J. W. Perry, *Angew. Chem. Int. Ed.* **2008**, *47*, 7095–7098.
[32] S. Ohira, J. M. Hales, K. J. Thorley, H. L. Anderson, J. W. Perry, J.-L. Brédas, *J. Am. Chem. Soc.* **2009**, *131*, 6099–6101.
[33] A. Tsuda, H. Furuda, A. Osuka, *J. Am. Chem. Soc.* **2001**, *123*, 10304–10321.
[34] A. Tsuda, A. Osuka, *Science* **2001**, *293*, 79–82.
[35] D. Beljonne, G. E. O‘Keefe, P. J. Hamer, R. H. Friend, H. L. Anderson, J.-L. Brédas, *J. Chem. Phys.* **1997**, *106*, 9439–9460.
[36] V. S.-Y. Lin, M. J. Therien, *Chem. Eur. J.* **1995**, *1*, 645–651.
[37] R. Stranger, J. E. McGrady, D. P. Arnold, I. Lane, G. A. Heath, *Inorg. Chem.* **1996**, *35*, 7791–7797.
[38] M. U. Winters, J. Kärnbratt, M. Eng, C. J. Wilson, H. L. Anderson, B. Albinsson, *J. Phys. Chem. C* **2007**, *111*, 7192–7199.
[39] H. L. Anderson, *Adv. Mater.* **1994**, *6*, 834–836.
[40] R. Kumble, S. Palese, V. S.-Y. Lin, M. J. Therien, R. M. Hochstrasser, *J. Am. Chem. Soc.* **1998**, *120*, 11489–11498.
[41] M.-H. Chang, M. Hoffmann, H. L. Anderson, L. M. Herz, *J. Am. Chem. Soc.* **2008**, *130*, 10171–10178.
[42] K. Susumu, M. J. Therien, *J. Am. Chem. Soc.* **2002**, *124*, 8550–8552.
[43] P. N. Taylor, J. Huuskonen, G. Rumbles, R. T. Aplin, E. Williams, H. L. Anderson, *Chem. Commun.* **1998**, 909–910.
[44] T. E. O. Screen, K. B. Lawton, G. S. Wilson, N. Dolney, R. Ispasoiu, T. Goodson III, S. J. Martin, D. D. C. Bradley, H. L. Anderson, *J. Mater. Chem.* **2001**, *11*, 312–320.
[45] M. U. Winters, E. Dahlstedt, H. E. Blades, C. J. Wilson, M. J. Frampton, H. L. Anderson, B. Albinsson, *J. Am. Chem. Soc.* **2007**, *129*, 4291–4297.
[46] S. D. Stranks, J. K. Sprafke, H. L. Anderson, R. J. Nicholas, *ACS Nano* **2011**, *5*, 2307–2315.
[47] G. Sedghi, K. Sawada, L. J. Esdaile, M. Hoffmann, H. L. Anderson, D. Bethell, W. Haiss, S. J. Higgins, R. J. Nichols, *J. Am. Chem. Soc.* **2008**, *130*, 8582–8583.

[48] F. C. Grozema, C. Houarner-Rassin, P. Prins, L. D. A. Siebbeles, H. L. Anderson, *J. Am. Chem. Soc.* **2007**, *129*, 13370–13371.

[49] C. J. Wilson, *Large Porphyrin Based π-Systems*, DPhil Thesis, University of Oxford, Oxford, **2006**.

[50] P. N. Taylor, H. L. Anderson, *J. Am. Chem. Soc.* **1999**, *121*, 11538–11545.

[51] J. S. Lindsey, *Acc. Chem. Res.* **2010**, *43*, 300–311.

[52] B. J. Littler, M. A. Miller, C.-H. Hung, R. W. Wagner, D. F. O'Shea, P. D. Boyle, J. S. Lindsey, *J. Org. Chem.* **1999**, *64*, 1391–1396.

[53] M. S. Newman, L. F. Lee, *J. Org. Chem.* **1972**, *37*, 4468–4469.

[54] A. Krivokapic, *Meso-Alkynyl Porphyrins and Porphyrinoids for Nonlinear Optics*, DPhil Thesis, University of Oxford, Oxford, **2003**.

[55] H. L. Anderson, S. J. Martin, D. D. C. Bradley, *Angew. Chem. Int. Ed. Engl.* **1994**, *33*, 655–657.

[56] M. Mayor, C. Dischdies, *Angew. Chem. Int. Ed.* **2003**, *42*, 3176–3179.

[57] K. Nakao, M. Nishimura, T. Tamachi, Y. Kuwatami, H. Miyasaka, T. Nishinaga, M. Iyoda, *J. Am. Chem. Soc.* **2006**, *128*, 16740–16747.

[58] M. Williams-Harry, A. Bhaskar, G. Ramakrishna, T. Goodson III, M. Imamura, A. Mawatari, K. Nakao, H. Enozawa, T. Nishinaga, M. Iyoda, M. *J. Am. Chem. Soc.* **2008**, *130*, 3252–3253.

[59] J. E. Donehue, O. P. Varnavski, R. Cemborski, M. Iyoda, T. Goodson III, *J. Am. Chem. Soc.* **2011**, *133*, 4819–4828.

[60] J. Krömer, I. Rios-Carreras, G. Fuhrmann, C, Musch, M. Wunderlin, T. Debaerdemaeker, E. Mena-Osteritz, P. Bäuerle, *Angew. Chem. Int. Ed.* **2000**, *39*, 2481–3486.

[61] G. Fuhrmann, T. Debaerdemaeker, P. Bäuerle, *Chem. Commun.* **2003**, 948–949.

[62] F. Zhang, G. Götz, H. D. F. Winkler, C. A. Schalley, P. Bäuerle, *Angew. Chem. Int. Ed.* **2009**, *48*, 6632–6635.

[63] W. Zhang, J. S. Moore, *J. Am. Chem. Soc.* **2004**, *126*, 12796.

[64] W. Zhang, J. S. Moore, *Angew. Chem. Int. Ed.* **2006**, *45*, 4416–4439.

[65] W. Zhang, S. Kraft, J. S. Moore, *J. Am. Chem. Soc.* **2004**, *126*, 329–335.

[66] D. Mössinger, J. Hornung, S. Lei, S. De Feyter, S. Höger, *Angew. Chem. Int. Ed.* **2007**, *46*, 6802–6806.

[67] S.-H. Jung, W. Pisula, A. Rouhanipour, H. J. Räder, J. Jacob, K. Müllen, *Angew. Chem. Int. Ed.* **2006**, *45*, 4685–4690.

[68] S. C. Simon, B. Schmaltz, A. Rouhanipour, H. J. Räder, K. Müllen, *Adv. Mater.* **2009**, *21*, 83–85.

[69] B. Schmaltz, A. Rouhanipour, H. J. Räder, W. Pisula, K. Müllen, *Angew. Chem. Int. Ed.* **2009**, *48*, 720–724.

[70] T. Kawase, H. Darabi, M. Oda, *Angew. Chem. Int. Ed. Engl.* **1996**, *35*, 2664–2666.

[71] T. Kawase, N. Ueda, K. Tanaka, Y. Seirai, M. Oda, *Tet. Lett.* **2001**, *42*, 5509–5511.

[72] K. Tahara, Y. Tobe, *Chem. Rev.* **2006**, *106*, 5274–5290.

[73] T. Kawase, K. Tanaka, N. Fujiwara, H. R. Darabi, M. Oda, *Angew. Chem. Int. Ed.* **2003**, *42*, 1624–1628.

[74] T. Kawase, Y. Nishiyama, T. Nakamura, T. Ebi, K. Matsumoto, H. Kurata, M. Oda, *Angew. Chem. Int. Ed.* **2007**, *46*, 1086–1088.

[75] T. Kawase, H. Kurata, *Chem. Rev.* **2006**, *106*, 5250–5273.

[76] S. Yamago, Y. Watanabe, T. Iwamoto, *Angew. Chem. Int. Ed.* **2010**, *49*, 757–759.

[77] R. Jasti, J. Bhattacharjee, J. B. Neaton, C. R. Bertozzi, *J. Am. Chem. Soc.* **2008**, *130*, 17646–17647.

[78] H. Takaba, H. Omachi, Y. Yamamoto, J. Bouffard, K. Itami, *Angew. Chem. Int. Ed.* **2009**, *48*, 6112–6116.

[79] H. Omachi, S. Matsuura, Y. Segawa, K. Itami, *Angew. Chem. Int. Ed.* **2010**, *49*, 10202–10205.

[80] Y. Segawa, S. Miyamoto, H. Omachi, S. Matsuura, P. Šenel, T. Sasamori, N. Tokitoh, K. Itami, *Angew. Chem. Int. Ed.* **2011**, *50*, 3244–3248.

[81] H. L. Anderson, J. K. M. Sanders, *Angew. Chem. Int. Ed. Engl.* **1990**, *29*, 1400–1403.

[82] S. Anderson, H. L. Anderson, J. K. M. Sanders, *Acc. Chem. Res.* **1993**, *26*, 469–475.

[83] J. Li, A. Ambroise, S. I. Yang, J. R. Diers, J. Seth, C. R. Wack, D. F. Bocian, D. Holten, J. S. Lindsey, *J. Am. Chem. Soc.* **1999,** *121*, 8927–8940.

[84] S. Rucareanu, A. Schuwey, A. Gossauer, *J. Am. Chem. Soc.* **2006,** *128*, 3396–3413.

[85] M. Hoffmann, C. J. Wilson, B. Odell, H. L. Anderson, *Angew. Chem. Int. Ed.* **2007**, *46*, 3122–3125.

[86] M.-H. Chang, M. Hoffmann, H. L. Anderson, L. M. Herz, *J. Am. Chem. Soc.* **2008,** *130*, 10171–10178.

[87] M. Hoffmann, J. Kärnbratt, M.-H. Chang, L. M. Herz, B. Albinsson, H. L. Anderson, *Angew. Chem. Int. Ed.* **2008**, *47*, 4993–4996.

[88] J. K. M. Sanders, N. Bampos, Z. Clyde-Watson, S. L. Darling, J. C. Hawley, H.-J. Kim, C. C. Mak, S. J. Webb, in *The porphyrin handbook*, Vol. 3 (Eds. K. M. Kadish, K. M. Smith, R. Guilard, Academic Press, New York, 1999, pp. 1–40.

[89] I. Beletskaya, . V. S. Tyurin, A. Y. Tsivadze, R. Guilard, C. Stern, *Chem. Rev.* **2009**, *109*, 1659–1713.

[90] B. M. J. M. Suijkerbuijk, D. M. Tooke, A. L. Spek, G. von Koten, R. J. M. Klein Gebbink, *Chem. Asian J.* **2007**, *2*, 889–903.

[91] C. A. Hunter, H. L. Anderson, *Angew. Chem. Int. Ed.* **2009**, *48*, 7488–7499.

[92] W. F. Bailey, A. S. Monahan, *J. Chem. Educ.* **1978**, *55*, 489–493.

[93] L. D. Byers, *J. Chem. Educ.* **1977**, *54*, 352–354.

[94] M. Hutin, B. Odell, T. D. W. Claridge, H. L. Anderson, *manuscript in preparation*.

[95] F. Yang, L. G. Moss, G. N. Phillips, Jr., *Nat. Biotechnol.* **1996**, *14*, 1246–1251.

[96] D. I. Svergun, M. H. J. Koch, *Rep. Prog. Phys.* **2003**, *66*, 1735–1782.

[97] C. D. Putnam, M. Hammel, G. L. Hura, J. A. Tainer, *Quart. Rev. Biophys.* **2007**, *40*, 191–285.

[98] D. M. Tiede, X. Zuo, in *Biophysical Techniques in Photosynthesis*, Vol. 2 (Eds. T. J. Aartsma, J. Martysik), Springer, **2008**, pp. 151–165.

[99] D. M. Tiede, R. Zhang, L. X. Chen, L. Yu, J. S. Lindsey, *J. Am. Chem. Soc.* **2004**, *126*, 14054–14062.

[100] R. F. Kelley, R. H. Goldsmith, M. R. Wasielewski, *J. Am. Chem. Soc.* **2007**, *129*, 6384–6385.

[101] X. Zuo, D. M. Tiede, *J. Am. Chem. Soc.* **2005**, *127*, 16–17.

[102] E. Mylonas, D. I. Svergun, *J. Appl. Cryst.* **2007**, *40*, s245–s249.

[103] P. V. Konarev, V. V. Volkov, A. V. Sokolova, M. H. J. Koch, D. I. Svergun, *J. Appl. Cryst.* **2003**, *36*, 1277–1282.

[104] O. Glatter, *J. Appl. Cryst.* **1977**, *10*, 415–421.

[105] D. I. Svergun, *J. Appl. Cryst.* **1992**, *25*, 495–503.

[106] P. B. Moore, *J. Appl. Cryst.* **1980**, *13*, 168–175.

[107] A. Bergmann, G. Fritz, O. Glatter, *J. Appl. Cryst.* **2000**, *33*, 1212–1216.

[108] D. Svergun, C. Barberato, M. H. J. Koch, *J. Appl. Cryst.* **1995**, *28*, 768–773.

[109] K. László, O. Czakkel, K. Josepovits, C. Rochas, E. Geissler, *Langmuir* **2005**, *21*, 8443–8451.

[110] X. Zuo, G. Cui, K. M. Mertz, L. Zhang, F. D. Lewis, D. M. Tiede, *Proc. Natl. Acad. Sci. U.S.A.* **2006**, *113*, 2516–2523.

[111] K. L. Mardis, H. M. Sutton, X. Zuo, J. S. Lindsey, D. M. Tiede, *J. Phys. Chem. A.* **2009**, *113*, 2516–2523.

[112] D. I. Svergun, *Biophys. J.* **1999**, *76*, 2879–2886.

Chapter 2

Improved Synthesis, Structure and Optoelectronic Properties of a [6]Porphyrin Nanoring

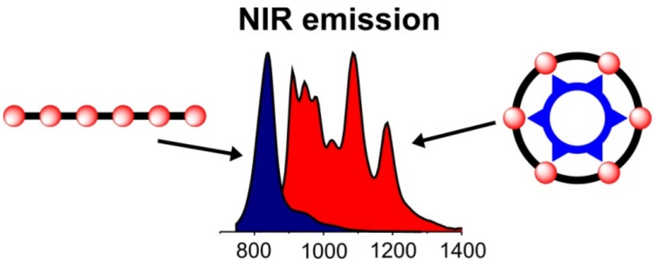

This chapter describes advances in the synthesis, solution structure elucidation and optoelectronic properties of a fully π*-conjugated cyclic porphyrin hexamer. Optimized reaction conditions and purification methods now allow template directed synthesis of the nanoring from readily available porphyrin monomer. Small angle X-ray scattering in solution has demonstrated the great rigidity and shape persistence of the nanoring in the presence and absence of the template. The template inhibits rotation of the porphyrin units and locks the nanoring in a conformation with maximal* π*-overlap. This high rigidity combined with the* D_{6h} *symmetry of the cyclic molecule result in a dramatic red-shift of the absorption and emission spectra compared to the linear analogue with emission reaching far into the NIR. The optical HOMO-LUMO gap of the nanoring is significantly reduced compared to linear hexamer and is even smaller than that of a linear polymer. Electronic structure calculations allow rationalization of these changes. The chapter closes with results on the fabrication of NIR organic light emitting diodes based on the emission of the nanoring and linear hexamer.*

Parts of the results in this chapter have been published in the following article:

Linear and Cyclic Porphyrin Hexamers as Near-Infrared Emitters in Organic Light-Emitting Diodes
O. Fenwick, J. K. Sprafke, J. Binas, D. V. Kondratuk, F. Di Stasio, H. L. Anderson, F. Cacialli
Nano Lett. **2011**, *11*, 2451–2456.

2.1 Background

The cyclic porphyrin hexamer ***c*-P6** (Figure 1.10 or Scheme 2.1), first synthesized by Dr. Markus Hoffmann, is a fascinating molecule in many ways.[1] It is a π-conjugated belt-like macrocycle with radially oriented p-orbitals pointing towards the center of the ring. Few examples of similar compounds exist in the literature and the unusual geometry results in unique optoelectronic properties. Additionally the molecule is strained (101 kJ mol^{-1}) and binds extremely strongly to the hexadentate template; the binding constant for this process is the highest reported thus far ($K_f = 7 \times 10^{38}$ M^{-1}) for a supramolecular 1:1 complex. Further progress in the development of the nanoring from a lab curiosity to an advanced material requires an improved synthesis so that we can easily access >100 mg of material per reaction. Some open questions also remain about the detailed structure of the nanoring, namely its shape persistence and rigidity. Although a coarse exciton model has been developed that can account for some of the optoelectronic properties of the nanoring, there is as yet no detailed, fully conclusive picture of the electronic structure of the nanoring to explain its remarkably structured absorption and fluorescence spectra.

2.2 Synthesis of the Nanoring from Porphyrin Monomer

The oxidative cyclization of linear porphyrin building blocks in the presence of a hexadentate template is the crucial step in the synthesis of porphyrin nanorings ***c*-P6** and ***c*-P6$_{\mathbf{C8}}$** (Scheme 1.9 and Scheme 2.1). In the initial procedure developed by Dr. Craig Wilson,[2] acetylene homo-coupling was carried out using a Pd/Cu co-catalyst system with iodine as an oxidant to regenerate the catalyst. The reaction mixture was passed over a pad of silica to remove the catalyst and the nanoring template complex was isolated from polymeric side-products by means of size-exclusion chromatography (SEC). In order to obtain the free nanoring, complexes ***c*-P6·T6** and ***c*-P6$_{\mathbf{C8}}$·T6** were then passed over a short SEC column in THF at high concentrations of the competing ligand DABCO. It was found that the high ring strain of the nanorings results in an increased reactivity towards secondary amines[3] and peroxides. The presence of small amounts of such compounds during synthesis and purification led to decomposition that was only detectable from the emission spectrum, whereas high concentrations resulted in complete decomposition of the nanorings. A series of changes in purification conditions were established to successfully avoid decomposition (Table 2.1). Additionally, the coupling conditions were modified according to a procedure reported by Swager to increase the catalytic activity and suppress side-reactions by replacing iodine with 1,4-benzoquinone.[4] The modified catalyst also allow the cyclization reaction to be carried out at room temperature instead of 60 °C.

Table 2.1. *Changes in reaction conditions for the synthesis of nanorings **c-P6** and **c-P6$_{C8}$**.*

Reagent	**Role in synthesis**	**Problem**	**New reagent**
THF	SEC purification and template removal	Peroxide contaminants cause decomposition	Toluene for SEC and freshly distilled THF for template removal
DABCO	Template removal	Presence of secondary amine impurity may cause decomposition by nucleophilic addition to the acetylenes[3]	DABCO, recrystallized from petroleum ether 40/60
Silica	Catalyst removal	Causes slight decomposition	Alumina
Iodine	Oxidant to regenerate catalyst	Side reactions of I_2 with terminal acetylenes reduces yield	1,4-Benzoquinone

Under the previous reaction conditions three molecules of porphyrin dimer ***l*-dP2** bound to the template were coupled to yield the cyclic hexamer template complex ***c*-P6·T6** in 33–44% yield (dependent on the side-chains). Attempts at direct synthesis from porphyrin monomer ***l*-dP1** resulted in a dramatically reduced yield of 5%; this is probably because the fraction of template-bound porphyrin at 60 °C is small and thus polymerization dominates. At room temperature more than 90% of monomer is bound to the template at the beginning of the reaction as calculated from the binding constant. The new conditions give significantly improved yields of 21% and 31% when starting from ***l*-dP1** and ***l*-dP1$_{C8}$**, respectively. The synthetic effort to obtain these porphyrin monomers is small as illustrated in Scheme 2.1. The starting materials, dipyrromethane and *meta*-substituted benzaldehyde derivatives, are both accessible on multigram scales. Porphyrin synthesis and attachment of acetylenes in the *meso*-positions can be carried out on a gram scale in 4 steps with overall yields of 45% for ***l*-dP1** and 37% for ***l*-dP1$_{C8}$** (for details see Scheme 1.1). The complementary hexa-pyridyl template **T6** is accessible in two steps (50% overall yield) *via* bromination of hexaphenyl benzene followed by a six-fold Suzuki coupling with 4-pyridineboronic acid. After cyclization, the addition of a large excess of the competing ligand DABCO to ***c*-P6·T6** (or ***c*-P6·T6$_{C8}$**) results in removal of the template and the free nanoring is obtained in high yield by size-exclusion chromatography.

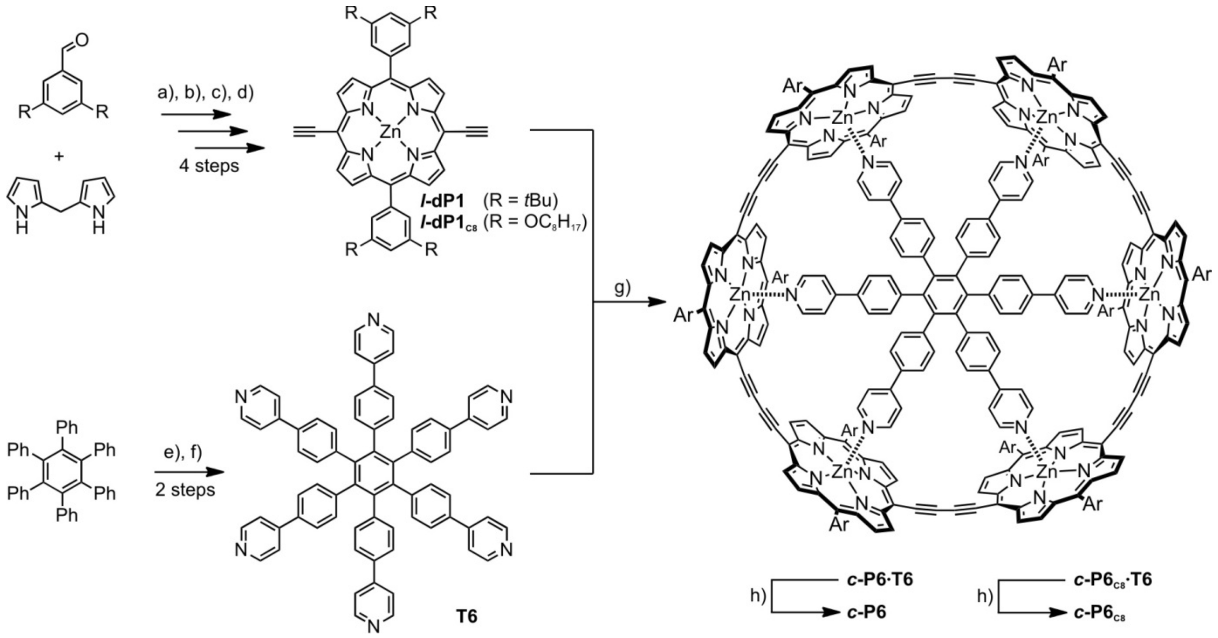

Scheme 2.1. *Synthesis of porphyrin nanorings* ***c-P6·T6*** *and* ***c-P6$_{C8}$·T6****. Reaction conditions and yields (****l-P1/l-P1$_{C8}$****): a) TFA then DDQ then Zn(OAc)$_2$ (56%/47%); b) NBS (92%/98%); c) trihexylsilylacetylene, Pd$_2$(dba)$_3$, CuI, PPh$_3$ (99%/89%); d) TBAF (92%/90%); e) Br$_2$ (96%); f) 4-pyridineboronic acid, PdCl$_2$(PPh$_3$)$_2$, NaHCO$_3$ (50%) g) PdCl$_2$(PPh$_3$)$_2$, CuI, 1,4-benzoquinone, i-Pr$_2$NH (21%/31%); h) DABCO (81%/89%).*

The main by-product of the cyclization reaction is linear polymer. When using the more active catalyst system with 1,4-benzoquinone rather than iodine, the molecular weight of these polymers increases and they become less soluble. As a result, purification of the nanoring is more convenient. After passing the reaction mixture over a pad of alumina the only remaining products are cyclic species that can be readily separated by size exclusion chromatography (Figure 2.1). Besides cyclic hexamer, the figure-of-eight complex ***c*****-P12·(T6)**$_2$ can be isolated in 4% yield.[†]

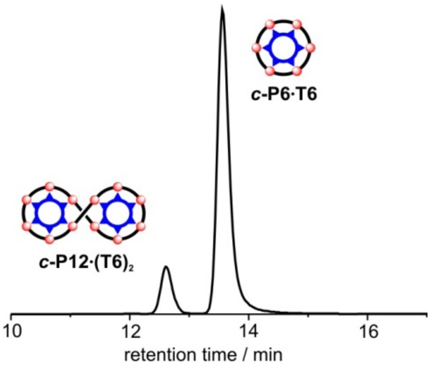

Figure 2.1. *Analytical gel permeation chromatogram of the crude cyclization product eluted in THF. The larger figure-of-eight complex* ***c-P12·(T6)$_2$*** *is eluting first, followed by* ***c-P6·T6****.*

[†] This finding will be discussed in more detail in Chapter 3.

2.3 Solution Structure of *c*-P6·T6 and *c*-P6

The high symmetry and rigidity of the nanoring template complex ***c*-P6·T6** is reflected in its remarkably simple ^{1}H NMR spectrum (Figure 2a). The two faces of each porphyrin unit are inequivalent due to the presence of the hexadentate ligand **T6**. This results in three singlets in the aromatic region, corresponding to the aryl protons c_1, c_2 and d as well as two singlets from *tert*-butyl protons i_1 and i_2. Upon removal of the template, the signals of aryl protons c_1 and c_2 as well as *tert*-butyl protons i_1 and i_2 merge into one signal. This means that rotation of the porphyrin units, which was hindered by the template, is now occurring rapidly on the NMR time-scale.

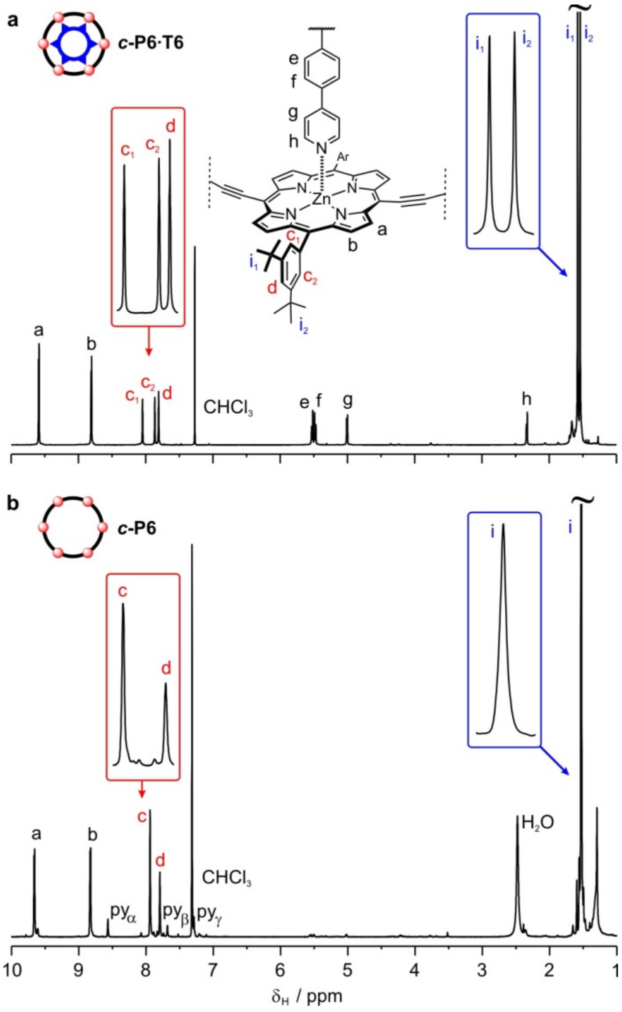

Figure 2.2. *^{1}H NMR spectrum (500 MHz, 298 K) of (a)* ***c-P6·T6*** *in $CDCl_3$ and (b)* ***c-P6*** *in $CDCl_3$/1% d_5-pyridine. Pyridine was added to the sample of* ***c-P6*** *to prevent aggregation.*

Solution small angle X-ray scattering (SAXS) experiments were carried out to gather more information about the solution structure and particularly the shape persistence of ***c*-P6·T6** and ***c*-P6**. We found very good agreement between the experimental scattering data and simulated scattering curves calculated from molecular models of ***c*-P6·T6** and ***c*-P6** (Figure 3 top). The radii of gyration R_g, determined from a Guinier fit match the values calculated from the models. The pair distribution function (PDF) is the normalized probability of a pair of electron densities at distance *r*, and can be interpreted more intuitively than the scattering data from which it is obtained by indirect Fourier transformation. PDFs of porphyrin assemblies are particularly informative due to the local point symmetry of the porphyrin cores and the presence of a high atomic number metal in their centers. This often results in well resolved peaks that can be attributed to particular metal-metal distances.[5] The high symmetry of ***c*-P6** and ***c*-P6·T6** results in two distinct peaks that correspond to the distance between two neighboring and two opposite porphyrin units. All features in the PDFs are well reproduced by curves calculated from molecular models. For comparison, more flexible molecules such as cyclic dodecamer (Chapter 3) or linear hexamer (Chapter 5) give significantly poorer overlap, particularly at longer distances. The excellent agreement between experimental and simulated PDFs for both ***c*-P6** and ***c*-P6·T6** highlights the rigidity and shape persistence of these nanorings.

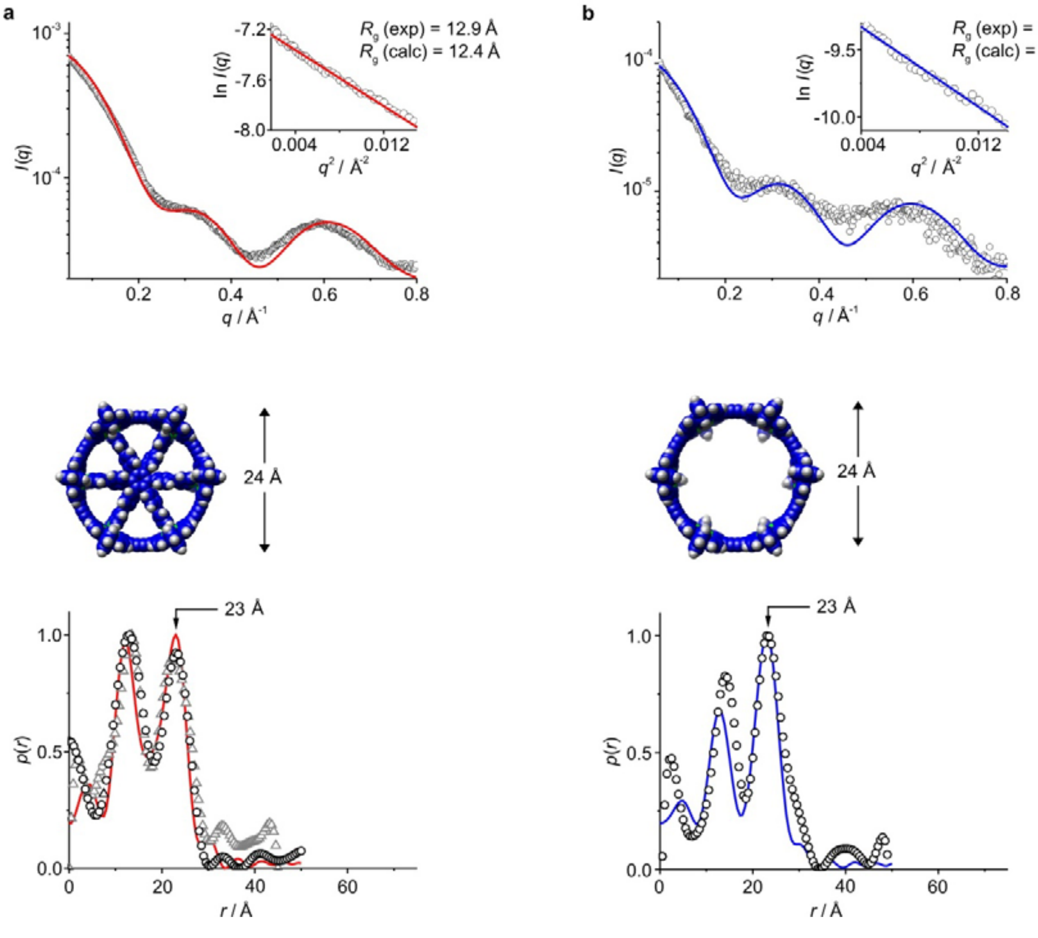

Figure 2.3. *SAXS data of (a)* ***c-P6·T6*** *and (b)* ***c-P6*** *acquired in toluene and toluene/1% pyridine, respectively at 298 K at Diamond Light Source, UK. The top row shows the raw scattering data (black circles) together with the simulated curves based on calculated models (lines). The insets are Guinier fits that were used to determine the radii of gyration* R_g*. The middle row contains the molecular models that were used to simulate SAXS data. Energy minimized structures were obtained using the MM+ force field implemented in the package HyperChem*^{TM}*. The distances are the calculated Zn-Zn distances between opposite porphyrins in the cyclic structures and between the first and the last porphyrin unit of the linear hexamer. The bottom row shows pair-distribution functions determined experimentally (black circles) and from models (lines). Experimental data for* ***c-P6·T6*** *was also acquired by Joseph Bullock (Northwestern University, USA) at the Advanced Photon Source at the Argonne National Laboratory. The PDF (gray triangles) is in excellent agreement with the data measured at Diamond Light Source.*

2.4 Optoelectronic Properties of *c*-P6·T6

The optoelectronic properties in π-conjugated macrocycles are strongly influenced by symmetry, strain and the lack of end-group effects.[1,6,7] Structural flexibility but also conformational freedom as in the free nanoring ***c*-P6** or cyclic oligothiophenes, result in weakening of these effects. The high rigidity and conformational stability of the nanoring template complex ***c*-P6·T6**, even in solution at room temperature, enables a detailed analysis of the various ring-specific effects on the optoelectronic properties of belt-like chromophores.

Bending of porphyrin hexamer results in significant changes in its absorption and emission behavior (Figure 2.4). The onset of absorption and the first emission maxima in ***c*-P6** and ***c*-P6·T6**, are both red-shifted by 60–80 nm compared to ***l*-P6**. A similar trend is observed in the bent open loop ***l*-P6·T6**. This effect cannot be explained solely by the small porphyrin-porphyrin torsional angles, and thus increased π-overlap, since such strong shifts are not observed in self-assembled porphyrin ladder complexes. Thus, the reason for these shifts must lie either in the change of symmetry or the induced strain and distortion of the π-system. At the same time we observe the appearance of low energy emission bands that extend far into the NIR.[†] The relative intensity of these bands increases in the order ***l*-P6·T6** < ***c*-P6** < ***c*-P6·T6**, which correlates with the growing rigidity of the porphyrin oligomers. ***c*-P6·T6** as the most rigid species shows emission over a very broad range that extends to 1300 nm. The appearance of these low energy bands is accompanied by a dramatic decrease in the fluorescence quantum yields Φ_f for the bent species. Again, this effect is more pronounced with increased rigidity, so that the absolute emission intensity of all bent species in the NIR is lower than in ***l*-P6**. Absorption and emission spectra of ***c*-P6·T6** were also measured at low temperatures (80 K, in methylcyclohexane to allow glass formation; measured by Rokas Drevinskas and Dr. Donatas Zigmantas, University of Lund, Sweden) resulting in a sharpening of all peaks and thereby facilitating comparison with calculated spectra (see below).

[†] The NIR emission features beyond 950 nm were not found in the original study,[1,3] probably due to detector insensitivity.

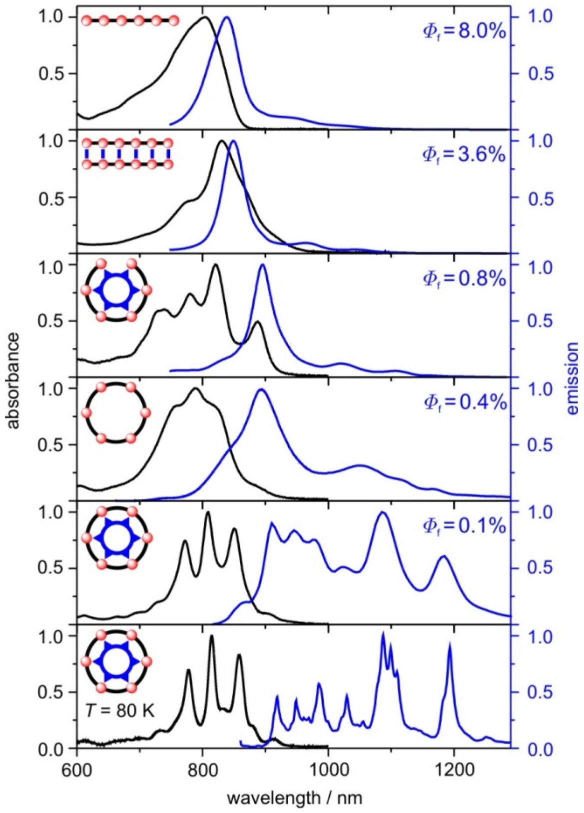

***Figure 2.4** Normalized steady state absorption (black lines) and emission (blue lines) spectra of (from top to bottom) **l-P6** in toluene/1% pyridine, hexamer ladder complex (**l-P6**)$_2$·(4,4'-bipyridine)$_6$ in toluene, **l-P6·T6** in toluene, **c-P6** in toluene/1% pyridine, **c-P6·T6** in toluene, **c-P6·T6** in methylcyclohexane at 80 K (the last sample was measured by Rokas Drevinskas). Samples were excited at 489 nm, except **c-P6·T6** (λ_{ex} = 809 nm at 295 K, λ_{ex} = 856 nm at 80 K).*

It was originally suggested that the absorption and emission behavior of the porphyrin nanorings can be explained with a simple exciton model (Figure 2.5).[1] In contrast to the linear species, the transition dipole moments of the S_0-S_1 transition in the nanorings cancel out, making this transition symmetry forbidden. As a consequence the absorption is dominated by the strongly allowed S_0-S_2 transition and the emission rate from S_1 is dramatically reduced. Structural flexibility in ***l*-P6·T6** and ***c*-P6** leads to desymmetrization and thus increased quantum efficiencies compared to the rigid ***c*-P6·T6**.

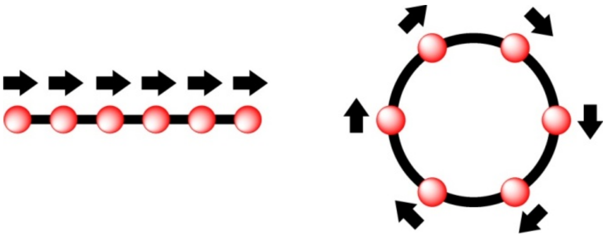

***Figure 2.5.** Exciton model to explain absorption and emission behavior of the nanorings. The cartoon on the left represents **l-P6** and the one on the right **c-P6**. The black arrows symbolize the transition dipole moments of the S_0-S_1 transition. The overall transition dipole moment in the cyclic species is zero, thus the transition is forbidden.*

While the exciton model gives an explanation for the reduced fluorescence quantum yields of the cyclic species ***l*-P6·T6**, ***c*-P6** and ***c*-P6·T6**, the reason for the appearance of strongly red-shifted NIR emission bands remains unclear. In order to gain a more detailed understanding of the complex emission behavior of ***c*-P6·T6**, Mike Wykes and Dr. David Beljonne (University of Mons, Belgium) modeled its electronic structure. The ground state geometry of ***c*-P6·T6** (without solublizing aryl side groups and restricted to D_6 symmetry) was optimized using the DFT functionals B3LYP and BHLYP with the 6-31g(d,p) basis set. Semi-empirical INDO/SCI (Intermediate Neglect of Differential Overlap Single Configuration Interaction) and TD-DFT (Time Dependent Density Functional Theory) calculations using a range of functionals have been performed to study the electronic structure and the singlet excited states of the optimized geometry. In summary, the transition to the lowest singlet excited state S_1 has zero oscillator strength, in agreement with the exciton model described above, whilst a doubly degenerate higher excited state has a significant oscillator strength. Unfortunately, the absolute and relative energies of these electronic transitions vary significantly with the modeling methods affordable for a molecule of the size of ***c*-P6·T6**. Experimental evidence suggests that the low-energy emission bands are not due to phosphorescence.† Furthermore, the fluorescence lifetimes up to 1000 nm are all nearly identical, suggesting only one emissive state. In order to investigate the possibility of vibrational coupling to the S_1 transition the normal modes were calculated using the BHLYP functional with the 6-31g(d,p) basis set. Comparing the simulated IR spectrum with the experimental IR spectrum in CCl_4 shows good overall agreement (Figure 2.6). However, some frequencies are either shifted or even missing, which may be due the lack of aryl side-groups in the models.

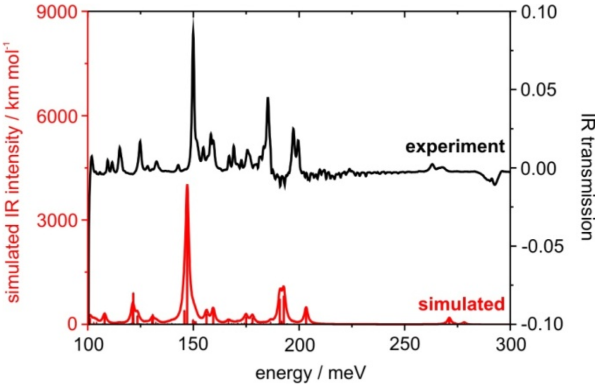

Figure 2.6. *Infra-red spectra of* ***c-P6·T6****: experimental spectrum in CCl_4 (black line), DFT stick spectrum (red bars) and DFT convoluted spectrum (red line, Lorentzian $\gamma = 0.01$ eV) modeled by Mike Wykes.*

The dark S_1 and bright S_2 excited state geometries were optimized using TD-DFT and the BHLYP functional. The calculations showed that the geometric relaxation of the excited states is very small,

---

† The emission spectrum is insensitive to the presence of oxygen and the lifetimes at 950 nm, 1100 nm and 1200 nm are all smaller than 20 ns.

indicating that a standard Franck-Condon vibronic progression cannot explain the complex spectrum. Symmetry forbidden electronic transitions can become allowed by Herzberg-Teller (HT) intensity borrowing through coupling to a non-symmetric vibrational mode that breaks the symmetry of the molecule.[8] This effect has been observed for example in the case of benzene, which has the same D_{6h} symmetry as the nanoring ***c*-P6**.[9,10]

Symmetry analysis showed that coupling of S_1 to several non-symmetric normal modes makes this transition strongly allowed. Most of these HT-active vibrational modes involve stretching of a butadiyne link thereby modulating the local coupling between porphyrin units. Figure 2.7 shows how distortion of the ideal geometry along the vibrational mode at 278 meV ("mode 968") dramatically increases the oscillator strength (*f*) of the S_0-S_1 transition. At the same time the oscillator strength of the S_0-S_2 transition decreases, thus confirming the intensity borrowing effect.

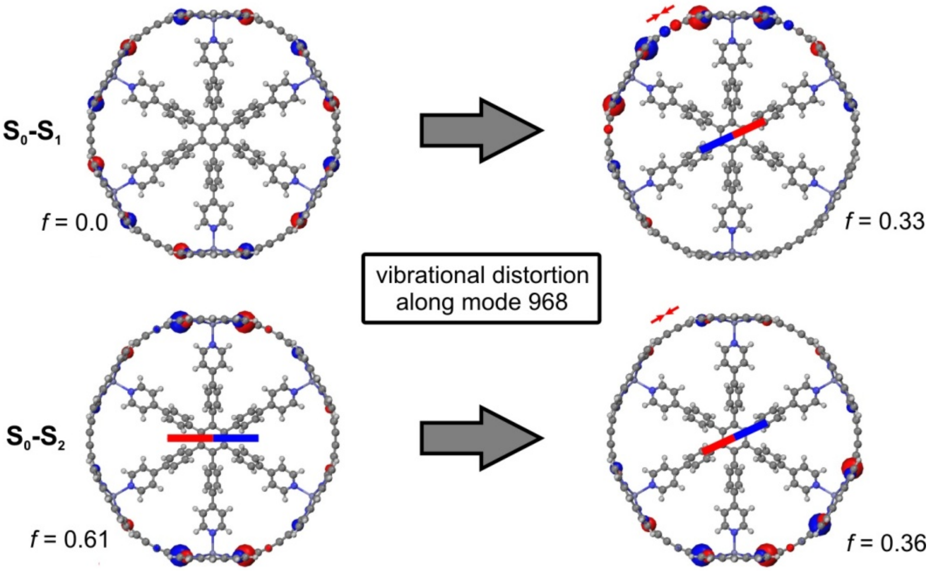

Figure 2.7. *Effect of vibrational distortion on the oscillator strengths f of the transitions to the first two electronic excited states. Perfectly symmetric D_6 ground state geometry (left) and ground state geometry distorted along vibrational mode 968 (right) with atomic transition densities (red, blue). The red arrows indicate the displacement of butadiyne carbons along mode 968 and the red-blue bars show the overall transition dipole. Calculations performed by Mike Wykes.*

The HT spectrum of S_1 was calculated on the INDO/SCI level, considering all non-symmetric 0-1 vibronic transitions, by calculating the derivative of the transition dipole moment with respect to displacement along each mode. The simulated HT spectrum reproduces the experimental vibrational structure of the low temperature emission spectrum well (Figure 2.8). However, as stated above, the calculated absolute energy of the electronic transition varies strongly with the applied method and thus a value of 1.31 eV for the S_0-S_1 0-0 vibronic transition was assumed by matching the calculated with the experimental spectrum. The accuracy of the HT simulation is confirmed by the good agreement between the calculated radiative rate constants of the HT transitions (7×10^6 s^{-1}) with the experimentally determined values (3×10^6 s^{-1}).[1]

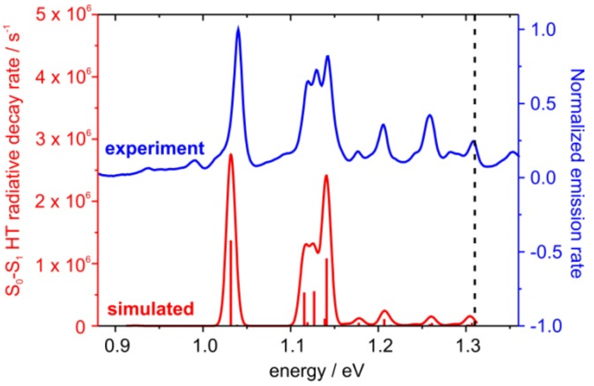

Figure 2.8. *Emission spectra of **c-P6·T6**: Measured spectrum in methylcyclohexane at 78 K upon excitation at 1.45 eV (856 nm) (blue line, measured by Rokas Drevinskas), Herzberg-Teller stick spectrum (red bars) and Herzberg-Teller convoluted spectrum (red line, Gaussian σ = 5 meV) calculated by Mike Wykes. The vertical dashed line marks the energy of the S_0-S_1 (0-0) vibrational transition. The difference in relative peak intensities between the experimental emission spectrum on the energy scale I(E) and the spectrum on the wavelength scale I(λ) from Figure 2.4 is due to the applied correction for the bandpass differences between the wavelength and energy scales ($I(E) = \lambda^2 \times I(\lambda)$). The weak emission peak at 1.36 eV in the experimental spectrum is a decomposition product of **c-P6·T6**.*[11]

The absorption spectrum of ***c*-P6·T6** is expected to be based on a combination of transitions to the first and second excited states. The size of the molecule makes modeling of this spectrum computationally expensive and no conclusive results have been obtained thus far.

The energy of the S_0-S_1 0-0 transition (1.31 eV) of ***c*-P6·T6** determined by the combination of the low temperature emission spectrum and the calculated emission spectrum gives an estimate of the optical HOMO-LUMO energy gap E_g. Comparison of this value with the bandgap of an infinite linear polymer chain allows evaluation of the consequences of cyclization on the π-conjugation. Since the synthesis of the analogous polymer ***l*-P*n*** is prevented by its insolubility, the optical bandgap was estimated by extrapolation from the emission energies of a series of oligomers from monomer ***l*-P1** to hexamer ***l*-P6**.[12] Different models exist that take saturation effects ("effective conjugation length") with increasing chain length into account.[13] The model by Meier uses the exponential Equation (2.1) to extrapolate the polymer bandgap E_∞ from the optical gaps of oligomers with N repeat units E_N and the empirical parameter a.[14,†]

$$E_N = E_\infty + (E_1 - E_\infty)\mathrm{e}^{-a(N-1)} \tag{3.1}$$

The model by Kuhn is based on classical mechanics and was initially developed for polyenes but has also been applied for a range of other conjugated polymers.[13,15] Each double bond is regarded as an oscillator vibrating at the energy E_0,

$$E_0 = h\sqrt{\frac{k_0}{4\pi^2\mu_0}} \tag{3.2}$$

[†] In Meier's original paper[14] the number of π-electrons rather than the number of repeat units was used to allow the comparison of a for different polymers. If such a fit is performed with the porphyrin oligomers, a is 0.12 which is significantly lower than for most conjugated polymers and reaches the value obtained for oligoynes.[16]

defined by the force constant k_0 and the reduced mass μ_0. If N oscillators are coupled with a force constant k', the lowest energy of the "eigenmodes" E_N is given by Equation (3.3).

$$E_N = E_0\sqrt{1+2\frac{k'}{k_0}\cos\frac{\pi}{N+1}} \tag{3.3}$$

Both models were used to extrapolate the bandgap of ***l*-P*n*** from the series of oligomers and gave energies of 1.38 eV and 1.44 eV, respectively (Figure 2.9a). The validity of the extrapolation is confirmed by the good agreement between the extrapolated values from the series ***l*-P1**$_{\mathbf{C8}}$ – ***l*-P8**$_{\mathbf{C8}}$, and the experimental value for the polymer ***l*-P*n***$_{\mathbf{C8}}$ (***n*** ~ 30–50) (Figure 2.9b).

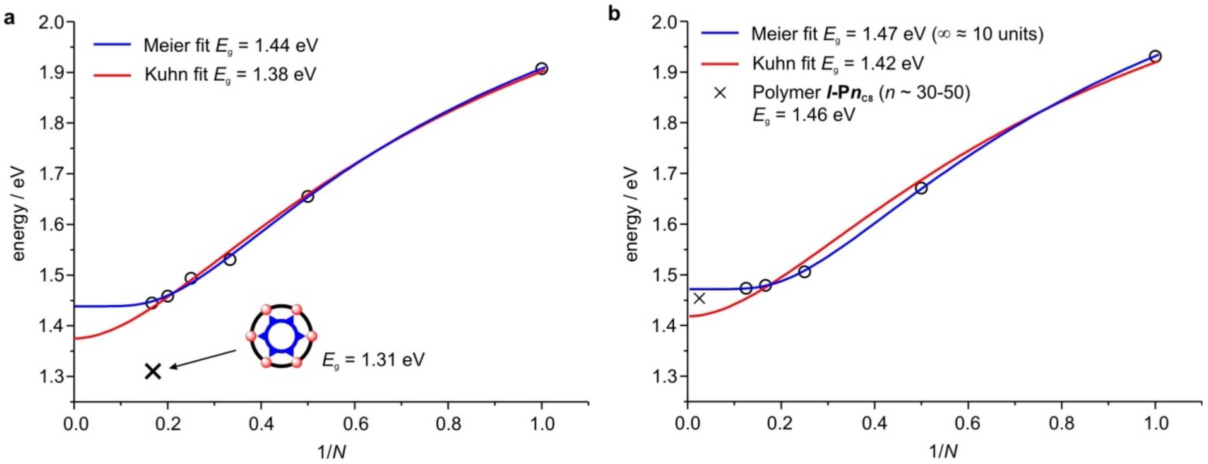

Figure 2.9. *Estimation of polymer bandgaps using Meier (blue line) and Kuhn (red line) fits. (a) Fit based on emission maxima of linear oligomers **l-P1** – **l-P6** measured in CH_2Cl_2/1% pyridine, emission maxima are from ref. 11; (b) fit based on emission maxima of linear oligomers **l-P1**$_{C8}$ – **l-P8**$_{C8}$ measured in toluene/1% pyridine.*[†]

The reduced energy gap of ***c*-P6·T6** compared to the linear polymer by at least 70 meV demonstrates the enhanced conjugation in the cyclic structure. This significant increase in conjugation in the nanoring cannot be explained by the reduced torsional freedom due to the presence of the template. It has been shown that although the ground state geometries of the linear oligomers consist of a broad distribution of conformations, emission at room temperature stems largely from a planar conformation with small torsional angles between the porphyrin units.[17,18] This means that unlike an extrapolation from the absorption spectra, the fits based on the emission maxima of the oligomers should yield the bandgap for an almost co-planar polymer, which is a good reference for the nanoring template complex ***c*-P6·T6**. Additionally, electrochemistry measurements by Dmitry Kondratuk show that the electrochemical energy gap of ***c*-P6·T6** and the torsionally flexible ***c*-P6** are very similar, but smaller than the extrapolated value for the polymer ***l*-P*n***.[11] Since end-group effects should be negligible in the polymer, the enhanced conjugation in the nanorings is therefore likely to result from the bending of the π-electron system. This rather counter-intuitive result was investigated theoretically

---

[†] The emission maxima correspond to the S_0-S_1 0-0 vibronic transitions, thus allowing comparison with the value determined for the nanoring. Absorption and emission wavelengths of linear oligomers in CH_2Cl_2/1% pyridine and toluene/1% pyridine are very similar and differ by only several nanometers.

by Wong for the case of cycloparaphenylenes.[7] He found that cyclic *para*-phenylenes always have lower computed optical gaps than their linear analogues and that this effect is the strongest for the smallest, most strained rings (Figure 2.10a). A comparable trend can be found for the emission energies of linear and cyclic porphyrin oligomers indicating that similar strain effects may be responsible for the smaller HOMO-LUMO gap of ***c*-P6·T6** compared to the polymer ***l*-P*n***.

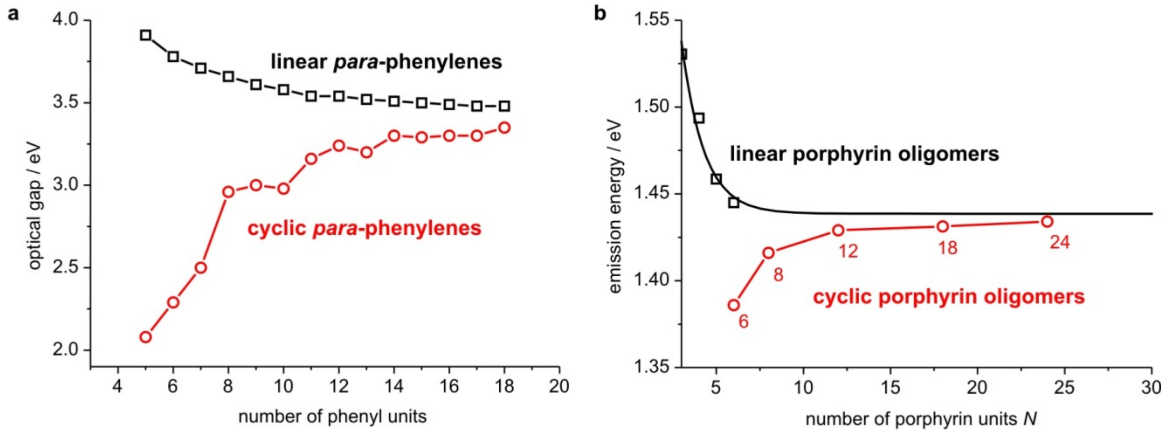

***Figure 2.10**. Trends in optical gaps in linear (black squares) and cyclic (red circles) (a) paraphenylenes as calculated in ref. 6 and (b) porphyrin oligomers measured in toluene/1% pyridine (cyclic) and dichloromethane/1% pyridine (linear). Emission data from linear oligomers is from ref. 11 and a Meier fit to these data is shown to extrapolate the trend for longer oligomers. Cyclic porphyrin octamer **c-P8** was synthesized by Melanie O'Sullivan and **c-P18** and **c-P24** were synthesized by Dmitry Kondratuk.*

According to Wong, the distortion of the π-system in cycloparaphenylenes causes a decrease in conjugation within the individual phenyl units and thus reduces their aromaticity as confirmed by nucleus-independent chemical shift (NICS) calculations. At the same time an increased quinoidal character of the phenyl-phenyl bond was found to result in an overall enhanced conjugation around the nanoring. Similar effects may contribute to the enhanced conjugation in ***c*-P6.**

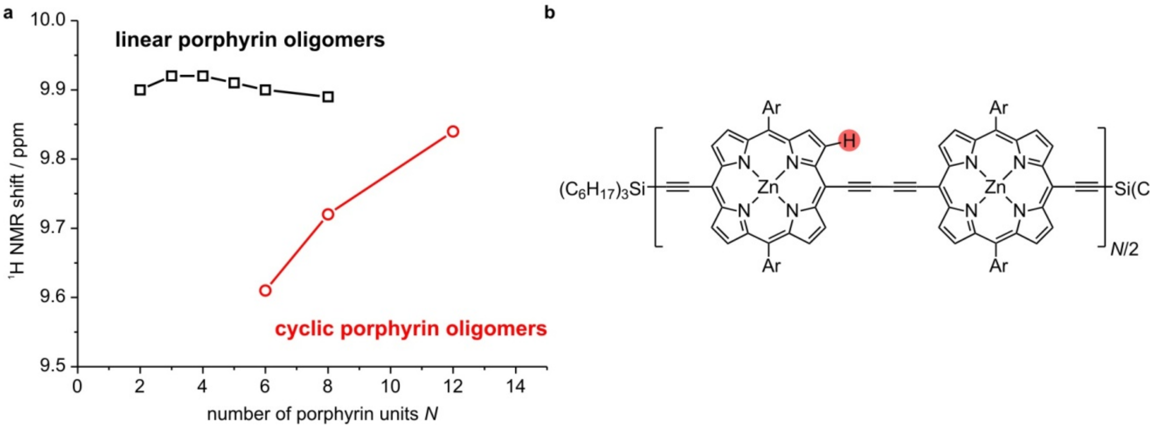

***Figure 2.11.** (a) Dependency of porphyrin β-proton ^{1}H NMR shifts on the number of porphyrin units in linear (black squares) and cyclic oligomers (red circles); (b) Structure of linear oligomers used to compare shifts of cyclic oligomers. The chemical shift of proton marked in red was used for the plot in (a). Ar = 3,5-bis(tert-butyl)phenyl except in the linear and cyclic octamer where Ar = 3,5-bis(octyoxy)phenyl. The different aryl side group has only little effect on the shifts of porphyrin β-protons ($\Delta\delta < 0.04$ ppm averaged over oligomers **l-P2** – **l-P6** and **c-P6**). All spectra acquired in $CDCl_3$/1% d_5-pyridine at 298 K at 500 MHz.*

Analysis of ^{1}H NMR chemical shifts in aromatic compounds is a commonly used tool to quantify aromaticity.[19] Ring-currents cause deshielding of outer protons resulting in high chemical shifts. Figure 2.11a shows the ^{1}H NMR chemical shifts of the most deshielded aromatic β-proton (Figure 2.11b) of a series of linear and cyclic oligomers in $CDCl_3$/1% d_5-pyridine. A clear trend is observable in the nanorings with decreasing shifts for smaller, more strained rings, while the shifts in the linear series remain almost constant. In a tentative interpretation of these data the smaller shift in more strained rings could be attributed to a decrease in porphyrin aromaticity, analogous to Wong's theoretical results on cycloparaphenylenes. Other effects, such as the influence of the inner-ring current from an opposite porphyrin unit, may contribute to these shifts and in order to confirm the proposed interpretation, additional experiments or calculations such as NICS scans would be required.

2.5 Linear and Cyclic Hexamers as Near-Infrared Emitters in OLEDs

Organic light-emitting diodes (OLEDs) are the subject of intense research in academia and industry because of their application in flexible displays and lighting panels.[20] In addition to devices covering the visible spectrum, near-infrared (NIR) emitting OLEDs are expected to enter a niche, targeting applications such as optical communications, night-vision devices or line-of-sight remote control. Fluorescence quantum efficiencies in the NIR decrease dramatically due to vibrational deactivation of excited states.[21] Linear porphyrin hexamer ***l*-P6$_{C8}$** is a promising candidate for NIR-OLED applications because it has a relatively good quantum efficiency (Φ_f = 8.0%), given the emission maximum at 840 nm. Cyclic hexamer ***c*-P6·T6** has a significantly lower quantum efficiency (Φ_f = 0.1%), but has a curved π-system which should result in reduced aggregation in solid thin films compared to its linear analogue. Aggregation of conjugated molecules or polymers in OLEDs can reduce device efficiencies and color purity because of formation of intermolecular excited states such as excimers.[22]

Devices were fabricated and tested by Dr. Oliver Fenwick and Prof. Franco Cacialli (University College London) and only the key results and conclusions are reported here.[23] The OLED (Figure 2.12a) consists of a transparent indium-tin-oxide (ITO) anode on a glass substrate for hole injection, which is covered by a layer of PEDOT:PSS that serves as a conductive layer for hole transport from the anode to the emissive layer. The emissive layer was formed from a blend of the porphyrin NIR emitter with the conjugated polymer poly (9,9'-dioctylfluorene)-*alt*-benzothiadiazole (F8BT, Figure 2.12b) used as a charge transport matrix in a ratio *w*/*w* 1/9. A calcium cathode was evaporated on the emissive layer and then covered by a protective aluminium layer.

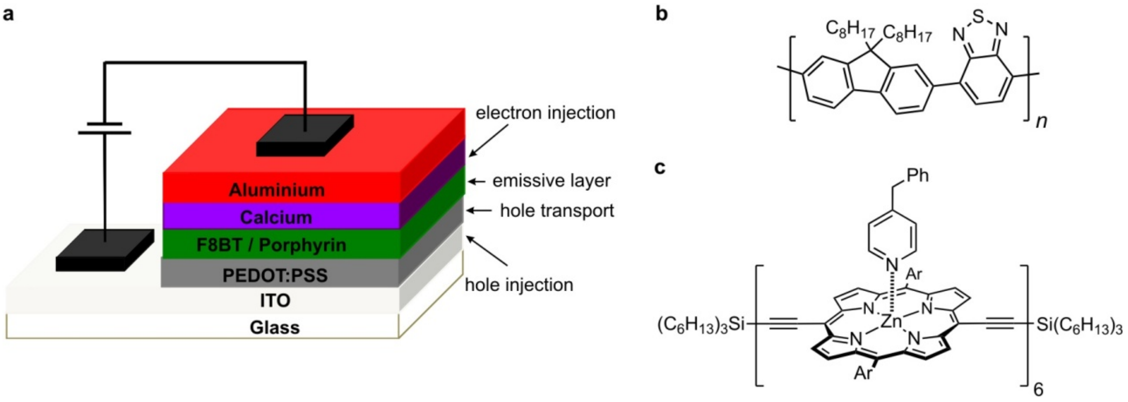

Figure 2.12. *(a) OLED device architecture; (b) structure of F8BT; (c) structure of the **l-P6$_{C8}$**·bpy complex.*

The most important characteristics for assessing the device performance and the electroluminescence (EL, Figure 2.13) efficiency of the emissive species are the external (EQE) and internal quantum efficiencies (IQE), respectively. The IQE of the device with ***c*-P6·T6** as the emissive species, is very similar to the photoluminescence (PL) efficiency in thin film and in solution (IQE ~ $\Phi_f = 0.1\%$). Although the device performance is not outstanding due to the intrinsically low emission efficiency of the nanoring, the similarity in emission efficiency in solution and the solid state indicates the absence of nanoring aggregation, probably as a result of the curved π-surface. In contrast, both PL and EL efficiency of ***l*-P6$_{C8}$** based devices are significantly lower in the solid state than in solution, most likely due to aggregation. Addition of the non-volatile ligand 4-benzylpyridine (bpy) to the linear hexamer (Figure 2.12c) results in a significant increase of the PL and EL efficiency, almost reaching the value in solution (Φ_f (film) = 7.7%, Φ_f (solution) = 8%).

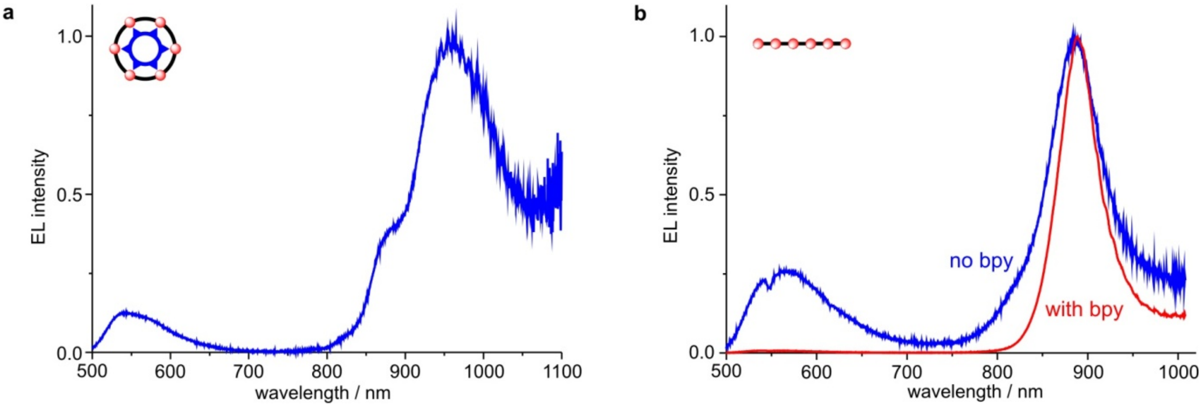

Figure 2.13. *Electroluminescence spectra from F8BT/porphyrin OLED devices. (a) **c-P6·T6** (b) **l-P6$_{C8}$** with (red line) and without (blue line) 4-benzylpyridine (bpy).*

The stronger PL in the presence of the coordinating ligand shows the potential of such a supramolecular approach to reduce aggregation in the solid state and to improve device performance.

2.6 Conclusions and Outlook

The results presented in this chapter highlight the importance of the cyclic porphyrin hexamer for the fundamental understanding of fully π-conjugated macrocycles but also indicate its potential as a novel material in organic optoelectronic applications. It was demonstrated by analysis of the solution structure that the template gives the nanoring high rigidity and restricts the torsional freedom of the porphyrin units. The importance of the template for understanding the electronic structure of the nanoring is clear from the differences in absorption and emission behavior of the free nanoring and the nanoring template complex. Structural flexibility of the free nanoring relaxes the symmetry-related selection rules and only the well-resolved NIR bands in the highly rigid template complex ***c*-P6·T6** allowed identification of Herzberg-Teller coupling as an important mechanism in excited state deactivation of the nanorings. The development of a nanoring synthesis from simple building blocks should pave the way for the facile synthesis of new derivatives and enable the synthesis of large quantities of cyclic hexamer required for novel materials applications. This potential was demonstrated with the fabrication of NIR-emitting OLED devices and this work represents a proof of concept for the use of molecules with curved π-surfaces as efficient, non-aggregating solid state emitters.

The increased reactivity of the nanoring that has so far only been identified as a complication affecting the synthesis, could be used to develop new reactions that will allow further functionalization of the nanorings. Introduction of functional groups in the nanoring, which may also be achieved by changing the aryl side groups, should open new possibilities of interfacing the nanoring with other functional molecules or surfaces.

2.7 References

[1] M. Hoffmann, J. Kärnbratt, M.-H. Chang, L. M. Herz, B. Albinsson, H. L. Anderson, *Angew. Chem. Int. Ed.* **2008**, *47*, 4993–4996.
[2] M. Hoffmann, C. J. Wilson, B. Odell, H. L. Anderson, *Angew. Chem. Int. Ed.* **2007**, *46*, 3122–3125.
[3] M. Hoffmann, *Nanosized Porphyrin Molecular Wires and Rings*, D.Phil. Thesis, University of Oxford, Oxford, **2008**.
[4] V. E. Williams, T. M. Swager, *J. Polym. Sci., Part A: Polym. Chem.* **2000**, *38*, 4669–4676.
[5] R. F. Kelley, R. H. Goldsmith, M. R. Wasielewski, *J. Am. Chem. Soc.* **2007**, *129*, 6384–6385.
[6] M. Bednarz, P. Reineker, E. Mena-Osteritz, P. Bäuerle, *J. Lumin.* **2004**, *110*, 225–231.
[7] B. M. Wong, *J. Phys. Chem. C* **2009**, *113*, 21921–21927.
[8] G. Herzberg, E. Teller, *Z. Phys. Chem. B* **1933**, *21*, 410.
[9] A. Hiraya, K. Shobatake, *J. Chem. Phys.* **1991,** *94*, 7700–7706.
[10] A. Bernhardsson, N. Forsberg, P. Malmqvist, B. O. Roos, L. Serrano-Andrés, *J. Chem. Phys.* **2000**, *112,* 2798–2809.
[11] J. K. Sprafke, D. V. Kondratuk, M. Wykes, A. L. Thompson, M. Hoffmann, R. Drevinskas, J. Kärnbratt, J. E. Bullock, M. Malfois, M. R. Wasielewski, B. Albinsson, D. Zigmantas, D. Beljonne, H. L. Anderson, *manuscript in preparation*.

[12] P. N. Taylor, J. Huuskonen, G. Rumbles, R. T. Aplin, E. Williams, H. L. Anderson, Chem. *Comm.* **1998**, 909–910.
[13] J. Gierschner, J. Cornil, H.-J. Egelhaaf, *Adv. Mater.* **2007**, 19, 173–191.
[14] H. Meier, U. Stalmach, H. Kolshorn, *Acta Polymer.* **1997**, *40*, 379–384.
[15] W. Kuhn, *Helv. Chim. Acta* **1948**, *31*, 1780–1799.
[16] W. A. Chalifoux, R. R. Tykwinski, *Nature Chem.* **2010**, *2*, 967–971.
[17] M. U. Winters, J. Kärnbratt, M. Eng, C. J. Wilson, H. L. Anderson, B. Albinsson, *J. Phys. Chem. C* **2007**, *111*, 7192–7199.
[18] M.-H. Chang, M. Hoffmann, H. L. Anderson, L. M. Herz, *J. Am. Chem. Soc.* **2008**, *130*, 10171–10178.
[19] P. v. R. Schleyer, H. Jiao, *Pure Appl. Chem.* **1996**, *68*, 209–218.
[20] R. H. Friend, R. W. Gymer, A. B. Holmes, J. H. Burroughes, R. N. Marks, C. Taliani, D. D. C. Bradley, D. A. Dos Santos, J.-L. Brédas, M. Lögdlund, W. R. Salaneck, *Nature* **1999**, *297*, 121–128.
[21] R. Englman, J. Jortner, *J. Mol. Phys.* **1970**, *18*, 145–164.
[22] J. Cornil, D. A. dos Santos, X. Crispin, R. Silbey, J. L. Brédas, *J. Am. Chem. Soc.* **1998**, *120*, 1289–1299.
[23] O. Fenwick, J. K. Sprafke, J. Binas, D. V. Kondratuk, F. Di Stasio, H. L. Anderson, F. Cacialli, *Nano Lett.* **2011**, *11*, 2451–2456.

Chapter 3

Synthesis and Properties of a [12]Porphyrin Nanoring

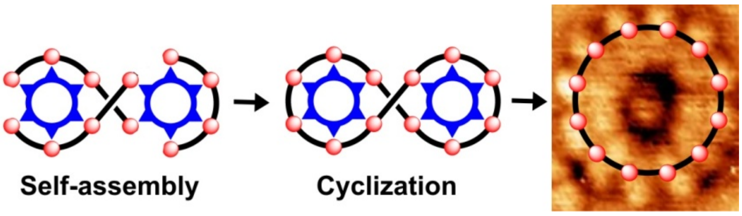

From the discovery of a figure-of-eight shaped [12]porphyrin nanoring template complex as a side-product in the synthesis of a [6]porphyrin nanoring, an efficient synthesis of this molecule is developed based on the mismatch in binding sites between a linear porphyrin tetramer and a radial hexadentate template. This concept can be generalized and leads to the development of 'Vernier templating' as a strategy for the synthesis of large, monodisperse macrocycles. The structure of the figure-of-eight complex and the free nanoring is investigated in detail and the formation of a Vernier complex is proved. MALDI-MS, SAXS, NMR and STM imaging give the picture of a rigid and stericially congested figure-of-eight complex, while the free [12]porphyrin nanoring shows significant flexibility. Studies on the formation of the figure-of-eight complex from the free nanoring demonstrate that binding of the two templates is a cooperative process, with either both or no template being bound.

Parts of the results in this chapter have been published in the following article:

Vernier templating and synthesis of a 12-porphyrin nano-ring
M. C. O'Sullivan, J. K. Sprafke, D. V. Kondratuk, C. Rinfray, T. D. W. Claridge, A. Saywell, M. O. Blunt, J. N. O'Shea, P. H. Beton, M. Malfois, H. L. Anderson
Nature **2011**, *469*, 72–75.

3.1 Background

Fully π-conjugated porphyrin nanorings are intriguing compounds in terms of their synthesis, self-assembly and electronic structure (see Introduction and Chapters 2 and 4). With increasing ring-size the dimensions of natural light-harvesting systems are approached. A [12]porphyrin nanoring having a calculated diameter of 5.1 nm would be as large as the bacterial light harvesting complex I ($d = 5.0$ nm).[1] Due to complete π-conjugation around the nanoring, the electronic coupling between individual porphyrin units would probably be even higher than in the natural pigments and may enable the study of fundamental processes of light harvesting and charge separation. Small aromatic molecules show persistent ring-currents and the same effect has been found in mesoscopic metal rings with sub-micrometer diameters.[2] The strong electronic coupling in porphyrin nanorings may allow the observation of similar effects in overall non-aromatic (yet conjugated) organic macrocycles, thereby bridging the gap between the two extremes known to date. The synthesis of macrocycles large enough to measure such effects is a formidable synthetic challenge. The use of radial templates, as practiced in the synthesis of cyclic hexamer and octamer, is expected to be extremely challenging for larger macrocycles because of the synthetic difficulties in obtaining very large and rigid templates. It is therefore desirable to develop new methodologies going beyond the traditional approach. Such a development would be an important step towards the synthesis of large, monodisperse macromolecules. It has been shown that such materials can have very different properties compared to analogous polydisperse mixtures and may rival their biological counterparts in terms of catalytic, informational and transcriptional properties.[3]

3.2 Synthesis of a [12]Porphyrin Nanoring and Vernier Templating

As outlined in Chapter 2, the oxidative acetylene homocoupling of monomer ***l*-dP1** in the presence of hexadentate template **T6** leads to formation of a minor product in 4% yield along with the original target, the [6]porphyrin nanoring ***c*-P6·T6** (Figure 2.1). The same products, but in overall higher yields, are obtained when using dimer ***l*-dP2**. The new product was identified as a complex between the [12]porphyrin nanoring ***c*-P12** and two molecules of template **T6** that fold the nanoring into a figure-of-eight (Figure 3.1). The templates can be replaced from this complex by addition of an excess of the competing ligand pyridine yielding the free nanoring **c-P12** in nearly quantitative yield (96%). Two extreme cases can be envisioned for the mechanism by which the figure-of-eight complex ***c*-P12·(T6)$_2$** is formed. The first possibility involves chain growth of unbound porphyrin oligomers with subsequent cyclization around the two templates, whilst in the second case coupling occurs between template bound porphyrins and the figure-of-eight complex is formed by the coupling of two such porphyrin oligomer–template complexes. At the beginning of the reaction only 90% of ***l*-dP1** is bound to the template, as calculated from the binding constant, implying that it is probably a combination of the two processes that results in formation of ***c*-P12·(T6)**$_2$ with numerous coupling sequences being conceivable. From this mechanism one can expect the formation of even larger macrocycles ***c*-P*N*** with ***N*** being a multiple of six (the number of template binding sites).

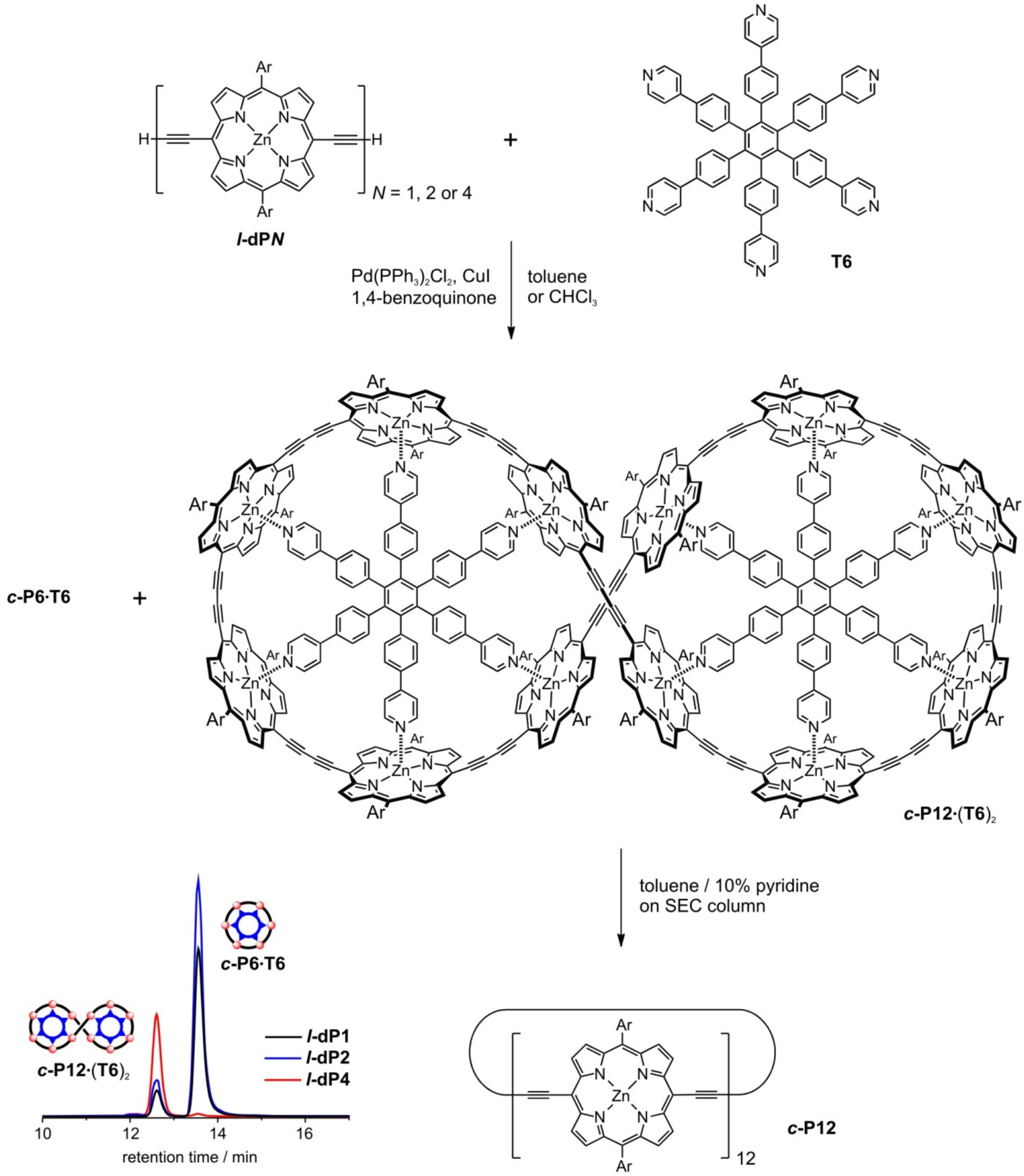

__Figure 3.1.__ Synthesis of __c-P12·(T6)__$_2$ and __c-P12__ from linear oligomers __l-dP1__, __l-dP2__ and __l-dP4__ and hexadentate template __T6__ with Ar = 3,5-bis(tert-butyl)phenyl. The same synthesis was also performed using oligomers with Ar = 3,5-bis(octyloxy)phenyl leading to the formation of __c-P12__$_{C8}$__·(T6)__$_2$ (not isolated) and __c-P12__$_{C8}$. The inset shows analytical gel permeation chromatograms (detection at 360 nm) with the relative analytical yields of __c-P6·T6__ and __c-P12·(T6)__$_2$ synthesized from __l-dP1__, __l-dP2__ or __l-dP4__. In all runs the same volume of crude reaction mixture was injected with identical concentrations of porphyrin subunits at the start of the reaction.

The expected outcome of the reaction when coupling porphyrin tetramer ***l*-dP4** in the presence of **T6** differs to the cases of ***l*-dP1** and ***l*-dP2** because the number of template binding sites n_T is not a multiple of the number of binding sites of the porphyrin oligomer n_P, making the formation of cyclic porphyrin hexamer ***c*-P6·T6** impossible. Such a mismatch in the number of binding sites has been used by Kelly[4] and Hunter[5] to assemble linear Vernier complexes with well defined sizes (Figure 3.2a). The number of noncovalent bonds n_C formed in such a complex is the smallest common multiple of n_P and n_T because for enthalpic reasons all binding sites have to be saturated and for entropic reasons a minimum number of components has to be involved in complex formation. In consequence the linear porphyrin tetramer ***l*-dP4**, with $n_P = 4$, and the hexadentate template **T6**, with $n_T = 6$, should form two isomeric cyclic Vernier complexes (***l*-dP4**)$_3$·(**T6**)$_2$ with $n_C = 12$ (Figure 3.2b). Covalent capture[6] of this complex by acetylene homocoupling is expected to lead to a significantly more efficient formation of the figure-of-eight complex ***c*-P12**·(**T6**)$_2$ than by synthesis from ***l*-dP1** and ***l*-dP2**.

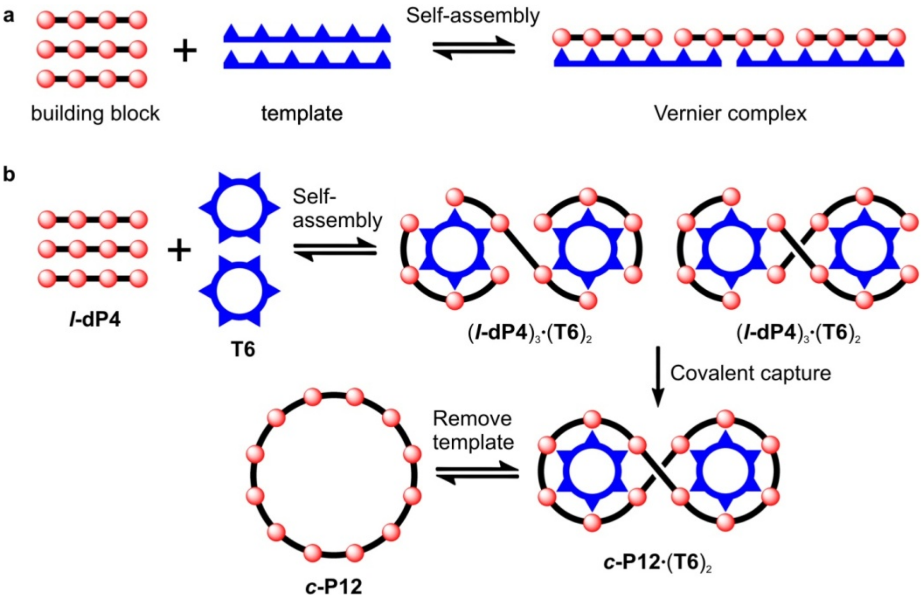

Figure 3.2. *Vernier templating for the synthesis of large macrocycles. (a) Formation of a linear Vernier complex; (b) synthesis of **c-P12** from **l-dP4** and **T6** via formation of the Vernier complex (**l-dP4**)$_3$·(**T6**)$_2$.*

The synthesis of the figure-of-eight ***c*-P12**·(**T6**)$_2$ from ***l*-dP4** proceeds in 40% isolated yield, with the [12]porphyrin nanoring as essentially the only cyclic product (Figure 3.1). The formation of a Vernier-complex at the start of the reaction is advantageous but not an absolute requirement for formation of the figure-of-eight. In analogy to the case of monomer and dimer, the 12-ring can still be formed from unbound linear octamer (with tetramer) or dodecamer. This convergent mechanism is probably one of the reasons for the high yielding cyclization.

3.3 Structural Characterization of Vernier Complex, Figure-of-Eight and Free Nanoring

3.3.1 MALDI-TOF Mass Spectrometry

The first evidence for formation of a porphyrin dodecamer came from MALDI-TOF mass spectrometry (Figure 3.3). The spectrum of the figure-of-eight shows three peaks that correspond to the expected product peak at *m*/*z* 11554, the partially disassembled complex between the nanoring and one molecule of **T6** (*m*/*z* 10557) and the fully disassembled product, free nanoring **c-P12** at *m*/*z* 9560.

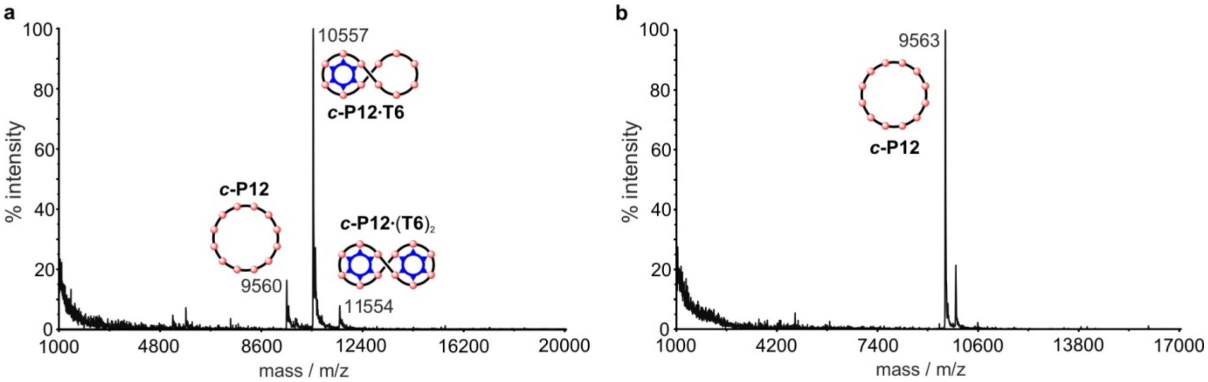

Figure 3.3. *(a) MALDI-TOF analysis of* ***c-P12·(T6)$_2$****. The three peaks correspond to* ***c-P12·(T6)$_2$*** *(m/z 11554, expected 11551),* ***c-P12·T6*** *(m/z 10557, expected 10554) and* ***c-P12*** *(m/z 9560, expected 9557); (b) MALDI-TOF analysis of* ***c-P12****. The major peak corresponds to the expected mass for* ***c-P12*** *(m/z 9563, expected 9557). The origin of the peak at m/z 9896 is unknown. Both spectra were acquired by the EPSRC National Mass Spectrometry Service Centre at Swansea University.*

3.3.2 ^{1}H NMR Analysis

The ^{1}H NMR spectrum of the figure-of-eight complex is significantly more complicated than the spectra of either the highly symmetric cyclic hexamer template complex ***c*****-P6·T6** or the linear porphyrin oligomers. Assignment of the peaks is challenging, however as a result of the D_2 symmetry of the figure-of-eight ***c*****-P12·(T6)**$_2$ (three perpendicular C_2 axes through the center, Figure 3.4) it is sufficient to consider only one quarter of the molecule for interpretation of the NMR spectrum. The structure drawn in Figure 3.4b comprises of three porphyrin units P1–P3, with P1 being the closest to the center (marked with a red cross). The top side of the molecule, pointing away from the template is drawn in bold. The part of the template that is coordinating to these three porphyrins is also shown.

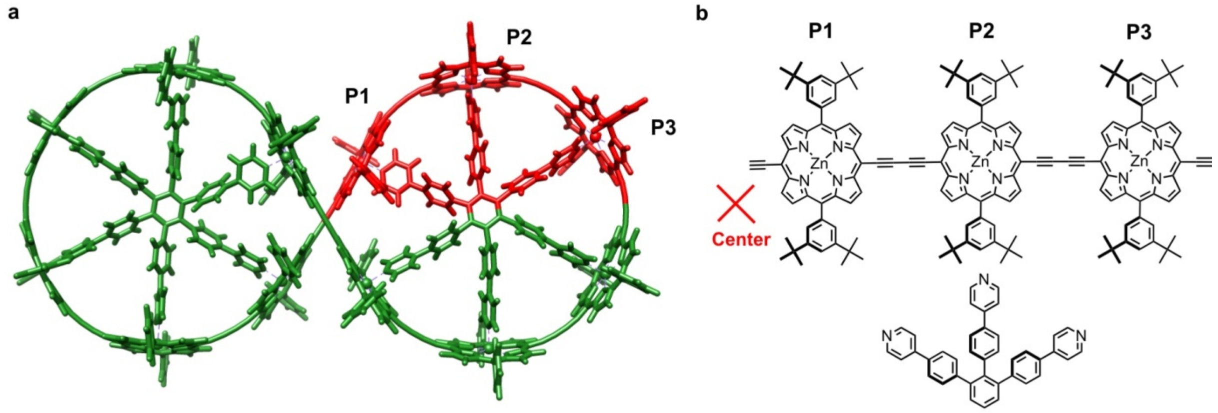

Figure 3.4. *(a) Model of figure-of-eight* ***c-P12·(T6)***$_2$*; (b) chemical structure of one quarter of the molecule.*

Comparison with NMR data from similar compounds, such as cyclic porphyrin hexamer template complex ***c*****-P6·T6** (Figure 2.2a), allows the assignment of distinct spectral regions for protons in similar environments (Figure 3.5): The porphyrin β-pyrrole protons are most deshielded, followed by the aryl protons. The aromatic protons of the template are more shielded due to the ring current of the porphyrin. The *tert*-butyl protons appear in the alkyl region as expected.

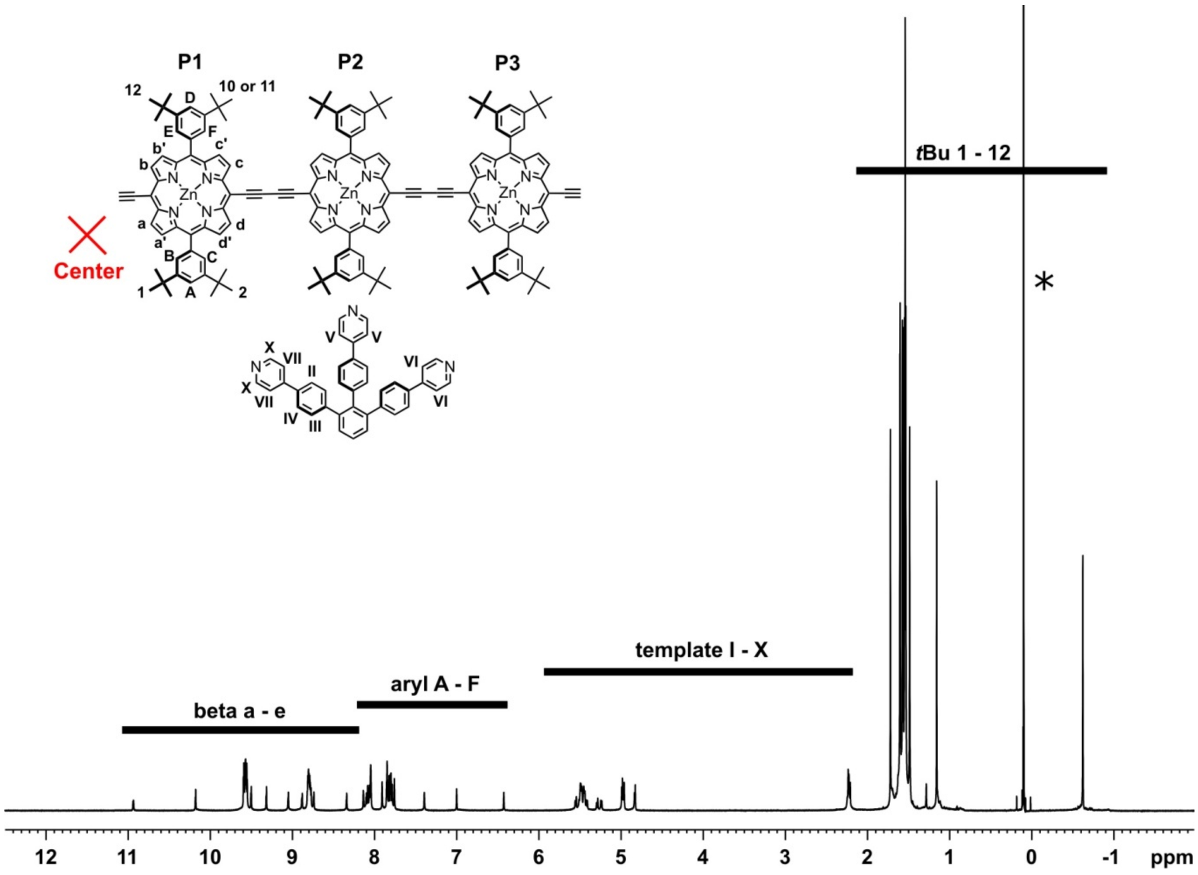

Figure 3.5. *Diffusion-edited* ^{1}*H NMR spectrum of* ***c-P12·(T6)***$_2$ *acquired by Dr. Tim Cladridge (700 MHz, CDCl*$_3$*, 298 K; * indicates a silicon grease impurity).*

All nine protons of each *tert*-butyl group are equivalent and thus result in one singlet. In each quarter of the molecule, the top and the bottom face as well as all sides are non-equivalent, which should result in 12 signals for the *tert*-butyl protons. Figure 3.6 shows the alkyl region consisting of the expected 12 singlets.

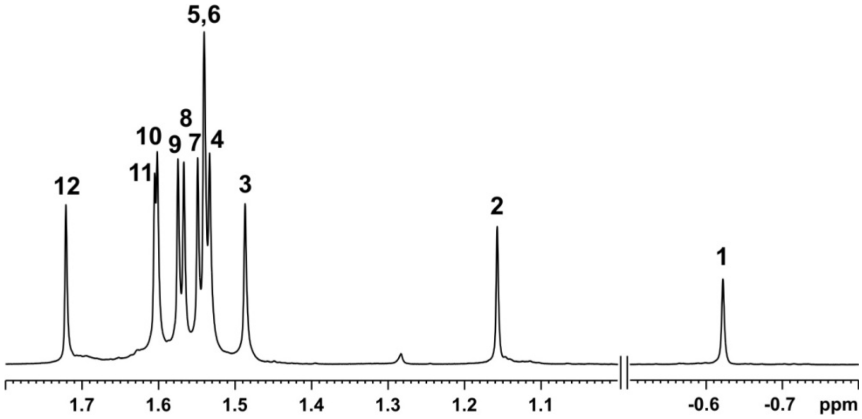

Figure 3.6. *Alkyl region of ^{1}H NMR spectrum, showing the 12 tert-butyl resonances of* c-***P12·(T6)***$_2$ *(700 MHz, CDCl$_3$, 298 K).*

The pyridyl and phenyl protons of the template are expected to be shielded by the ring current of the porphyrin macrocycles. The α-pyridyl protons (VIII–X) are closest to the porphyrin and thus, as in ***c*-P6·T6**, resonate at 2.2 ppm (Figure 3.7). β-Pyridyl protons (V–VII) are less shifted and give rise to three doublets, one for each arm of the template. The inner phenyl protons (I–IV, 5.2–5.6 ppm) are furthest from the porphyrin and are thus the least shifted. Interestingly, fully resolved phenyl peaks such as III or IV integrate to only one proton, which demonstrates that there is slow rotation of the *para*-phenylene links and that, as expected, the edges of the *para*-phenylenes are non-equivalent, whereas the pyridyl groups rotate freely.

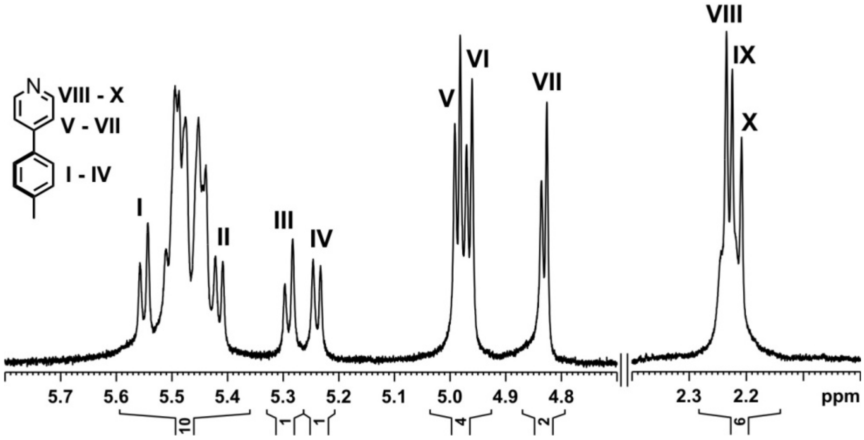

Figure 3.7. *Region of the ^{1}H NMR spectrum showing signals of template protons (700 MHz, CDCl$_3$, 298 K).*

The signals of porphyrin β-pyrrole (a–e') and aryl (A–F) protons are in the aromatic region of the spectrum, with the latter being generally more shielded (Figure 3.8). Only protons of porphyrin unit P1 can be assigned unambiguously, due to their unusual shifts. All other protons are too similar to give well separated signals, thus resulting in overlapping β-pyrrole doublets at 8.8 and 9.6 ppm as well as aryl singlets between 7.7 and 8.2 ppm.

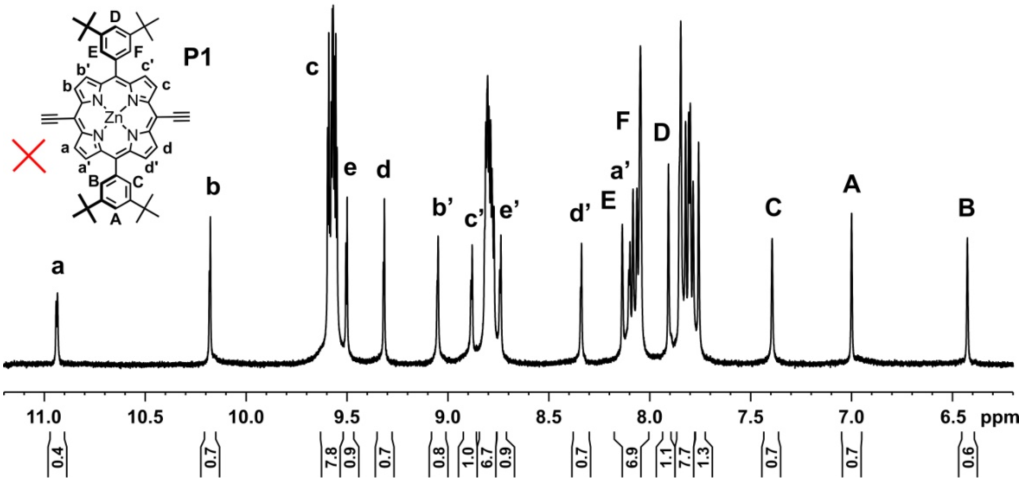

Figure 3.8. *Aromatic region of the ^1H NMR spectrum (diffusion-edited, no $CHCl_3$ peak) with resonances due to porphyrin unit P1 labeled. (700 MHz, $CDCl_3$, 298 K).*

Due to their unusual shift to very low frequencies and by comparison with ***c*-P6·T6**, protons VIII–X can be assigned as the α-pyridyl protons of the template. In the COSY spectrum proton VII clearly couples with X, thus the signal corresponds to the β-pyridyl protons of the same pyridyl group (Figure 3.9). Protons V, VI and VIII, IX belong to the other arms of the template, but due to overlap, precise assignment is difficult. Proximity to the crowded center of ***c*-P12**·(**T6**)$_2$, with many porphyrins in close spatial proximity should cause unusual chemical shifts and thus protons X and VII are tentatively assigned to the arm of the template coordinating to P1.

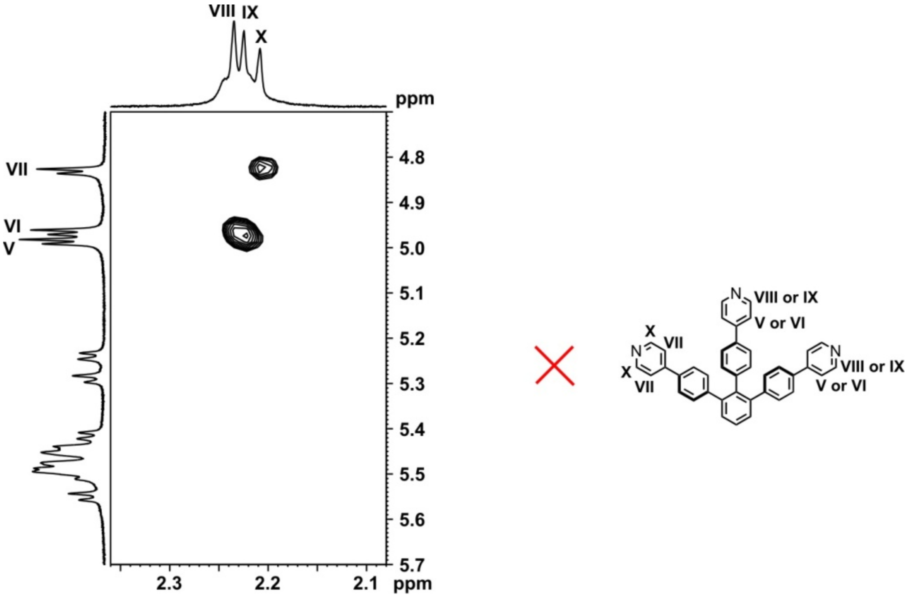

Figure 3.9. *Part of the ^{1}H-^{1}H COSY spectrum showing coupling of pyridyl protons (700 MHz, CDCl$_3$, 298 K).*

β-Pyridyl protons VII are expected to show NOEs with all eight β-pyrrole protons from porphyrin unit P1. In the NOESY seven cross peaks, plus one that overlaps with another signal, can be found and thus protons a–d can be assigned as β-pyrrole protons of P1 (Figure 3.10). The widely spread chemical shifts of these eight β-pyrrole doublets give further evidence that this porphyrin is the one in closest proximity to the center where ring-current effects from other porphyrin units are greatest.

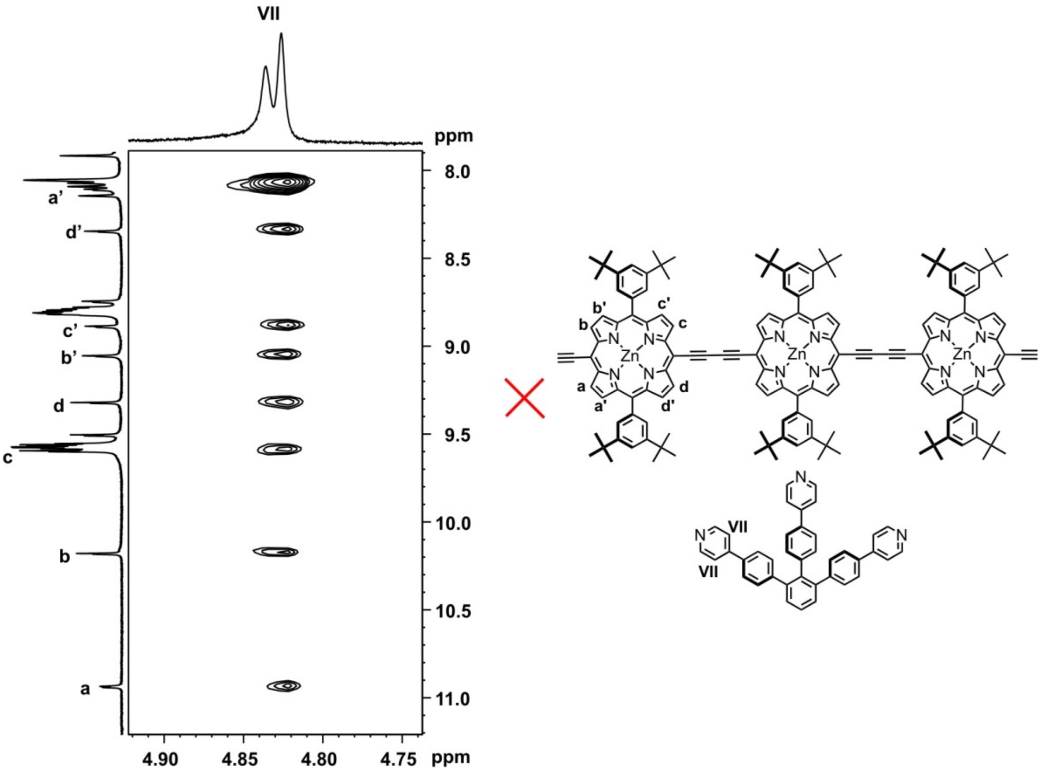

Figure 3.10. *Part of the NOESY spectrum showing assignment of P1 β-pyrrole protons (700 MHz, mixing time = 200 ms, CDCl$_3$, 298 K).*

Having identified all P1 β-pyrrole protons, COSY allows identification of pairs such as a and a', belonging to the same pyrrole unit (Figure 3.11). It is remarkable that protons a and a' are separated by almost 3 ppm although their chemical environments are very similar. This effect must be due to the influence of the ring current from a nearby porphyrin unit in the crowded center of the figure-of-eight. Whilst assignment of P1 protons is straightforward, the β-pyrrole protons of porphyrin units P2 and P3 (resonate at 9.6 and 8.8 ppm) overlap and cannot be distinguished.

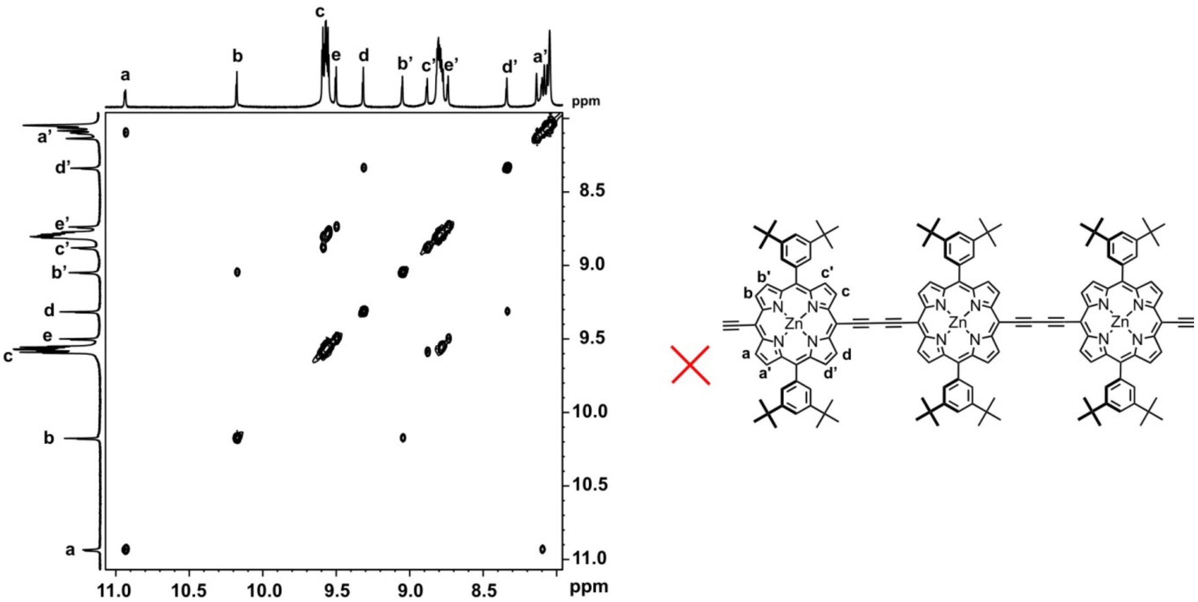

Figure 3.11. *Part of the ^{1}H-^{1}H COSY spectrum showing coupling between porphyrin β-pyrrole protons of porphyrin unit P1 (700 MHz, $CDCl_3$, 298 K).*

In the aryl region three well separated singlets A, B and C correspond to protons from the same aryl group, as confirmed by the COSY spectrum shown in Figure 3.12.

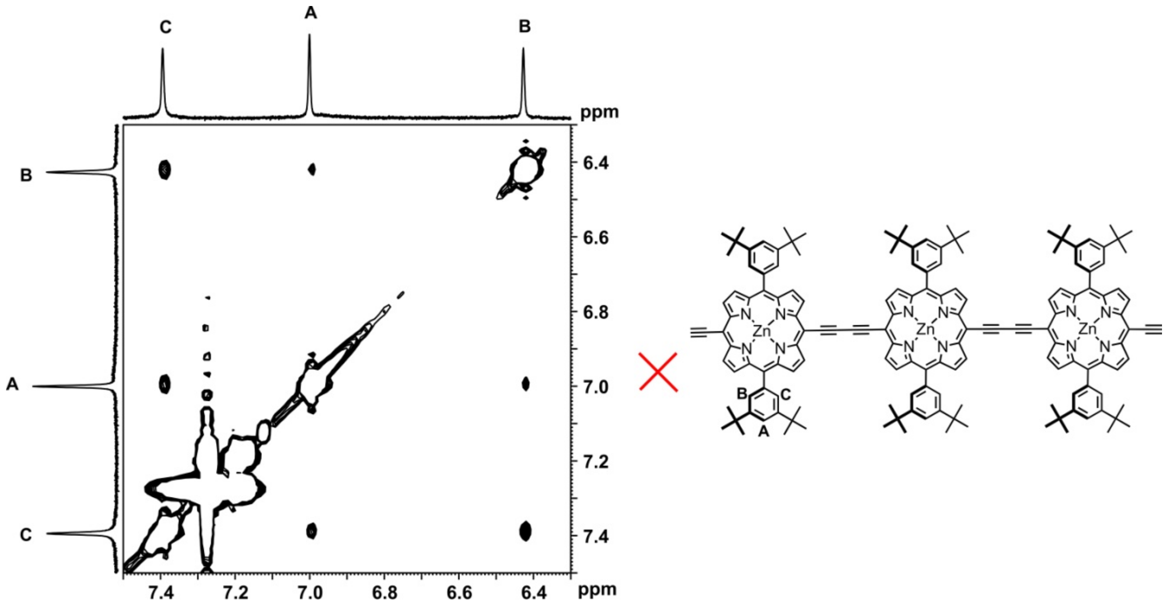

Figure 3.12. *Selected region of the ^{1}H-^{1}H COSY spectrum showing coupling between aryl protons A, B and C of porphyrin unit P1 (700 MHz, $CDCl_3$, 298 K).*

Aryl proton C shows a strong NOE with α-pyridyl proton X (Figure 3.13). Consequently aryl protons A–C must belong to porphyrin unit P1 with proton C pointing towards the template. Aryl protons C and B show strong NOEs with β-pyrrole protons a' and d' and weak NOE with a and d (Figure 3.14).

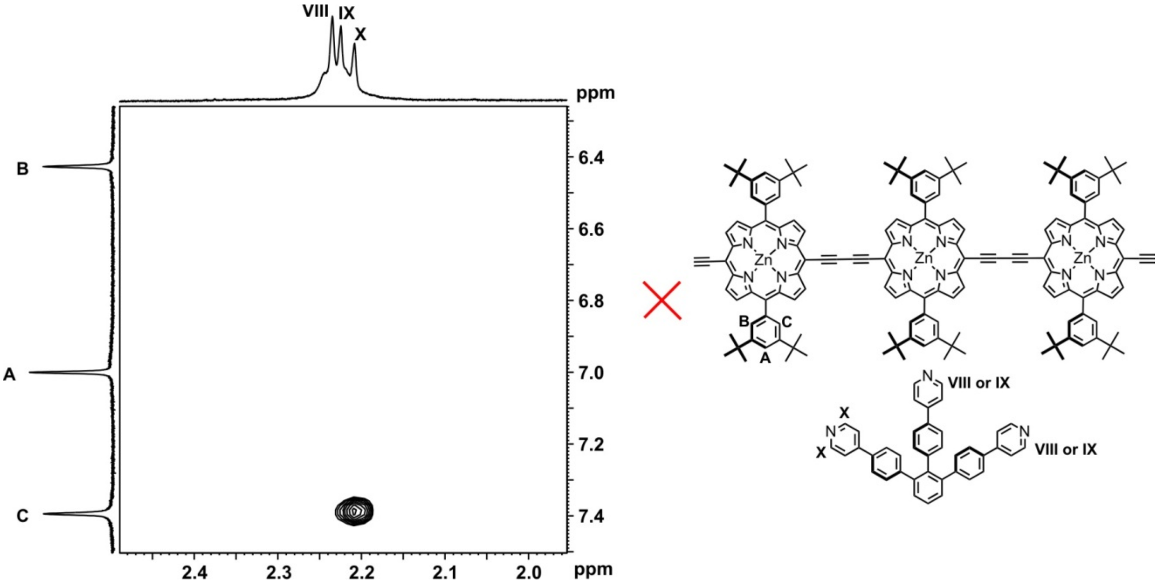

Figure 3.13. Part of the NOESY spectrum shows correlation between aryl proton C and template proton X (700 MHz, mixing time = 200 ms, $CDCl_3$, 298 K).

Aryl proton A only has a weak cross peak with a' and d' which probably arises through spin diffusion processes. Thus A is *para* to the porphyrin, and a’ and d’ are the β-pyrrole protons adjacent to the aryl group whilst a and d are adjacent to the acetylenes. The unusual shifts of A, B and C, as well as β-pyrrole protons a and a', indicate that this is the side of porphyrin unit P1 pointing towards the center of the figure-of-eight complex. Strongly shifted protons a and a' are probably pointing towards the center, whereas d and d’ point towards porphyrin unit P2. This is confirmed by the observation of weak NOEs between d and e which belong to porphyrin unit P2 (Figure 3.16).

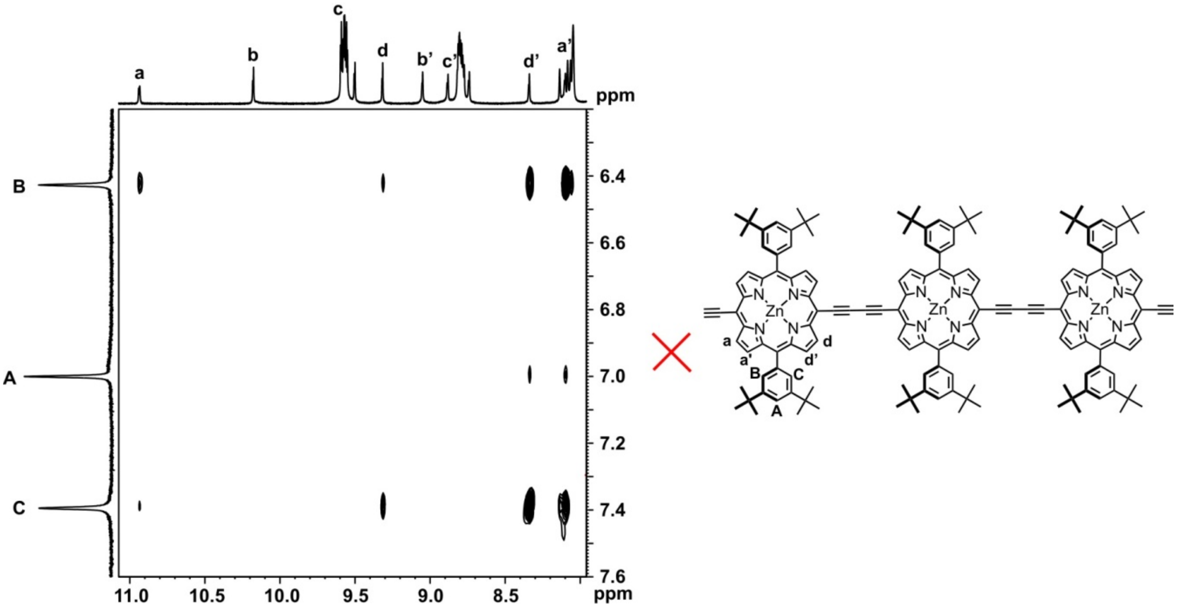

Figure 3.14. *Part of the NOESY spectrum showing correlations between aryl and β-pyrrole protons at porphyrin unit P1 (700 MHz, mixing time = 200 ms, $CDCl_3$, 298 K).*

Interestingly, the NOE between aryl proton B (pointing away from template) and a' is stronger than with d'. At the same time the NOE between C (pointing towards template) and d' is stronger than with a' (Figures 3.14 and 3.15). These effects indicate a twist of the aryl group, with the top side leaning towards the center of the eight. The result also indicates a certain rigidity in the center of the molecule, that holds the aryl groups in a single conformation. Steric restrictions in the crowded center can explain this behavior.

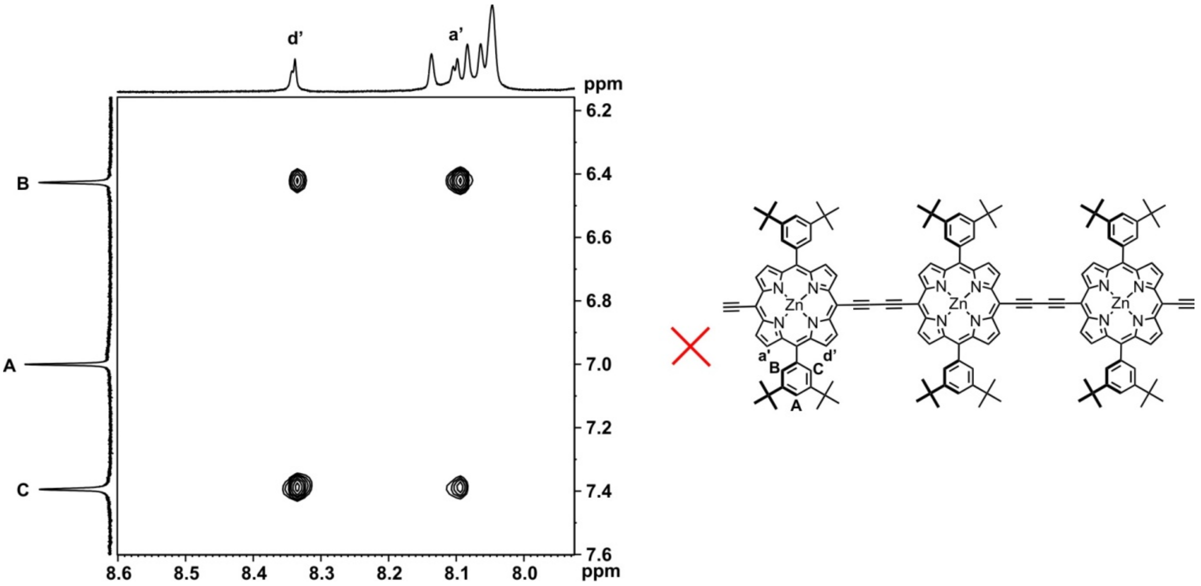

Figure 3.15. *Part of the NOESY spectrum showing correlations between aryl and β-pyrrole protons, revealing the preferential twist of the aryl group (700 MHz, mixing time = 200 ms, $CDCl_3$, 298 K).*

As expected from COSY, β-pyrrole protons a, d and b' all display strong NOEs with their neighboring protons a', d' and b, respectively. Additionally, each of these protons has a weaker NOE with the nearer proton on the adjacent pyrrole and consequently these can be assigned to b, c and c' respectively (Figure 3.16). This completes the assignment of all β-pyrrole protons at porphyrin unit P1.

There is also a weak NOE between d and e. This means that protons e and e' belong to porphyrin unit P2. However, the exact position of e and e' is unclear since c is buried under many other peaks making it impossible to exclude that c has a stronger NOE with e than has d.

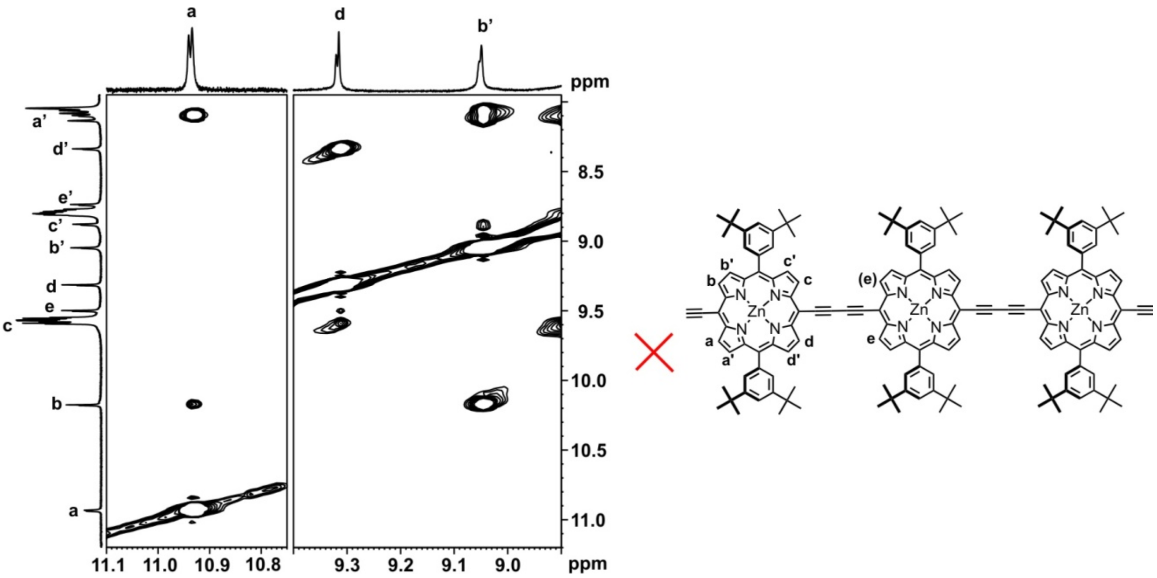

Figure 3.16. *Part of the NOESY spectrum correlating β-pyrrole protons of different pyrroles. The third, intense crosspeak for b' arises from a NOE with the adjacent aryl proton (700 MHz, mixing time = 200 ms, $CDCl_3$, 298 K).*

Some of the *tert*-butyl singlets can be assigned by their NOEs with the pyridyl protons of the template (Figure 3.17). The two singlets that have stronger NOE with pyridyl protons VII belong to porphyrin unit P1 and point towards the template (2 and either 10 or 11). The two signals that show weaker NOEs correspond to the protons pointing away from the template (1 and 12). These signals are likely to arise from spin diffusion. Additionally, there is a weak NOE between 2 and V; this means that V must be part of the 'middle arm' of the template that coordinates to porphyrin unit P2.

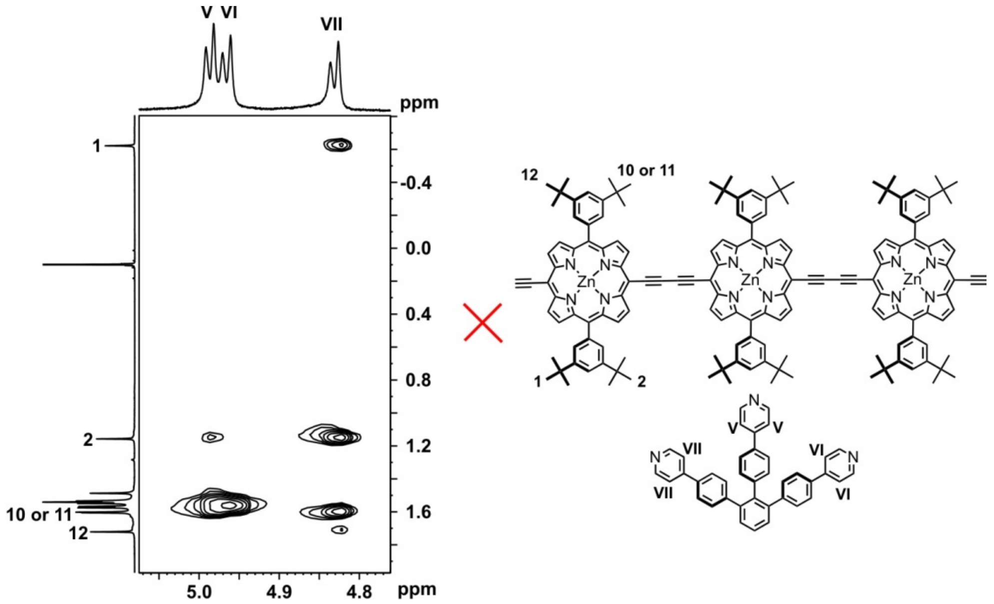

Figure 3.17. This region of the NOESY spectrum shows correlation of tert-butyl protons with the pyridyl protons of the template (700 MHz, mixing time = 200 ms, $CDCl_3$, 298 K).

NOEs of *tert*-butyl singlets 1 and 2 with aryl signals A, B and C allow us to assign them to the aryl group that points towards the center of ***c*-P12·(T6)**$_2$ (Figure 3.18). Coupling between 1 and A as well as B confirms that this *tert*-butyl group points away from the template.

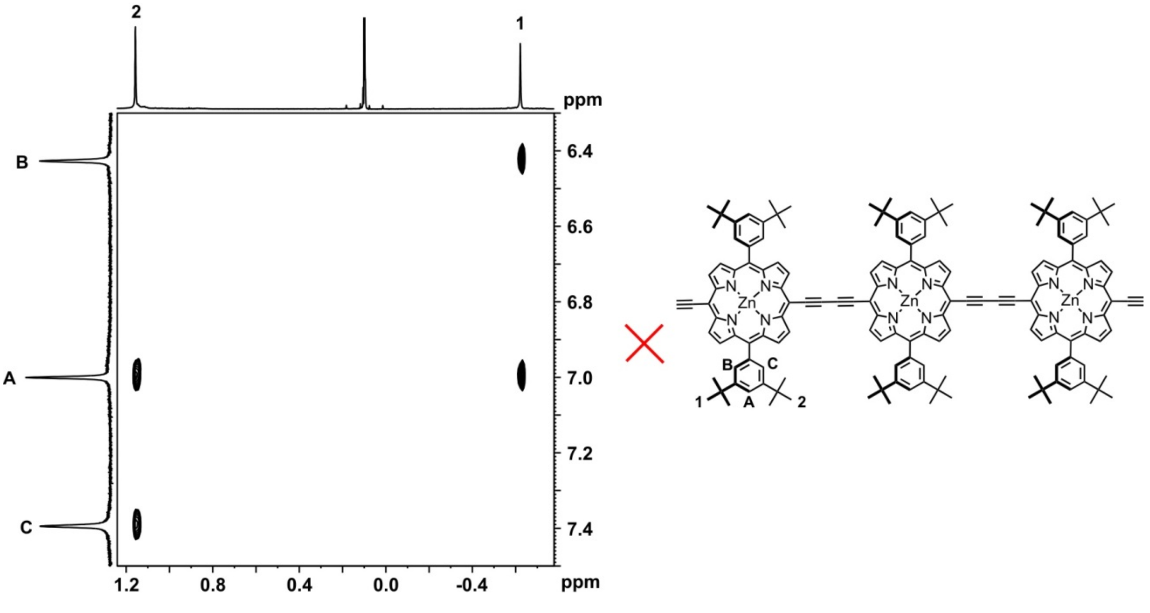

Figure 3.18. NOESY correlations between tert-butyl singlets and aryl protons (700 MHz, mixing time = 200 ms, $CDCl_3$, 298 K).

The signals due to the aryl group of porphyrin P1 which points away from the center of the eight display similar shifts to the aryl protons of porphyrin units P2 and P3. This causes partial overlap of peaks and makes assignment more difficult. NOESY shows that *tert*-butyl 12 (pointing outwards) is close to aryl proton E and that proton D is *para* to the porphyrin because it also couples to *tert*-butyl proton 10/11. Due to overlaps, aryl proton F cannot be directly assigned from this part of the spectrum.

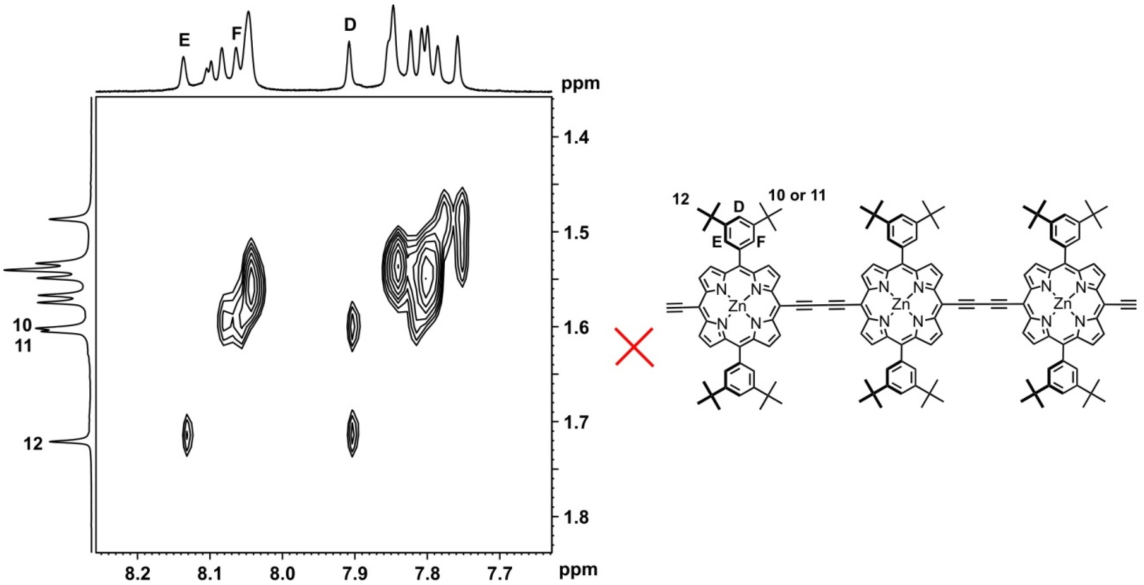

Figure 3.19. *NOESY correlations between tert-butyl singlets and aryl protons (700 MHz, mixing time = 200 ms, $CDCl_3$, 298 K).*

Aryl proton F can be assigned unambiguously using NOEs with porphyrin β-pyrrole protons. Protons b' and c' display NOEs with aryl signals E and F, but not D (pointing away from porphyrin P1). E has a stronger correlation with c' than with b' and F has a stronger correlation with b' than with c'. The relative intensities of these cross-peaks show that the top of the aryl group (pointing away from template) is leaning away from the center of ***c*-P12·(T6)**$_2$. It is therefore perpendicular to the aryl group on the opposite side of P1 (Figures 3.20 and 3.15).

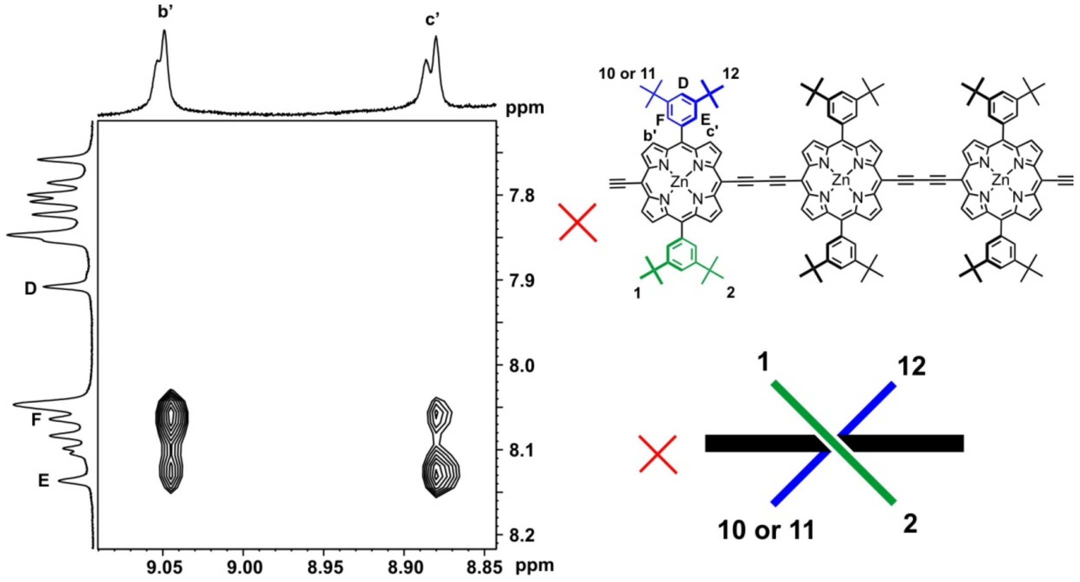

Figure 3.20. *NOESY correlations between β-pyrrole protons and aryl protons and cartoon showing twist of aryl groups of P1 (700 MHz, mixing time = 200 ms, $CDCl_3$, 298 K).*

Further assignments of template protons can be made using both NOESY and COSY data (Figure 3.21). One can observe NOEs between VII and IV as well as II. These are both phenyl protons *ortho* to the phenylene-pyridyl bond, but due to hindered rotation they give different signals. In the COSY of the same region, a cross peak between IV and III shows that they belong to the same phenylene unit.

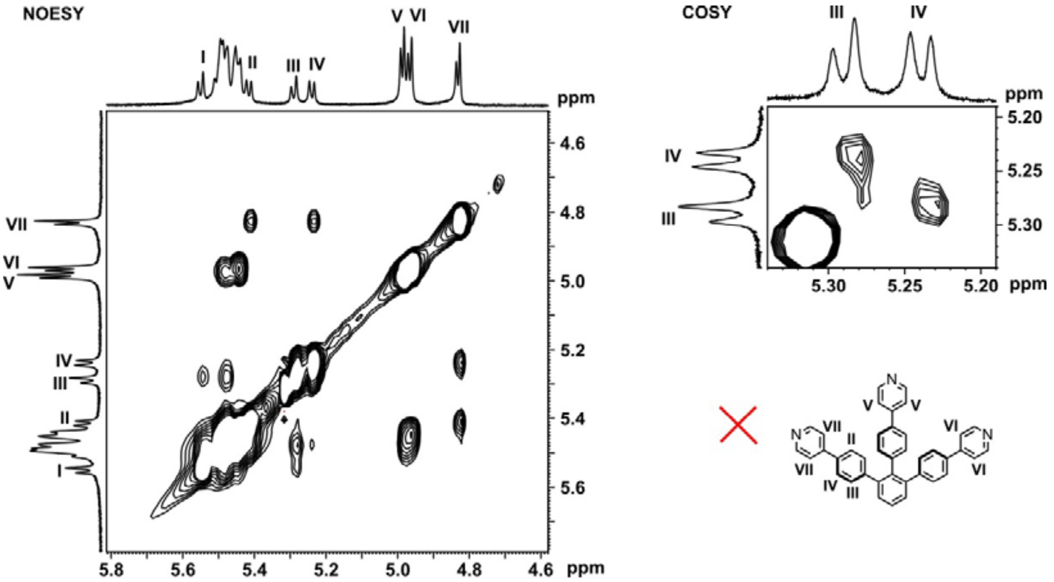

Figure 3.21. *NOESY and COSY cross peaks between template protons (700 MHz, mixing time = 200 ms, $CDCl_3$, 298 K). The intense diagonal cross peak in the COSY at 5.32 ppm is due to residual CH_2Cl_2. This peak is absent in the diffusion-edited 1D projection.*

NOESY data give good structural evidence for the structure of the figure-of-eight using correlations between different porphyrin units in the center of the molecule. As shown above, there are strong NOEs between β-pyrrole protons of porphyrin unit P1 and the adjacent aryl and *tert*-butyl protons (Figures 3.14 and 3.20). This effect is expected because of the close proximity of these protons (3–4 Å). There are also strong NOEs between *tert*-butyl protons 1 and 2 and the β-pyrrole protons b and b', respectively, on the opposite side of P1 (Figure 3.22a). The distance between these groups within the same porphyrin is 8–9 Å, which should not result in detectable NOEs. Thus, the interaction must be between two different but symmetry related porphyrin units. This can be rationalized using the molecular model in Figure 3.22b. In the model, the through-space distance between protons 1 and 2 of one P1 (grey, back) and β-pyrrole protons b and b' of a different P1 (black, front) are 2–3 Å. Along with symmetry arguments, these NOEs between proximate porphyrins in the center of the figure-of-eight unambiguously confirm its structure. If the crossing angle (between grey and black porphyrins) in the center of the figure-of-eight were 90°, the distance of both *tert*-butyl groups 1 and 2 to β-pyrrole protons b and thus their NOEs would be identical. However, in the calculated structure the distance from b' to 1 is slightly smaller than to 2, which is reflected in a stronger NOE. Similar behavior is observed between protons 1 and 2 with the more remote β-pyrrole proton c': A weak NOE can be observed between 1 and c' (distance 5.9 Å) but no NOE between 2 and c' (distance 8.3 Å). These differences in the intensities of the NOEs suggest that the crossing angle must be larger than 90°, which is in agreement with the model (116°).

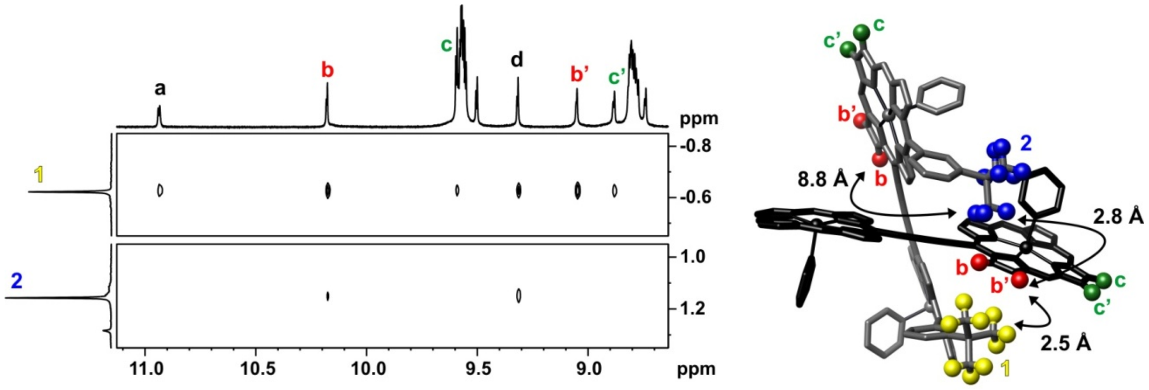

Figure 3.22. *Interporphyrin NOEs between β-pyrrole and tert-butyl protons and model of center of* ***c-P12·(T6)$_2$*** *(700 MHz, mixing time = 200 ms, $CDCl_3$, 298 K).*

Removal of the templates from the figure-of-eight complex results in a dramatic simplification of the ^{1}H NMR spectrum (Figure 3.23). Due to the D_{12h} symmetry of ***c*-P12** the spectrum consists of only two β-pyrrole doublets (a, b), two aryl signals (A, B) and one *tert*-butyl singlet (1). The simplicity of the spectrum is excellent evidence for formation of a single highly symmetric cyclic species.

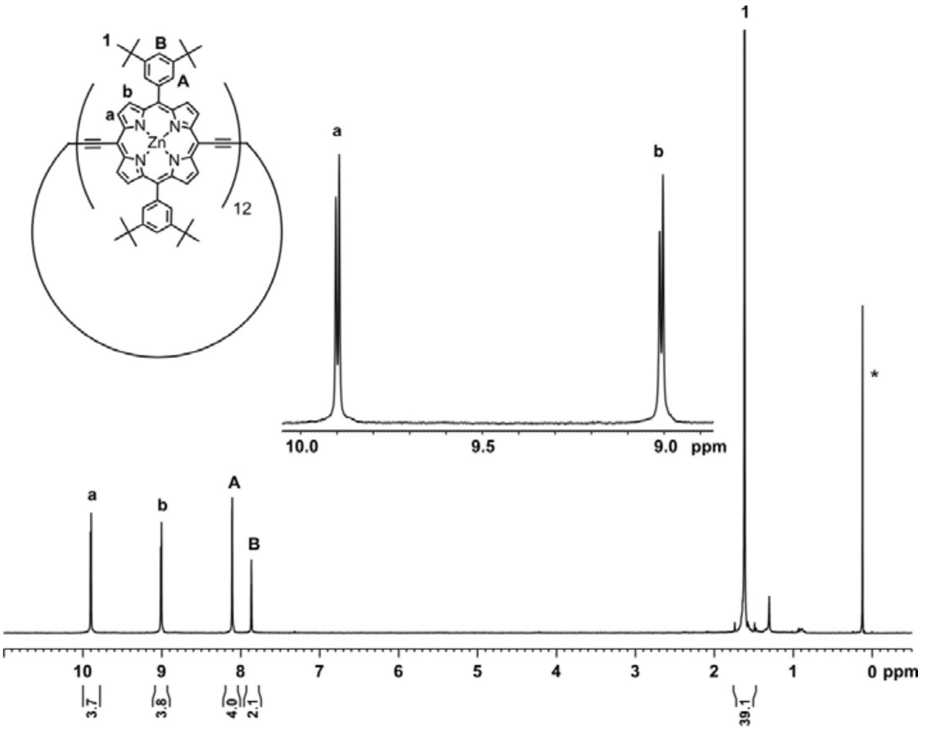

Figure 3.23. *Diffusion-edited ^{1}H NMR spectrum of* ***c-P12*** *with zoom on β-pyrrole region acquired by Dr. Barbara Odell (500 MHz, $CDCl_3$/1% d_5-pyridine, 298 K; * indicates a silicon grease impurity).*

Titration of template **T6** to linear tetramer ***l*-P4$_{C8}$** in the ratio 2:3 should result in formation of the Vernier complex (***l*-dP4$_{C8}$**)$_3$·(**T6**)$_2$, but the peaks in the ^{1}H NMR spectrum are broad and no useful structural information can be directly extracted. Diffusion-ordered NMR spectroscopy (DOSY) is a frequently used tool to determine volumes and masses of supramolecular complexes by comparing measured diffusion coefficients with those of known compounds.[7] The 2D DOSY spectrum of a 3:2 mixture of ***l*-dP4**$_{\mathbf{C8}}$ and **T6** shows similar diffusion coefficients for porphyrin and template signals thereby confirming the formation of one complex (Figure 3.24a). The similarity of the diffusion coefficients of this complex ($D = 1.92 \pm 0.14 \times 10^{-10}$ m^2 s^{-1}) and the figure of eight ***c*-P12**$_{\mathbf{C8}}$·(**T6**)$_2$ ($D = 1.91 \pm 0.07 \times 10^{-10}$ m^2 s^{-1}) suggest similar volumes for both species and thus formation of the Vernier complex (***l*-dP4**$_{\mathbf{C8}}$)$_3$·(**T6**)$_2$.

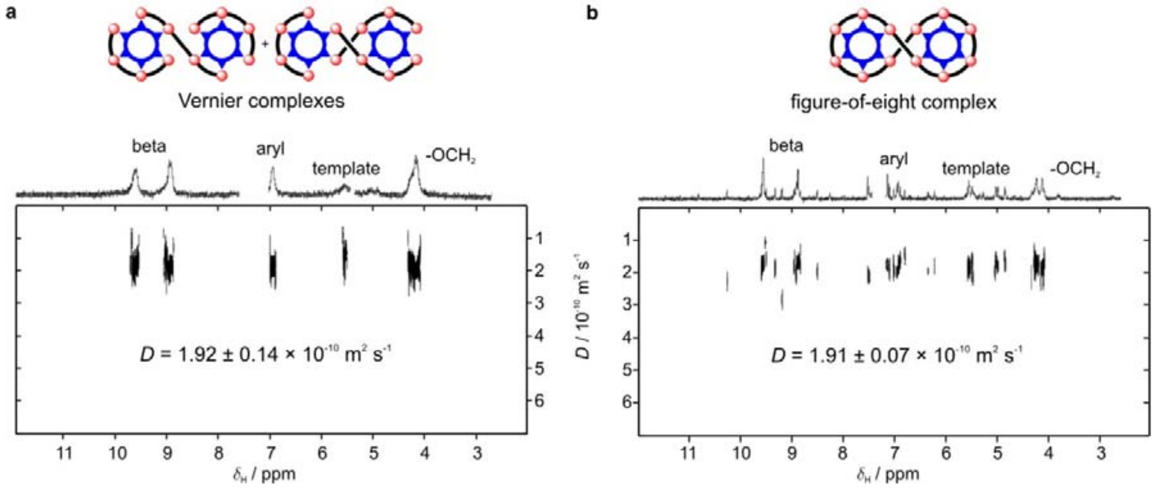

Figure 3.24. *DOSY spectra of (a) the Vernier complex (**l-dP4**$_{C8}$)$_3$·(**T6**)$_2$ and (b) the figure-of-eight complex (**c-P12**$_{C8}$)·(**T6**)$_2$ acquired by Dr. Barbara Odell using the double stimulated echo sequence (DSTE)[8] with a total diffusion time Δ = 100 ms and gradient pulse duration δ = 4 ms (500 MHz, CDCl$_3$, 298 K). 2D plots were created using the program DOSY toolbox. Diffusion coefficients were obtained from fitting porphyrin beta and aryl alkoxy signals. The regions with gaps in the 1D projections were not used for the creation of the DOSY plots because they are dominated by peaks due to fast diffusing solvent molecules.*

3.3.3 Small Angle X-ray Scattering in Solution

SAXS analysis was carried out in order to obtain more detailed structural information on the figure-of-eight, the free [12]porphyrin nanoring and the Vernier complex. Linearity of the scattering data in the Guinier region, for all three samples confirmed the monodispersity required to perform further analysis (Figure 3.25). The radii of gyration R_g for the three structures, determined using the program GNOM,[9] are in good agreement with the values calculated from molecular models (Table 3.1).

Table 3.1. *Comparison of experimentally determined and calculated radii of gyration R_g.*

Compound	**R_g (exp) in Å**	**R_g (calc) in Å**
Figure-of-eight (***c*-P12**)·(**T6**)$_2$	20.1	18.2
Cyclic dodecamer ***c*-P12**	23.7	24.8
Vernier complex (***l*-P4**$_{C8}$)$_3$·(**T6**)$_2$	19.0	18.4

The folded figure-of-eight structure with the two sub-cycles almost in plane is the lowest energy geometry for ***c*-P12·(T6)**$_2$ as calculated by the MM+ force field and also the semi-empirical PM3 method. Structures with a greater angle between the two sub-cycles with the extreme case of complete unfolding are all higher in energy. This prediction is confirmed by the good agreement of the experimental scattering data with the simulated curve based on the lowest energy model (Figure 3.25a). Similar good agreement is achieved between the calculated and experimental pair distribution function (PDF). The longest calculated zinc-zinc distance in the figure-of-eight structure is 53 Å and the width across one sub-cycle is 24 Å; well-resolved peaks that match these distances can be found in the PDF.

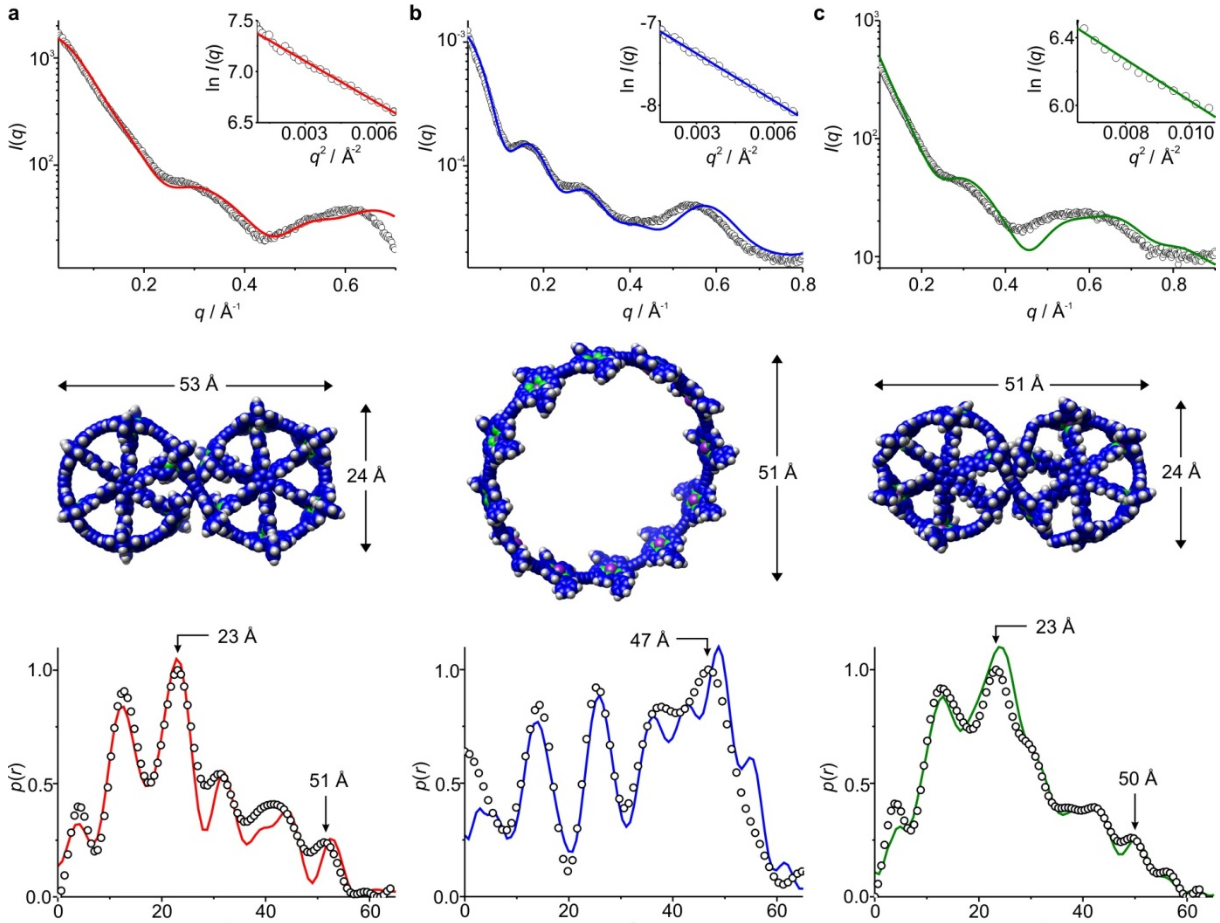

Figure 3.25. *SAXS analysis of (a) figure-of-eight (**c-P12)·(T6)**$_2$ in toluene, (b) cyclic dodecamer **c-P12** in toluene/1% pyridine and (c) Vernier complex (**l-P4**$_{C8}$)$_3$·**(T6)**$_2$ in toluene acquired at 298 K at Diamond Light Source, UK. The top row shows the raw scattering data (black circles) together with the simulated curves based on calculated models (lines). The insets are Guinier fits to the experimental scattering data based on the radii of gyration R_g determined by the program GNOM. The middle row contains the molecular models that were used to simulate SAXS data except in the case of **c-P12**.where an ensemble of structures was used. Energy minimized structures were obtained using the MM+ force field implemented in the package HyperChem^{TM}. The longer distances are the calculated Zn-Zn distances between the most distant porphyrins, and the shorter distances in figure-of-eight and Vernier complex are between two opposite porphyrins in the sub-cycles. The bottom row shows pair-distribution functions determined experimentally (black circles) and from models (lines).*

Simulation of a scattering curve and PDF from the perfectly round lowest energy structure of the cyclic dodecamer ***c*-P12** results in poor agreement with the data due to the great flexibility of the nanoring. Molecular dynamics simulations can reproduce the distribution of conformations in solution and it has been shown that this can significantly improve the accuracy of fits to experimental SAXS data.[11] In a simpler approach six different conformations of ***c*-P12** were calculated using the MM+ force field by restricting the distance between two opposite porphyrins to increasingly small values (Zn–Zn distances from 47–37 Å). The average of the scattering curves simulated from these six models is in excellent agreement with the experimental scattering data; good agreement is also observed between simulated and experimental PDFs (Figure 3.25b). The fact that the experimental data could only be reproduced by an ensemble of distorted structures demonstrates the greater flexibility of the [12]porphyrin nanoring ***c*-P12** compared to the shape-persistent [6]porphyrin nanoring ***c*-P6**.

In addition to the DOSY NMR data presented above, the formation of a Vernier complex between linear tetramer ***l*-P4**$_{\mathbf{C8}}$ and hexadentate template **T6** is unambiguously confirmed by the SAXS data. Both the simulated scattering curve and the PDF based on the model shown in Figure 3.25c are in excellent agreement with the experimental data which, as expected, is very similar to the curves of the figure-of-eight complex.

3.3.4 Scanning Tunneling Microscopy

The [12]porphyrin nanoring ***c*-P12**$_{\mathbf{C8}}$ was analyzed using scanning tunneling microscopy (STM) by Dr. Alex Saywell, Matthew Blunt, Dr. James O'Shea and Prof. Peter Beton (University of Nottingham, UK). Since sublimation of such large molecules on the surface is difficult, the molecules were deposited by electrospray[11] on a Au(111) surface in ultra-high vacuum to achieve sub-monolayer coverage. In an initial experiment a sample of ***c*-P12**$_{\mathbf{C8}}$ synthesized from porphyrin monomer ***l*-dP1**$_{\mathbf{C8}}$ was studied. A great number of nanometer-sized rings attached to gold step-edges (vertical lines) can be seen in the large area STM image shown in Figure 3.26a. Individual porphyrin units in the rings can be clearly identified allowing the determination of the number of porphyrin units in each ring. As expected, most of the rings are cyclic dodecamer ***c*-P12**$_{\mathbf{C8}}$ (~95%), but a small number of larger rings comprising 18 porphyrin units (***c*-P18**$_{\mathbf{C8}}$) can be identified as well (~5%). The presence of these rings is in agreement with the prediction that besides the isolated ***c*-P6**$_{\mathbf{C8}}$**·T6** and ***c*-P12**$_{\mathbf{C8}}$·(**T6**)$_2$ even larger rings are formed from monomer and dimer with a number of porphyrin units being a multiple of six. A sample of ***c*-P12**$_{\mathbf{C8}}$ made from ***l*-dP4**$_{\mathbf{C8}}$ was analyzed in a second experiment and almost exclusively 12-ring was identified (Figure 3.26b,c). This increased purity highlights the advantage of Vernier templating compared to the synthesis from monomer ***l*-dP1**$_{\mathbf{C8}}$ or dimer ***l*-dP2**$_{\mathbf{C8}}$. However, the formation of a small fraction of the larger [16]porphyrin ring ***c*-P16**$_{\mathbf{C8}}$ shows that a possibility of mismatches in Vernier templating remains (Figure 3.26c).

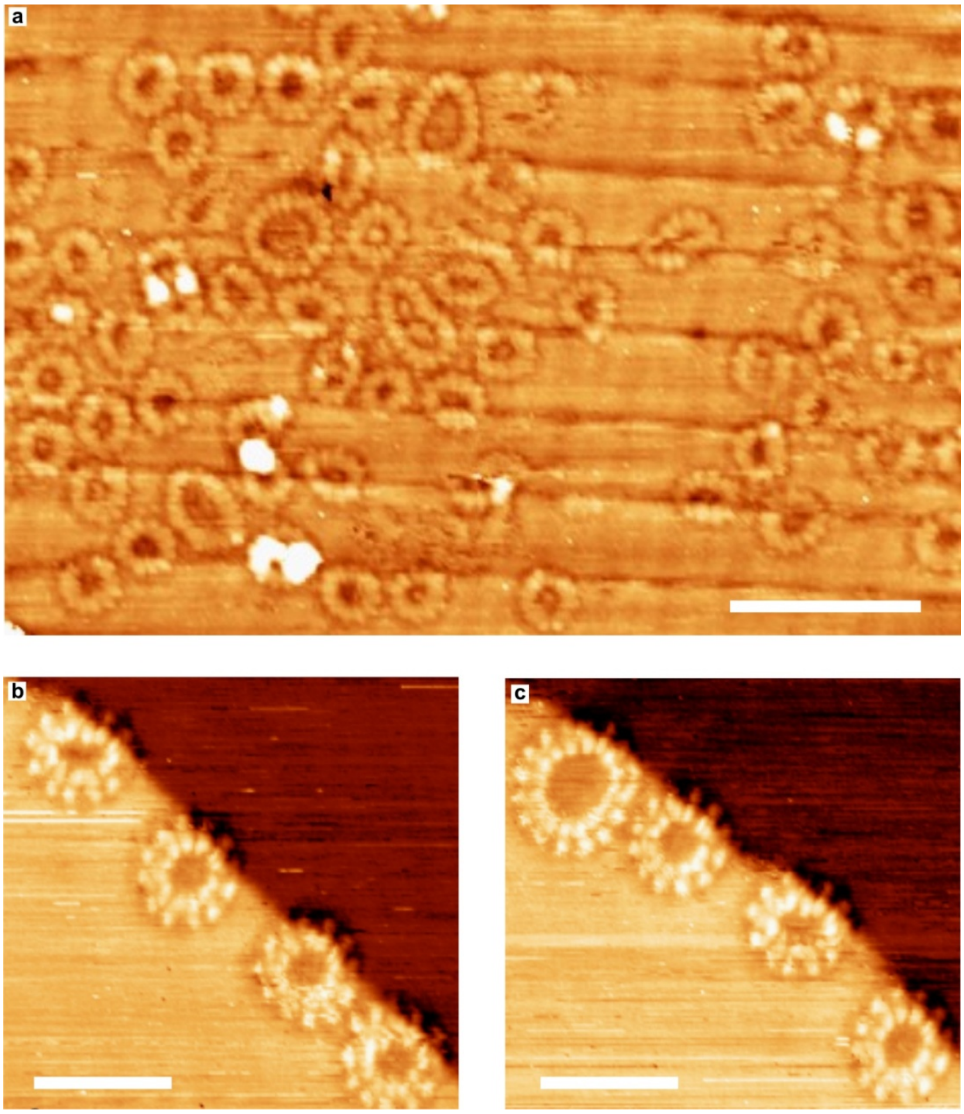

Figure 3.26. *STM imaging of* ***c-P12$_{C8}$*** *on a Au(111) surface. (a) Large area image of* ***c-P12$_{C8}$*** *synthesized from monomer* ***l-dP1$_{C8}$*** *and containing some molecules* ***c-P18$_{C8}$*** *(scale bar, 20 nm); (b) four molecules of* ***c-P12$_{C8}$*** *synthesized from* ***l-dP4$_{C8}$*** *at a gold step-edge (scale bar, 10 nm); (c) nanorings synthesized from* ***l-dP4$_{C8}$*** *with one molecule* ***c-P16$_{C8}$*** *at a gold step-edge (scale bar, 10 nm). All images were acquired by Dr. Alex Saywell and Matthew Blunt under ultra-high vacuum with a base pressure of 5×10^{-11} Torr, a sample voltage of -1.80 V and tunneling current of 0.03 nA.*

3.4 Thermodynamics of Template Binding

The transition from the flexible free nanoring ***c*-P12** to the compact figure-of-eight complex upon addition of template **T6** results in a decrease in the radius of gyration (Table 3.1) and an increase in the diffusion coefficient (Figures 3.24 and 4.4) and is thus best described as a folding event. In a simplified picture this process can be defined by two equilibria leading to formation of the figure-of-eight ***c*-P12·(T6)$_2$** *via* the complex ***c*-P12·T6** (Figure 3.27). The equilibrium constants of the two events are linked by the interaction parameter α that quantifies the allosteric or intermolecular cooperativity between the binding of the two templates; if $\alpha = 1$ then binding of the two **T6** molecules is statistical, if $\alpha >> 1$ there is strong positive cooperativity between the two binding events and the intermediate complex ***c*-P12·T6** is not significantly populated.

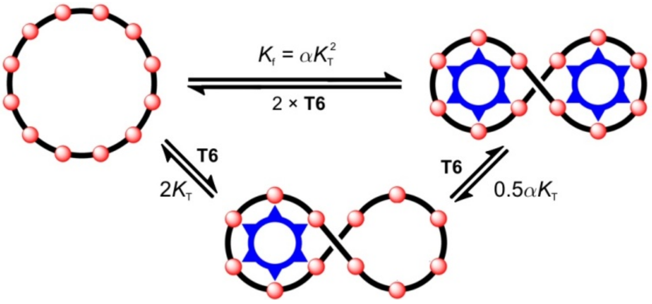

***Figure 3.27.** Simplified equilibria for the formation of the figure-of-eight complex (**c-P12**)·(**T6**)$_2$ from **c-P12**.*

When looking into the binding process in more detail it becomes clear that besides allosteric cooperativity between the two template molecules, one must also consider the chelate or intramolecular cooperativity between the six arms of one template. This type of cooperativity is expressed in terms of the effective molarity *EM*. Figure 3.28 shows the equilibria involved in the stepwise binding one molecule of template to ***c*-P12** and each of the *n* steps has its own effective molarity $EM_{n\text{-}1}$. A similar series of effective molarities governs the binding of the second template molecule. If the effective molarities are high, the intermediate species will not be significantly populated and it would be difficult to isolate the individual effective molarities. In this case the chelate cooperativity in the complex can only be quantified by the average effective molarity *EM*.[12,13]

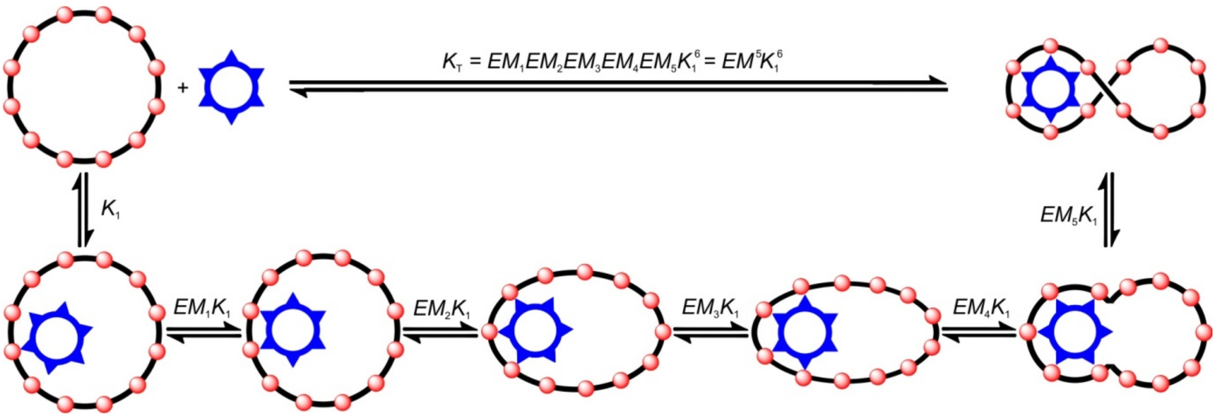

***Figure 3.28.** Equilibria involved in the binding of template **T6** to form the complex **c-P12·T6** from **c-P12**. Similar equilibria govern the binding of the second molecule **T6**. For simplicity statistical factors are not shown.*

The (statistically uncorrected) average effective molarity in ***c*-P6·T6** is extremely high (*EM* = 340 M)[12] and although significantly more strain is induced when binding **T6** to ***c*-P12**, one can still expect large *EM*s for this process. In terms of the allosteric cooperativity between the two template molecules one would expect that the energetic cost of nanoring folding is already mostly paid after the first template is bound. Binding of the second template should be favored because of the pre-organization of the binding pocket giving an interaction parameter α greater than 1. This picture of a process with high chelate as well as allosteric cooperativity was confirmed by a ^{1}H NMR titration of **T6** into ***c*-P12** where a clear transition occurs from the spectrum of ***c*-P12** to that of the figure-of-eight ***c*-P12·(T6)**$_2$ without any detectable intermediate species. Figure 3.29 shows the alkyl region of the spectra that is dominated by the *tert*-butyl singlet at δ_H = 1.56 ppm in ***c*-P12**. This signal converts cleanly to the various *tert*-butyl signals typical for the spectrum of the figure-of-eight ***c*-P12·(T6)**$_2$.

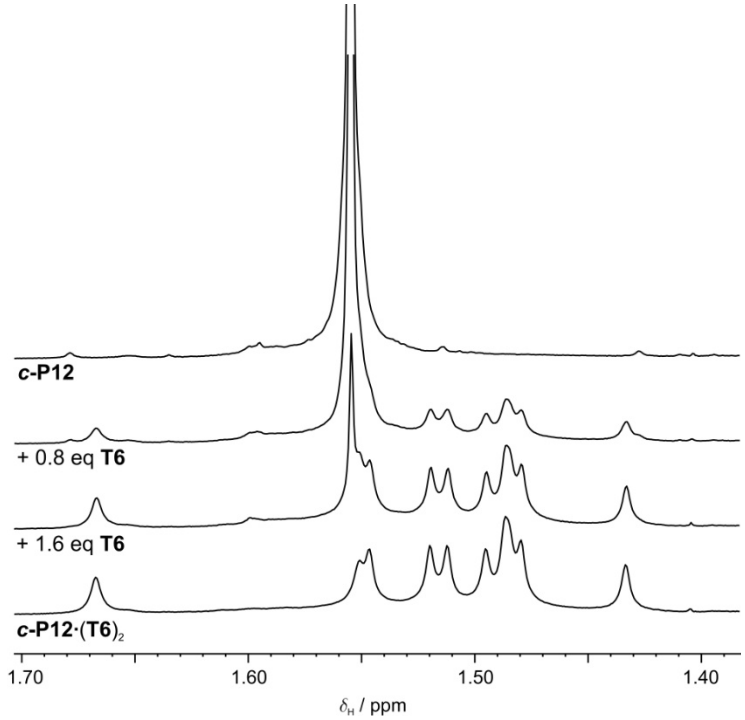

Figure 3.29. *^{1}H NMR titration of **c-P12** (**[c-P12]** = 3.6×10^{-4} mol L^{-1}) with **T6** in CDCl$_3$ /3% MeOD at 298 K. Concentration of **T6** increases from top to bottom. All spectra are superpositions of the pure spectra of **c-P12** and (**c-P12**)·(**T6**)$_2$ and no formation of intermediate species is observed.*

The clean all-or-nothing equilibrium between ***c*-P12** and the figure-of-eight is also observed at sub-micromolar concentrations by UV/vis/NIR titration (Figure 3.30). The presence of several isosbestic points indicates the presence of only two species, the free nanoring and the figure-of-eight complex. The binding isotherm is very square and reaches saturation after addition of two equivalents of **T6**, corresponding to the stoichiometry of ***c*-P12·(T6)**$_2$. In order to quantify the cooperativity it is necessary to first determine the formation constant of the figure-of-eight complex K_f. However, the squareness of the binding isotherm indicates extremely strong binding preventing the direct determination of K_f by means of a formation titration.

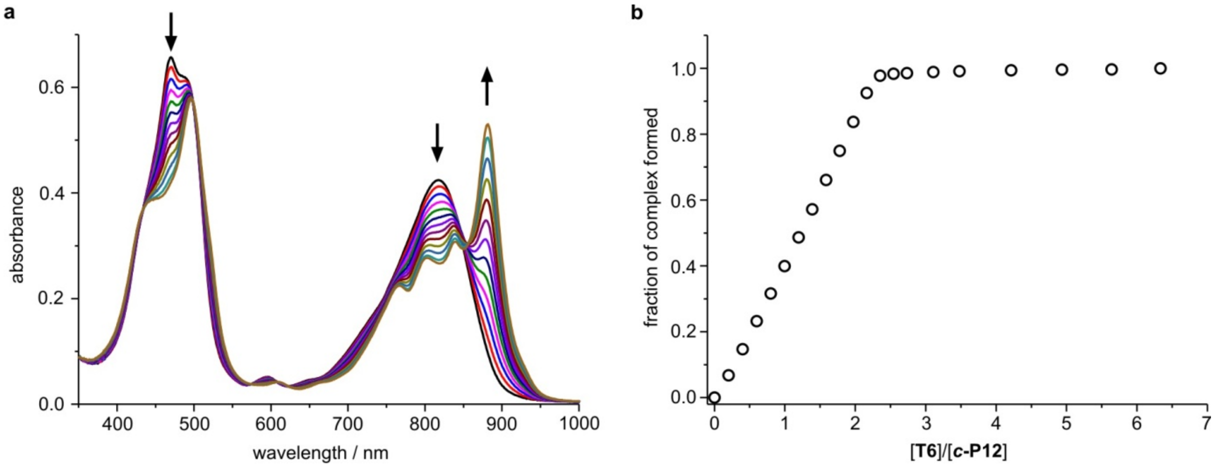

Figure 3.30. *UV/vis/NIR titration of **c-P12** ([**c-P12**] = 4.4 × 10^{-7} mol L^{-1}) with **T6** in $CHCl_3$ at 298 K. (a) Changes in absorption upon addition of **T6**; (b) fraction of formed figure-of-eight derived from the difference in absorption ΔA at (882 – 812) nm plotted against the ratio **T6**/**c-P12**. A small amount of pyridine ([pyridine] = 6.2 × 10^{-7} mol L^{-1}) was added at the beginning of the titration in order to disaggregate **c-P12**.*

Large equilibrium constants can be determined indirectly by using thermodynamic cycles and displacement or break-up experiments (Figure 3.31).[12,13,14] Addition of an excess of the competing ligand pyridine to the figure-of-eight complex will result in displacement of the template molecules and formation of the pyridyl complex ***c*-P12·**(pyridine)$_{12}$. According to the thermodynamic cycle in Figure 3.31, the equilibrium constant for this break-up process K_b and the binding constant of pyridine to ***c*-P12** K_{py} can be used to calculate K_f using Equation (3.1).

$$K_f = \frac{K_{py}^{12}}{K_b} \tag{3.1}$$

The binding constant of pyridine with ***c*-P12** is difficult to measure due to the insolubility of ***c*-P12** in the absence of pyridine. The association constant of pyridine with porphyrin monomer ***l*-P1** is expected to be very similar to that with ***c*-P12** and is therefore used as K_{py} (K_{py} = (1.0 ± 0.1) × 10^4 M^{-1}).[12,13]

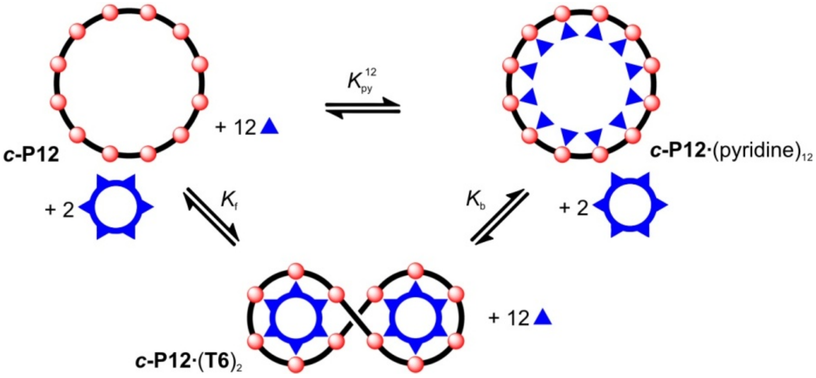

Figure 3.31. *Thermodynamic cycle used to determine the formation constant of the figure-of-eight K_f from the binding constant of pyridine to porphyrin monomer K_{py} and the measured break-up constant K_b.*

A large excess of pyridine (~ 500,000 equivalents) is necessary to completely displace the templates from the figure-of-eight complex at the concentration of a UV/vis/NIR titration (Figure 3.32). The presence of several isosbestic points confirms the expected two-state equilibrium and the sigmoidal binding curve indicates high cooperativity. The equilibrium constant ($K_\mathrm{b} = (7.9 \pm 0.8) \times 10^{-4}$ M^{-10}) was determined by fitting the binding isotherm at 883 nm using the program SPECFIT and the resulting formation constant of the figure-of-eight complex K_f is 1.8×10^{51} M^{-2}. The uncertainty in this number is very high because of the error propagation in K_py^{12} and the value is thus given as $\log K_\mathrm{f} = 51.3 \pm 0.6$.

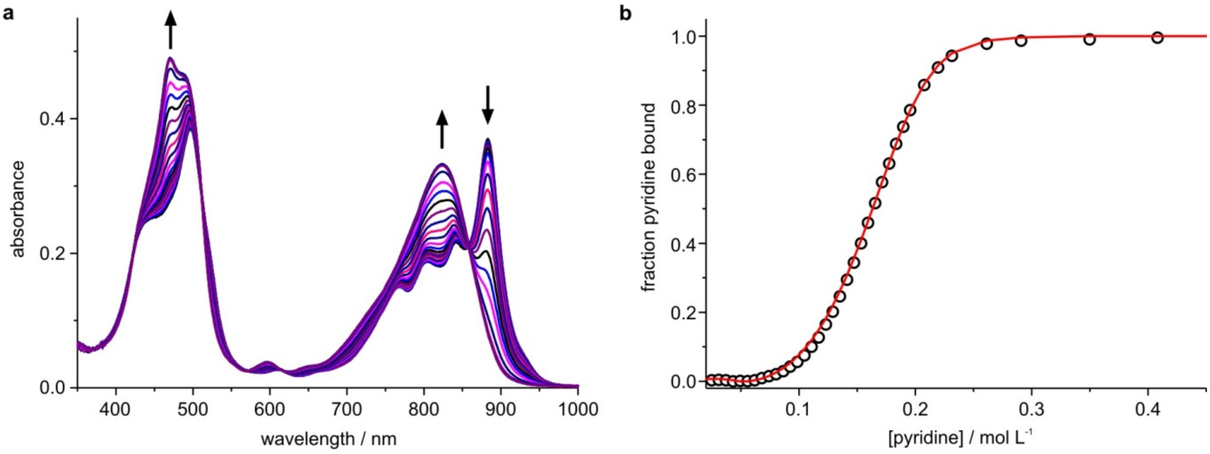

Figure 3.32.*UV/vis/NIR titration of figure-of-eight ([(**c-P12**)·(**T6**)$_2$] = 5.2 × 10^{-7} mol L^{-1}) with pyridine in CHCl$_3$ at 298 K. (a) Changes in absorption upon titration with pyridine (for clarity only half of the spectra acquired are shown here); (b) Binding isotherm (black circles) derived from absorption data at 883 nm and fit obtained from SPECFIT (red line) giving the break-up constant $K_b = (7.9 \pm 0.20) \times 10^{-4}$ M^{-10}.*

As shown in Figure 3.27, the formation constant of the figure-of-eight complex K_f can be expressed by the binding constant of one template K_T and the interaction parameter α accounting for the allosteric cooperativity.

$$K_\mathrm{f} = \alpha K_\mathrm{T}^2 \tag{3.2}$$

K_T depends on the binding constant of one arm of the template K_1 and the average effective molarity EM that quantifies the chelate cooperativity.

$$K_\mathrm{T} = EM^5 K_1^6 \tag{3.3}$$

From Equations (3.2) and (3.3), the combined allosteric and chelate cooperativity in the formation of the figure-of-eight complex is given by Equation (3.4).

$$\sqrt[10]{\alpha} EM = \sqrt[10]{\frac{K_\mathrm{f}}{K_1^{12}}} \approx EM \tag{3.4}$$

Since the interaction parameter α contributes only in the 10th root to this overall cooperativity, its effect on the value is negligible and the result will be a good approximation of the average effective molarity *EM*.[†] The binding constant of one arm of the template to ***c*-P12** K_1 can be approximated from the binding constant of 4-(phenyl)pyridine to porphyrin monomer ***l*-P1**.[13] With $K_1 = (1.9 \pm 0.2) \times 10^4$ M^{-1}, the (statistically uncorrected) average effective molarity of figure-of-eight formation is (1.0 ± 0.2) M. It is remarkable that this high effective molarity is comparable to the value of the cyclic octamer–octadentate template complex ***c*-P8·T8** (*EM* = 5.4 M) given that the figure-of-eight is a three component assembly and it is probably significantly more strained. One can only speculate about the contributions of the individual effective molarities to the average effective molarity. Presumably the first five *EM*s are relatively low because in these processes the majority of the strain is induced. The next five *EM*s corresponding to the binding of the second template are probably significantly higher and similar to the values measured for ligand binding in ***c*-P6**.[15] In this sense the information on the allosteric cooperativity between the two templates will be contained in the higher effective molarities of the second template.

3.5 Conclusions and Outlook

Vernier templating appears to be a promising methodology for the synthesis of large porphyrin macrocycles. Porphyrin oligomers up to octamer ***l*-P8** are readily available as are hexadentate and octadentate template giving numerous possible combinations of oligomers and templates. The largest rings that should be accessible by Vernier templating from these known or closely related building blocks are ***c*-P40** (from ***l*-P5** and **T8**) and ***c*-P56** (from ***l*-P7** and **T8**). Evidence from DOSY and SAXS experiments suggests the formation of a Vernier complex between porphyrin tetramer and hexadentate template. With increasing size such Vernier complexes should become less stable because of the larger number of components. In consequence the reaction mechanism may be dominated by initial coupling of oligomers that are either unbound or in complexes different from Vernier complexes. Cyclization will still occur at the specific Vernier length, but the probability of mismatches, resulting in by-products such as the 16-ring described above, is expected to increase.

Several experiments demonstrated the increased flexibility of ***c*-P12** compared to the smaller cyclic hexamer ***c*-P6**: the agreement of experimental SAXS data to an ensemble of distorted structures, the ability of ***c*-P12** to planarize on a Au(111) surface which was unsuccessfully attempted with ***c*-P6** and also the folding of ***c*-P12** into a figure-of-eight complex. This flexibility is promising towards the formation of novel complexes by applying the rich Zn-N coordination chemistry (see for example Chapter 4) and it will be interesting to study the effect of the induced conformational changes on the linear and non-linear optical properties as well as excited state delocalization.

[†] Even an exceedingly large assumed interaction parameter such as $\alpha = 100$ would reduce *EM* by significantly less than an order of magnitude (~60%).

The results of STM imaging of ***c*-P12** indicate the potential of this technique to provide both, structural characterization and a thorough check for purity with single molecule resolution that is much more sensitive than standard bulk characterization methods such as NMR or GPC.

Binding titrations demonstrate an interesting interplay of chelate and allosteric cooperativity that is not resolvable within the current system and would merit an in-depth study similar to the work on ***c*-P6·T6**.[15] It is curious that the titrations lead to the conclusion that the intermediate complex ***c*-P12·T6** is not formed in solution, but at the same time this complex results in the most intense peak in the MALDI-MS spectrum. Besides the fact that MALDI is not a quantitative technique, this behavior may be explained by different mechanisms of template removal. The displacement by excess pyridine, that saturates all binding sites in solution, leads to formation of the thermodynamic product. The knock-out of the template by collisions in the gas-phase or due to laser irradiation is expected to occur under kinetic control because the probability of subsequent collisions with free template, required for re-insertion, is very low and thus thermodynamic equilibration is prevented.

3.6 References

[1] S. Scheuring, J. N. Sturgis, *Science* **2005**, *309*, 484–487.

[2] A. C. Bleszynski-Jayich, W. E. Shanks, B. Peaudecerf, E. Ginossar, F. von Oppen, L. Glazman, J. G. E. Harris, *Science* **2009**, *326*, 272–275.

[3] S. M. Yu, V. P. Conticello, G. Zhang, C. Kayser, M. J. Fournier, T. L. Mason, D. A. Tirrell, *Nature* **1997**, *389*, 167–170.

[4] T. R. Kelly, R. L. Xie, C. K. Weinreb, T. Bregant, *Tetrahedron Lett.* **1998**, *39*, 3675–3678.

[5] C. A. Hunter, S. Tomas, *J. Am. Chem. Soc.* **2006**, *128*, 8975–8979.

[6] L. J. Prins, P. Scrimin, *Angew. Chem. Int. Ed.* **2009**, *48*, 2288–2306.

[7] Y. Cohen, L. Avram, L. Frish, *Angew. Chem. Int. Ed.* **2005**, *44*, 520–554.

[8] A. Jerschow, N. Müller, *J. Magn. Reson.* **1997**, *125*, 372–375.

[9] D. I. Svergun, *J. Appl. Cryst.* **1992**, *25*, 495–503.

[10] K. L. Mardis, H. M. Sutton, X. Zuo, J. S. Lindsey, D. M. Tiede, *J. Phys. Chem. A.* **2009,** 113, 2516–2523.

[11] A. Saywell, G. Magnano, C. J. Satterley, L. M. A. Perdigão, N. R. Champness, P. H. Beton, J. N. O'Shea, *J. Phys. Chem. C* **2008**, *112*, 7706–7709.

[12] M. Hoffmann, C. J. Wilson, B. Odell, H. L. Anderson, *Angew. Chem. Int. Ed.* **2007**, *46*, 3122–3125.

[13] M. Hoffmann, J. Kärnbratt, M.-H. Chang, L. M. Herz, B. Albinsson, H. L. Anderson, *Angew. Chem. Int. Ed.* **2008**, *47*, 4993–4996.

[14] P. N. Taylor, H. L. Anderson, *J. Am. Chem. Soc.* **1999**, *121*, 11538–11545.

[15] H. J. Hogben, Understanding Cooperativity of Binding to Porphyrin Oligomers, Part II Thesis, University of Oxford, Oxford, **2008**.

Chapter 4

Cooperative Self-Assembly of a Porphyrin Sandwich

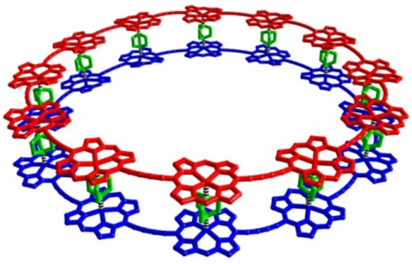

In this chapter double strand formation using the abundant ligand DABCO is developed as an efficient strategy to planarize and rigidify a [12]porphyrin nanoring. Evidence for formation of a double strand complex comes from ^{1}H NMR spectroscopy and in particular NOESY and DOSY. The self-assembly behavior is investigated in detail by UV/vis/NIR titrations, demonstrating the high cooperativity in the formation of the complex. The efficiency of double strand formation as a method to lock the conformation of the nanorings is demostrated by red-shifts and sharpening of the NIR absorption and fluorescence bands.

Parts of the results in this chapter have been published in the following article:

All-or-Nothing Cooperative Self-Assembly of an Annulene Sandwich
J. K. Sprafke, B. Odell, T. D. W. Claridge, H. L. Anderson
Angew. Chem. Int. Ed. **2011**, *50*, 5572–5575.

"Alles-oder-Nichts"-Kooperativität bei der Selbstorganisation eines Annulen-Sandwichs
J. K. Sprafke, B. Odell, T. D. W. Claridge, H. L. Anderson
Angew. Chem. **2011**, *123*, 5687–5690.

4.1 Background

As shown in the previous chapters, large π-conjugated macrocycles possess an intriguing electronic structure due to their high symmetry, bent π-systems and the lack of end-group effects. Some of these features lead to extraordinary linear and nonlinear optical properties[1,2] as well as unusual host-guest chemistry based on interactions between curved π-surfaces.[3] With increasing ring-size, these unique properties disappear because the rings become so flexible that they adopt polymer-like random coil conformations.[4,5] This trend was demonstrated in the previous chapters with the transition from the shape-persistent [6]porphyrin nanoring ***c*-P6** to the more flexible [12]porphyrin nanoring ***c*-P12**. Structural rigidification of such large macrocycles by coordination to radial templates becomes challenging due to the inaccessibility of large and rigid templates. Linear conjugated porphyrin oligomers bind bidentate ligands, such as 1,4-diazabicyclo[2.2.2]octane (DABCO) and 4,4'-bipyridine (bipy), to form rigid, self-supported double strands (Figure 4.1a).[6,7] Planarization of the π-systems in these ladder complexes enhances their two-photon absorption and charge carrier mobilities.[8,9] The STM images shown in Chapter 3 (Figure 3.26) indicate that the porphyrin nanoring ***c*-P12$_{\mathbf{C8}}$** lies flat on a Au(111) surface, with the porphyrin macrocycles parallel to the substrate. This is the conformation required to assemble a double-strand sandwich, implying that the formation of a rigid [12]porphyrin ring sandwich may be possible (Figure 4.1b).

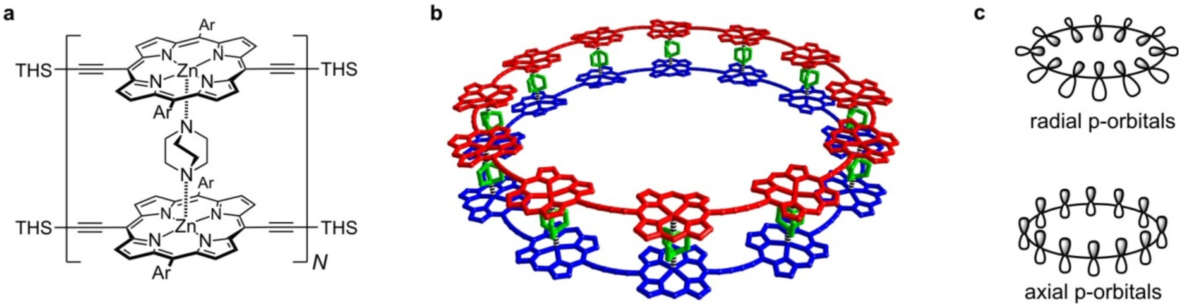

Figure 4.1. *(a) Structure of a double strand complex between linear porphyrin oligomers or polymers and DABCO; (b) calculated structure of the sandwich complex (MM+ force field, HyperChem^{TM}; aryl side groups and hydrogen atoms are omitted for clarity but were present during the calculation); (c) cartoons indicating the orientation of p-orbitals in conjugated macrocycles.*

The two simplest geometries providing complete π-overlap in a conjugated macrocycle are those in which the p-orbitals are either radial (as in carbon nanotubes) or axial (as in classical aromatic molecules) (Figure 4.1c).[3,10] In principle, the formation of a double-strand complex offers a unique opportunity to switch between these two geometries, without altering the covalent structure, thus potentially giving new insights into π-conjugation.

4.2 Complex Formation and Structure

The formation of a double-strand sandwich was attempted using all possible combinations between the two nanorings ***c*-P12** and ***c*-P12$_{\mathbf{C8}}$** as well as the bidentate ligands DABCO and 4,4'-bipyridine. Monitoring the formation by ^{1}H NMR showed that no sandwich complex was formed when either ***c*-P12** or bipy were involved. Bipy binds more weakly to zinc-porphyrins than DABCO, and the binding energy may not compensate for the strain induced by planarization of the nanoring. Steric hindrance could prevent complex formation using ***c*-P12** because the bulky and rigid *tert*-butyl aryl side groups of two opposite porphyrin units would be in close spatial proximity.

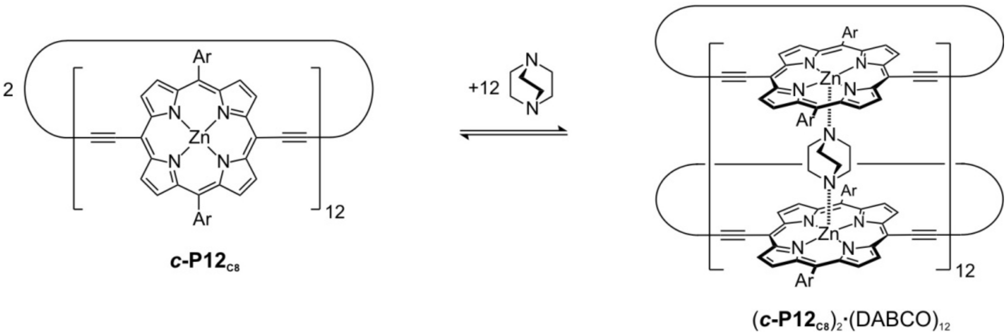

Scheme 4.1. *Formation of the sandwich complex by addition of DABCO to **c-P12$_{C8}$**.*

When following complex formation between ***c*-P12$_{\mathbf{C8}}$** and DABCO by ^{1}H NMR soectroscopy, the appearance of a new species of lower symmetry which is in slow exchange with ***c*-P12$_{\mathbf{C8}}$** is observed (Figure 4.2). The most obvious sign of complex formation is the resonance at δ_H = -4.1 ppm due to DABCO molecules bound between two porphyrins.[6,11] When a 12:2 stoichiometry is reached, the transformation is complete and further addition of DABCO only results in the growth of a broad peak due to free DABCO at δ_H = 2.7 ppm which is in slow exchange with the peak at -4.1 ppm. Formation of (***c*-P12$_{\mathbf{C8}}$**)$_2$•(DABCO)$_{12}$ holds the edges of the porphyrins in different environments. The top and bottom face of the porphyrins become inequivalent, as do the inside and outside (pointing towards and away from the center of the nanoring). This results in the observation of four signals for aryl alkoxy protons H$_c$, whereas only one signal is observed in the conformationally flexible unbound nanoring ***c*-P12$_{\mathbf{C8}}$**. Additionally, the number of β-pyrrole signals doubles from two to four.

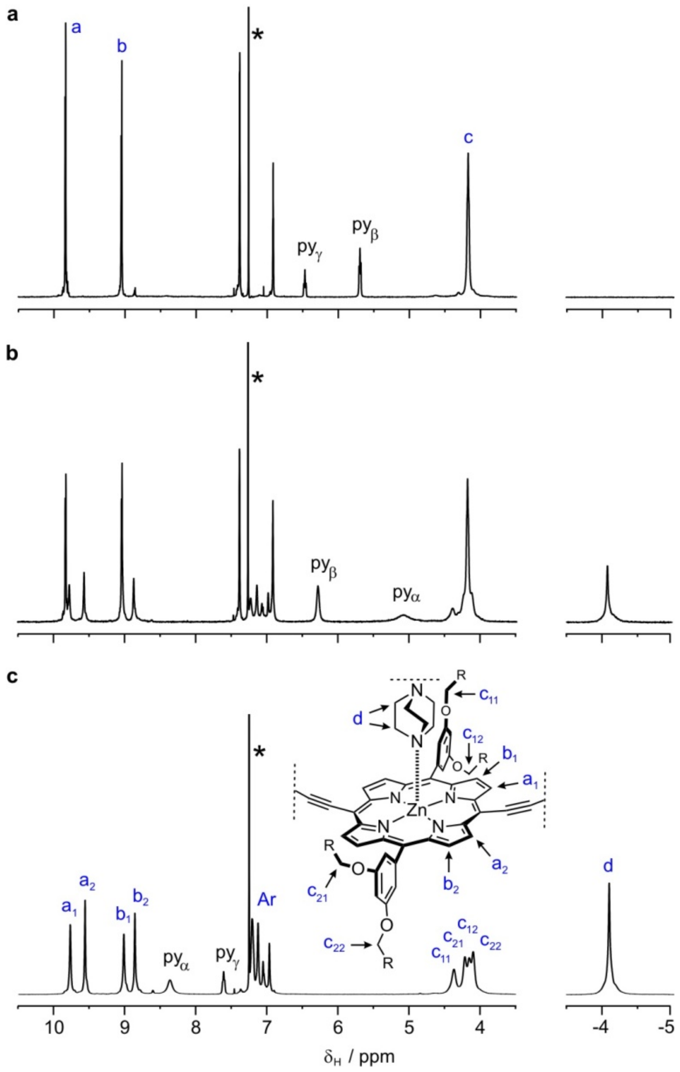

***Figure 4.2.** *^{1}H NMR titration of DABCO into **c-P12$_{C8}$** (CDCl$_3$, 298 K, 500 MHz) and assignment of peaks; (a) 0 equivalents DABCO; (b) 3 equivalents DABCO; (c) 6 equivalents DABCO; signals labeled as py are due to the presence of 12 equivalents of pyridine initially bound to **c-P12$_{C8}$** that are displaced by DABCO in the course of the titration. The asterisks mark the solvent signal (CHCl$_3$).*

The ^{1}H NMR spectrum of (***c*-P12$_{C8}$**)$_2$•(DABCO)$_{12}$ was fully assigned using NOESY NMR (Figure 4.3). NOEs between porphyrin β-protons H$_{a/b}$ and aryl (H$_e$) as well as alkoxy (H$_c$) resonances allow the division of the signals into two groups: Signals stemming from protons pointing to the inside and those on the outside of the nanoring (Figure 4.3 b). Protons on the top (close to DABCO) and bottom face of the porphyrin can be distinguished by the NOEs between the DABCO protons H$_d$ and porphyrin aryl (H$_e$) and alkoxy (H$_c$) protons shown in Figure 4.3c. The complete assignment of the overlapping aryl protons H$_e$ is based on their correlations with alkoxy protons H$_c$. Due to the symmetry of the sandwich complex it is not possible to directly differentiate between the inside and the outside of the nanorings. For the sake of clarity, the assignment in Figure 4.3a is under the assumption that the protons nearer the center of the nanoring (a$_1$, b$_1$, c$_{11}$, c$_{12}$, e$_{11}$, e$_{12}$) are more de-shielded than those on the outside (a$_2$, b$_2$, c$_{21}$, c$_{22}$, e$_{21}$, e$_{22}$), due to their closer proximity to the neighboring porphyrin units.

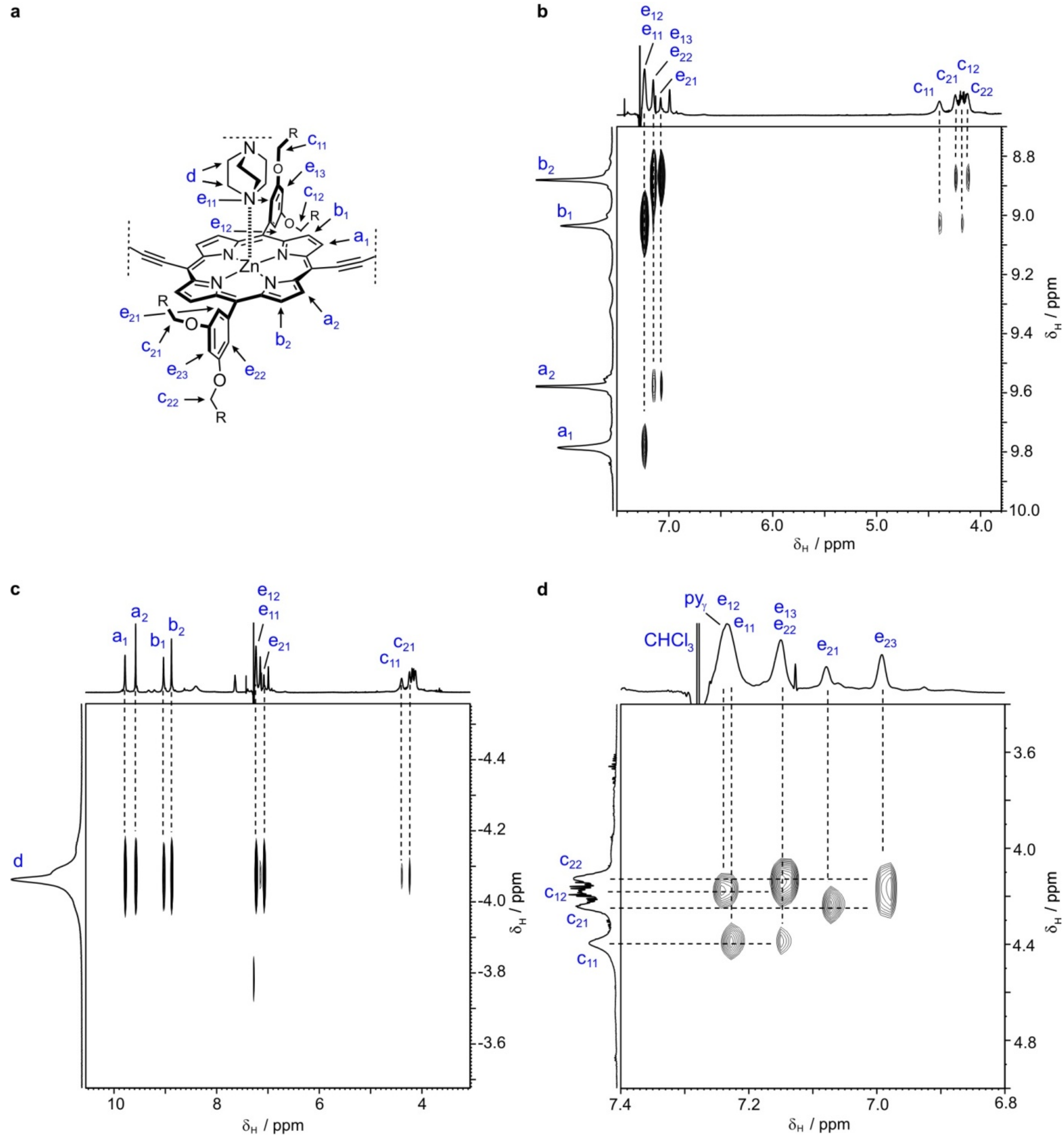

Figure 4.3. *^{1}H NOESY spectrum of (**c-P12$_{C8}$**)$_2$·(DABCO)$_{12}$ (CDCl$_3$, 298 K, 700 MHz, mixing time = 200 ms), measured by Dr. Barbara Odell; (a) chemical structure of 1/12 of (**c-P12$_{C8}$**)$_2$·(DABCO)$_{12}$ with assigned protons; (b) correlations between porphyrin β-pyrrole resonances H$_{a/b}$ and aryl (H$_e$) as well as alkoxy (H$_c$) resonances; (c) correlations between DABCO resonance H$_d$ and porphyrin β-pyrrole H$_{a/b}$, aryl (H$_e$) and alkoxy (H$_c$) resonances; (d) correlations between aryl (H$_e$) and alkoxy (H$_c$) resonances.*

To confirm formation of a discrete double-strand complex, rather than a mixture of oligomeric assemblies, the diffusion coefficient (*D*) was measured by diffusion-ordered NMR spectroscopy (DOSY). Molecular weights of unknown assemblies can be estimated from their diffusion coefficients using a calibration curve created from a series of structurally similar compounds.[12,13] Such a calibration was established using diffusion coefficients of the linear analogues of ***c*-P12$_{C8}$** (monomer ***l*-P1$_{C8}$**, dimer ***l*-P2$_{C8}$**, tetramer ***l*-P4$_{C8}$** and octamer ***l*-P8$_{C8}$**) measured previously by Dr. Craig Wilson and Dr. Tim Claridge (Oxford, NMR).[14] The diffusion coefficient determined for ***c*-P12** fits well on this curve, confirming the validity of the calibration (Figure 4.4a). The measured diffusion coefficient of (**c-P12**)$_2$•(DABCO)$_{12}$ of (1.39 ± 0.04) × 10^{-10} m^2 s^{-1} corresponds to an apparent molecular weight of 16.2 kDa, which is significantly less than the expected value of 27.4 kDa. The low apparent molecular weight of the sandwich complex reflects its compactness (Figure 4.4b) which is expressed in only a small increase of the calculated molecular volume (V = 36,900 Å^3) compared to the free nanoring. (V = 33,100 Å^3, both values calculated using HyperChem^{TM}). This result implies that large polymeric assemblies are not formed.

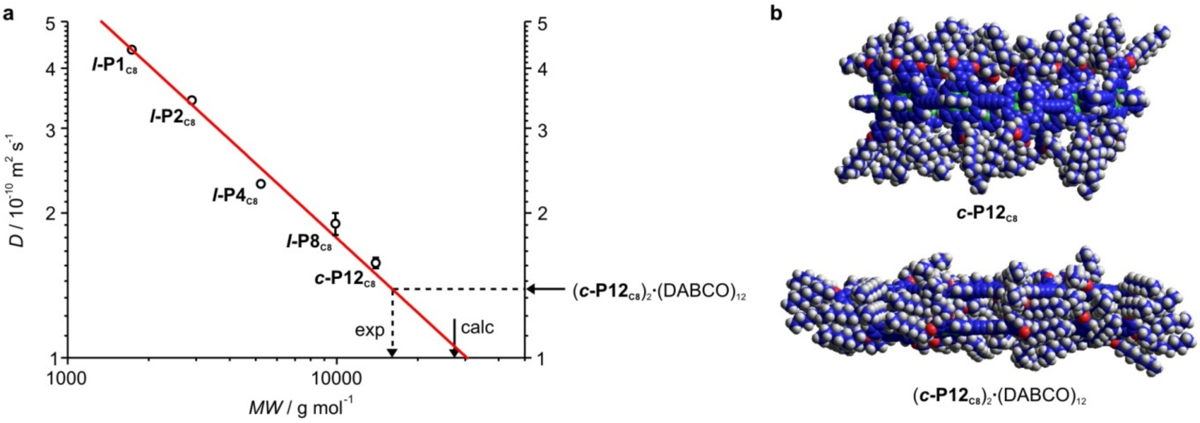

Figure 4.4. *(a) Diffusion coefficients (D) of the pyridine complexes of linear oligomers (**l-P1$_{C8}$–l-P8$_{C8}$**) and **c-P12$_{C8}$** (circles), plotted against their molecular weights (MW). An exponential decay fitted to data from linear oligomers (red line, D = 203 × 10^{-10} $MW^{-0.51}$) was used to estimate the molecular weight of (**c-P12$_{C8}$**)$_2$·(DABCO)$_{12}$ (dotted arrow) from its diffusion coefficient (horizontal black arrow). The vertical black arrow marks the calculated MW. Error bars are not shown for **l-P1$_{C8}$**, **l-P2$_{C8}$** and **l-P4$_{C8}$** because they are smaller than the corresponding data points. (b) Side views of MM+ minimized molecular models of **c-P12$_{C8}$** (top) and (**c-P12$_{C8}$**)$_2$·(DABCO)$_{12}$ (bottom) demonstrating the compactness of the sandwich complex. All DOSY spectra were acquired by Dr. Tim Claridge and Dr. Barbara Odell using the double stimulated echo sequence (DSTE) with a total diffusion time Δ = 150 ms and gradient pulse duration δ = 4 ms (500 MHz, $CDCl_3$, 298 K).*

4.3 Thermodynamics of Complex Formation

UV/vis/NIR titrations provided more insight into the self-assembly process. Titration of **c-P12$_{C8}$** with DABCO gave an abrupt end-point at 6 equivalents DABCO, confirming the 12:2 stoichiometry. However, the binding curve is too square to provide a measure of the formation constant K_f (Figure 4.5a,b). A large excess of DABCO (about 10^4 equivalents) resulted in a second spectroscopic change, corresponding to disassembly of the sandwich complex (Figure 4.5c,d).

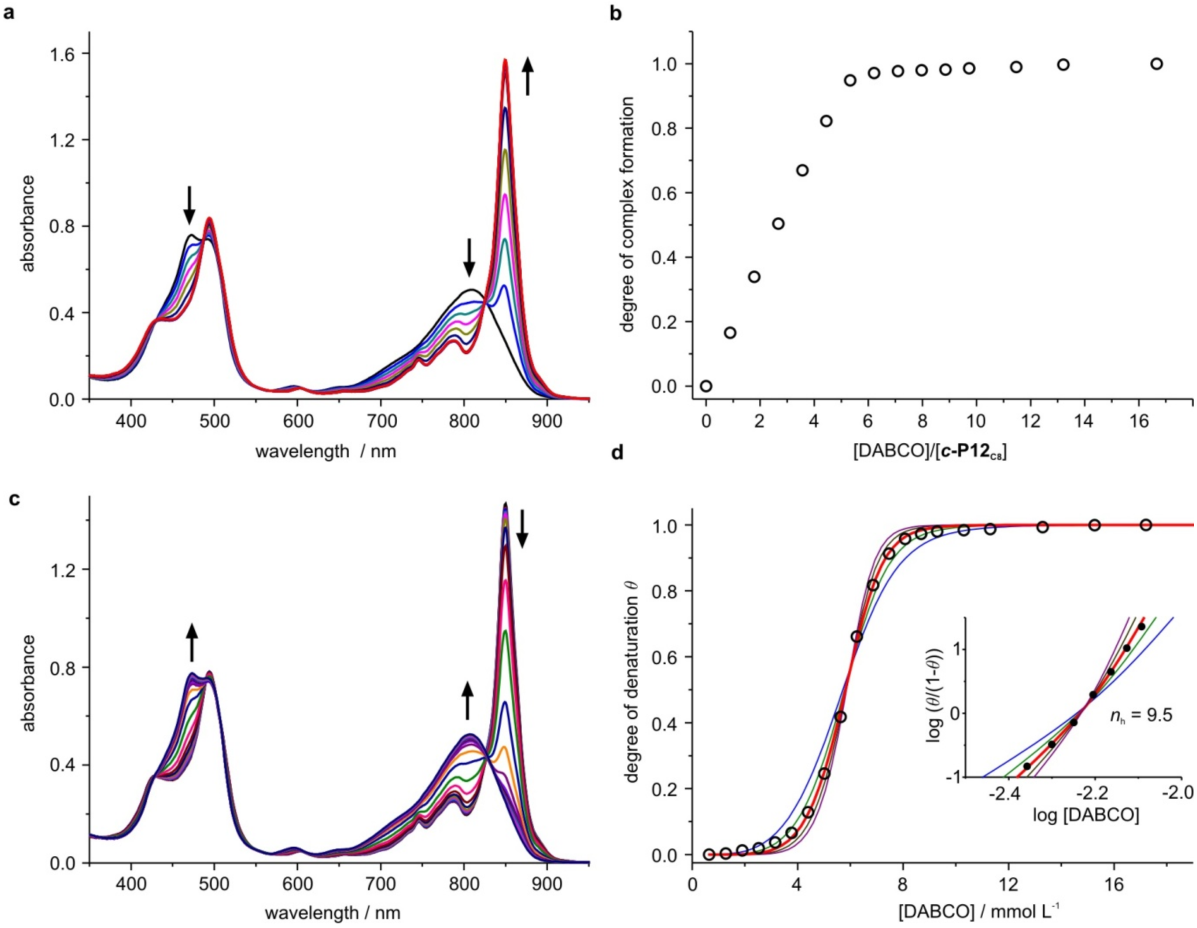

Figure 4.5. *UV/vis/NIR titration of DABCO into **c-P12$_{C8}$** (c = 0.39 µmol L^{-1}) (CHCl$_3$, 298 K). (a) First phase of the titration (complex formation); arrows indicate the spectral change with increasing DABCO concentration; (b) degree of complex formation from absorption data at 850 nm; (c) second phase of the titration (denaturation of complex); arrows indicate the spectral change with increasing DABCO concentration; (d) extent of denaturation of (**c-P12$_{C8}$**)$_2$·(DABCO)$_{12}$ (θ) derived from absorption data at 850 nm (black circles) fitted to the calculated curves for N = 8 (blue line), 10 (green line), 12 (red line), 14 (gray line) and 16 (purple line) binding sites. The inset shows the Hill plot with fits for the same values of N.*

The assembly and the disassembly processes can be understood by considering a general thermodynamic cycle (Figure 4.6).[7,15] Both phases of the titration have several isosbestic points, indicating that the processes behave as two-state equilibria and that the only four species that build up to significant concentrations are A (the receptor, ***c*-P12$_{C8}$**), B (the ligand, DABCO), A$_2$B$_N$ (the sandwich complex) and AB$_N$ (the ligand-saturated receptor).

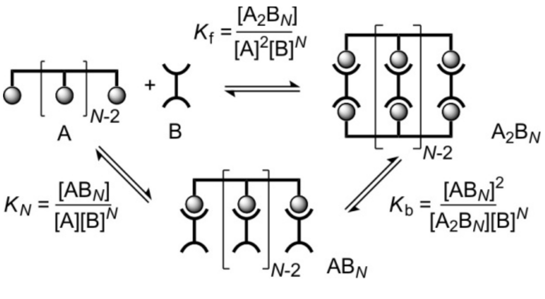

Figure 4.6. *Generic thermodynamic cycle for the formation of a double-strand complex; in the case studied here, N is the number of binding sites, A is a porphyrin oligomer and B is DABCO.*

The thermodynamic cycle allows the determination of the formation constant of the complex K_f from the break-up constant K_b and the binding constant of DABCO to ***c*-P12**$_{\mathbf{C8}}$ K_N according to Equation (4.1):

$$K_f = \frac{K_N^2}{K_b} \tag{4.1}$$

K_N can be estimated from the binding constant of DABCO to porphyrin monomer ***l*-P1**$_{\mathbf{C8}}$ (K_1 defined by Equation (4.2)).[7] The assumption that DABCO binds with the same strength to each porphyrin in ***c*-P12**$_{\mathbf{C8}}$ and that the twelve binding sites in ***c*-P12** act independently, leads to Equations (4.3) and (4.4). The assumption is based on the finding that in linear ladder complexes the interaction parameter α for these processes is 1 (see Section 1.4 and ref. 7).

$$K_1 = \frac{[\boldsymbol{l}-\mathbf{P1}_{\mathbf{C8}} \cdot \mathrm{DABCO}]}{[\boldsymbol{l}-\mathbf{P1}_{\mathbf{C8}}][\mathrm{DABCO}]} \tag{4.2}$$

$$K_N = K_1^{12} \tag{4.3}$$

$$K_f = \frac{K_1^{24}}{K_b} \tag{4.4}$$

K_1 in $CHCl_3$ at 298 K was determined previously[16] to be $K_1 = (2.0 \pm 0.2) \times 10^6\ M^{-1}$ and K_b can be determined from the disassembly phase of the titration by fitting to the binding isotherm derived below. The large excess (35,000 equivalents) of DABCO allows the approximation of the free DABCO concentration to the total DABCO concentration:

$$[B] = [B]_0 \tag{4.5}$$

The binding isotherm, Equation (4.11), is derived as follows, with $[A]_0$ as the total concentration of A.

$$[A]_0 = [AB_N] + 2[A_2B_N] \tag{4.6}$$

Substituting Equations (4.5) and (4.6) in the break-up equilibrium (Figure 4.6) gives:

$$K_b[A_2B_N][B]_0^N - ([A]_0 - 2[A_2B_N])^2 = 0 \tag{4.7}$$

Solving this quadratic equation for $[A_2B_N]$ gives Equation (4.8).

$$[A_2B_N] = \frac{[A]_0}{2} + \frac{K_b[B]_0^N \pm \sqrt{K_b^2[B]_0^{2N} + 8K_b[B]_0^N[A]_0}}{4} \tag{4.8}$$

The degree of denaturation θ is the ratio between the concentration of the ligand saturated receptor and the total receptor concentration:

$$\theta = \frac{[AB_N]}{[A]_0} = \frac{[A]_0 - 2[A_2B_N]}{[A]_0} \tag{4.9}$$

Combining Equations (4.9) and (4.8) gives:

$$\theta = \frac{-K_b[B]_0^N \pm \sqrt{K_b^2[B]_0^{2N} + 8K_b[B]_0^N[A]_0}}{4[A]_0} \tag{4.10}$$

Since θ must be positive, the correct solution is Equation (4.11):

$$\theta = \frac{-K_\mathrm{b}[\mathrm{B}]_0^N + \sqrt{K_\mathrm{b}^2[\mathrm{B}]_0^{2N} + 8K_\mathrm{b}[\mathrm{B}]_0^N[\mathrm{A}]_0}}{4[\mathrm{A}]_0} \tag{4.11}$$

From this binding isotherm it is clear that a plot of the extent of denaturation (θ) against $[\mathrm{B}]_0$ (Figure 4.5d) provides information on the number of binding sites N and the break-up constant K_b. In Figure 4.5d, the experimental data are fitted to the calculated curves for $N = 8$, 10, 12, 14, 16 and the best fit is obtained for $N = 12$. The denaturation of the sandwich complex into the DABCO saturated free nanoring ***c*-P12$_{\mathbf{C8}}$** displays allosteric cooperativity between the DABCO molecules that can be quantified by the Hill coefficient n_H.[15] The Hill plot (insert in Figure 4.5d) shows that the Hill coefficient increases with N and that the observed value ($n_\mathrm{H} = 9.5$) matches that predicted for $N = 12$. Although this is the expected result, the quality of the fits is amazingly good, indicating that this is a remarkably clean all-or-nothing two-state process, probably due to the lack of end-group effects; a linear duplex is expected to fray more easily than a cyclic one.

The break-up constant $K_\mathrm{b} = (4.6 \pm 0.2) \times 10^{20}$ M^{-11} was obtained from the fit for $N = 12$. According to Equation (4.4), this implies a formation constant of $K_\mathrm{f} = 5.9 \times 10^{130}$ M^{-13}. However the value has a high uncertainty (due mainly to the factor K_1^{24}) and so it is more convenient to express it as $\log K_\mathrm{f} = 131 \pm 1$. The value for K_f has the unit M^{-13} which makes it difficult to compare to other complexes, such as the linear ladders, consisting of fewer components. The concentration at which 50% of a complex is dissociated by dilution (c_{50}) is a measure of complex stability that is independent of the number of components in a complex and can be calculated according to Equation (4.12):[7]

$$c_{50} = \frac{1}{\sqrt[(N+1)]{4 \times N^N \times K_\mathrm{f}}} \tag{4.12}$$

For $N = 12$ and $\log K_\mathrm{f} = 131 \pm 1$ the value $c_{50} = (7.9 \pm 0.4) \times 10^{-12}$ M is obtained. In previous studies[7,16] on the analogous linear ladder complexes (Figure 4.1a) it was found that ladder stability increases with oligomer length. This trend is reflected in the decreasing c_{50} values (Figure 4.7a). Interestingly, the c_{50} value of the octamer ladder, which was the longest ladder under investigation, is nearly identical to the value of the nanoring sandwich. This result indicates a lower stability of the cyclic double strand complex which may be explained with the induced strain when forcing the porphyrin units in plane.

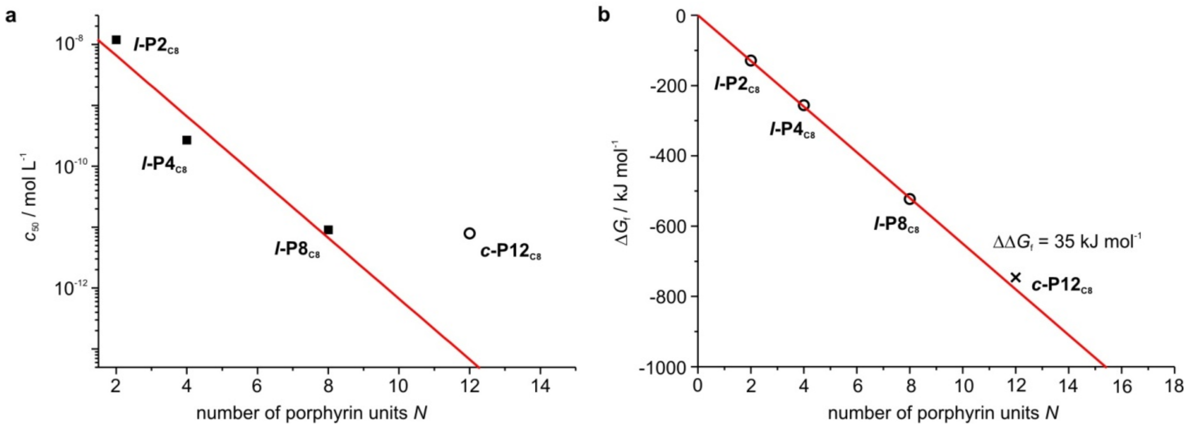

***Figure 4.7.** Comparison of sandwich stability with linear porphyrin ladders. (a) Plot of c_{50} values of linear ladders (black squares) and the sandwich complex (black circle). The red line is a linear fit to the data of linear oligomers and acts as a guide to the eye. (b) Gibbs free energies of formation ΔG_f of linear porphyrin ladders (black circles) and the sandwich complex (black cross). The red line is a linear fit to the data from linear oligomers.*

The lower stability of the cyclic double strand complex compared to a linear analogue can be quantified by comparing their Gibbs free energy of ladder formation ΔG_f:

$$\Delta G_\mathrm{f} = -RT \ln K_\mathrm{f} \tag{4.13}$$

The Gibbs free energy of ladder formation in the porphyrin oligomer series ***l*-P*N***[7] and ***l*-P*N*$_{\mathbf{C8}}$**[16] both show perfectly linear correlations, implying that addition of each rung adds the same amount of free energy (Figure 4.7b). This linearity allows extrapolation of the Gibbs free energy for the formation of the DABCO ladder of ***l*-P12$_{\mathbf{C8}}$** (ΔG_f = -780 kJ mol^{-1}). Comparison with the value calculated for the sandwich complex (***c*-P12**)$_2$•(DABCO)$_{12}$ from its formation constant K_f (ΔG_f = -745 kJ mol^{-1}) shows a significant reduction in the Gibbs free energy of formation ($\Delta\Delta G_\mathrm{f}$ = 35 kJ mol^{-1}), that is probably mostly due to strain induced by planarization of the nanoring.

4.4 Optical Properties

Molecular mechanics calculations confirm that the sandwich complex (***c*-P12$_{\mathbf{C8}}$**)$_2$•(DABCO)$_{12}$ adopts a conformation in which all 12 porphyrins of each ring are locked in a co-planar geometry, with axially aligned p-orbitals (Figure 4.1b). Planarization of ***c*-P12$_{\mathbf{C8}}$** results in dramatic changes in the absorption and emission spectra (Figure 4.8). Whilst the spectra of the free-nanoring ***c*-P12$_{\mathbf{C8}}$** are similar to those of the linear polymer (***l*-P*n*$_{\mathbf{C8}}$**, n = 30-50), there is a significant red-shift of the Q absorption band in (***c*-P12$_{\mathbf{C8}}$**)$_2$•(DABCO)$_{12}$ due to increased conjugation (ΔE = 78 meV). The rigid symmetric geometry of the complex, compared to the single-strand ring, is reflected by its sharper Q band (FWHM = 46 meV and 195 meV respectively), smaller Stokes shift (21 meV and 95 meV respectively) and decreased fluorescence quantum yield (Φ_f = 2.7% and Φ_f = 4.8% respectively). The emission maxima of the sandwich complex and the free nanoring ***c*-P12$_{\mathbf{C8}}$** are very similar (ΔE = 4 meV), as observed for linear hexamer ***l*-P6$_{C8}$** and its bipy ladder complex (ΔE = 17 meV, Figure 2.4).† As outlined in Chapter 2, this similarity is due to the planar geometry of the excited state in conjugated porphyrin oligomers[17,18] that results in only a small energy-difference between rigidified double strand and flexible single strand in the emission spectrum (but not in the absorption spectrum). In contrast, the emission spectrum of the figure-of-eight complex ***c*-P12·(T6)$_2$** is significantly red-shifted (ΔE = 49 meV) compared to the free nanoring ***c*-P12**, indicating enhanced conjugation that is not due to a reduction in the interporphyrin torsional angles. The reduction of the HOMO-LUMO gap is due to the more strongly bent π-system in the folded and strained figure-of-eight complex compared to either the free nanoring or the sandwich complex (see Section 2.4). The influence of significant bending in the figure-of-eight complex makes a quantitative comparison with the spectra of the sandwich complex difficult and it is thus not possible to draw conclusions about the effects of p-orbital orientation (radial in the figure-of-eight and free nanoring *vs*. axial in the sandwich complex) on the optical properties. However, a nanoring complex that also has radial p-orbitals, but should have a comparable bending effect to the sandwich is ***c*-P12·T12** (synthesized by Melanie O'Sullivan, see ref. 20 for structure). **T12** is a radial template analogous to **T6** and **T8** that rigidifies ***c*-P12** and enables efficient π-overlap. The emission of ***c*-P12·T12** is red-shifted compared to ***c*-P12** by 24 meV, however the shift is significantly less than that observed in the figure-of-eight complex (49 meV) as expected from the reduction of bending effects. The shift is 20 meV larger compared to the value found in the sandwich complex (4 meV), but it is difficult to judge the contribution of the p-orbital orientation to this relative reduction in the HOMO-LUMO gap. The reason lies in the difficulties in quantifying the blue-shift in the sandwich complex due to exciton coupling. Shifts in the order of tens of meV have been observed due to exciton coupling in porphyrin DABCO sandwiches,[6,11] indicating that this effect may fully account for the observed difference to ***c*-P12·T12**.

---

† The smaller red-shift upon formation of the DABCO sandwich compared to the bipy ladder can be explained with intermolecular exciton coupling between the face-to-face oriented oligomers that are in closer proximity when DABCO is used as a ligand. This effect has been observed before and results in a blue-shift of the transition.[11,19]

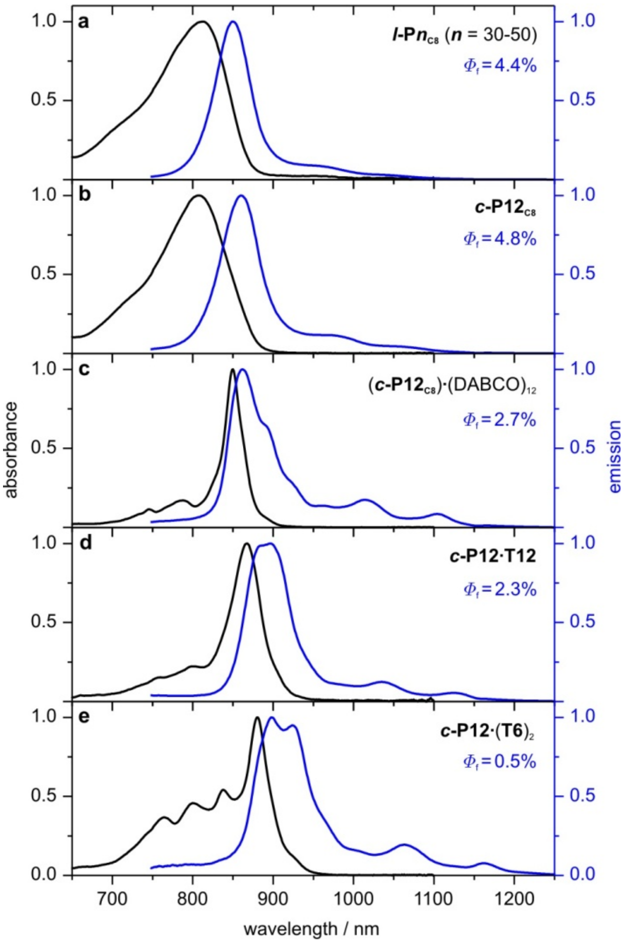

Figure 4.8. *Normalized steady state absorption (black lines) and emission (blue lines) spectra of (a) polymer* ***l-Pn$_{C8}$*** *in $CHCl_3$ /1% pyridine; (b) [12]porphyrin nanoring* ***c-P12$_{C8}$*** *in $CHCl_3$ /1% pyridine; (c) sandwich complex* ***(c-P12$_{C8}$)$_2$·(DABCO)$_{12}$*** *in $CHCl_3$; (d) nanoring template complex* ***c-P12·T12*** *in $CHCl_3$ (synthesized by Melanie O'Sullivan); (e) figure-of-eight-complex* ***c-P12·(T6)$_2$*** *in toluene. Samples were excited at 489 nm.*

4.5 Conclusions and Outlook

Sandwich formation is an elegant strategy that allows planarization and rigidification of the [12]porphyrin nanoring ***c*-P12$_{C8}$** using the commercial ligand DABCO. Complex formation is highly cooperative as indicated by the extremely large Hill coefficient (n_H = 9.5) which leads to great stability towards denaturation. It will be interesting to study the electronic structure of the [12]porphyrin nanorings in greater detail, particularly the influence of the different conformations.

This approach should be readily extendable to larger porphyrin nanorings and allow their efficient planarization using similar small molecule ligands. Since strain effects should be reduced with larger ring sizes it should be possible to use weaker binding ligands such as bipy. Synthesis of novel ligands should allow the variation of the distance between the two nanorings and also enable the introduction of functional moieties such as electron acceptors.

Another important perspective of the sandwich complexes is their use as receptors based on hydrophilic interactions. The top-view of the molecular model in Figure 4.9 shows a high density of solubilizing chains in the central cavity of the complex. The synthesis of nanoring derivatives with hydrophilic side-chains on one rim and hydrophobic chains on the other rim should be straightforward (Chapter 7). In a non-polar solvent such a sandwich should assemble in a way that all hydrophobic chains point outwards and give solubility whereas the polar chains create a hydrophilic pocket in the center of the sandwich complex. Initially such a receptor could be used to bind small water-soluble molecules and to transfer them in a non-polar environment, but the size of the cavity ($d \approx 4.5$ nm) should even allow encapsulation of small proteins or enzymes. It would be interesting to see whether enzymes can keep their catalytic activity in the cavity of the sandwich complex and whether such a nanoring-enzyme complex could be used for enzyme catalysis in organic media.

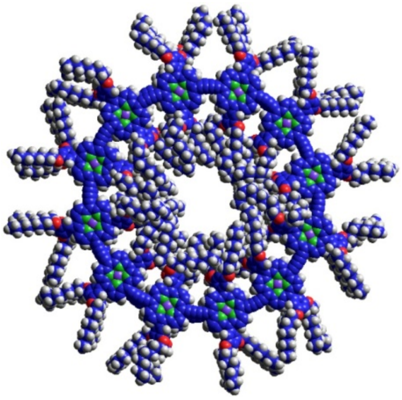

Figure 4.9. *Top view of a molecular model of the sandwich complex minimized using the MM+ force field.*

4.6 References

[1] A. Bhaskar, G. Ramakrishna, K. Hagedorn, O. Varnavski, E. Mena-Osteritz, P. Bäuerle, T. Goodson III, *J. Phys. Chem. B* **2007**, *111*, 946–954.

[2] M. Williams-Harry, A. Bhaskar, G. Ramakrishna, T. Goodson III, M. Imamura, A. Mawatari, K. Nakao, H. Enozawa, T. Nishinaga, M. Iyoda, *J. Am. Chem. Soc.* **2008**, *130*, 3252–3253.

[3] T. Kawase, H. Kurata, *Chem. Rev.* **2006**, *106*, 5250–5273.

[4] M. Mayor, C. Dischdies, *Angew. Chem. Int. Ed.* **2003**, *42*, 3176–3179.

[5] F. Zhang, G. Götz, H. D. F. Winkler, C. A. Schalley, P. Bäuerle, *Angew. Chem. Int. Ed.* **2009**, *48*, 6632–6635.

[6] H. L. Anderson, *Inorg. Chem.* **1994**, *33*, 972–981.

[7] P. N. Taylor, H. L. Anderson, *J. Am. Chem. Soc.* **1999**, *121*, 11538–11545.

[8] M. Drobizhev, Y. Stepanenko, A. Rebane, C. J. Wilson, T. E. O. Screen, H. L. Anderson, *J. Am. Chem. Soc.* **2006**, *128*, 12432–12433.

[9] F. C. Grozema, C. Houarner-Rassin, P. Prins, L. D. A. Siebbeles, H. L. Anderson, *J. Am. Chem. Soc.* **2007**, *129*, 13370–13371.

[10] K. Tahara, Y. Tobe, *Chem. Rev.* **2006**, *106*, 5274–5290.

[11] C. A. Hunter, M. N. Meah, J. K. M. Sanders, *J. Am. Chem. Soc.* **1990**, *112*, 5773–5780.

[12] Y. Cohen, L. Avram, L. Frish, *Angew. Chem. Int. Ed.* **2005**, *44*, 520–554.

[13] M. Quaranta, T. Gehring, B. Odell, J. M. Brown, D. G. Blackmond, *J. Am. Chem. Soc.* **2010**, *132*, 15104–15107.

[14] C. J. Wilson, *Large Porphyrin Based π-Systems*, DPhil Thesis, University of Oxford, Oxford, **2006**.

[15] C. A. Hunter, H. L. Anderson, *Angew. Chem. Int. Ed.* **2009**, *48*, 7488–7499.
[16] M. Hutin, B. Odell, T. D. W. Claridge, H. L. Anderson, *manuscript in preparation*.
[17] M. U. Winters, J. Kärnbratt, M. Eng, C. J. Wilson, H. L. Anderson, B. Albinsson, *J. Phys. Chem. C* **2007**, *111*, 7192–7199.
[18] M.-H. Chang, M. Hoffmann, H. L. Anderson, L. M. Herz, *J. Am. Chem. Soc.* **2008**, *130*, 10171–10178.
[19] C. A. Hunter, J. K. M. Sanders, A. J. Stone, *Chem. Phys.* **1989**, *133*, 395–404.
[20] M. C. O'Sullivan, J. K. Sprafke, D. V. Kondratuk, C. Rinfray, T. D. W. Claridge, A. Saywell, M. O. Blunt, J. N. O'Shea, P. H. Beton, M. Malfois, H. L. Anderson, *Nature* **2011**, *469*, 72–75.

Chapter 5

Probing the Flexibility of Linear Porphyrin Oligomers

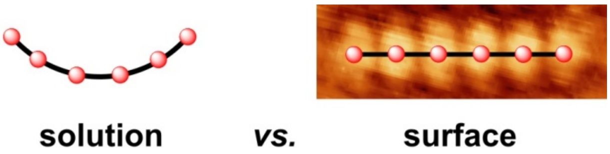

The strain energy in fully π-conjugated cyclic porphyrin oligomers depends on the intrinsic flexibility of the oligomer chains. In this chapter the persistence length L_p, a measure of polymer chain flexibility, is determined for linear butadiyne-linked porphyrin oligomers using small angle X-ray scattering in solution. The chains possess a rigidity that is fairly typical for conjugated polymers (L_p = 12.6 nm) and from an extrapolation of the bending angle it is expected that nanorings consisting of more than approximately 20 porphyrin units should not be significantly strained. In the second part of the chapter the solution flexibility of the oligomers is compared to the behavior on a gold surface. The oligomers have a significantly higher apparent rigidity than in solution (L_c = 25 nm), mostly due to packing effects and the confinement of the chains into two dimensions.

Parts of the results in this chapter have been published in the following articles:

Conformation and Packing of Porphyrin Polymer Chains Deposited Using Electrospray on a Gold Surface
A. Saywell, J. K. Sprafke, L. J. Esdaile, A. J. Britton, A. Rienzo, H. L. Anderson, J. N. O'Shea, P. H. Beton
Angew. Chem. Int. Ed. **2010**, *49*, 9236–9139.

5.1 Background

In the previous chapters the synthesis and properties of butadiyne-linked cyclic porphyrin oligomers were discussed. The [6]porphyrin nanoring ***c*-P6** possesses a significant strain energy (101 kJ/mol) that leads to an increased reactivity towards peroxides and secondary amines (see Chapter 2 and ref. 1 and 2). In the [12]porphyrin nanoring ***c*-P12** no such increased reactivity was observed, indicating the presence of significantly less strain. The question of cyclization-induced strain is closely related to the intrinsic flexibility of the linear analogues of the porphyrin nanorings. In polymer physics the flexibility of a worm-like chain (WLC) is quantified by its persistence length L_p defined as the distance at which two segments of a polymer chain lose their directional correlation. A polymer chain that is much longer than its persistence length behaves like a random coil whereas a chain that is significantly shorter than L_p can be treated as a rigid rod. A range of scattering[3,4] and microscopy[5,6] techniques have been applied to determine the flexibility of polymers usually with chain lengths much larger than their persistence lengths. For structurally well defined molecules on the length scale of only several nanometers the established techniques usually require the attachment of labels. Most commonly these are fluorescent labels to measure distances by fluorescence resonance energy transfer (FRET)[7,8] or spin labels when using EPR spectroscopy.[9] Recently small angle X-ray scattering (SAXS) has been used to determine the persistence length of double stranded DNA end-labeled with gold nanoparticles.[10,11]

Lovett, Anderson *et al.* have studied the conformations and flexibility of radical-labeled butadiyne-linked porphyrin oligomers by EPR using the double electron electron resonance (DEER) technique and extrapolated the persistence length of such oligomers to 19 nm.[12] SAXS should give access to similar information because the pair distribution function (PDF) often contains information on individual Zn-Zn distances in the molecule (see Sections 2.3 and 3.2.3).[13,14] In contrast to the established techniques, SAXS analysis does not require the attachment of end-labels to the oligomers and neither is it necessary to synthesize a range of oligomers with different lengths because one molecule usually contains several Zn-Zn distances.

Whilst SAXS analysis provides information on the flexibility of oligomers in solution, it is also important to study their flexibility on surfaces, particularly in light of potential applications in molecular electronics where knowledge of interfacial organization is crucial. Scanning tunneling microscopy (STM) allows the detailed analysis of porphyrin oligomers on gold surfaces with resolution of the individual porphyrin units (see Section 3.2.4). Statistical structural analysis of analogous porphyrin polymers should give the persistence length of butadiyne-linked porphyrin oligomers confined to two dimensions and under the influence of packing effects.

5.2 Flexibility in Solution

SAXS analysis was carried out on porphyrin tetramer ***l*-P4$_{C8}$** and hexamer ***l*-P6$_{C8}$** in toluene/1% pyridine at Diamond Light Source, UK. Excellent agreement was found between the experimental scattering data (and the corresponding radii of gyration) and simulated data based on molecular models minimized using the semi-empirical AM1 method (Figure 5.1). The well resolved peaks in the PDFs correspond to the n possible distances between the zinc centers of individual porphyrin units in the oligomers ($n \leq 3$ in ***l*-P4$_{C8}$** and $n \leq 5$ in ***l*-P6$_{C8}$**). The shapes of the PDFs are well reproduced by data based on the molecular models, however at increasing distances the model overestimates r. This discrepancy between the Zn-Zn distances in the rigid models L_n and the measured Zn-Zn distances R_n is due to the flexibility of the oligomers in solution which results in an averaged experimental PDF.

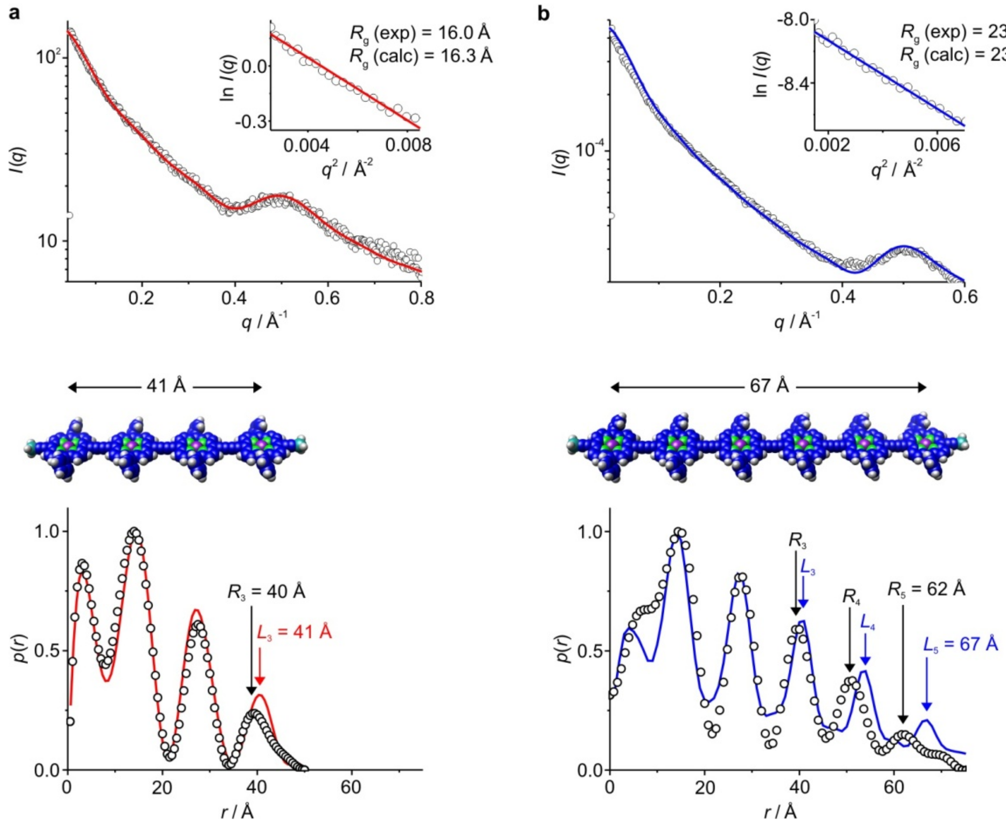

Figure 5.1. *SAXS analysis of (a) linear porphyrin tetramer* ***l-P4$_{C8}$*** *and (b) linear porphyrin hexamer* ***l-P6$_{C8}$*** *in toluene/1% pyridine at 298 K at Diamond Light Source, UK. The top row shows the raw scattering data (black circles) together with the simulated curves based on calculated models (lines). The insets are Guinier fits to the experimental scattering data based on the radii of gyration R_g determined by the program Gnom. The middle row contains the molecular models that were used to simulate the SAXS data. Energy minimized structures were obtained using the semi-empirial AM1 method implemented in the package HyperChem^{TM}. The distances are the calculated Zn-Zn distances between the most distant porphyrins. The bottom row shows pair-distribution functions determined experimentally (black circles) and from models (lines) with black arrows marking experimental Zn-Zn distances R_n and colored arrows marking distances from the simulated curves L_n.*

In the framework of the wormlike chain model a polymer chain is described as a continuously curved semi-flexible thread that is stiff on short length scales, but behaves like a flexible coil at large lengths.[15] This model has been successful in describing the flexibility of many rigid polymers such as DNA[5] or poly(isocyanides).[6] Applied to the porphyrin oligomers, the Zn-Zn distances from the rigid model L_n correspond to the contour length of the chain and the maxima of the Zn-Zn peaks in the experimental PDF are the mean end-to-end distances $\langle R_n\rangle$ (Figure 5.2b). In a three dimensional polymer chain the mean square end-to-end distance $\langle R_n{}^2\rangle$ and L_n are related to the persistence length L_p according to Equation (5.1).[5,16]

$$\left\langle R_n{}^2\right\rangle = 2L_\mathrm{p}L_n\left(1-\frac{L_\mathrm{p}}{L_n}\left(1-\mathrm{e}^{\frac{L_n}{L_\mathrm{p}}}\right)\right) \tag{5.1}$$

The mean Zn-Zn distances $\langle R_n\rangle$ from the PDFs were obtained by fitting Gaussians to the individual peaks. One dataset from ***l*-P4$_\mathbf{C8}$** and two datasets from ***l*-P6$_\mathbf{C8}$** that were acquired at different beamtimes using different detectors were used to obtain averaged values for $\langle R_n\rangle$. The standard deviations of these values are small ($\langle R_1\rangle$ = 14.4 ± 0.2 Å, $\langle R_2\rangle$ = 27.6 ± 0.1 Å $\langle R_3\rangle$ = 39.8 ± 0.3 Å, $\langle R_4\rangle$ = 51.0 ± 0.1 Å, $\langle R_5\rangle$ = 62.0 ± 0.2 Å) thus confirming the accuracy of the absolute distances determined by SAXS. To ensure the greatest accuracy, the contour lengths L_n were taken from an extrapolation of the Zn-Zn distance in the crystal structure of porphyrin dimer ***l*-P2**[17] (L_n') rather than from the AM1 optimized structure. Only the longer distances with $n \geq 3$ were used for fitting L_n' and $\langle R_n{}^2\rangle$ to Equation (5.1) because the values at smaller distances are not significantly different (Figure 5.1). The persistence length obtained from the fit is 13.8 ± 1.4 nm and is slightly below the value measured by EPR.[12]

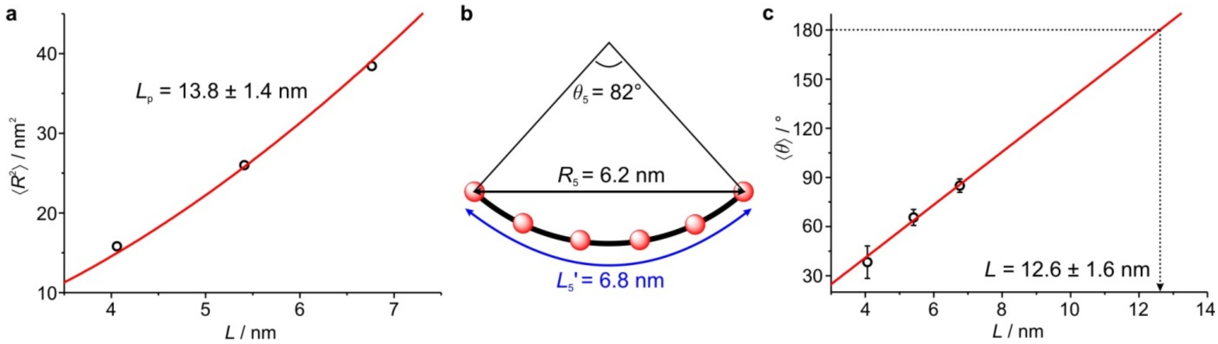

Figure 5.2. *Evaluation of the flexibility of porphyrin oligomers. (a) Distances from extrapolation of the dimer crystal structure plotted against the mean squared SAXS distance (black circles) fitted to Equation (5.1) (red line), the error bars in the experimental points obtained from averaging over several measurements are smaller than the data points and thus are not shown; (b) definition of the angle θ corresponding to the angle between the tangents at the ends of the contour (not drawn, perpendicular to the lines representing the radius of the circular segment); (c) extrapolation of the contour length L at θ = 180° from $\langle\theta_3\rangle-\langle\theta_5\rangle$. The errors bars are the standard deviation from averaging the angles obtained from several measurements.*

The determined persistence length L_p strongly depends on the chosen contour length. When using the Zn-Zn distances from the AM1 minimized molecular model, which are systematically 1.5% shorter than in the crystal structure, the resulting persistence length increases to 17.9 ± 3.0 nm.

In a simplified picture a worm-like chain of a length well below the persistence length may be regarded as, on average, an evenly bent rod (Figure 5.2b). The angle θ defined in Figure 5.2b corresponds to the angle between the two tangents at the ends of the chain (not drawn) and provides an alternative description of the porphyrin oligomer flexibility. The relation between L_n and R_n can be described as part of a circular segment with the contour length L_n as the arc length, the SAXS Zn-Zn distance R_n as the chord length and the angle θ_n as the circular angle of the segment. Using numerical methods,[18] θ_n was calculated from R_n and L_n' for n = 3, 4 and 5. The two ends of the oligomer lose their correlation when θ reaches 180° and the chain takes the shape of a semicircle. This angle can be extrapolated from the known angles θ_3–θ_5 leading to a contour length of 12.6 ± 1.6 nm for $\theta = 180°$, which is in good agreement with the determined persistence length. Such a semicircle with L = 12.6 nm contains approximately nine to ten porphyrin units. As a consequence, no significant strain energy at 295 K is expected in butadiyne-linked porphyrin nanorings **c-P*N*** ($\theta = 360°$) containing more than approximately 20 porphyrin units ($N \geq 20$).

5.3 Flexibility on a Gold Surface

The assembly of linear porphyrin hexamer ***l*-P6$_{\mathrm{C8}}$** and polymer ***l*-Pn$_{\mathrm{C8}}$** (n = 30–50) on a Au(111) surface was analyzed by Dr. Alex Saywell, Dr. James O'Shea and Professor Peter Beton (University of Nottingham, UK) using STM under ultrahigh vacuum (UHV) conditions. Since the molecules are too large to be sublimed on the surface, they were deposited on the gold substrate by injection of a dilute solution in the UHV system using a home-built electrospray ionization (ESI) system. After deposition of sub-monolayer coverage, highly ordered islands of closely packed hexamer molecules form (Figure 5.3a) that become larger after annealing the sample at 100 °C (Figure 5.3b).

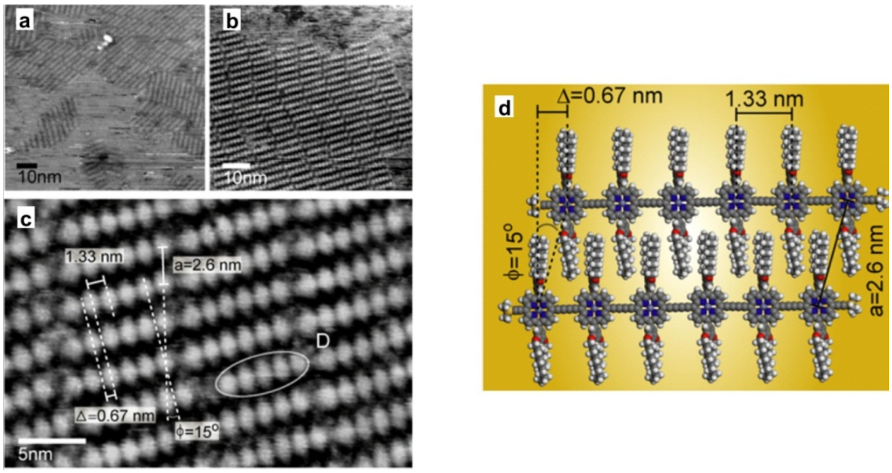

Figure 5.3. *STM analysis of porphyrin hexamer **l-P6$_{\mathrm{C8}}$** on Au(111) under UHV conditions applying a sample voltage of -1.80 V and a tunneling current of 0.03 nA. (a) After deposition on the surface by ESI; (b) after annealing at 100°C; (c) high resolution image with measured molecular distances. The area marked with a D seems to contain a molecule of pentamer that could either stem from an impurity in the sample or be due to damage upon landing on the surface; (d) molecular models demonstrating the orientation of two neighboring hexamer molecules. All images acquired and all figures made by Alex Saywell and reprinted from ref. 19.*

The high-resolution image in Figure 5.3c allows the unambiguous identification of the hexamer structure. The porphyrin units are all individually resolved and the measured spacing between two units (1.33 ± 0.07 nm) is in good agreement with the Zn-Zn distance measured in the crystal structure of porphyrin dimer ***l*-P2** (1.353 nm).[17] Neighboring hexamer molecules are offset by 0.67 nm to allow interdigitation of the octlyoxy solubilizing chains as shown by the models in Figure 5.3d. The ordered packing and the rigid hexamer backbone found in the STM images is in contrast to the flexible solution structure discussed in the previous section and highlights the effect of confining conformational flexibility to two dimensions. Additionally, the hexamer is probably stabilized by packing forces from van-der-Waals interactions between the interdigitated alkyl chains, which is a common driving force in surface self-assembly.[19]

The polymer ***l*-Pn**$_{\mathbf{C8}}$ deposited by ESI shows significantly less ordering on the gold surface in comparison to the hexamer (Figure 5.4a). Apart from some ordered domains, that have similar interchain spacing as observed for the hexamer, the polymer chains seem to be randomly oriented and many crossing points (bright spots) can be identified. Interestingly, polymer chains tend to cross at a 90° angle, possibly to avoid the steric clash of the aryl side groups. The bending is not evenly distributed over individual polymer chains: besides regions with smooth curvature domains with sharp kinks can be found (Figure 5.4b).

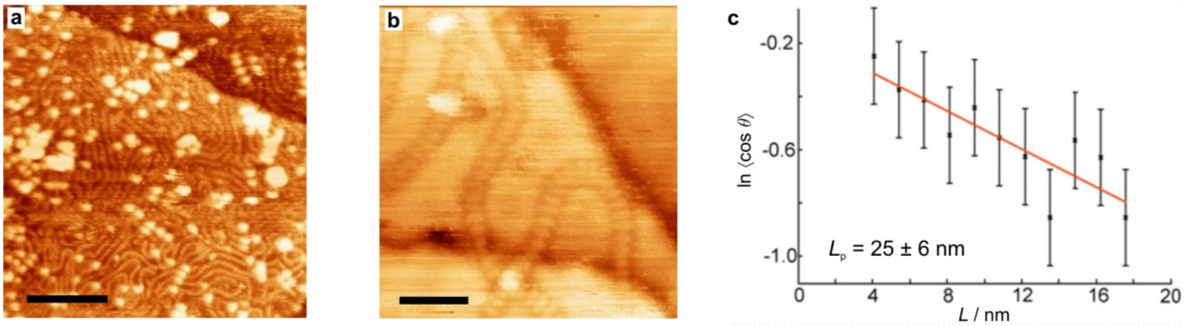

Figure 5.4. *STM analysis of* ***l*-Pn**$_{\mathbf{C8}}$ *deposited on a Au(111) surface under UHV conditions applying a sample voltage of -1.80 V and a tunneling current of 0.03 nA. (a) large area image (scale bar, 30 nm) (b) close-up on a sharp kink in the polymer chain (scale bar, 10 nm); (c) Plot of the contour length L against ln* $\langle \cos\theta \rangle$ *(black dots) and linear fit to obtain the angular correlation length* L_c *from the gradient (red line). All images acquired by Alex Saywell and Figure 5.4c reprinted from ref. 19.*

The angular correlation length L_c can be estimated from the cosine of the mean angle $\langle \theta \rangle$ formed between two tangents to the polymer chain separated by the contour length L (see Figure 5.2b) using Equation (5.2).[21]

$$\langle \cos\theta \rangle = \mathrm{e}^{-\frac{L}{L_c}} \tag{5.2}$$

Plotting L against ln $\langle \cos\theta \rangle$ gives L_c from the gradient of a linear fit (L_c = 25 ± 6 nm). The angular correlation length L_c is identical to the persistence length L_p if each polymer chain is isolated from neighboring chains. Since this is not the case here due to the interactions with the surface and neighboring molecules, the value cannot be directly compared with the persistence length in solution of 12.6 nm. However, the large difference between the two values of about a factor of two, demonstrates the strong influence of packing effects and two dimensional confinement on the polymer chain rigidity.

The resolution of individual porphyrin units in the STM images allows determination of the chain length and molecular weight M_n of the polymer by simply counting the number of porphyrin units in a chain. The average chain length was found to be 40 ± 9 porphyrin units which is consistent with the chain length determined by gel permeation chromatography (M_n = 43,000 Da, ~40 units).[19]

5.4 Conclusions and Outlook

The persistence length determined for butadiyne-linked porphyrin oligomers is significantly longer than for conventional non-conjugated polymers such as polyethylene (L_p = 0.8 nm)[4] or for non-linear conjugated polymers such as poly-3-hexyl thiophene (L_p = 2.1 nm).[22] The rigidity of the porphyrin oligomers is slightly lower compared to other linear conjugated polymers such as poly(phenyleneethynylene) (L_p = 15 nm)[23] or poly(*p*-phenylene-*cis*-benzobisoxazole) (L_p = 19–25 nm)[24] commonly regarded as 'rigid rods' and significantly lower than polymers that are stabilized by non-covalent interactions such as poly(isocyanides) (L_p = 76 nm)[6] or double stranded DNA (L_p = 50 nm)[5,11]. The reduced rigidity of porphyrin oligomers is probably due to the well studied flexibility of the acetylenic linkers.[25]

The use of SAXS in measuring metal-metal distances in porphyrin oligomers and assemblies could be improved by replacing zinc (atomic number 30) with heavy metal ions such as lead (atomic number 82) that have a higher electron density and will result in more intense peaks in the PDF. Investigation of oligomer chain flexibility in solution using SAXS is not limited to porphyrin oligomers. It would be interesting to study the flexibility of other short metallopolymers[26] or the platinum capped oligoynes synthesized by Gladysz *et al*.[27]

The STM analysis of porphyrin hexamer ***l*-P6$_{C8}$** and polymer ***l*-Pn$_{C8}$** on a gold surface demonstrated the effects of interchain interactions and the constraints imposed by the two dimensional surface on the chain flexibility. The groups of Beton[28] and Barth[29] recently extended the classical 2D surface self-assembly towards the formation of three dimensional supramolecular structures on surfaces. It would be interesting to probe whether DABCO or 4,4'-bipyridine ladders would form on surfaces i.e. whether the free energy of ladder formation is higher than the surface binding energy. Analysis of the self-sorting behavior, which is observed in solution, would be particularly worth investigating in the case of the polymer ladders. It would be interesting to see whether the rigidity of the polymer on the surface increases upon ladder formation as observed in solution.

5.5 References

[1] M. Hoffmann, J. Kärnbratt, M.-H. Chang, L. M. Herz, B. Albinsson, H. L. Anderson, *Angew. Chem. Int. Ed.* **2008**, *47*, 4993–4996.

[2] M. Hoffmann, *Nanosized Porphyrin Molecular Wires and Rings*, D.Phil. Thesis, University of Oxford, Oxford, **2008**.

[3] G. Wenz, M. A. Müller, M. Schmidt, G. Wegner, *Macromolecules* **1984**, *17*, 837–850.

[4] R. Ramachandran, G. Beaucage, A. S. Kulkarni, D. McFaddin, J. Merrick-Mack, V. Galiatsatos, *Macromolecules* **2008**, *41*, 9802–9806.

[5] C. Rivetti, M. Guthold, C. Bustamante, *J. Mol. Biol.* **1996**, *264*, 919–932.

[6] P. Samorí, C. Ecker, I. Gössl, P. A. J. de Witte, J. J. L. M. Cornelissen, G. A. Metselaar, M. B. J. Otten, A. E. Rowan, R. J. M. Nolte, J. P. Rabe, *Macromolecules* **2002**, *35*, 5290–5294.

[7] E. Hass, *ChemPhysChem* **2005**, *6*, 858–870.

[8] C. Yuan, H. Chen, X. W. Lou, L. A. Archer, *Phys. Rev. Lett.* **2008**, *100*, 018102.

[9] A. Godt, M. Schulte, H. Zimmermann, G. Jeschke, *Angew. Chem. Int. Ed.* **2006**, *45*, 7560–7564.

[10] R. S. Mathew-Fenn, R. Das, P. A. B. Harbury, *Science* **2008**, *322*, 446–449.

[11] A. J. Mastroianni, D. A. Sivak, P. L. Geissler, A. P. Alivisatos, *Biophys. J.* **2009**, *97*, 1408–1417.

[12] J. E. Lovett, M. Hoffmann, A. Cnossen, A. T. J. Shutter, H. J. Hogben, J. E. Warren, S. I. Pascu, C. W. M. Kay, C. R. Timmel, H. L. Anderson, *J. Am. Chem. Soc.* **2009**, *131*, 13852–13859.

[13] D. M. Tiede, R. Zhang, L. X. Chen, L. Yu, J. S. Lindsey, *J. Am. Chem. Soc.* **2004**, *126*, 14054–14062.

[14] R. F. Kelley, R. H. Goldsmith, M. R. Wasielewski, *J. Am. Chem. Soc.* **2004**, *129*, 6384–6385.

[15] O. Kratky, G. Porod, *Recl. Trav. Chim. Pays-Bas* **1949**, *68*, 1106–1122.

[16] P. J. Flory, *Statistical Mechanics of Chain Molecules*, Interscience Publishers, New York, **1969**.

[17] P. N. Taylor, J. Huuskonen, G. Rumbles, R. T. Aplin, E. Williams, H. L. Anderson, *Chem. Comm.* **1998**, 909–910.

[18] http://www.1728.com/circsect.htm (10. April 2011).

[19] A. Saywell, J. K. Sprafke, L. J. Esdaile, A. J. Britton, A. Rienzo, H. L. Anderson, J. N. O'Shea, P. H. Beton, *Angew. Chem. Int. Ed.* **2010**, *49*, 9236–9139.

[20] T. Kudernac, S. B. Lei, J. A. A. W. Elemans, S. DeFeyter, *Chem. Soc. Rev.* **2009**, *38*, 402–421.

[21] G. S. Manning, *Phys. Rev. A* **1986**, *34*, 668–670.

[22] G. W. Heffner, D. S. Pearson, C. L. Gettinger, *Poly. Eng. Sci.* **1995**, *35*, 860–867.

[23] P. M. Cotts, T. M. Swager, Q. Zhou, *Macromolecules* **1996**, *29*, 7323–7328.

[24] D. B. Boitman, R. A. Wessling, J. McAlister, *Macromolecules* **1993**, *26*, 5174–5184.

[25] S. Szafert, J. A. Gladysz, *Chem. Rev.* **2006**, *106*, PR1–PR33.

[26] G. R. Whittell, M. D. Hager, U. S. Schubert, I. Manners, *Nat. Mater.* **2011**, *10*, 176–188.

[27] Q. Zheng, J. A. Gladysz, *J. Am. Chem. Soc.* **2005**, *127*, 10508–10509.

[28] M. O. Blunt, J. C. Russell, M. del Carmen Gimenez-Lopez, N. Taleb, X. Ling, M. Schröder, N. R. Champness, P. H. Beton, *Nat. Chem.* **2011**, *3*, 74 – 78.

[29] D. Écija, W. Auwärter, S. Vijayaraghavan, K. Seufert, F. Bischoff, K. Tashiro, J. V. Barth, *Angew. Chem. Int. Ed.* **2011**, *50*, 3872–3877.

Chapter 6

Noncovalent Binding of Carbon Nanotubes by Porphyrin Oligomers

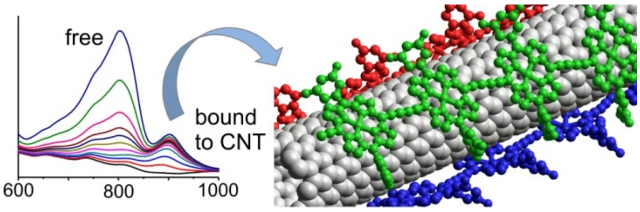

This chapter describes the noncovalent functionalization of single-walled carbon nanotubes with linear and cyclic porphyrin oligomers. The first section gives a brief introduction to the synthesis and physical properties of carbon nanotubes (CNTs). In the main part of this chapter a detailed analysis of the binding of linear conjugated porphyrin oligomers to CNTs is presented. Photoluminescence-excitation mapping and UV/vis/NIR absorption reveal that the oligomers bind strongest to (7,5) and (8,6) CNTs. The strength of binding increases sharply with the length of the oligomer, with tetramer and hexamer binding constants being too strong to be measured by absorption or fluorescence titrations. Besides allowing the quantification of binding strengths, these titrations also give information on the degree and kinetics of CNT debundling. The binding of porphyrin oligomers induces strain on the nanotubes that is comparable to that observed under hydrostatic pressure. This phenomenon has not been previously observed in solution as a consequence of noncovalent binding and is probably a direct result of the strong interactions between porphyrins and nanotubes. The predicted formation of a type-II heterojunction between the longer oligomers and small diameter carbon nanotubes would be favorable for photo-induced charge transfer, suggesting application of these complexes in photovoltaic devices. This expected band alignment is confirmed experimentally by trends in changes of the nanotube transitions upon porphyrin binding. The chapter ends with an account of the attempted formation of a pseudo-polyrotaxane between CNTs and cyclic porphyrin hexamer.

Parts of the results in this chapter have been published in the following articles:

Noncovalent Binding of Carbon Nanotubes by Porphyrin Oligomers
J. K. Sprafke, S. D. Stranks, J. H. Warner, R. J. Nicholas, H. L. Anderson
Angew. Chem. Int. Ed. **2011**, *50*, 2313–2316.

Electronic and Mechanical Modification of Single-Walled Carbon Nanotubes by Binding to Porphyrin Oligomers
S. D. Stranks, J. K. Sprafke, H. L. Anderson, R. J. Nicolas
ACS Nano, **2011**, *5*, 2307–2315.

6.1 Background to Carbon Nanotubes

Single-walled carbon nanotubes (SWCNTs) are hollow cylinders that consist of a graphitic layer of sp^2-carbon atoms, and have diameters around one nanometer and typical lengths of several micrometers. Several concentrically nested SWCNTs are commonly known as multi-walled carbon nanotubes (MWCNTs, Figure 6.1). Together with fullerenes, carbon nanotubes (CNTs) are regarded as non-natural carbon allotropes as opposed to the naturally occurring graphite and diamond. Following the seminal report of Iijima in 1991,[1] CNTs have developed into one of the most promising materials in nanotechnology with their unique electronic and mechanical properties leading to diverse potential applications.[2]

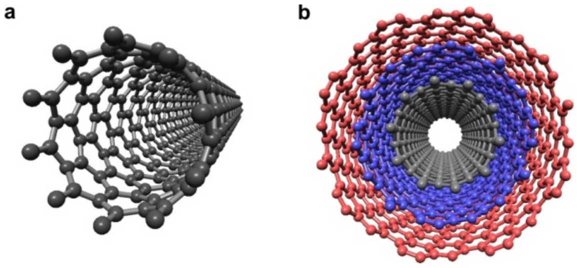

Figure 6.1. *Models of (a) a (7,6) SWCNT and (b) MWCNT, created using the program Nanotube Modeler.*

6.1.1 Synthesis and Physical Properties of Carbon Nanotubes

Common requirements for all CNT production processes are the presence of a carbonaceous precursor, high temperatures and often a metal catalyst, especially for the selective formation of SWCNTs over MWCNTs.[3,4] Three primary methods are used: 1) electric arc discharge, where the CNTs are formed in the plasma between two graphite electrodes;[5] 2) laser ablation, where a high intensity laser vaporizes graphite;[6] 3) chemical vapor deposition, where CNTs grow on a surface or metal catalyst particle from a carbon containing precursor in the gas phase. Many precursors such as acetylene or ethylene can be used, but the most commercially successful process utilizes carbon monoxide at high pressures, known as the HiPCO process.[7] While most production methods give mixtures of tubes with different diameters, the HiPCO process allows the synthesis of relatively narrow distributions of diameters dependent on the reaction conditions and particularly on the catalyst. The use of iron catalysts results in diameters of 0.8 – 1.2 nm, whereas a combination of cobalt and molybdenum ("CoMoCat") gives only smaller diameter tubes with a narrower distribution (0.7 – 0.9 nm).[8] In the past few years organic chemists have made some progress towards the rational synthesis of carbon nanotubes.[9] The most promising strategy is based on the recently synthesized cycloparaphenylenes[10] that could act as a template from which CNTs may grow by multiple Diels-Alder reactions with acetylene (or a more reactive equivalent).[11] Although it seems unlikely that very long CNTs could be grown by this method, the accessibility of CNTs with a monodisperse diameter distribution would be an important step towards the use of CNTs in many applications.[4]

Besides their diameter, CNTs can also differ in their "chirality". In the context of CNTs this term is used in a broader way than in organic chemistry. As well as the "handedness" of a tube, chirality also means the helical twist of the graphene hexagons of a CNT, which is based on the idea of describing CNTs as rolled-up graphene sheets. A graphene sheet map allows formal construction of any CNT species (Figure 6.2) by rolling the sheet up along its chiral vector $C_\mathrm{h} = n\mathrm{a}_1 + m\mathrm{a}_2$. Here (n,m) are integers defined as the chiral indices of a CNT species, a_1 and a_2 are the unit vectors of the graphene lattice (Figure 6.2a), and the chiral vector C_h defines the chiral angle θ.[4] The length of the chiral vector C_h is the circumference of the CNT species and thus determines the diameter of the nanotube.

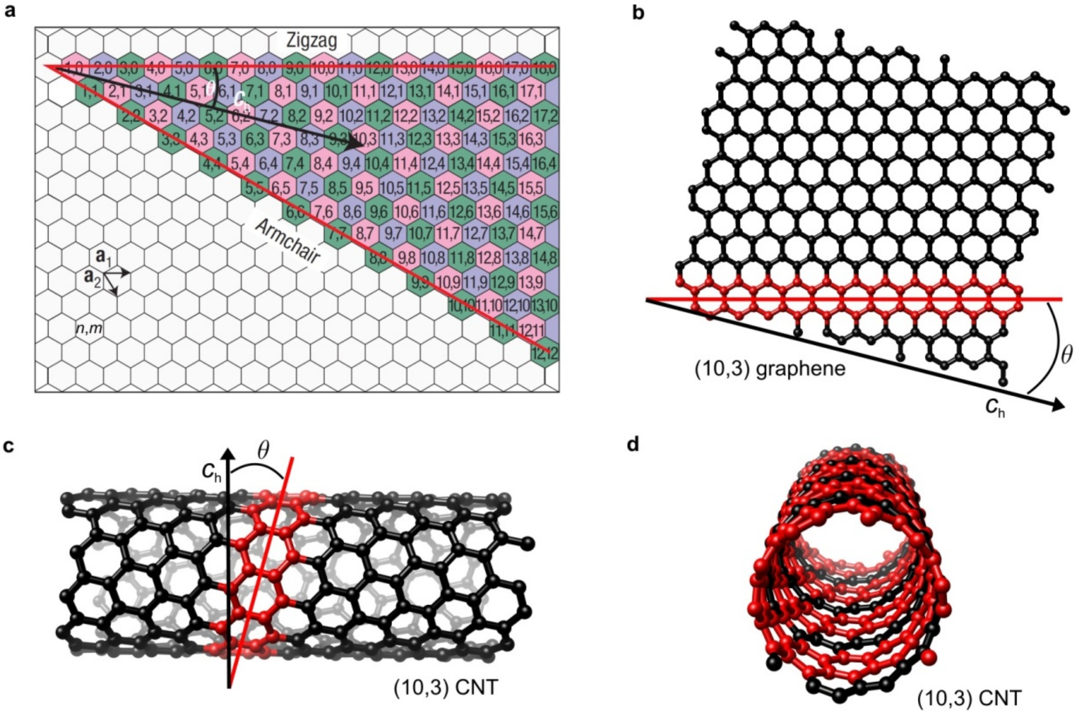

Figure 6.2. *CNT species from rolling-up a graphene sheet. (a) Graphene sheet map with CNT species defined by their chiral indices (n,m). The black arrow represents the chiral vector* C_h, θ *is the chiral angle and* a_1 *and* a_2 *are the unit vectors of the graphene lattice. CNT species are either metallic (labeled green) or semiconducting with q = +1 (labeled pink) or q = -1 (labeled purple). Figure (a) reprinted with permission from ref. 4; (b) (10,3) graphene sheet based on the black chiral vector shown in a); (c) (10,3) CNT formed by formally rolling-up a (10,3) graphene sheet; (d) front view of a (10,3) CNT. Nanotube and graphene structures were created using the program Nanotube Modeler.*

According to the regular pattern at their rims, CNT species with $n = m$ ($\theta = 30°$) are called "armchair" tubes and species with $m = 0$ ($\theta = 0°$) are "zigzag" tubes. These two groups of CNTs are achiral in the sense of handedness. All other species ($0 < \theta < 30°$) show chiral handedness and accordingly Cotton effects have been observed after separation of the enantiomers.[12]

The electronic structure of CNTs is not treated in terms of discrete molecular orbitals, but rather in terms of a band structure because of the essentially infinite π-conjugation along the tube. The simplest model to describe the band structure is the zone-folding approximation that is based on the above described concept of a CNT as a folded graphene sheet. The model only considers the π-electrons and applies the band theory of graphite.[13] According to this model, the CNT adopts a one-dimensional band structure that has to fulfill certain boundary conditions arising from the finite circumference and the infinite length. From these boundary conditions one can obtain the graphene wrapping condition $n - m = 3p + q$, where p is an integer.[14] This simple equation determines whether a nanotube is metallic or semiconducting based on the chiral index (n,m); a tube is metallic if $q = 0$, or semiconducting if $q = \pm 1$ (Figure 6.2a). Within the group of semiconducting nanotubes, the band gap inversely depends on the tube diameter, since larger diameter tubes are less curved and become more similar to graphene which is a zero band gap semiconductor. This means that generally the optical transitions of large diameter tubes occur at lower energies compared to small diameter tubes. Additionally, the position of the energy levels depends on the chiral indices.

A schematic representation of the band structure of a semiconducting CNT is shown in Figure 6.3, where the density of electronic states (DOS) is plotted about the Fermi level (energy = 0). The unique one-dimensional band structure in the CNT results in discontinuities in the DOS, unlike in a three-dimensional crystal where the DOS are continuous. The discontinuities are called van Hove singularities (VHS)[15] and transitions between the first two pairs of these states are, for most species, in the vis/NIR region of the spectrum. In the case of HiPCO nanotubes, the first van Hove transition E_{11} is above 1000 nm and the second van Hove transition E_{22} is below (e.g. (7,6) CNT: E_{11} = 1120 nm, E_{22} = 648 nm).[16]

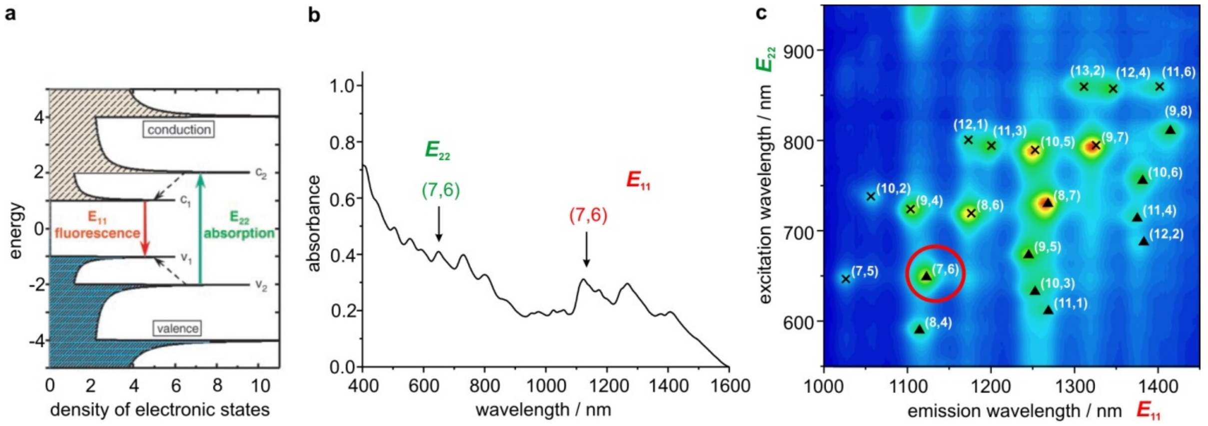

Figure 6.3. *(a) Density of states of semiconducting CNTs with valence bands in blue and conduction bands in black stripes. The plain arrows indicate the two lowest electronic transitions, E_{11} (red) and E_{22} (green). Figure reprinted with permission from ref. 17; (b) vis/NIR absorption of HiPCO CNTs in D_2O with the surfactant sodium dodecylbenzene sulfonate (SDBS). E_{11} bands are predominantly beyond 1000 nm, E_{22} bands are below 1000 nm; (c) PLE map of HiPCO CNTs in D_2O/SDBS with the CNT species labeled according to ref. 16. Emission intensity increases from blue to red and the CNT families are marked with black triangles ($q = +1$) or crosses ($q = -1$).*

Since current CNT production methods usually give rise to a mixture of many different CNT species, absorption spectra are usually broad with overlapping peaks that make it difficult to assess the composition of a sample (Figure 6.3b). Photoluminescence excitation (PLE) mapping offers a way around this problem by taking advantage of the band gap fluorescence of CNTs.[17] In a typical PLE experiment the E_{22} transitions are excited and fluorescence from E_{11} is measured (Figure 6.3a) resulting in a two-dimensional contour map (Figure 6.3c). In such a map the emission of each species is resolved as an individual cross peak, which allows quantification of the sample composition.

The one-dimensional band structure of CNTs leads to extraordinary electrical properties. Metallic CNTs are ballistic conductors[18] and the charge carrier mobilities in semiconducting CNTs are extremely high, surpassing common inorganic semiconductors such as silicon (see Table 6.1).[19] Compared to organic materials, such as conjugated polymers, the measured mobilities in individual tubes[16] (compared to polymer chains)[20] as well as in ordered thin films[21,22] are several orders of magnitude higher. The reason for the high charge carrier mobilities lies in the CNT's unique band structure as well as in the absence of phonon scattering i.e. dynamic structural fluctuations such as vibrations that can scatter electrons and thus obstruct charge transport.[19] For similar reasons the thermal conductivity of CNTs is exceptionally high, superior to benchmark materials such as copper or silver.[23] However, it is important to treat these record-breaking numbers with care: The remarkable electrical and thermal transport behavior is only found when measuring along the length of a tube. Conductance between tubes is significantly lower, with important consequences for the bulk properties: The charge carrier mobility in thin films of randomly oriented CNTs is relatively low (~10 cm^2 V^{-1} s^{-1}) and only aligned arrays of CNTs exhibit higher values (~1000 cm^2 V^{-1} s^{-1}).[21]

Table 6.1. *Comparison between physical properties of CNTs and other materials.*

Parameter	SWCNT	Benchmark material
Charge carrier mobility [cm^2 V^{-1} s^{-1}]	Individual tube[19] 2500 – 20 000	Conjugated polymer (intrachain)[20] < 600
	Aligned array (bulk)[21] ~1000	Conjugated polymer (thin film)[22] < 1
		Silicon[22] ~1000
Thermal conductance [W m^{-1} K^{-1}]	Individual tube[23] 3500	Silver 429
Tensile strength [GPa]	SWCNT rope[24] 30	Steel[5] ~1

The peculiar structural features of CNTs also result in extraordinary mechanical properties. The area normalized tensile strength or breaking strength of SWCNT ropes consisting of bundled tubes is significantly higher than in steel or Kevlar.[5] This high stiffness is very promising for using CNTs to increase the strength of polymer based materials, similar to carbon fiber-reinforced polymers that are commonly used as robust and light-weight materials.

6.1.2 Project Aims

The outstanding electronic and mechanical properties of CNTs described above make them one of the most promising materials in nanotechnology. However, strong van-der-Waals interactions between nanotubes cause the formation of multi-tube bundles. Such aggregates are insoluble and thus not processable in common solvents which hampers device fabrication. Noncovalent functionalization of CNT sidewalls with surfactants, polymers or small aromatic molecules improves their solubility and enables the introduction of functionality without damaging the electronic structure of the nanotube.[25,26] Composite materials based on this concept are being developed as sensors,[27,28] field-effect transistors[29] and photovoltaic (PV) devices.[30,31] The reason for the great promise that CNTs hold for PVs lies mostly in their excellent charge-transport behavior. Furthermore, photophysical studies on CNTs functionalized with porphyrins revealed the presence of long-lived charge-separated states, which is a prerequisite for efficient generation of photocurrents in PV devices.[32-34] Compared to the porphyrin derivatives studied in these reports, conjugated porphyrin oligomers ***l*-P2$_{C8}$**, ***l*-P4$_{C8}$** and ***l*-P6$_{C8}$** display significantly broader absorption that extends over the whole visible spectrum into the NIR. The improved overlap with the solar spectrum should lead to increased PV efficiencies. Besides this long term goal, we aimed to gain a detailed understanding of the noncovalent binding of CNTs by porphyrin oligomers using binding titrations. This technique, which is very common in supramolecular chemistry, has so far not been used to study the noncovalent interactions between organic molecules and CNTs, and should provide new insights into the supramolecular chemistry of CNTs.

6.2 Binding of Linear Porphyrin Oligomers

Porphyrin oligomers with 3,5-bis-(octyloxy) phenyl side groups ***l*-P*N*$_{C8}$** (Figure 6.4) were chosen for CNT functionalization because their long flexible alkyl chains were expected to provide sufficient solubility to allow formation of CNT solutions in organic solvents. The oligomers used in this study were monomer ***l*-P1$_{C8}$**, dimer ***l*-P2$_{C8}$**, tetramer ***l*-P4$_{C8}$**, hexamer ***l*-P6$_{C8}$**, octamer ***l*-P8$_{C8}$** as well as the porphyrin polymer ***l*-P*n*$_{C8}$** (***n*** = 30–50).

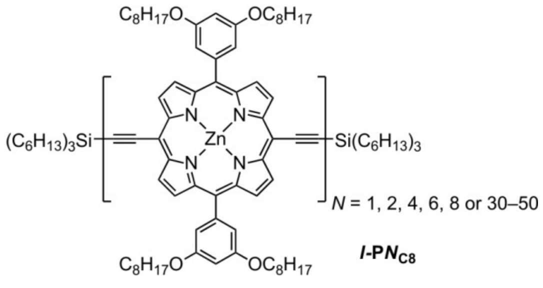

Figure 6.4. *Structure of linear porphyrin oligomers **l-PN$_{C8}$** used in CNT binding experiments.*

***l*-P1**$_{\mathbf{C8}}$, ***l*-P2**$_{\mathbf{C8}}$ and ***l*-P4**$_{\mathbf{C8}}$ were synthesized according to the route provided in Scheme 1.1. Porphyrin hexamer ***l*-P6**$_{\mathbf{C8}}$ was synthesized from trimer ***l*-P3**$_{\mathbf{C8}}$ by statistical mono-deprotection and subsequent palladium catalyzed oxidative acetylene homo-coupling as outlined in Scheme 1.2. Octamer ***l*-P8**$_{\mathbf{C8}}$, was obtained from Miquel Planells, a visiting student from Tarragona, as a mixture with ***l*-P4**$_{\mathbf{C8}}$ and was purified using preparative GPC. The purity of all compounds was confirmed by ^{1}H NMR and analytical GPC. The initial study on the binding behavior of porphyrin oligomers to CNTs (Sections 6.2.1 and 6.2.2) was limited to the monomer and oligomers up to hexamer. The work on modification of the CNTs electronic structure by the presence of porphyrins (Section 6.2.3) was carried out with the complete family of oligomers and the polymer.

6.2.1 Complex Formation and Selectivity of Binding

Sonication of HiPCO CNTs with oligomers ***l*-P2**$_{\mathbf{C8}}$, ***l*-P4**$_{\mathbf{C8}}$ and ***l*-P6**$_{\mathbf{C8}}$ in THF (ca 0.1 mM porphyrin concentration) resulted in complete dispersion of CNTs, whereas monomer ***l*-P1**$_{\mathbf{C8}}$ did not disperse CNTs under these conditions. The CNT complexes of ***l*-P2**$_{\mathbf{C8}}$, ***l*-P4**$_{\mathbf{C8}}$ and ***l*-P6**$_{\mathbf{C8}}$ were filtered off with a microfilter (nylon membrane, pore-size 200 nm) and washed with THF to remove excess unbound porphyrin. Isolated CNT complexes of ***l*-P4**$_{\mathbf{C8}}$ and ***l*-P6**$_{\mathbf{C8}}$ prepared in this way can be redispersed in THF. The dispersions displayed good stability, whereas the CNT complex of ***l*-P2**$_{\mathbf{C8}}$ precipitated immediately in the absence of an excess porphyrin. The ability of porphyrin oligomers to disperse HiPCO CNTs in THF thus increases with oligomers length, following the trend: ***l*-P1**$_{\mathbf{C8}}$ < ***l*-P2**$_{\mathbf{C8}}$ < ***l*-P4**$_{\mathbf{C8}}$, ***l*-P6**$_{\mathbf{C8}}$.

Dr. Jamie Warner (Department of Materials, Oxford) analyzed the hexamer complex ***l*-P6**$_{\mathbf{C8}}$**·**CNT with high resolution transmission electron microscopy (HRTEM) to obtain direct evidence for the binding of the oligomers with the nanotube sidewalls. The images clearly show the hexamer coating the sidewalls of a CNT, which is absent in a sample of pristine CNTs (Figure 6.5).

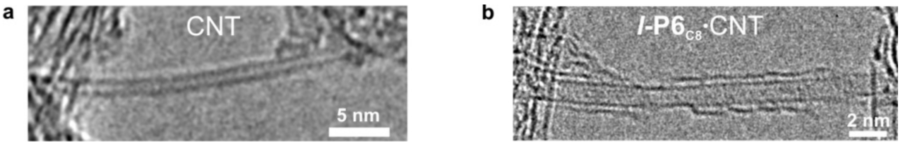

Figure 6.5. *HRTEM images of (a) pristine HiPCO CNTs and (b)* ***l-P6***$_{C8}$***·****CNT. HRTEM was performed using a JEOL 2200MCO FEG HRTEM operating at an accelerating voltage of 80 kV.*

When ***l*-P4**$_{\mathbf{C8}}$ and ***l*-P6**$_{\mathbf{C8}}$ bind to CNTs, their Q-absorption bands become sharper and are red-shifted by about 120 nm (220 meV, Figure 6.6a). These spectral changes (which have also been reported in porphyrin polymer-CNT complexes)[35] are clear evidence for planarization of the porphyrin oligomer π-system.[36-38] The many well-resolved absorption peaks in the region of the first electronic transition E_{11} of the CNTs (>1000 nm) show that numerous different CNT species are present in the dispersion. Photoluminescence excitation (PLE) maps show distinct cross-peaks for each semiconducting nanotube species, thereby allowing the selectivity of CNT binding to be assessed by comparison with non-selective surfactants.[17,39] PLE maps of **_l_-P4**$_{C8}$·CNT and **_l_-P6**$_{C8}$·CNT in THF (Figure 6.6b and 6.6c, respectively) show significantly fewer emitting species than the PLE map of HiPCO CNTs dispersed in D_2O† (Figure 6.6d) using the non-selective surfactant sodium dodecylbenzene sulfonate (SDBS). Comparison of the absorption (Figure 6.6a) and emission spectra indicates that (8,6) and (7,5) tubes emit with a higher quantum yield than the other CNTs in the presence of **_l_-P4**$_{C8}$ and **_l_-P6**$_{C8}$. In CNT bundles fluorescence is quenched by metallic tubes,[40] thus the brighter fluorescence from (8,6) and (7,5) tubes indicates stronger binding, and consequently more efficient debundling by the porphyrin oligomers. The PLE maps also reveal energy-transfer from the porphyrin oligomers to the nanotubes. Excitation of the porphyrin Q band (850–900 nm) results in nanotube emission which is not otherwise observed in the absence of porphyrin (horizontal dashed lines in Figure 6.6b,c).

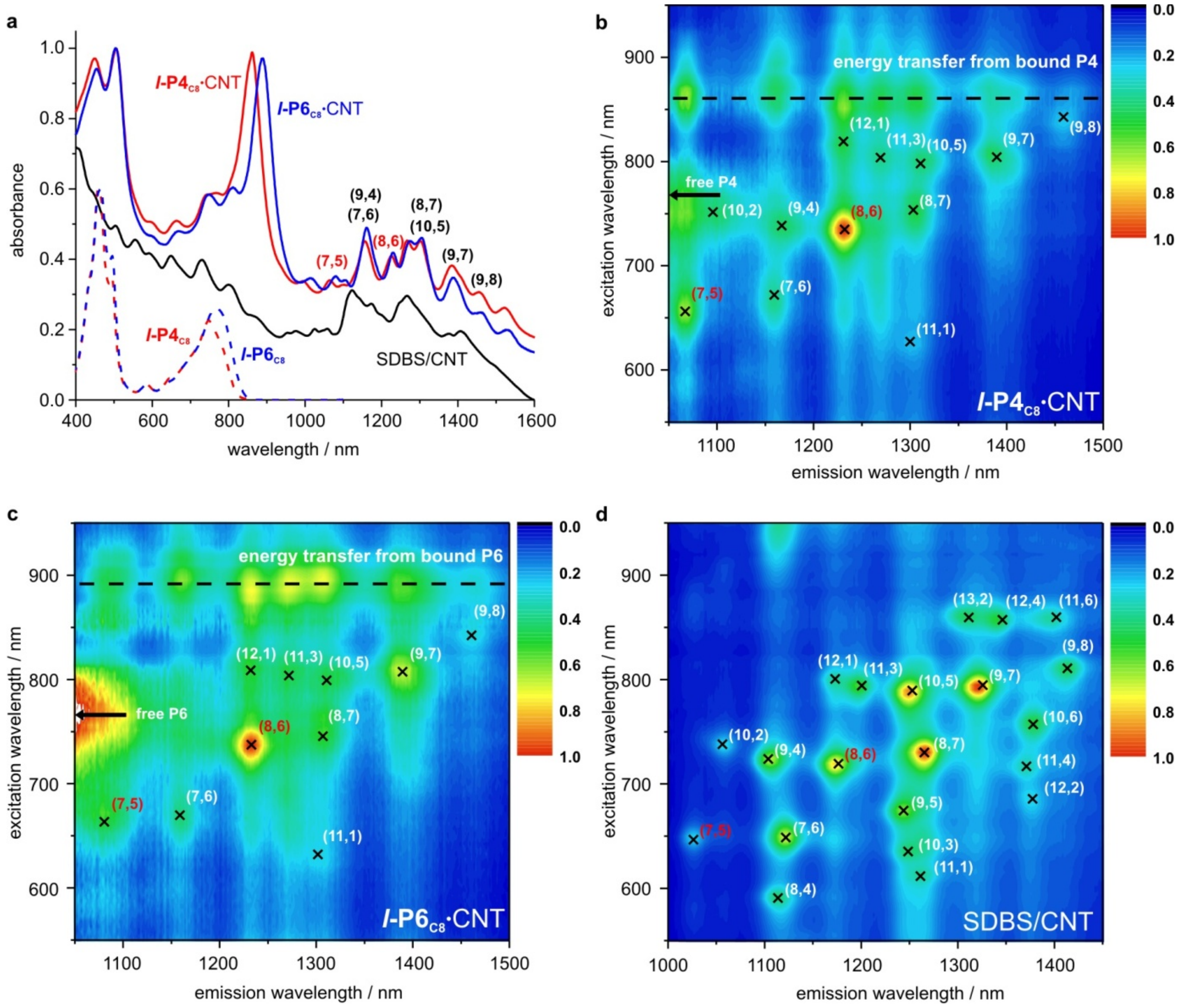

Figure 6.6. *(a) Vis/NIR absorption spectra of* **_l-P4_**$_{C8}$ *(dashed red line),* **_l-P6_**$_{C8}$ *(dashed blue line),* **_l-P4_**$_{C8}$*·CNT (red line),* **_l-P6_**$_{C8}$*·CNT (blue line) all in THF, and SDBS-solubilized CNT (black line) in* D_2O *(b) PLE map of* **_l-P4_**$_{C8}$*·CNT in THF; (c) PLE map of* **_l-P6_**$_{C8}$*·CNT in THF; (d) PLE map of SDBS/CNT in* D_2O*. Emission intensity in all maps is normalized and tube species are labelled with their (n,m) indices according to ref. 16. Horizontal dashed lines in (b) and (c) indicate energy transfer from porphyrin oligomers.*

---

† D_2O was used to avoid OH vibrational overtones in the NIR absorption spectrum.

Binding to CNTs completely quenches emission from porphyrin oligomers. All emission from **_l_-P6$_{C8}$**·CNT that does not originate from the CNT is due to traces of unbound **_l_-P6$_{C8}$**, as demonstrated by the perfect overlap of the excitation spectrum of **_l_-P6$_{C8}$**·CNT at 1020 nm with the absorption of free rather than bound **_l_-P6$_{C8}$** (Figure 6.7a). The quenching effect can be exploited to determine the stoichiometry of the CNT complexes. Upon addition of CNT to a solution of **_l_-P6$_{C8}$** ([**_l_-P6$_{C8}$**] = 2.1 mg L^{-1} = 0.3 μM), the porphyrin emission intensity decreases linearly with increasing CNT concentration (Figure 6.7b). At the point where all **_l_-P6$_{C8}$** is bound, porphyrin emission is completely quenched. The CNT/**_l_-P6$_{C8}$** mass ratio at this end-point is 1.35 and corresponds to a number of CNT carbon atoms per porphyrin subunit of $n_{C/P}$ = 132. The vis/NIR absorption spectrum of the **_l_-P6$_{C8}$**·CNT complex isolated on a preparative scale ([**_l_-P6$_{C8}$**] = 500 mg L^{-1} = 70 μM) shows a 40% increase in bound porphyrin compared to the absorption spectrum at the end-point of the fluorescence titration, due to a higher degree of CNT debundling at higher porphyrin concentrations. The increased debundling is reflected in a decrease of CNT carbon atoms per porphyrin unit to $n_{C/P}$ = 94, which means that one molecule of **_l_-P6$_{C8}$** saturates a segment of (8,6) CNT of 4.9 nm length.

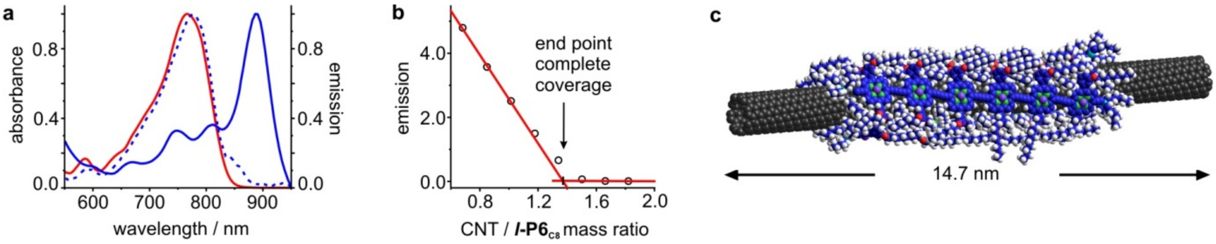

Figure 6.7. *(a) Vis/NIR absorption spectra of **l-P6$_{C8}$** (red line), **l-P6$_{C8}$**·CNT (blue line) and excitation spectrum of **l-P6$_{C8}$**·CNT at 1020 nm (blue dashed line) all in THF; (b) **l-P6$_{C8}$** emission at 930 nm with increasing concentration of CNT. The arrow marks the point where all porphyrin is bound to CNT. **[P6]** = 2.1 mg/L; (c) molecular mechanics optimized structure of 3 x **l-P6$_{C8}$**·*(8,6) CNT *based on the calculated mass ratio.*

Molecular mechanics simulations showed that three molecules of **_l_-P6$_{C8}$** can form a tight layer around an (8,6) tube. Based on this result the measured mass ratio is visualized in Figure 6.7c: Three **_l_-P6$_{C8}$** molecules wrap around 14.7 nm (3 × 4.9 nm) of an (8,6) nanotube showing almost monolayer coverage.† Incomplete monolayer formation may be due to partial CNT bundling, which reduces the available surface area.

6.2.2 Thermodynamics and Kinetics of Binding

UV/vis and fluorescence titrations are often used to quantify supramolecular interactions.[41] Papdimitrakopoulos *et al.* determined relative binding constants to CNTs from competitive binding titrations between the surfactant SDBS and a flavin nucleotide.[42] However, so far no absolute binding

---

† In this model 100% (8,6) CNT were assumed in the sample. Similar calculations with different CNT species showed that the polydispersity of diameters has a small influence on the length of CNT per porphyrin, because the distribution of CNT diameters is quite narrow and (8,6) tubes are in the center of the distribution.

constants for noncovalent nanotube functionalization have been reported, perhaps due to the insolubility of pristine CNTs in most solvents. 1,2-Dichlorobenzene is one of the few solvents that give stable CNT dispersions suitable for optical measurements[43,44] and thus more detailed binding studies were carried out using this solvent.

Titrations with all porphyrin oligomers were performed using both vis/NIR absorption and fluorescence spectroscopy (Figure 6.8a). In each case, the data were fitted to a 1:1 binding isotherm making three assumptions: 1) Binding constants for different CNT species are very similar, which is supported by Papadimitrakopoulos' finding that relative binding constants to CNT species differ by a maximum factor of 2.[42] 2) One porphyrin oligomer binds to one CNT binding site and 3) these binding sites act independently. The parameters obtained from the fits are the binding constant $K_{\mathbf{P}\boldsymbol{N}}$ and the concentration of CNT binding sites. This value can be converted into the number of carbon atoms corresponding to a CNT binding site $Nn_{\mathrm{C/P}}$ using the CNT mass concentration.

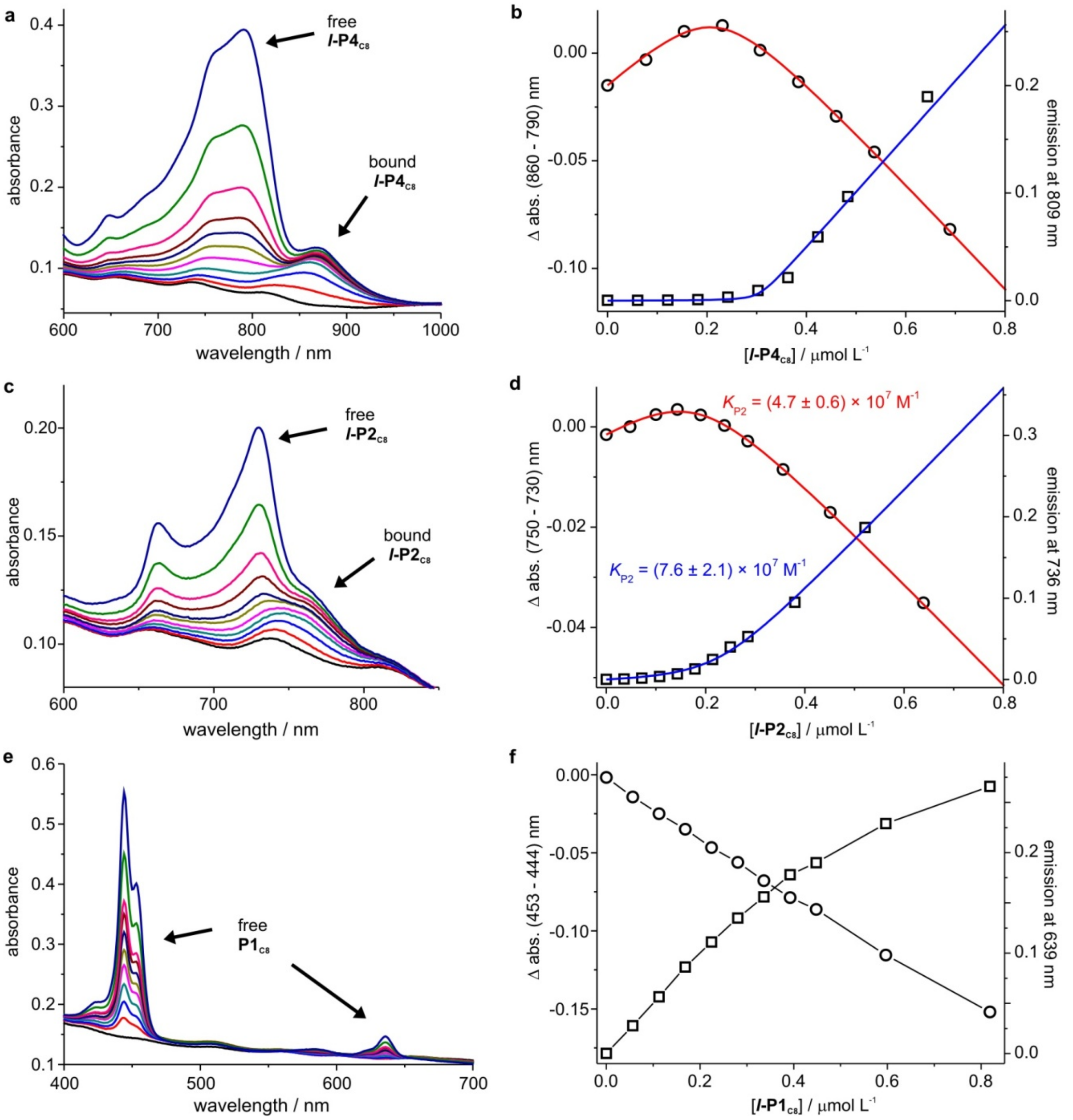

Figure 6.8. *Vis/NIR absorption and fluorescence titrations of* ***$P1_{C8}$****,* ***l-$P2_{C8}$*** *and* ***l-$P4_{C8}$*** *into HiPCO CNTs in DCB at 298 K. The left column (a, c, e) shows the absorption spectra, the right column (b, d, f) shows the difference in absorption at two chosen wavelengths (circles). The fit to a 1:1 binding isotherm (red line) as well as the emission intensity of free porphyrin (squares) with the fit (blue line) are also displayed. Binding isotherms for* ***l-$P6_{C8}$*** *were very similar to* ***l-$P4_{C8}$****[42] and are thus not shown. Experimental details of the different titrations: (b) abs: [CNT] = 1.6 mg L^{-1}; em: [CNT] = 1.6 mg L^{-1}, λ_{ex} = 460 nm. (d) abs: [CNT] = 1.9 mg L^{-1}; em: [CNT] = 1.7 mg L^{-1}, λ_{ex} = 460 nm. (f) abs: [CNT] = 1.7 mg L^{-1}; em: [CNT] = 1.7 mg L^{-1}, λ_{ex} = 444 nm. The black lines are guides to the eye. The non-linear increase in emission intensity at higher* ***$P1_{C8}$*** *concentrations is probably due to self-quenching and is also observed in the absence of CNTs.*

The affinities of **l-$P4_{C8}$** and **l-$P6_{C8}$** for CNTs are too strong to be measured by UV/vis or fluorescence titrations ($K > 10^9$ M^{-1}), as illustrated by the square binding isotherm for **l-$P4_{C8}$** in Figure 6.8b. The binding constant of **l-$P2_{C8}$** is $K_{P2} = (4.7 \pm 0.6) \times 10^7$ M^{-1} from absorption titrations; fluorescence titrations gave a similar value (Figure 6.8c,d). There is no evidence for complex formation of **$P1_{C8}$** with CNTs, because the absorption spectrum does not change and the fluorescence is not quenched (Figure 6.8e,f). This behavior can be interpreted as either weak or no binding ($K < 10^3$

M^{-1}), or as insensitivity of both absorption and emission of ***l*-P1**$_{\mathbf{C8}}$ towards CNT binding. However, in light of the efficient fluorescence quenching of the longer oligomers, the latter possibility seems unlikely.

The relative affinities of ***l*-P2**$_{\mathbf{C8}}$ – ***l*-P6**$_{\mathbf{C8}}$ for CNTs were also investigated by UV/vis/NIR competition experiments. The Q bands of the porphyrin oligomers occur at progressively longer wavelengths so that, for example, it is possible to observe the Q-band of bound ***l*-P6**$_{\mathbf{C8}}$ in the presence of a high concentration of free ***l*-P2**$_{\mathbf{C8}}$. In a first experiment, ***l*-P2**$_{\mathbf{C8}}$ was added to ***l*-P6**$_{\mathbf{C8}}$**·**CNT, but even a 2500-fold excess of the dimer does not replace bound ***l*-P6**$_{\mathbf{C8}}$ (Figure 6.9a). Slow kinetics can be excluded as the reason for the reluctance towards displacement of ***l*-P6**$_{\mathbf{C8}}$ because a second experiment showed that ***l*-P6**$_{\mathbf{C8}}$**·**CNT can be formed, even when the 2500-fold excess of ***l*-P2**$_{\mathbf{C8}}$ is already present (Figure 6.9b). Evidence for replacement of ***l*-P2**$_{\mathbf{C8}}$ by ***l*-P6**$_{\mathbf{C8}}$, rather than binding to the complex ***l*-P2**$_{\mathbf{C8}}$**·**CNT comes from a third experiment involving the addition of ***l*-P6**$_{\mathbf{C8}}$ to ***l*-P2**$_{\mathbf{C8}}$**·**CNT. This results in the appearance of free ***l*-P2**$_{\mathbf{C8}}$, as indicated by the blue-shift of the ***l*-P2**$_{\mathbf{C8}}$ Q-band (Figure 6.9c). Repeating the same experiments with ***l*-P4**$_{\mathbf{C8}}$ instead of ***l*-P6**$_{\mathbf{C8}}$ showed, that even an 800-fold excess of ***l*-P2**$_{\mathbf{C8}}$ cannot replace ***l*-P4**$_{\mathbf{C8}}$.[†] Attempted competition experiments between ***l*-P4**$_{\mathbf{C8}}$ and ***l*-P6**$_{\mathbf{C8}}$ did not reach equilibrium after 24 h; whichever oligomer was added first remained bound, even in the presence of a large excess of the other oligomer.

Lower limits of $K_{\mathbf{P4}}$ and $K_{\mathbf{P6}}$ can be deduced from the excess of dimer used in the competition experiments and its binding constant $K_{\mathbf{P2}}$, assuming that one molecule of ***l*-P4**$_{\mathbf{C8}}$ or ***l*-P6**$_{\mathbf{C8}}$ replaces one molecule of ***l*-P2**$_{\mathbf{C8}}$. The ratio between the binding constants of the oligomers is given by Equation (6.1):

$$\frac{K_{\mathbf{P}\boldsymbol{N}}}{K_{\mathbf{P2}}} = \frac{[\boldsymbol{l}\text{-}\mathbf{P}\boldsymbol{N}_{\mathbf{C8}} \cdot \mathrm{CNT}]}{[\boldsymbol{l}\text{-}\mathbf{P}\boldsymbol{N}_{\mathbf{C8}}][\mathrm{CNT}]} \times \frac{[\boldsymbol{l}\text{-}\mathbf{P2}_{\mathbf{C8}}][\mathrm{CNT}]}{[\boldsymbol{l}\text{-}\mathbf{P2}_{\mathbf{C8}} \cdot \mathrm{CNT}]} \tag{6.1}$$

When 50% **P*N*** is replaced by ***l*-P2**$_{\mathbf{C8}}$ this equation simplifies to equation 6.2:

$$K_{\mathbf{P}\boldsymbol{N}} = K_{\mathbf{P2}} \frac{[\boldsymbol{l}\text{-}\mathbf{P2}_{\mathbf{C8}}]}{[\boldsymbol{l}\text{-}\mathbf{P}\boldsymbol{N}_{\mathbf{C8}}]} = K_{\mathbf{P2}} \left(\frac{[\boldsymbol{l}\text{-}\mathbf{P2}_{\mathbf{C8}}] - [\boldsymbol{l}\text{-}\mathbf{P}\boldsymbol{N}_{\mathbf{C8}} \cdot \mathrm{CNT}] \times 0.5}{[\boldsymbol{l}\text{-}\mathbf{P}\boldsymbol{N}_{\mathbf{C8}} \cdot \mathrm{CNT}] \times 0.5} \right) \tag{6.2}$$

The point of 50% displacement is not reached in the competition experiments and thus the values calculated using Equation (6.2) and $K_{\mathbf{P2}} = 4.7 \times 10^{7}\ \mathrm{M}^{-1}$ are lower limits: $K_{\mathbf{P4}} > 7.6 \times 10^{10}\ \mathrm{M}^{-1}$ and $K_{\mathbf{P6}} > 2.3 \times 10^{11}\ \mathrm{M}^{-1}$. These lower limits would be substantially higher under the assumption that one molecule ***l*-P4**$_{\mathbf{C8}}$ or ***l*-P6**$_{\mathbf{C8}}$ replaces two or three molecules of ***l*-P2**$_{\mathbf{C8}}$, respectively.

[†] The maximum concentrations of ***l*-P2**$_{\mathbf{C8}}$ used in the competition experiments depend on when the Q-bands of bound and unbound oligomers ***l*-P4**$_{\mathbf{C8}}$ or ***l*-P6**$_{\mathbf{C8}}$ become indistinguishable.

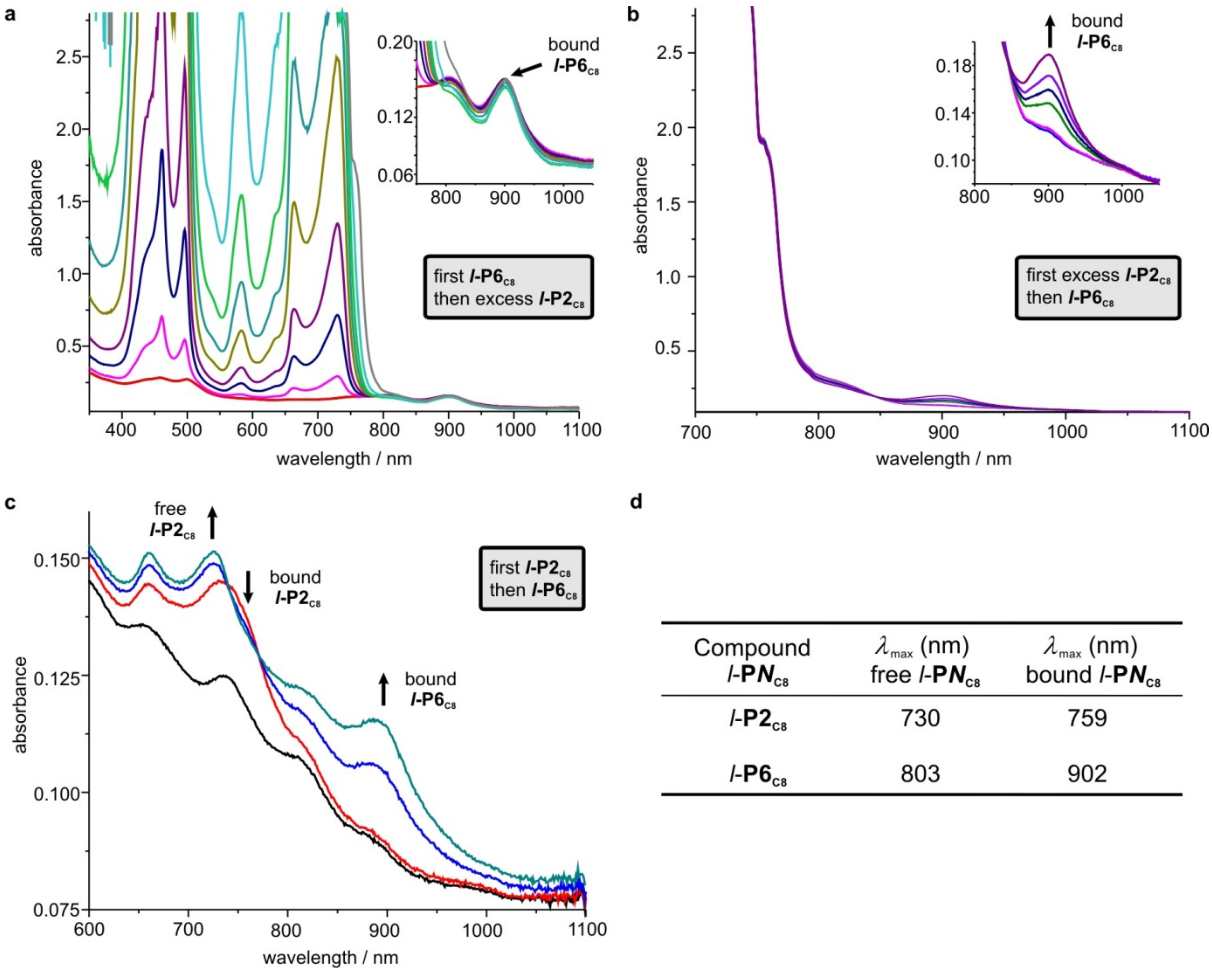

Compound *l*-**PN**$_{C8}$	λ_{max} (nm) free *l*-**PN**$_{C8}$	λ_{max} (nm) bound *l*-**PN**$_{C8}$
l-**P2**$_{C8}$	730	759
l-**P6**$_{C8}$	803	902

Figure 6.9. *Competition experiments between* ***l-P2***$_{C8}$ *and* ***l-P6***$_{C8}$ *in DCB at 298 K. (a) Addition of* ***l-P6***$_{C8}$ *to a solution of CNTs to allow monolayer coverage ([****l-P6***$_{C8}$*] = 0.26 μM), followed by addition of* ***l-P2***$_{C8}$ *until the detector below 750 nm is saturated ([****l-P2***$_{C8}$*]$_{max}$ = 0.65 mM). The inset shows the region of CNT bound* ***l-P6***$_{C8}$ *that remains unchanged with increasing dimer concentration; (b) addition of the same large excess of* ***l-P2***$_{C8}$ *as in (a) to CNTs, followed by addition of the same amount* ***l-P6***$_{C8}$ *as in (a). The inset shows changes in the region of CNT bound* ***l-P6***$_{C8}$ *over several hours; (c) addition of* ***l-P2***$_{C8}$ *to CNTs ([****l-P2***$_{C8}$*] = 0.15 μM, red line), followed by the addition of* ***l-P6***$_{C8}$*. Concentration of* ***l-P6***$_{C8}$ *increases from red to turquoise (0, 0.03 μM, 0.06 μM); (d) table with the absorption maxima of porphyrin Q-bands λ_{max} of free and CNT bound porphyrin oligomers.*

Besides the binding constant, the binding titrations in DCB (Figure 6.8) also give the number of carbon atoms corresponding to a CNT binding site $Nn_{C/P}$. Dividing $Nn_{C/P}$ by the number of porphyrin subunits in the oligomer gives the number of CNT carbon atoms per porphyrin subunit $n_{C/P}$, introduced in Section 6.2.1. This value is a direct measure of the degree of debundling of the nanotubes. The number of CNT carbon atoms per porphyrin subunit in the ***l*-P6**$_{C8}$•CNT complex formed in DCB ($n_{C/P}$ = 115) is intermediate between the value from fluorescence titrations in THF ($n_{C/P}$ = 132) and the value for the isolated complex ($n_{C/P}$ = 94), indicating an intermediate level of debundling in DCB. When comparing oligomers ***l*-P2**$_{C8}$ – ***l*-P6**$_{C8}$ in DCB, we observe a slight increase in $n_{C/P}$ from 115 for ***l*-P6**$_{C8}$ to 150 for ***l*-P4**$_{C8}$, and a substantial increase for ***l*-P2**$_{C8}$ (420). The weaker porphyrin-nanotube interaction in ***l*-P2**$_{C8}$•CNT evidently results in a much lower degree of debundling. Kinetic observations support this conclusion. When ***l*-P4**$_{C8}$ or ***l*-P6**$_{C8}$ is added to CNTs in DCB, complexation is biphasic; rapid initial binding is followed by a slower process with a half-life of 6 ± 1 min for both oligomers. This behavior is interpreted in terms of a fast, diffusion-controlled binding event to the outside of nanotube bundles, followed by a slow debundling process. In the case of ***l*-P2$_{C8}$**, only the fast initial process is observed and thus no debundling occurs (Figure 6.10).

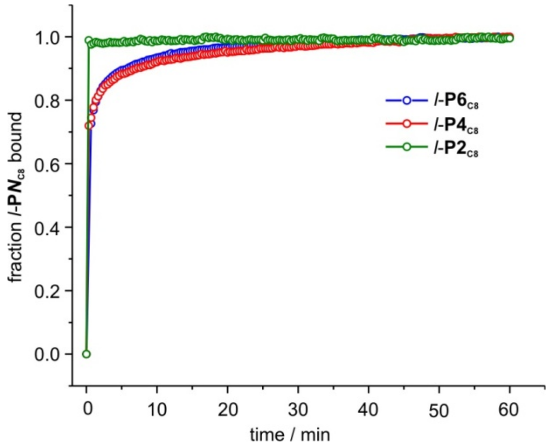

***Figure 6.10.** Kinetics of CNT binding by oligomers **l-P2$_{C8}$** (green circles and line), **l-P4$_{C8}$** (red circles and line) and **l-P6$_{C8}$** (blue circles and line) in DCB at 298 K.*

The results from the different binding experiments give a coherent picture that correlates with the ability of the oligomers to disperse CNTs in THF. The affinity of oligomers ***l*-P4$_{C8}$** and ***l*-P6$_{C8}$** for CNTs is high enough to allow efficient nanotube debundling, which explains their ability to disperse CNTs in THF. The affinity of dimer ***l*-P2$_{C8}$** appears to be insufficient to debundle CNTs in DCB and the dispersions in THF are only stable when excess dimer is present. No evidence for binding of monomer ***l*-P1$_{C8}$** to CNTs was found which explains the inability of ***l*-P1$_{C8}$** to disperse CNTs in THF.

6.2.3 Consequences of Binding on the Electronic Structure of CNTs

The van Hove singularities in CNTs are very sensitive to environmental effects. It has been shown that changes in the electronic environment of the tubes through noncovalent functionalization[46] or mechanical strains[47-49] can significantly influence the energy of the E_{11} and E_{22} transitions. Shifts in these transitions can be readily analyzed using PLE maps. The PLE maps of porphyrin oligomer-CNT complexes display unusual patterns in the shifts of E_{11} and E_{22} compared to SDBS-dispersed tubes. To explore these effects further, PLE maps of the HiPCO CNT complexes of octamer ***l*-P8$_{C8}$**·CNT and polymer ***l*-P*n*$_{C8}$**·CNT were measured, as well as PLE maps of all oligomers and the polymer bound to smaller diameter CoMoCat tubes. Interestingly, dispersions of ***l*-P8$_{C8}$**·CNT and ***l*-P*n*$_{C8}$**·CNT in THF were less stable than those of tetramer and hexamer CNT complexes. The data obtained from the collection of PLE maps were analyzed and interpreted by Samuel Stranks and Professor Robin Nicholas (Department of Physics, Oxford) and only a summary is given here.

Figure 6.11a shows an analysis of the shifts in the E_{11} and E_{22} transitions of ***l*-P6$_{C8}$**·CNT relative to values reported for SDBS·CNT.[16] For all CNT species with $q = +1$, the E_{11} transition is more shifted than the E_{22} transition and for species with q = -1 the opposite trend is observed. This effect is most pronounced for tubes with small chiral angles (n>>m) and has previously been attributed to the presence of mechanical strains on the nanotube.[47-49] In contrast to literature reports of such strain effects, the shifts in the porphyrin-CNT complexes also contain a constant electronic component that can be separated from the strain effect.[50] Fitting the strain component of the shifts to the model by Yang and Han[47] allows extraction of torsional and axial strains. The deformation of the CNTs is small (<0.2%), but comparable to that in polymer wrapped CNTs in the solid state.[48] Strain effects as a result of noncovalent CNT functionalization have not been observed in solution before and they are probably a consequence of the extremely strong binding of the porphyrins. The strain effects increase with oligomer length correlating with the increase in binding strength found in the vis/NIR absorption and fluorescence titrations. The energy of the binding induced strain is 1–4 kJ mol^{-1} per porphyrin oligomer, with the highest value being reached for hexamer. Both strain energy and CNT deformation are lower in ***l*-P8$_{\mathrm{C8}}$**·CNT than in ***l*-P6$_{\mathrm{C8}}$**·CNT. This effect indicates weaker binding and may explain the decrease in stability of solutions of the octamer CNT complex in THF.

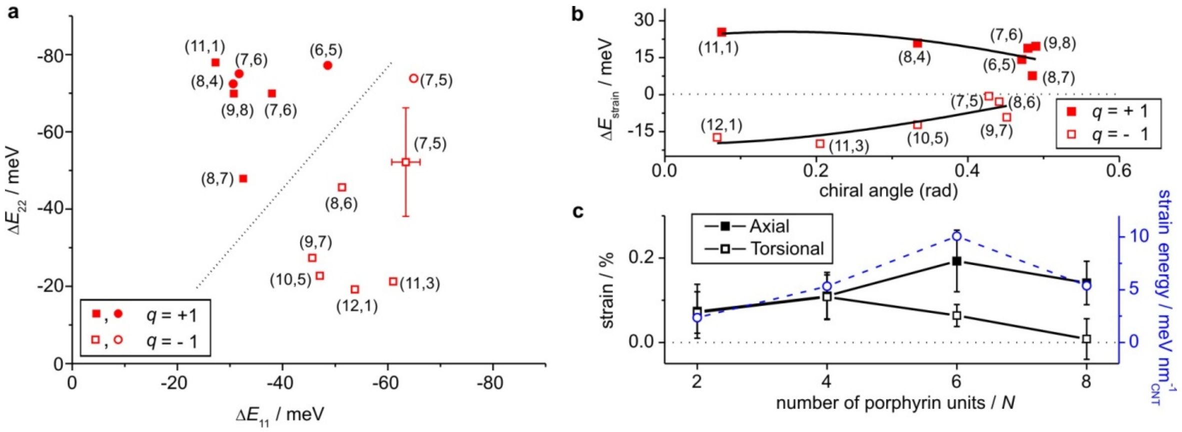

Figure 6.11. *(a) Shifts of E_{11} and E_{22} in **l-P6$_{\mathrm{C8}}$**·CNT relative to the values reported in ref. 16. The data are from HiPCO (squares) and CoMoCat (circles) CNTs. The dotted line is a guide to the eye to show the differences for the two families q = +1 (filled) and q = -1 (open). The representative error bar is estimated from the instrument resolution and errors in peak fitting; (b) strain induced shifts for **l-P6$_{\mathrm{C8}}$**·CNT plotted against the chiral angle of the CNT (squares) fitted to the Yang and Han model (black line); (c) axial (filled square) and torsional (open square) strain components and strain energy per nm of CNT (open blue circles) for the porphyrin oligomers.*

Two types of band alignments at the interface between two semiconductors are relevant for photovoltaics. In a type-I heterojunction the valence and conduction bands form a straddling gap, whereas a staggered energy level alignment is found in a type-II heterojunction (Figure 6.12a). Type-I alignment usually results in energy transfer whilst type-II alignment allows charge transfer, which is the desirable process for photovoltaics. Figure 6.12b shows the E_1 energy levels of CNTs dependent on their diameter and the HOMO and LUMO levels of the porphyrin oligomers. From the alignment of the energy levels one expects the formation of a type II heterojunction between small diameter CNTs (d < 0.9–1.0 nm) and the longer oligomers (***l*-P4$_{\mathrm{C8}}$** – ***l*-P*n*$_{\mathrm{C8}}$**).

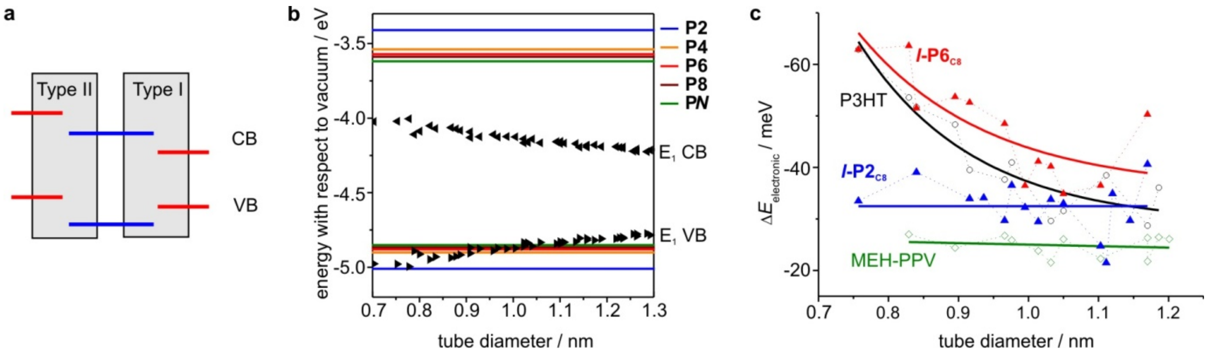

Figure 6.12. *(a) Energy level alignment for type-I and type-II heterojunctions between two semiconductors. CB is conduction band and VB is valence band; (b) HOMO and LUMO levels of porphyrin oligomers (lines) and* E_1 *energy levels of CNTs according to their diameter (black triangles); (c) electronic component of CNT shifts of porphyrin oligomer or polymer complexes with CNTs as a function of tube diameter.*

Schuettfort *et al.* showed that the formation of a type-II heterojunction between poly-3-hexyl thiophene (P3HT) and CNTs results in red-shifts of the nanotube transitions that are strongest for the smallest tubes where the type-II alignment is most pronounced.[46] This trend is not observed in type-I polymers such as poly(2-methoxy-5-(2-ethylhexyloxy)-1,4-phenylenevinylene (MEH-PPV). Excitation of the CNT results in formation of an exciton (or electron-hole pair). If the HOMO of the polymer lies higher in energy than the valence band of the CNT (type-II alignment), the wave function of the hole can delocalize into the polymer. As a consequence, the recombination energy of the exciton is reduced, which results in a red-shift of the emission. In a type-I heterojunction this delocalization is not possible and thus no increase in red-shift for smaller tubes is observed. When plotting the electronic component of shifts in the CNT transitions in porphyrin-CNT complexes, a clear diameter dependence is observed for ***l*-P8**$_{\mathbf{C8}}$·CNT and ***l*-P6**$_{\mathbf{C8}}$·CNT, an intermediate dependence for ***l*-P4**$_{\mathbf{C8}}$·CNT and no dependence for ***l*-P2**$_{\mathbf{C8}}$·CNT (Figure 6.12c and ref. 50). This result suggests the most pronounced type-II character for the longest oligomers which corresponds well to the expected behavior from the energy level alignment.

6.3 Attempted Binding of Cyclic Porphyrin Hexamer to CNTs

The synthesis of a polyrotaxane or pseudo-polyrotaxane from an organic macrocycle and a carbon nanotube as the dumbbell is an attractive target. In such a mechanically interlocked structure the irreversibility of covalent CNT sidewall functionalization could be combined with the mildness of the noncovalent functionalization approach. Binding should be preferential for a narrow distribution of CNT diameters because of the geometric restrictions of a macrocycle. Selective binding to only one CNT species is a long sought goal on the way to obtaining monodisperse CNT samples that are required for many potential applications.[7] Dieckmann *et al.* used oligopeptides that can be covalently cyclized after binding to CNTs and demonstrated selectivity for certain CNT diameter ranges as a function of oligopeptide length.[51] In order to test whether a similar effect can be achieved with cyclic porphyrin hexamer, a new derivative ***c*-P6$_{es}$** with *para*-ester aryl side groups was synthesized (Figure 6.13a).[†] The branched decyl-2-hexyl chains provide good solubility and their location in the *para*-aryl position should result in a larger ring cavity compared to ***c*-P6** and ***c*-P6$_{C8}$**, by avoiding bulky *meta* substituents on the aryl side groups.

Sonication of ***c*-P6$_{es}$** with HiPCO CNTs (2:1 mass ratio) in THF leads to formation of a stable dispersion. Removal of excess ***c*-P6$_{es}$** by microfiltration, followed by re-sonication in THF gives dispersions that are significantly less stable and after 10–30 minutes all nanotubes have precipitated. When an excess of the nanoring-template complex ***c*-P6$_{es}$·T** is sonicated with CNTs, immediate precipitation occurs, indicating the necessity of the absence of the template for CNT binding.

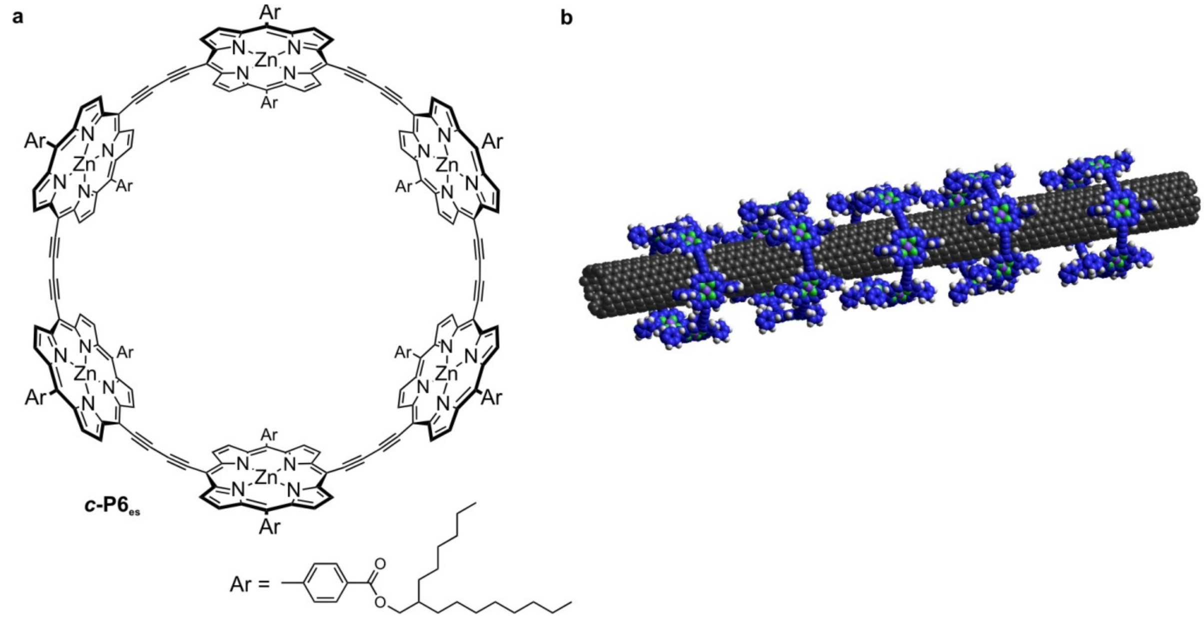

Figure 6.13. *(a) Structure of nanoring* ***c*-P6$_{es}$***; (b) model of a pseudo-polyrotaxane from* ***c*-P6$_{es}$** *and an (8,7) CNT.*

Threading of the nanorings on CNTs should restrict rotation of the porphyrin units and lead to increased π-conjugation. However, unlike in the CNT complexes of linear oligomers, the Q-absorption band is not red-shifted compared to the free nanoring ***c*-P6$_{es}$** (Figure 6.14a). The CNT absorption peaks above 1000 nm are not as well resolved as in the CNT complexes of linear oligomers, which indicates less efficient debundling. This is consistent with the absence of CNT emission in the PLE map of ***c*-P6$_{es}$**·CNT, where free nanoring is the only detectable emissive species (Figure 6.14b). This complete quenching of emission is evidence for strong nanotube bundling[40] which explains the low solubility of ***c*-P6$_{es}$**·CNT in THF.

[†] The synthesis of ***c*-P6$_{es}$** is detailed in Chapter 7.

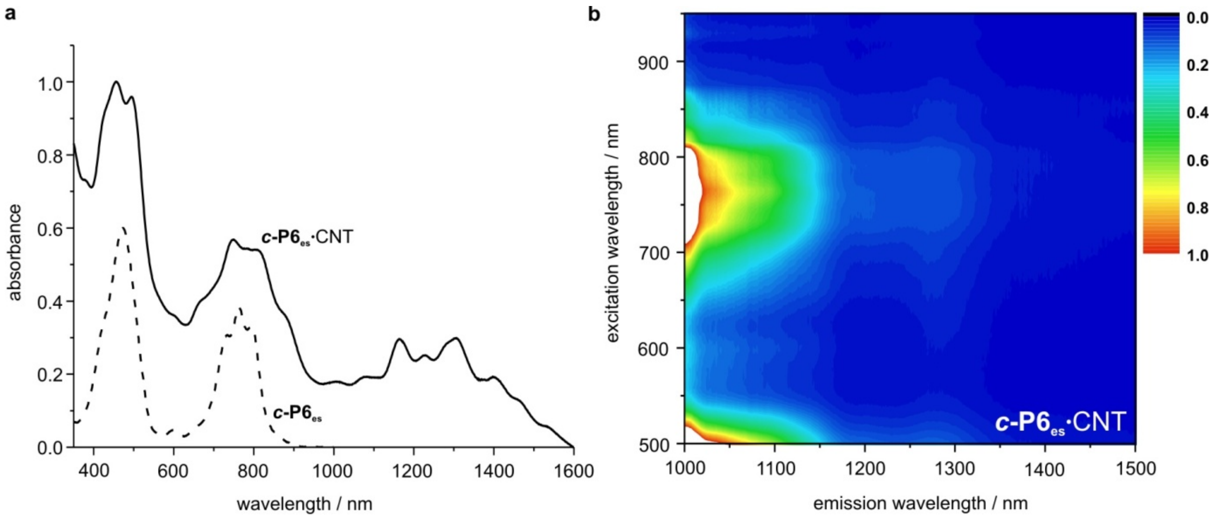

Figure 6.14. *(a) Vis/NIR absorption spectra of* **c-*P6*$_{es}$** *(dashed) and* **c-*P6*$_{es}$***·CNT (line); (b) normalized PLE map of* **c-*P6*$_{es}$***·CNT. All spectra were measured in THF.*

The experimental data suggest that ***c*-P6$_{es}$** binds to CNTs and that the absence of the hexadentate template is crucial for this binding process. There is no evidence for formation of a pseudo-polyrotaxane and it seems more likely that the nanoring binds predominantly to the outside of the CNTs. Such binding is expected to be weak based on the low amenability of ***c*-P6$_{es}$** for π-π-interactions (see Chapter 1) and therefore explains the inability of the nanoring to efficiently disaggregate nanotube bundles. However, more detailed investigation is necessary to draw definitive conclusions.

6.4 Conclusions and Outlook

In this chapter the selectivity, thermodynamics and kinetics of the noncovalent binding of a series of linear porphyrin oligomers to carbon nanotubes have been analyzed and the mechanical and electronic consequences of this binding were investigated. There are three reasons why complexes of the longer oligomers, particularly ***l*-P4$_{C8}$**·CNT and ***l*-P6$_{C8}$**·CNT, are promising for application in photovoltaic devices: 1) The formation of a type-II heterojunction between these oligomers and small diameter CNTs is a prerequisite for the generation of photocurrents. 2) These oligomers are most effective at debundling and solubilizing CNTs, which is important in allowing solution processing and the formation of homogenous thin films. 3) From the competition experiments it seems that the binding is not only extremely strong, but also the complexes are probably kinetically very stable which is important for the long term stability and performance of solid state devices. Rebundling of CNTs in such devices would dramatically reduce the PV efficiency. The focus of future experiments may be the complete photophysical characterization of the complexes using time-resolved spectroscopy in order to gain more insight into energy and charge transfer processes. It should be possible to use time-resolved THz measurements to directly probe mobile electrons on the CNTs generated by photoinduced charge transfer from the porphyrin oligomer. Incorporation of these complexes in photovoltaic devices is the crucial step to reveal the potential of these materials.

In general conclusion, a strategy to analyze noncovalent CNT functionalization in solution has been developed that allows the study of such complexes in more detail than has been achieved previously. Binding titrations offer a wealth of information, ranging from thermodynamics and kinetics of binding to measuring the degree of CNT debundling. Measuring nanotube debundling directly in solution is an innovative approach, which avoids drying effects that can be found when analyzing CNT bundles using microscopy. This work could be an important step to a more rational supramolecular chemistry of carbon nanotubes, because it gives quantitative information on binding processes which is crucial for comparison of different systems and should enable systematic engineering of new molecules for the binding of CNTs.

The formation of a carbon nanotube based pseudo-polyrotaxane remains an attractive target that merits further research. The length of the nanotube and its diameter are two parameters that appear crucial in this context. The use of smaller diameter CNTs should make it easier for the nanorings to slip onto the nanotube, and the use of chemically cut ultra-short CNTs[52] would make it more likely to achieve an appreciable loading of rings and good solubility. Selective functionalization of the nanotubes rims would allow the installation of bulky stopper groups to form a true rotaxane.[53]

6.5 References

[1] S. Iijima, *Nature* **1991**, *354*, 56–58.
[2] R. H. Baughman, A. A. Zakhidov, W. A. de Heer, *Science* **2002**, *297*, 787–792.
[3] K. Awasthi, A. Srivastava, O. N. Srivastava, *arXiv:cond-mat/0505526v1*.
[4] M. C. Hersam, *Nat. Nanotechnol.* **2008**, *3*, 387–394.
[5] T. W. Ebbesen, P. M. Ajayan, *Nature* **1992**, *358*, 220–222.
[6] T. Guo, P. Nikolaev, A. G. Rinzler, D. Tomanek, D. T. Colbert, R. E. Smalley, *J. Phys. Chem.* **1995**, *99*, 10694–10697.
[7] M. J. Bronikowski, P. A. Willis, D. T. Colbert, K. A. Smith, R. E. Smalley, *J. Vac. Sci. Technol. A* **2001**, *19*, 1800–1805.
[8] G. Lolli, L. Zhang, L. Balzano, N. Sakulchaicharoen, Y. Tan, D. E. Resasco, *J. Phys. Chem. B* **2006**, *110*, 2108–2115.
[9] B. D. Steinberg, L. T. Scott, *Angew. Chem. Int. Ed.* **2009**, *48*, 5400–5402.
[10] Y. Segawa, S. Miyamoto, H. Omachi, S. Matsuura, P. Šenel, T. Sasamori, N. Tokitoh, K. Itami, *Angew. Chem. Int. Ed.* **2011**, *50*, doi:10.1002/anie.201007232.
[11] E. H. Fort, L.T. Scott, *Angew. Chem. Int. Ed.* **2010**, *49*, 6626–6628.
[12] X. Peng, N. Komatsu, S. Bhattacharya, T. Shimawaki, S. Aonuma, T. Kimura, A. Osuka, *Nat. Nanotechnol.* **2007**, 2, 361–365.
[13] P. R. Wallace, *Phys. Rev.* **1947**, *71*, 622–634.
[14] R. Saito, M. Fujita, G. Dresselhaus, M. S. Dresselhaus, *Appl. Phys. Lett.* **1992**, *60*, 2204–2206.
[15] P. Kim, T. W. Odom, J.-L. Huang, C. M. Lieber, *Phys. Rev. Lett.* **1999**, *82*, 1225–1228.
[16] R. B. Weisman, S. M. Bachilo, *Nano. Lett.* **2003**, *3*, 1235–1238.
[17] S. M. Bachilo, M. S. Strano, C. Kittrell, R. H. Hauge, R. E. Smalley, R. B. Weisman, *Science* **2002**, *298*, 2361–2366.

[18] A. Bachtold, M. S. Fuhrer, S. Plyasunov, M. Forero, E. H. Anderson, A. Zettl, P. L. McEuen, *Phys. Rev. Lett.* **2000**, *84*, 6082–6085.

[19] X. Zhou, J.-Y. Park, S. Huang, J. Liu, P. L. McEuen, *Phys. Rev. Lett.* **2005**, *95*, 146805.

[20] P. Prins, F. C. Grozema, J. M. Schins, S. Patil, U. Scherf, L. D. A. Siebbeles, *Phys. Rev. Lett.* **2006**, *96*, 146601.

[21] C. Kocabas, M. Shim, J. A. Rogers, *J. Am. Chem. Soc.* **2006**, *128*, 4540–4541.

[22] S. Hong, S. Myung, *Nat. Nanotechnol.* **2007**, 2, 207–208.

[23] E. Pop, D. Mann, Q. Wang, K. Goodson, H. Dai, *Nano. Lett.* **2006**, *6*, 96–100.

[24] M.-F. Yu, B. S. Files, S. Arepalli, R. S. Ruoff, *Phys. Rev. Lett.* **2000**, *84*, 5552–5555.

[25] D. Tasis, N. Tagmatarchis, A. Bianco, M. Prato, *Chem. Rev.* **2006**, *106*, 1105–1136.

[26] D. A. Britz, A. N. Khlobystov, *Chem. Soc. Rev.* **2006**, *35*, 637–659.

[27] F. Wang, Y. Yang, T. M. Swager, *Angew. Chem. Int. Ed.* **2008**, *47*, 8394–8396.

[28] D. A. Heller, H. Jin, B. M. Martinez, D. Patel, B. M. Miller, T.-K. Yeung, P. V. Jena, C.Höbartner, T. Ha, S. K. Silverman, M. S. Strano, *Nat. Nanotechnol.* **2009**, *4*, 114–120.

[29] D. R. Kauffman, A. Star, *Chem. Soc. Rev.* **2008**, *37*, 1197–1206.

[30] Chaudhary, H. Lu, A. M. Müller, C. J. Bardeen, M. Ozkan, *Nano Lett.* **2007**, *7*, 1973–1979.

[31] M. W. Rowell, M. A. Topinka, M. D. McGehee, H.-J. Prall, G. Dennler, N. S. Sariciftci, L. Hu, G. Gruner, *Appl. Phys. Lett.* **2006**, *88*, 233506.

[32] D. M. Guldi, G. M. A. Rahman, F. Zerbretto, M. Prato, *Acc. Chem. Res.* **2005**, *38*, 871–878.

[33] J. Bartelmess, B. Ballesteros, G. de la Torre, D. Kiessling, S. Campidelli, M. Prato, T. Torres, D. M. Guldi, *J. Am. Chem. Soc.* **2010**, *132*, 16202–16211.

[34] E. Maligaspe, A. S. D. Sandanayaka, T. Hasobe, O. Ito, F. D'Souza, *J. Am. Chem. Soc.* **2010**, *132*, 8158–8164.

[35] F. Cheng, A. Adronov, *Chem. Eur. J.* **2006**, *12*, 5053–5059.

[36] M. U. Winters, J. Kärnbratt, M. Eng, C. J. Wilson, H. L. Anderson, B. Albinsson, *J. Phys. Chem. C* **2007**, *111*, 7192–7199.

[37] H. L. Anderson, *Inorg. Chem.* **1994**, *33*, 972–981.

[38] P. N. Taylor, H. L. Anderson, *J. Am. Chem. Soc.* **1999**, *121*, 11538–11545.

[39] A. Nish, J.-Y. Hwang, J. Doig, R. J. Nicholas, *Nat. Nanotechnol.* **2007**, *2*, 640–646.

[40] P. H. Tan, A. G. Roshin, T. Hasan, P. Hu, V. Scardaci, W. I. Milne, A. C. Ferrari, *Phys. Rev. Lett.* **2007**, *99*, 137402.

[41] K. Hirose, in *Analytical methods in supramolecular chemistry*, (Ed: C. A. Schalley), WILEY-VCH, Weinheim, **2007**, pp. 17–54.

[42] S.-Y. Ju, J. Doll, I. Sharma, F. Papadimitrakopoulos, *Nat. Nanotechnol.* **2008**, *3*, 356–362.

[43] J. L. Bahr, E. T. Mickelson, M. J. Bronikowski, R. E. Smalley, J. M. Tour, *Chem. Commun.* **2001**, 193–194.

[44] D. S. Kim, D. Nepal, K. E. Geckeler, *Small* **2005**, *11*, 1117–1124.

[45] J. K. Sprafke, S. D. Stranks, J. H. Warner, R. J. Nicholas, and H. L. Anderson, *Angew. Chem.* Int. *Ed.* **2011**, *50*, 2313–2316.

[46] T. Schuettfort, A. Nish, R. J. Nicholas, *Nano Lett.* **2009**, *9*, 3871–3876.

[47] L. Yang, J. Han, *Phys. Rev. Lett.* **2000**, *85*, 154–157.

[48] L. J. Li, R. J. Nicholas, R. S. Deacon, P. A. Shields, *Phys. Rev. Lett.* **2004**, *93*, 156104.

[49] R. S. Deacon, K. C. Chuang, J. Doig, I. B. Mortimer, R. J. Nicholas, *Phys. Rev. B* **2006**, *74*, 201402.

[50] S. D. Stranks, J. K. Sprafke, H. L. Anderson, and R. J. Nicolas, *ACS Nano*, **2011**, *5*, 2307–2315.

[51] A. Ortiz-Acevdeo, H. Xie, V. Zorbas, W. M. Sampson, A. B. Dalton, R. H. Baughman, R. K. Draper, I. H. Musselman, G. R. Dieckmann, *J. Am. Chem. Soc.* **2005**, *127*, 9512–9517.

[52] Z. Gu, H. Peng, R. H. Hauge, R. E. Smalley, J. L. Margrave, *Nano Lett.* **2002**, *2*, 1009–1013.

[53] Y. Weizmann, J. Lim, D. M. Chenoweth, T. M. Swager, *Nano Lett.* **2010**, *10*, 2466–2469.

Chapter 7

Hydrogen-bonded Porphyrin Assemblies

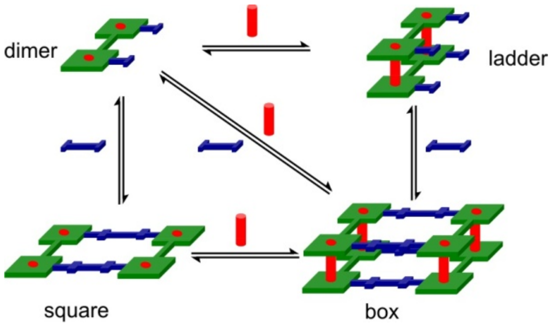

In this chapter the potential of hydrogen bonds and salt bridges for the formation of novel supramolecular architectures based on butadiyne-linked porphyrin oligomers is explored. Porphyrin dimers bearing lateral carboxylic acid groups can assemble into square, ladder or box shaped complexes by combining Zn-N coordination with amidinium-carboxylate salt bridge formation. The assemblies are characterized by ^{1}*H NMR, diffusion ordered NMR and small angle X-ray scattering. UV/vis absorption demonstrates the efficiency of square and box formation in rigidifying and planarizing the porphyrin dimer. At the end of the chapter the attempted formation of supramolecular nanotubes based on the stacking of the [6]porphyrin nanoring is described.*

7.1 Background

Chapters 2 and 3 discussed the monodisperse synthesis of very large molecules with dimensions on the nanometer scale and molecular weights over 10 kDa. In order to create even larger structures from these molecular components, or to interface them with other molecules or materials, it is important to understand and control their self-assembly behavior. Control over intermolecular interactions could also allow tuning of the bulk properties required for the development of these molecules into functional materials. Zn-N coordination chemistry (Chapters 2–4) and π-π interactions (Chapter 6) have been used in previous chapters to create supramolecular assemblies based on butadiyne-linked porphyrin oligomers. The use of more than one type of supramolecular interaction is advantageous for attaining high degrees of structural complexity in self-organized materials. It is an important prerequisite that these interactions are orthogonal, i.e. non-interacting and self-consistent,[1] in order to produce well-defined assemblies.[2] Examples of such compatible non-covalent or reversible covalent interactions include metal-ligand coordination paired with either ion-dipole interactions,[1] reversible covalent bonds[3] or hydrogen bonding.[4] Hydrogen bonds are ubiquitous in biological systems and are widely used in supramolecular chemistry because of their strength, tunability and directionality.[5] Amidines form particularly strong hydrogen bonds with carboxylic acids because of an additional ionic component to the interaction. The basic amidines usually deprotonate the carboxylic acids leading to the formation of amidinium-carboxylate salt bridges analogous to the guanidinium-carboxylate interaction found in biological systems.[6] In synthetic supramolecular systems the amidinium-carboxylate motif has been used in the assembly of chiral double helices,[7,8] capsules,[9,10] donor-acceptor systems[11,12] and also in crystal engineering (Figure 7.1).[13] Yashima has reported that Zn-N interactions and amidinium-carboxylate salt bridges are orthogonal in self-assembled capsules.[10]

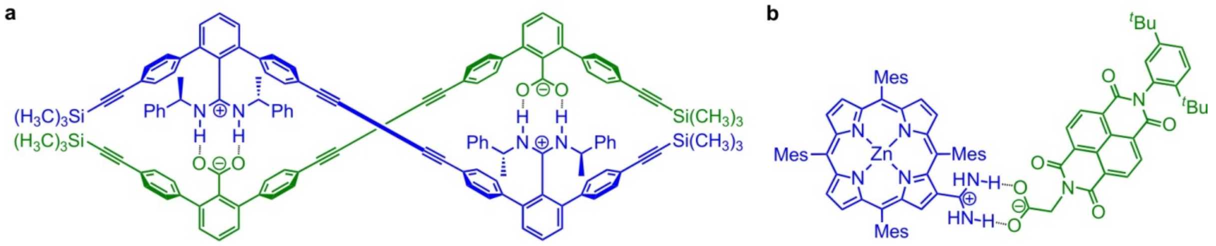

***Figure 7.1** Examples for amidinium-carboxylate salt bridges. (a) Self-assembled short chiral double helix;[8] (b) donor-acceptor system between a zinc porphyrin and a naphthalene diimide derivative.[15]*

Many synthetic supramolecular dye, and particularly porphyrin, assemblies have been designed as models of natural light-harvesting complexes. Nocera[11,14,15] and others]12,16-18] have studied electron transfer through amidinium carboxylate salt bridges and other hydrogen bonded systems in porphyrin based assemblies and found that electron transfer is more efficient in hydrogen bonded systems than in covalently linked (σ- or π-bond) systems.

All the properties listed above (strong binding, directionality, orthogonality with Zn-N coordination, efficient electron transfer) make amidinium-carboxylate salt bridges promising candidates for use in the self-assembly of linear and cyclic butadiyne-linked porphyrin oligomers.

7.2 Hydrogen-Bonded Squares and Boxes

In order to trial the use of amidinium-carboxylate salt bridges in the assembly of porphyrin oligomers, a porphyrin dimer was selected because it is readily accessible by established synthetic routes and its self-assembly behavior, using Zn-N or π-π interactions, is well understood.[19,20] A modular approach, similar to the assembly of porphyrin ladders (Chapers 1 and 4), where self-assembly is triggered by the addition of a small molecule linker, allows for greater synthetic flexibility and control over the binding processes. The higher entropy of such a process in comparison to a direct connection, as in Yashima's helices (Figure 7.1a), is often compensated by a large chelate cooperativity.[19]

Porphyrin dimer ***l*-P2ac** (Figure 7.2) bears lateral carboxylic acid groups that can act as proton donors in the formation of amidinium-carboxylate salt bridges. Addition of a rigid linear bis-amidine linker such as 1,2-benzenebis(*N*,*N*'-dicyclohexylamidine) **BA** should result in the formation of the square shaped complex (***l*-P2ac**)$_2$•(**BA**)$_2$. If a bidentate *N*-terminated ligand such as 1,4-diazabicyclo[2.2.2]octane (DABCO) is added to ***l*-P2ac** the two-rung ladder complex (***l*-P2ac**)$_2$•(DABCO)$_2$ is expected to form as shown previously for ***l*-P2** and ***l*-P2$_{\mathbf{C8}}$**.[19,20] The orthogonality between Zn-N coordination and the salt bridges should allow the combination of the two processes and lead to formation of a 12-component assembly, the box shaped complex (***l*-P2ac**)$_4$•(**BA**)$_4$•(DABCO)$_4$ (Figure 7.2).

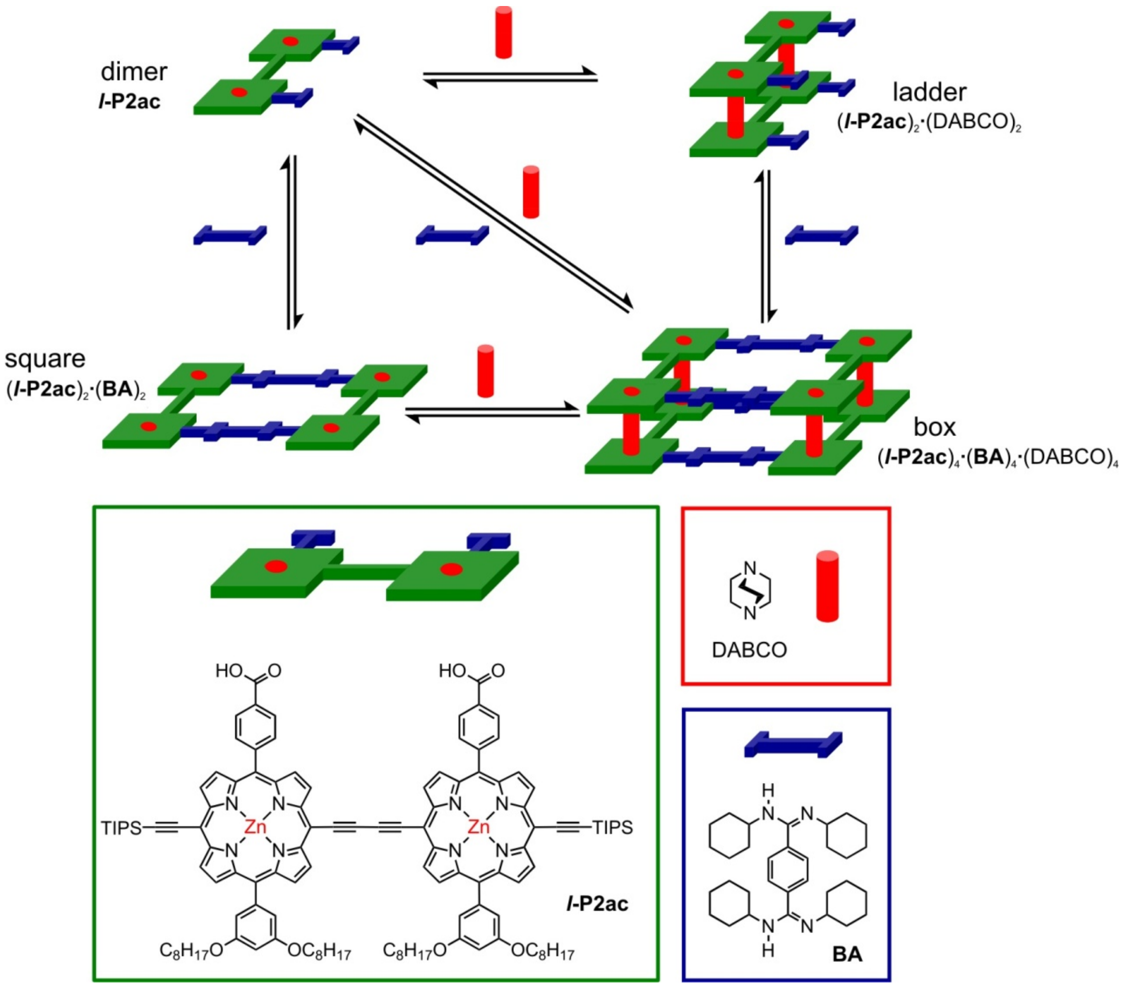

Figure 7.2. *Self-assembly of square, ladder and box shaped complexes from porphyrin dimer **l-P2ac** and bidentate ligands DABCO and bisamidine **BA**.*

The bidentate linkers required for formation of the various complexes are both easily accessible: while DABCO is commercially available, the bisamidine linker **BA** was synthesized in a one-pot-reaction by lithiation of *p*-dibromobenzene followed by addition of dicyclohexylcarbodiimide (DCC) and subsequent conversion of the lithium salt to the bisamidine with water (Scheme 7.1a).[21] This cyclohexyl substituted amidine was chosen for three reasons: 1) the cyclohexyl group increases solubility in organic solvents, 2) the greater bulkiness and higher rigidity of the cyclohexyl group compared to a linear alkyl chain should reduce coordination of the amidines to the Zn-centers of the porphyrins and improve the orthogonality to DABCO binding and 3) DCC is a widely used coupling reagent and thus commercially available, while the synthesis of tailored carbodiimides requires several synthetic steps.

The porphyrin precursor for formation of dimer ***l*-P2ac** was synthesized by statistical co-condensation of 3,5-bis-(octyloxy) benzaldehyde **2a** and triethyleneglycol-monomethyl-ether-4-formylbenzoate **1** with dipyrromethane **1** (Scheme 7.1c). The acid group was protected as the triethyleneglycol (TEG) ester throughout the synthesis in order to improve solubility and to ease purification by silica chromatography. This was particularly helpful in the synthesis of free base porphyrin **2** because the other statistical products move either much faster (two bis-(octyloxy) phenyl groups) or slower (two TEG ester groups) on silica.

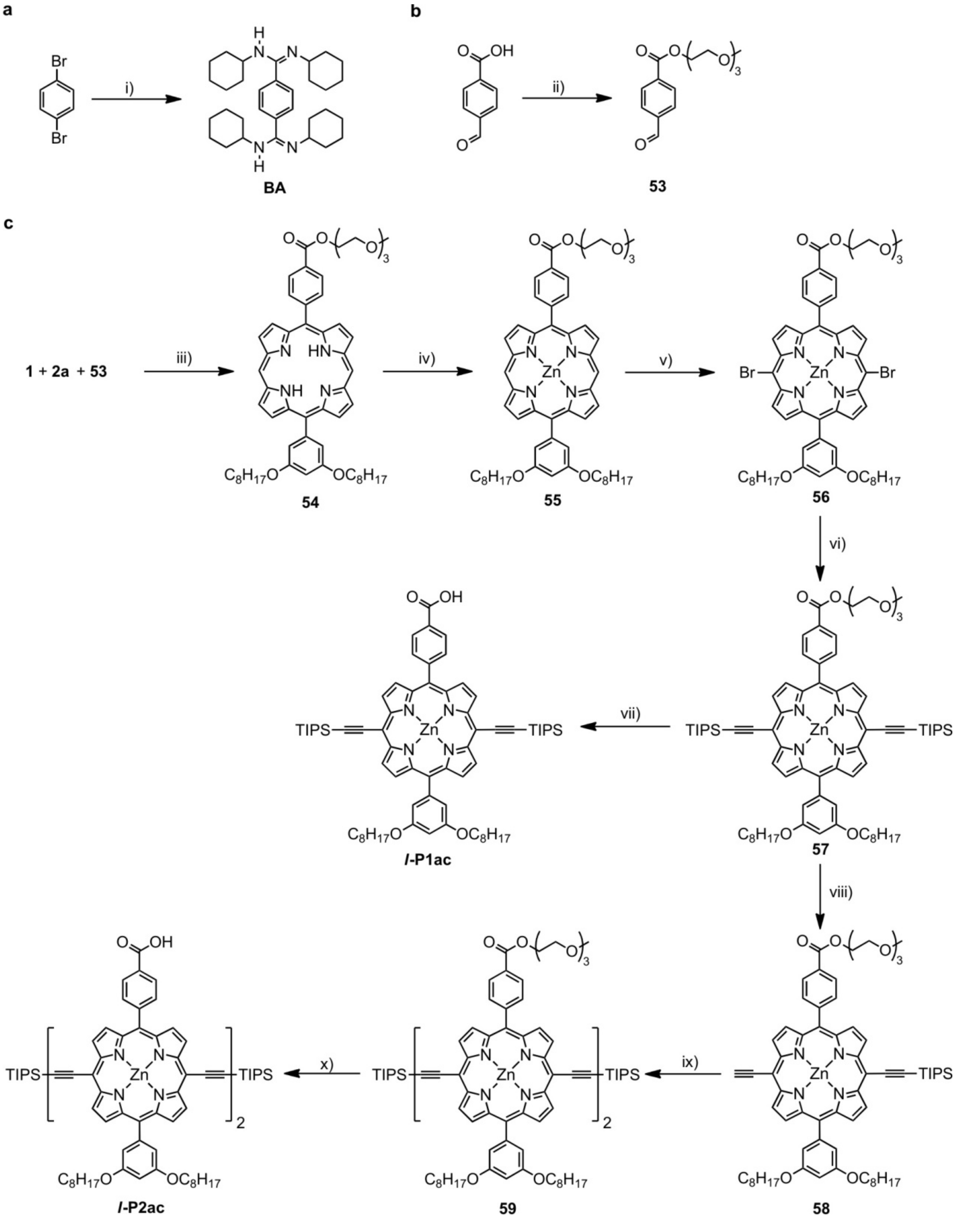

Scheme 7.1 *Synthesis of (a) 1,2-benzenebis(N,N'-dicyclohexylamidine)* ***BA****; (b) triethyleneglycol-monomethyl-ether-4-formylbenzoate* ***1****; (c) carboxylic acid functionalized porphyrin monomer* ***l-P1ac*** *and dimer* ***l-P2ac****; TIPS stands for triisopropylsilyl. Reagents and conditions: i) n-BuLi, then DCC, then H_2O (45%); ii) triethylene glycol monomethyl ether, EDC, DMAP (95%); iii) TFA, then DDQ (23%); iv) $Zn(OAc)_2$ (99%); v) NBS (97%); vi) (triisopropylsilyl)acetylene, $Pd(OAc)_2$, PPh_3, CuI, NEt_3 (91%); vii) NaOH (86%); viii) TBAF (39%); ix) CuCl, TMEDA (75%); x) NaOH (78%).*

Free base porphyrin **54** was converted to its zinc complex **55** and then brominated using NBS in excellent yields. Sonogashira coupling with triisopropylsilyl (TIPS) acetylene afforded porphyrin monomer **57** that was converted into model compound ***l*-P1ac** by basic ester hydrolysis with NaOH. TIPS protecting groups were used to cap the acetylenes because in initial trials trihexylsilyl (THS) groups were found to be unstable towards the basic ester hydrolysis conditions. Statistical TIPS deprotection of porphyrin monomer **57** using TBAF gave mono-deprotected monomer **58** that was converted to dimer **59** by Glaser coupling. The final basic ester hydrolysis step proceeded smoothly in good yields to give dimer ***l*-P2ac**.

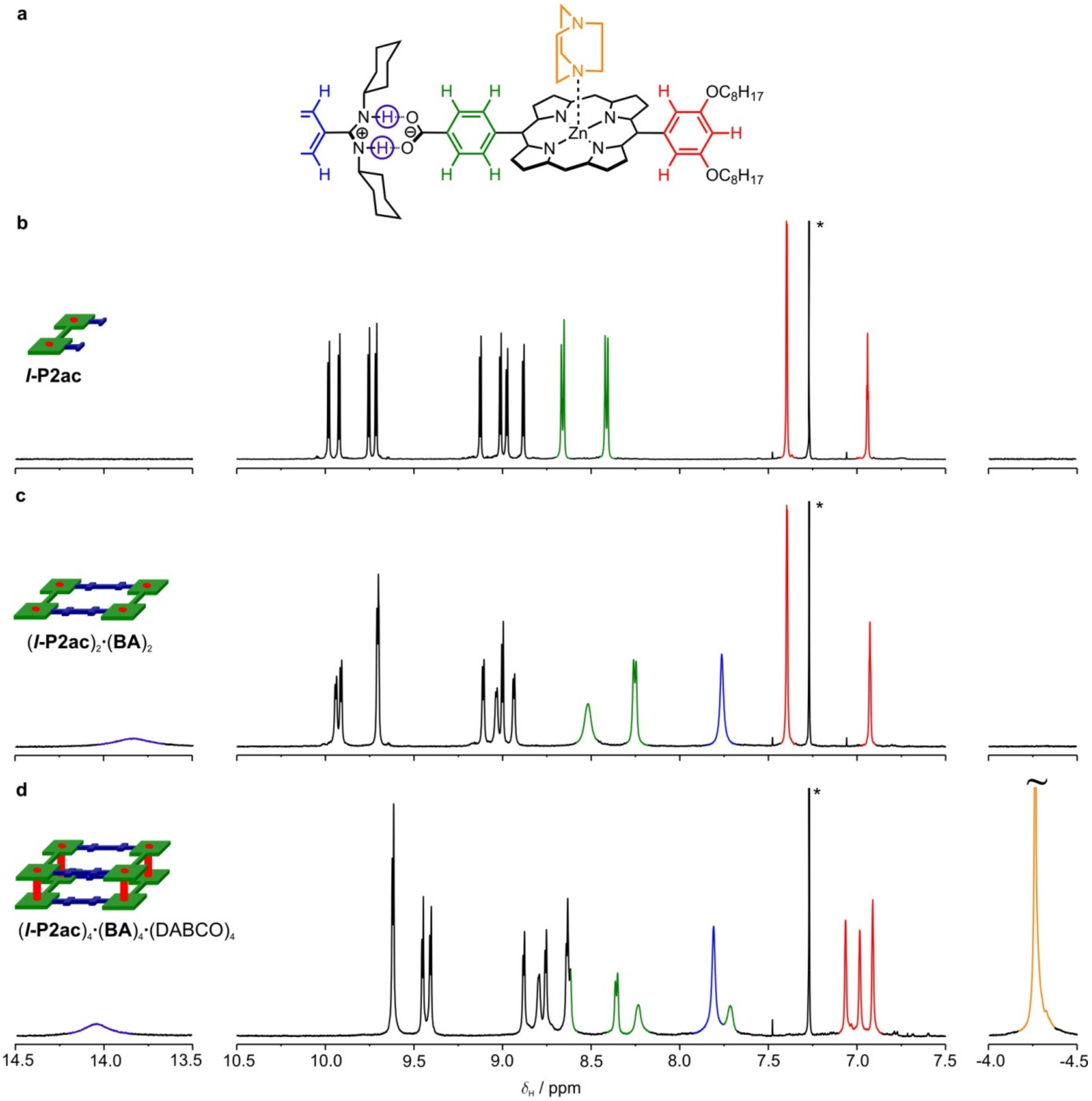

Figure 7.3. *^{1}H NMR spectra of **l-P2ac** assemblies (CDCl$_3$, 500 MHz, 298 K). (a) Structure of 1/8 of the box structure; (b) spectrum of dimer **l-P2ac** with a stoichiometric amount of d_5-pyridine to prevent aggregation; (c) spectrum of square complex (**l-P2ac**)$_2$·(**BA**)$_2$ with a stoichiometric amount of d_5-pyridine to prevent aggregation; (d) spectrum of box complex (**l-P2ac**)$_4$·(**BA**)$_4$·(DABCO)$_4$. The asterisks in all spectra mark the solvent peak (CHCl$_3$).*

The lower local symmetry of the **_l_-P2ac** porphyrin macrocycles compared to dimers **_l_-P2** and **_l_-P2$_{C8}$** results in the appearance of eight doublets from the eight β-pyrrole protons (Figure 7.3b). Addition of 1 equivalent of **BA** does not significantly shift these peaks, however two new peaks can be observed at low magnetic fields: a singlet at δ_H = 7.8 ppm (blue) due to the phenyl protons of the bisamidine and more importantly a broad peak at 13.8 ppm (purple) that is indicative of an amidine NH-proton in a salt bridge (Figure 7.3c).[10] Formation of the box complex (**_l_-P2ac**)$_4$·(**BA**)$_4$·(DABCO)$_4$ by addition of DABCO results in the appearance of a peak -4.1 ppm that can be assigned to the protons of a molecule of DABCO bound between two porphyrins.[20,22] The two faces of the porphyrin macrocycle become inequivalent in the box complex and thus aryl protons pointing towards the inside and the outside of the box now lead to different signals: the number of aryl alkoxy signals (red) increases from two to three and the number of aryl carboxylate signals (green) grows from two to four (Figure 7.3d). It is worth noting that the addition sequence of the ligands is irrelevant for formation of the complexes. In UV/vis experiments the final spectrum was identical when the components were added in any order, implying that the system rapidly reaches thermodynamic equilibrium.

Formation of the square complex (**_l_-P2ac**)$_2$·(**BA**)$_2$ was confirmed by small angle X-ray scattering (SAXS) acquired in toluene at Diamond Light Source, UK. All three indicators, the radius of gyration, the scattering data (Figure 7.4a) and the pair distribution function (Figure 7.4c), are reproduced well by data simulated from the molecular model shown in Figure 7.4b. The solubility of the box complex in toluene was insufficient to acquire SAXS data.

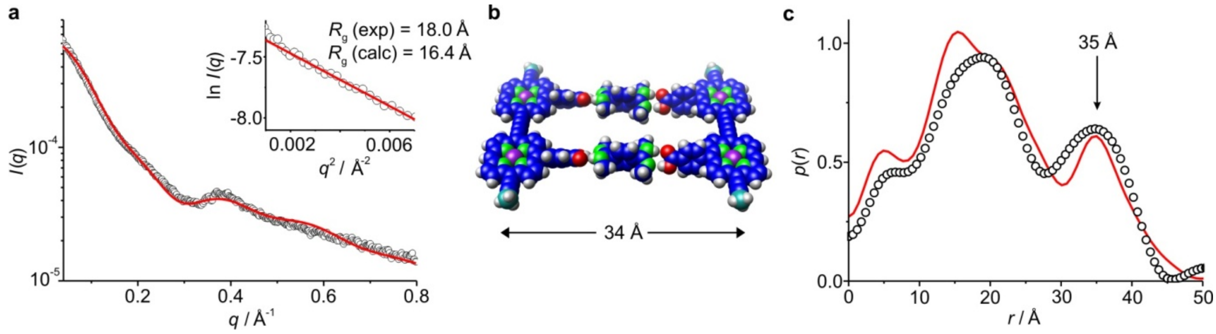

Figure 7.4. *SAXS data of the square complex (**l-P2ac**)$_2$·(**BA**)$_2$ acquired in toluene at 298 K at Diamond Light Source, UK. (a) Scattering data (black circles) with simulated data from a molecular model (red line); the inset shows a Guinier fit to the experimental scattering data at very small angles that was used to obtain the radius of gyration; (b) molecular model calculated using the MM+ force field implemented in the HyperChem^{TM} package (the arrow indicates the Zn-Zn distance of two opposite Zn atoms); (c) pair-distribution functions determined from experimental scattering data (black circles) and from the molecular model (red line).*

Diffusion ordered NMR spectroscopy (DOSY) allows the determination of the diffusion coefficient D that depends on the volume and shape of a molecule or an assembly.[23] If the shape of a series of assemblies is similar, the diffusion coefficient decays exponentially with the molecular mass of the assemblies (see Chapter 4 and ref 23). Dr. Barbara Odell (Oxford, NMR) measured DOSY spectra of all assemblies shown in Figure 7.2 (dimer, square, ladder and box) and the equivalent structures formed from porphyrin monomer ***l*-P1ac** (except the DABCO sandwich). In Figure 7.5 the resulting diffusion coefficients are plotted against the molecular weights of the complexes. The planar complexes (monomer, dimer, salt bridged monomer and square) fit well to an exponential decay, but the diffusion coefficients of the DABCO complexes (monomer and dimer based boxes) are larger than expected from this fit. This behavior, which was also observed in the case of the [12]porphyrin nanoring sandwich complex (Chapter 4), can be explained by the compactness of the DABCO complexes that results in the diffusion coefficients underestimating the molecular weight. Overall, the DOSY data confirm the formation of the various assemblies.

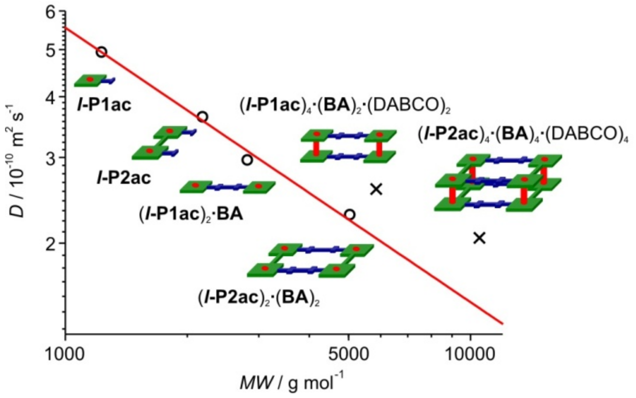

Compound	D / 10^{-10} m^2 s^{-1}
***l*-P1ac**	4.94
***l*-P2ac**	3.64
(***l*-P1ac**)$_2$·**BA**	2.97
(***l*-P2ac**)$_2$·(**BA**)$_2$	2.29
(***l*-P1ac**)$_4$·(**BA**)$_2$·(DABCO)$_2$	2.58
(***l*-P2ac**)$_4$·(**BA**)$_4$·(DABCO)$_4$	2.05

Figure 7.5. *Diffusion coefficients of porphyrin assemblies plotted against their molecular weight. An exponential decay was fitted to data from assemblies without DABCO (red line, $D = 272 \times 10^{-10}\ MW^{-0.56}$). In these samples a stoichiometric amount of d_5-pyridine was present to avoid aggregation. All DOSY spectra were acquired by Dr. Barbara Odell using the double stimulated echo sequence (DSTE) with a total diffusion time Δ = 100 ms and gradient pulse duration δ = 5 ms (500 MHz, $CDCl_3$, 298 K).*

Formation of square, ladder or box assemblies restricts the free rotation around the butadiyne-linker between the two porphyrin macrocycles of dimer ***l*-P2ac**. The resulting increased π-overlap leads to an increase in intensity of the most red-shifted component of the Q absorption band.[24] The rigidity and efficiency of planarization can thus be qualitatively evaluated by the absorption spectra.

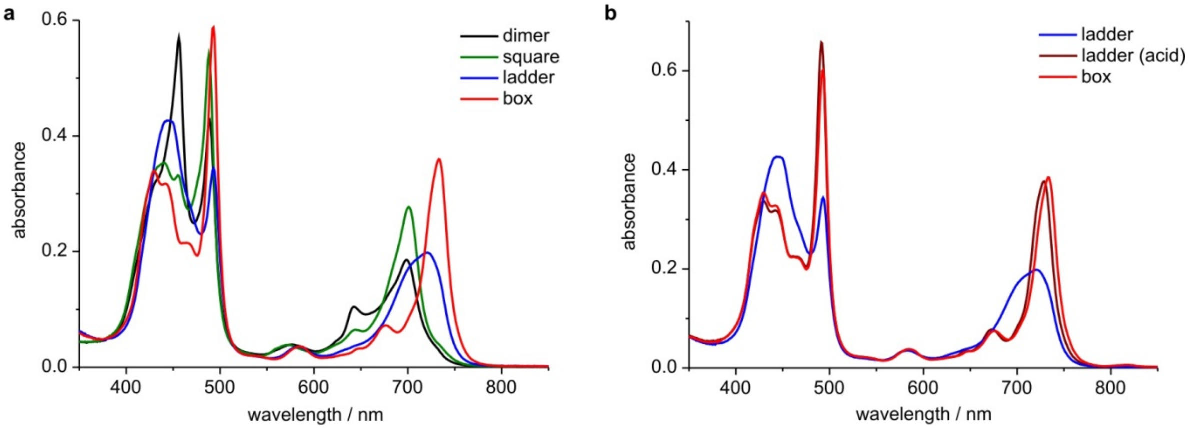

Figure 7.6. *UV/vis/NIR absorption spectra of porphyrin assemblies in $CHCl_3$. (a) Spectra of dimer **l-P2ac**, square complex (**l-P2ac**)$_2$·(**BA**)$_2$ and ladder complex (**l-P2ac**)$_2$·(DABCO)$_2$ in the presence of a large excess of bisamidine and box complex (**l-P2ac**)$_4$·(**BA**)$_4$·(DABCO)$_4$; (b) spectra of ladder complex (**l-P2ac**)$_2$·(DABCO)$_2$, ladder complex with carboxylic acid binding (**l-P2ac**)$_2$·(DABCO)$_2$ and box complex (**l-P2ac**)$_4$·(**BA**)$_4$·(DABCO)$_4$.*

Addition of **BA** to porphyrin dimer ***l*-P2ac** leads to a significant sharpening of the longest wavelength component of the Q absorption band, indicating efficient planarization. This sharpening effect is significantly reduced in the ladder complex† which is unsurprising as it has been suggested that the porphyrin dimers in this complex are significantly twisted.[20] The sharpest and most intense Q band is observed in the box complex due to its high rigidity and the planarity of the porphyrin dimers. (Figure 7.6a).

An important question about these complexes is whether the presence of the bisamidine linker is absolutely necessary for complex formation or whether the square and box complexes could also be formed simply by carboxylic acid dimerization. In dimer ***l*-P2ac** only a small population of hydrogen bonded square complex is present at μM concentrations because the absorption sharpens significantly upon addition of the bisamidine, indicating a transition from free to restricted rotation in the dimer. When comparing the spectra of the ladder complex with 'free' carboxylic acids and the ladder complex with an excess bisamidine (to suppress carboxylic acid dimerization) a dramatic difference is observed: whilst the spectrum of the non-hydrogen bonded ladder is broad, the Q band of the hydrogen bonded ladder complex is significantly sharper and very similar to the spectrum of the box complex (Figure 7.6c). This is a clear indication of the presence of a hydrogen bonded box complex. The reason why the hydrogen bonded complex can form in this case, but does not form a square, lies within the increased number of interactions and probably the presence of chelate cooperativity between the carboxylic acid groups: in the box assembly four pairs of carboxylic acids are binding, whereas only two pairs are binding to form a hydrogen-bonded square.

7.3 Towards Self-Assembled Porphyrin Nanotubes

Having demonstrated the value of amidinium-carboxylate salt bridges and carboxylic acid dimerization in the formation of hydrogen-bonded assemblies based on dimer ***l*-P2ac**, we aimed to extend this strategy to create tubular structures from cyclic oligomers such as the [6]porphyrin nanoring. Cyclic hexamer ***c*-P6ac** (Scheme 7.2, the analogue of dimer ***l*-P2ac**) has carboxylic acids on one rim and should form a short 'dimeric tube' by hydrogen bonding or salt bridge formation (Figure 7.7a). Extended to larger rings, where no radial templates are available, the formation of a self-supported ring dimer could be a method to rigidify nanorings and fix the torsional angles between the individual porphyrin units (as demonstrated for the sandwich complexes in Chapter 4). Cyclic hexamer ***c*-P6ac$_2$** bearing carboxylic acids on both rims could self-assemble into infinite tubes held together by hydrogen bonds or salt bridges. Many examples of such self-assembled nanotubes based on the stacking of nanorings exist[25,26] and they have found applications as artificial trans-membrane

---

† The absorption spectrum of this ladder complex was recorded in the presence of a large excess bisamidine in order to prevent hydrogen bonding between the carboxylic acid groups.

ion channels,[27] molecular reaction vessels,[28] templates for dye assemblies[29] and microporous solids.[30] Two porphyrin based nanorings have been equipped with hydrogen bonding sites at the rims, but either no[31] or only limited[32] tube formation was observed.

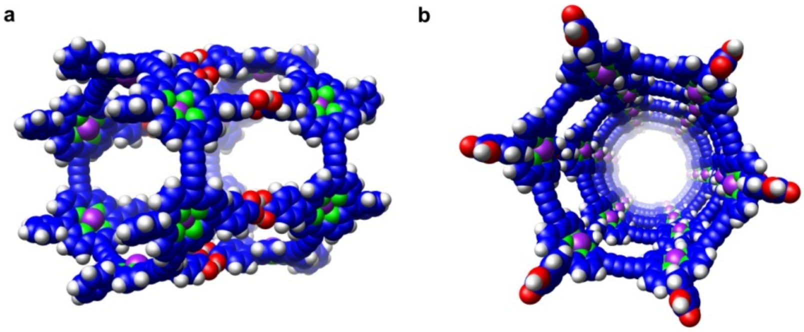

Figure 7.7. *Molecular models of self-assembled porphyrin nanotubes based on carboxylic acid dimerization. (a) Short 'dimeric tube' consisting of two nanorings* ***c-P6ac****; (b) view down an infinite tube from nanoring* ***c-P6ac*** $_2$*. Both models were calculated using the MM+ force field implemented in HyperChem*^{TM}*.*

Porphyrin dimer **67a**, the precursor for formation of nanoring ***c*-P6ac**, was synthesized by an identical route as dimer **59** (the precursor for ***l*-P2ac**) but trihexylsilyl (THS) groups were used instead of TIPS to protect the terminal acetylenes (Scheme 7.2). Deprotection of the THS groups using TBAF as a fluoride source was followed by palladium catalyzed cyclization around template **T6**. The template was then removed on a size-exclusion column using the competing ligand DABCO to yield the TEG-ester protected nanoring **69a**. The nanoring ***c*-P6ac**$_2$, with twelve carboxylic acid groups should be accessible in a similar way. The carboxylic acid groups in the precursor porphyrins were protected by formation of the octyl-ester which should be hydrolyzed in the final step of the synthesis. However, the attempted synthesis of the corresponding nanoring template complex **69b·T6** yielded only products with very low solubility. In order to achieve higher solubility of the nanoring, the branched 2-hexyldecyl chain was used instead of the octyl chain. Synthesis of the corresponding dimer **67c** was performed in two ways: by titanate-mediated transesterification of the octyl-ester protected dimer **67b** and by the synthesis from the basic building blocks dipyrromethane **1** and 2-hexyldecyl-4-formylbenzoate **61** according to the previously described synthetic strategy shown in Scheme 7.2. The synthesis of dimer **67c** by the latter route was carried out with Markus Döbbelin (visiting student from CIDETEC, Spain). The dimer was converted to the free nanoring **69c** as described above.

With both ester protected nanorings **69a** and **69c** in hand, basic hydrolysis applying the same conditions used for the synthesis of dimer ***l*-P2ac** was performed. However, after aqueous work-up the products were found to be completely insoluble in organic solvents and water, as both the carboxylic acid and the sodium carboxylate salt. Addition of an excess of bisamidine **BA** did not improve the solubility and due to time-constraints no additional experiments were carried out. Future attempts to improve the solubility of the nanorings could rely on the variation of the counterion in the carboxylate salts or the attachment of solubilizing groups to the phenyl carboxylate rings which would require significant synthetic effort.

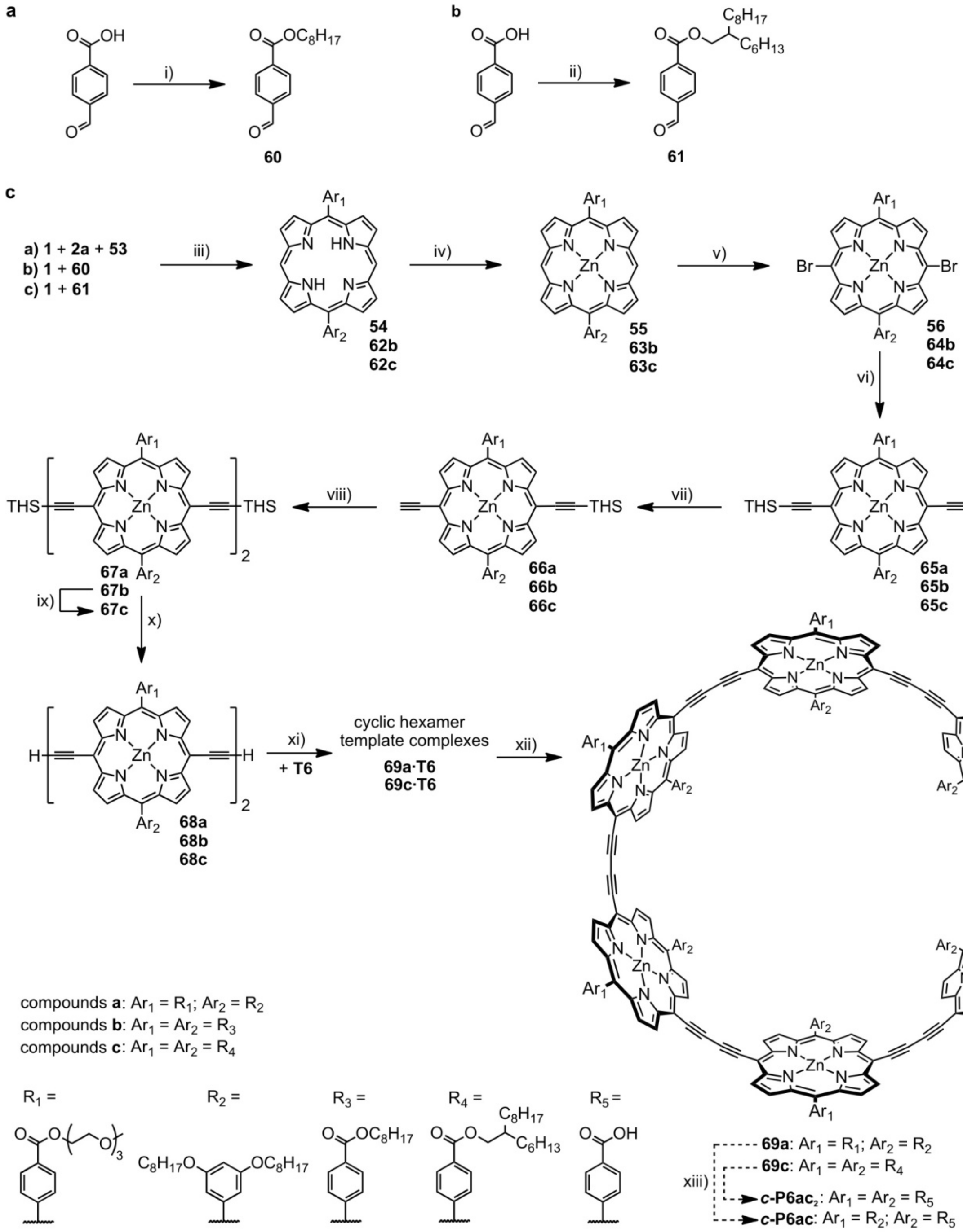

Scheme 7.2. *Synthesis of a) octyl-4-formylbenzoate* ***60****; (b) 2-hexyldecyl-4-formylbenzoate* ***61****; (c) porphyrin nanorings* ***69a*** *and* ***69c****; THS stands for trihexylsilyl. Reagents and conditions (yields are in the order a/b/c): i) 1-bromooctane, K_2CO_3 (88%); ii) 2-hexyl-1-decanol, EDC, DMAP (78%); iii) TFA, then DDQ, (22%/33%/38%); iv) $Zn(OAc)_2$ (97%/99%/98%); v) NBS (96%/98%/98%); vi) (trihexylsilyl)acetylene, $Pd(OAc)_2$, PPh_3, CuI, NEt_3 (77%/78%/90%); vii) TBAF, (38%/42%/22%); viii)* ***67a/b****: CuCl, TMEDA (73%/88%);* ***67c****: $PdCl_2(PPh_3)_2$, CuI, 1,4-benzoquinone, i-Pr_2NH (73%); ix) 2-hexyl-1-decanol, $Ti(i\text{-}OPr)_4$,97%; x) TBAF (80%/80%/98%); xi)* ***69a·T6****: $PdCl_2(PPh_3)_2$, CuI, I_2, i-Pr_2NH (32%);* ***69c·T6****: $PdCl_2(PPh_3)_2$, CuI, 1,4-benzoquinone, i-Pr_2NH (47%); xii) DABCO (87%/86%); xiii) NaOH.*

7.4 Conclusions and Outlook

Initial experiments on hydrogen-bonded porphyrin oligomers indicate that a wealth of structures and topologies is accessible by combining Zn-N coordination chemistry and hydrogen bondings or saltbridges. The bisamidine linker **BA** introduced here may be useful for supramolecular self-assembly of any molecular components bearing carboxylic acids because of its high binding strength and directionality. Future work on the assemblies based on dimer ***l*-P2ac** may include a detailed analysis of the equilibria that govern formation of the various complexes. The concept of square and box formation could be extended to achieve efficient planarization of longer oligomers or polymers with the perspective of extending the well-studied double strand formation to quadruple strand formation. Such polymer quadruple strands should be very efficient in transporting charges over long distances because the porphyrin units in each strand would be completely co-planar and a defect in one strand could be compensated by the other strands, extending the concept of a molecular wire to a ‘molecular cable’.

The results reported in the first section on square formation could also open a different approach to the synthesis of the short ‘dimeric tube’ attempted in the second section of the chapter. Addition of hexadentate template **T6** to the square complex (formed from silyl deprotected dimer) followed by palladium catalyzed cyclization could yield the short ‘dimeric tube’ by a ‘double templating’ approach.

In general the newly synthesized linear and cyclic porphyrin oligomers are large amphiphiles and by tuning size and shape of the hydrophilic head (carboxylic acid or carboxylate) and the hydrophobic tail (porphyrin and alkyl solubilizing chains) it may be possible to assemble larger structures such as micelles or membranes. In the case of the nanoring ***c*-P6ac** such assemblies would be porous due to the cavity of the ring, with a pore size of about 2 nm.

7.5 References

[1] H.-B. Yang, K. Ghosh, B. H. Northrop, Y.-R. Zheng, M. M. Lyndon, D. C. Muddiman, P. J. Stang, *J. Am. Chem. Soc.* **2007**, *129*, 14187–14189.

[2] M. Schmittel, K. Mahata, *Angew. Chem. Int. Ed.* **2008**, *47*, 5284–5286.

[3] K. S. Chichak, S. J. Cantrill, A. R. Pease, S.-H. Chiu, G. W. V. Cave, J. L. Atwood, J. F. Stoddart, *Science* **2004**, *304*, 1308–1312.

[4] Y. L. Cho, H. Uh, S.-Y. Chang, H.-Y. Chang, M.-G. Choi, I. Shin, K.-S. Jeong, *J. Am. Chem. Soc.* **2007**, *123*, 1258–1259.

[5] L. J. Prins, D. N. Reinhoudt, P. Timmerman, *Angew. Chem. Int. Ed.* **2001**, *40*, 2382–2426.

[6] F. P. Schmidtchen, M. Berger, *Chem. Rev.* **1997**, *97*, 1609–1646.

[7] H. Ito, Y. Furusho, T. Hasegawa, E. Yashima, *J. Am. Chem. Soc.* **2008**, *130*, 14008–14015.

[8] T. Maeda, Y. Furusho, S.-I. Sakurai, J. Kumaki, K. Okoshi, E. Yashima, *J. Am. Chem. Soc.* **2008**, *130*, 7938–7945.

[9] F. Corbellini, L. Di Costanzo, M. Crego-Calama, S. Geremia, D. N. Reinhoudt, *J. Am. Chem. Soc.* **2003**, *125*, 9946–9947.

[10] H. Katagiri, Y. Tanaka, Y. Furusho, E. Yashima, *Angew. Chem. Int. Ed.* **2007**, *119*, 2487–2491.

[11] Y. Deng, J. A. Roberts, S.-M. Peng, C. K. Chang, D. G. Nocera, *Angew. Chem. Int. Ed. Engl.* **1997**, *36*, 2124–2127.

[12] L. Sánchez, M. Sierra, N. Martín, A. L. Myles, T. J. Dale, J. Rebek, Jr., W. Seitz, D. M. Guldi, *Angew. Chem. Int. Ed.* **2006**, *45*, 4637–4641.

[13] D. Braga, A. Decian, O. Felix, J. Fischer, M. W. Hosseini, F. Grepioni, L. Maini, *New J. Chem.* **2000**, *24*, 547–553.

[14] J. Rosenthal, J. M. Hodgkiss, E. R. Young, D. G. Nocera, *J. Am. Chem. Soc.* **2006**, *128*, 10474–10483.

[15] E. R. Young, J. Rosenthal, J. M. Hodgkiss, D. G. Nocera, *J. Am. Chem. Soc.* **2009**, *131*, 7678–7684.

[16] P. J. F. de Rege, S. A. Williams, M. J. Therien, *Science* **1995**, *269*, 1409–1413.

[17] J. L. Sessler, B. Wang, A. Harriman, *J. Am. Chem. Soc.* **1995**, *117*, 704–714.

[18] J. Otsuki, Y. Kanazawa, A. Kaito, D.-M. S. Islam, Y. Araki, O. Ito, *Chem. Eur. J.* **2008**, *14*, 3776 – 3784.

[19] P. N. Taylor, H. L. Anderson, *J. Am. Chem. Soc.* **1999**, *121*, 11538–11545.

[20] H. L. Anderson, *Inorg. Chem.* **1994**, *33*, 972–981.

[21] J. Grundy, M. P. Coles, P. B. Hitchcock, *J. Organomet. Chem.* **2002**, *662*, 178–187.

[22] C. A. Hunter, M. N. Meah, J. K. M. Sanders, *J. Am. Chem. Soc.* **1990**, *112*, 5773–5780.

[23] Y. Cohen, L. Avram, L. Frish, *Angew. Chem. Int. Ed.* **2005**, *44*, 520–554.

[24] M. U. Winters, J. Kärnbratt, M. Eng, C. J. Wilson, H. L. Anderson, B. Albinsson, *J. Phys. Chem. C* **2007**, *111*, 7192–7199.

[25] D. T. Bong, T. D. Clark, J. R. Granja, M. R. Ghadiri, *Angew. Chem. Int. Ed.* **2001**, *40*, 988–1011.

[26] R. J. Brea, C. Reiriz, J. R. Granja, *Chem. Soc. Rev.* **2010**, *39*, 1448–1456.

[27] M. R. Ghadiri, J. R. Granja, L. K. Buehler, *Nature* **1994**, *369*, 301–304.

[28] J. Yang, M. B. Dewal, L. S. Shimizu, *J. Am. Chem. Soc.* **2006**, *128*, 8122–8123.

[29] C. Reiriz, R. J. Brea, R. Arranz, J. L. Carrascosa, A. Garibotti, B. Manning, J. M. Valpuesta, R. Eritja, L. Castedo, J. R. Granja, *J. Am. Chem. Soc.* **2009**, *131*, 11335–11337.

[30] D. Venkataraman, S. Lee, J. Zhang, J. S. Moore, *Nature* **1994**, *371*, 591–593.

[31] K. Tomizaki, L. Yu, L. Wei, D. F. Bocian, J. S. Lindsey, *J. Org. Chem.* **2003**, *68*, 8199–8207.

[32] A. Satake, S. Azuma, Y. Kuramochi, S. Hirota, Y. Kobuke, *Chem. Eur. J.* **2011**, *17*, 855–865.

Chapter 8

Experimental Procedures

This chapter provides experimental details about the techniques used in this work and contains the experimental procedures and characterization data for all compounds synthesized in the work for this thesis.

8.1 General Procedures

All manipulations of air or water sensitive compounds were performed using standard high-vacuum techniques. When required, solutions were degassed by boiling under reduced pressure followed by saturating with N_2. This cycle was then repeated twice further. Dried tetrahydrofuran, dichloromethane and toluene were obtained by passing through alumina under N_2 pressure. Triethylamine was distilled over CaH_2 under nitrogen before use. All other reagents were used as commercially supplied. Flash column chromatography was carried out on silica gel 60 under positive pressure. Where mixtures of solvents were used, ratios are reported by volume. Size exclusion chromatography was carried out using Bio-Beads S-X1, 200–400 mesh (Bio Rad).

NMR data were collected at 700 MHz using a Bruker AVIII 700, at 500 MHz using a Bruker AVII 500 or a Bruker DRX 500, at 400 MHz using a Bruker DPX 400 or at 250 MHz using a Bruker DPX250. Samples were measured in $CDCl_3$ or $CDCl_3$/1% *d*$_5$-pyridine at 298 K and chemical shifts are quoted as parts per million (ppm) relative to residual $CHCl_3$ at $\delta_H = 7.27$ ppm and $\delta_C = 77.16$ ppm. Coupling constants (J) are quoted in Hertz (Hz). When diffusion editing of ^1H spectra was used to preferentially suppress solvent resonances the bipolar-pair LED sequence (BPP-LED) was employed. DOSY experiments were carried out using the double stimulated echo sequence (DSTE) which directly incorporates convection compensation. Diffusion coefficients were obtained by fitting intensity decays to: $I = I_0 \exp(-D\gamma^2\delta^2g^2(\Delta-\delta/3))$ where I and I_0 represent signal intensities in the presence and absence of gradient pulses respectively, D is the required diffusion coefficient, γ is the ^1H magnetogyric ratio, δ is the gradient pulse duration, Δ is the total diffusion time and g is the applied gradient strength. Mass spectra were measured by electrospray ionisation (ESI) using a Bruker micOTOF or by the matrix assisted laser desorption ionisation time of flight (MALDI-TOF) technique on a Micromass MALDI micro MX or by the EPSRC National Mass Spectrometry Service Centre on a Applied Biosystems Voyager-DE-STR. The MALDI-TOF mass spectra were recorded using dithranol (1,8,9-trihydroxyanthracene) or DCTB (*trans*-2-[3-(4-*tert*-butylphenyl)-2-methyl-2-propenylidene]malononitrile) as the matrix. Only the peak of the molecular ion (100%, most intense peak) is given. Analytical GPC was carried out using PLgel 3 μm Mixed-E columns (2 × 300 mm length, 7.5 mm diameter), with a flow rate of 1 mL/min.

UV-vis absorption spectra were measured on with Perkin Elmer Lambda 9 and Perkin Elmer Lambda 20 photospectrometers with a scan rate of 960 nm/min. Fully corrected emission spectra were measured using a custom-build system consisting of a 75 W Xenon Lamp and a nitrogen cooled InGaAs detector. Vis/NIR emission spectra and photoluminescence excitation (PLE) maps were recorded using an automated custom-built system consisting of a 75 W xenon lamp focused into a monochromator, which then illuminated the sample in a quartz fluorescence cell. A silicon photodiode was used to normalize the incident excitation intensities. Luminescence from the sample was collected at 90° to the excitation beam and focused into a spectrograph fitted with a liquid nitrogen cooled InGaAs photodiode array. The spectral response of the detector was corrected by using a standard tungsten lamp (OL 245U, Optronic Laboratories Inc.).

The synchrotron radiation small angle X-ray scattering (SAXS) data were collected using standard procedures on the I22 beamline at Diamond Light Source (UK) equipped with a photon counting detector. The beam was focused onto the detector placed at a distance of 1.25 m from the sample cell. The covered range of momentum transfer was $0.03 < q < 1.0$ Å^{-1} ($q = 4\pi\sin(\theta)/\lambda$ where 2θ is the scattering angle and $\lambda = 1.00$ Å is the X-ray wavelength). The data were normalized to the intensity of the incident beam; the scattering of the solvent was subtracted using an in-house program. To check for radiation damage and aggregation during the SAXS experiment, the data were collected in 10 successive 60 s frames. All SAXS measurements were performed in either toluene or toluene/1% pyridine at known concentrations (~10^{-4} M) in a solution cell with mica windows.

HiPCO carbon nanotubes were purchased from Carbon Nanotech Inc. and 7,6-CoMoCat nanotubes from SouthWest Nanotechnologies (SWeNT). Both types of tubes were used without further treatment. For preparation of porphyrin-nanotube complexes we used a Branson 1510E-MT sonicator bath (80 W, 40 kHz).

Molecular modelling was carried out using the MM+ force field (molecular mechanics) and the semi-empirical AM1 and PM3 methods integrated in the HyperChem^{TM} 8.0 (Hypercube Inc.) package.

8.2 Synthetic Procedures for Previously Known Compounds

***meso*-β-Unsubstituted dipyrromethane 1**[1]

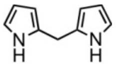

Formaldehyde (33% w/w solution in water, 5.4 mL, 60 mmol) was added to pyrrole (100 mL, 1.44 mol) and the solution degassed. Trifluoroacetic acid (0.54 mL, 3.09 mmol) was added with vigorous stirring, and the reaction was allowed to proceed for 5 minutes before CH_2Cl_2 (100 mL) was added, followed immediately by $NaCO_3$ (aq) (sat., 100 mL). The organic layer was washed with $NaCO_3$ (aq) (sat., 2 × 100 mL) and water (100 mL). Distillation of the oily residue in a Kugelrohr apparatus yielded the product as a white crystalline solid (3.37 g, 39%).

^{1}H NMR (250 MHz, $CDCl_3$) δ_H 3.96 (s, 2H, -C*H*$_2$), 6.06 (m, 2H, -pyrrole*H*$_\beta$), 6.17 (m, 2H, -pyrrole*H*$_\beta$), 6.66 (m, 2H, -pyrrole*H*$_\alpha$), 7.83 (br. s, 2H, -N*H*). As lit.

Free Base 5,15-bis-(3,5-bis-octyloxy-phenyl)-porphyrin 3a[2]

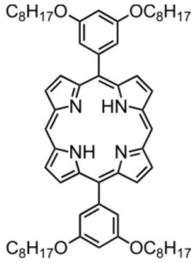

Dipyrromethane **1** (5.15 g, 28.0 mmol) and 3,5-bis-octyloxy-benzaldehyde **2a**[2] (12.8 g, 28.0 mmol) were dissolved in CH_2Cl_2 (5.00 L). The reaction mixture was deoxygenated and TFA (1.80 mL, 57.5 mmol) was added. After stirring in the dark for 3 hours, DDQ (12.9 g, 53.5 mmol) was added and the mixture stirred for 20 minutes before NEt_3 (15.0 mL, 108 mmol) was added to quench the acid. The volume was reduced and the mixture passed through a short silica gel column using CH_2Cl_2 to separate the tary side products. The product was recrystallized by layer addition (CH_2Cl_2/methanol) to give a bright purple powder (8.51 g, 48%).

^{1}H NMR (400 MHz, $CDCl_3$): δ_H -3.10 (s, 2H, N*H*), 0.91 (t, 12H, *J* = 6.5 Hz, -CH_3), 1.33–1.63 (m, 40H, -CH_2), 1.88–1.95 (m, 8H, -CH_2), 4.18 (t, 8H, *J* = 6.5 Hz, -OCH_2), 6.97 (t, 2H, *J* = 2.0 Hz, -ArH_{para}), 7.48 (d, 4H, *J* = 2.0 Hz, -ArH_{ortho}), 9.18 (d, 4H, *J* = 4.5 Hz, -ArH_β), 9.37 (d, 4H, *J* = 4.5 Hz, -ArH_β), 10.33 (s, 2H, -ArH_{meso}). As lit.[2]

Zinc 5,15-bis-(3,5-bis-octyloxy-phenyl)-porphyrin 4a[2]

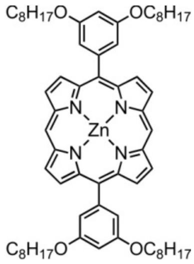

$Zn(OAc)_2 \cdot 2H_2O$ (3.84 g, 17.5 mmol) was dissolved in MeOH (48 mL) and added to a solution of free base 5,15-bis-(3,5-bis-octyloxy-phenyl)-porphyrin **3a** (3.55 g, 3.56 mmol) in $CHCl_3$ (370 mL). The reaction mixture was stirred at room temperature for 1 hour when UV/vis and TLC confirmed metallation was complete. Chromatography on a short silica gel column (CH_2Cl_2) removed excess $Zn(OAc)_2$. The product was recrystallized by layer addition (CH_2Cl_2/methanol) to give a purple powder (3.70 g, 98%).

^{1}H NMR (400 MHz, $CDCl_3$): δ_H 0.91 (t, 12H, *J* = 6.5 Hz, -CH_3), 1.25–1.61 (m, 40H, -CH_2), 1.87–1.94 (m, 8H, -CH_2), 4.18 (t, 8H, *J* = 6.5 Hz, -OCH_2), 6.94 (t, 2H, *J* = 2.0 Hz, -ArH_{para}), 7.46 (d, 4H,

$J = 2.0$ Hz, -ArH_{ortho}), 9.25 (d, 4H, $J = 4.5$ Hz, -ArH_{β}), 9.40 (d, 4H, $J = 4.5$ Hz, -ArH_{β}), 10.23 (s, 2H -ArH_{meso}). As lit.[2]

Zinc 5,15-bis-(3,5-bis-octyloxy-phenyl)-10,20-dibromo-porphyrin 5a[2]

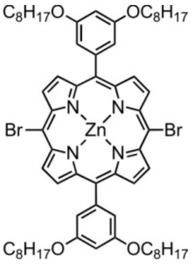

A solution of *N*-bromosuccinimide (3.05 g, 17.1 mmol) in $CHCl_3$ (200 mL) was added in the dark dropwise over one hour to a solution of zinc 5,15-bis-(3,5-bis-octyloxy-phenyl)-porphyrin **4a** (8.87 g, 8.56 mmol) in $CHCl_3$ (280 mL) and pyridine (4 mL). The reaction was quenched with acetone (1 mL). The product was recrystallized ($CHCl_3$/methanol) to give a purple crystalline solid (10.1 g, 98%).

^{1}H NMR (400 MHz, $CDCl_3$): δ_H 0.87 (t, 12H, $J = 6.5$ Hz, -CH_3), 1.28–1. 63 (m, 40H, -CH_2), 1.84–1.91 (m, 8H, -CH_2), 4.13 (t, 8H, $J = 6.5$ Hz, -OCH_2), 6.89 (t, 2H, $J = 2.0$ Hz, -ArH_{para}), 7.31 (d, 4H, $J = 2.0$ Hz, -ArH_{ortho}), 8.99 (m, 4H, -ArH_{β}), 9.63 (m, 4H, -ArH_{β}). As lit.[2]

Ethynyltrihexylsilane[3]

$\equiv\!-Si(C_6H_{13})_3$

Chlorotrihexylsilane (15.24 mL, 41.6 mmol) was added dropwise under N_2 to a stirred solution of ethynylmagnesium bromide (0.5 mol l^{-1} in THF, 100 mL, 50.0 mmol). The reaction mixture was heated at reflux for 1 hr before HCl (aq) (10%, 80 mL) was added. The organic layer was washed with water (80 mL) and dried over $MgSO_4$ to yield a yellow oil (10.7 g, 83%).

^{1}H NMR (400 MHz, $CDCl_3$) δ_H 0.63-0.56 (m, 6H, CH), 0.89-0.83 (m, 9H, CH), 1.41-1.26 (m, 24H, -CH_2), 2.35 (s, 1H, ≡CH). as lit.[3]

Zinc 5,15-bis-(3,5-bis-octyloxy-phenyl)-10,20-bis-trihexylsilanylethynyl-porphyrin *l*-P1$_{C8}$[2]

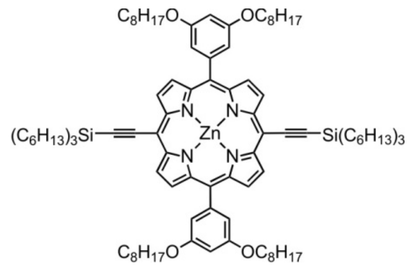

Zinc 5,15-bis-(3,5-bis-octyloxy-phenyl)-10,20-dibromo-porphyrin **5a** (3.00 g, 2.50 mmol), *tris*-(dibenzylideneacetone)-di-palladium(0) (147 mg, 0.16 mmol) PPh_3 (314 mg, 1.20 mmol) and CuI (114 mg, 0.60 mmol) were dried under vacuum before dry toluene (100 mL) and NEt_3 (100 mL) were added and the mixture deoxygenated. Ethynyltrihexylsilane (4.25 mL, 11.0 mmol) was added and the reaction stirred at 40 °C for 2 hours when TLC (10:1:1, 40-60 petroleum ether : ethyl acetate : pyridine) showed completion of the reaction. The volume was reduced and the mixture passed through a short silica gel column (100:1, 40-60 °C petroleum ether : pyridine), to remove baseline impurities and excess ethynyltrihexylsilane. Recrystallization by layer addition (CH_2Cl_2/methanol) gave a dark green solid (3.68 g, 89%).

^1H NMR (400 MHz, $CDCl_3$/1% d_5-pyridine): δ_H 1.15–1.01 (m, 40H, -CH_2,-CH_3), 1.34–1.68 (m, 78H, -CH_2), 1.75–1.94 (m, 20H, -CH_2), 4.15 (t, 8H, J = 6.5 Hz, -OCH_2), 6.89 (t, 2H, J = 2.0 Hz, -ArH_{para}), 7.32 (d, 4H, J = 2.0 Hz, -ArH_{ortho}), 9.08 (d, 4H, J = 4.5 Hz, -ArH_β), 9.76 (d, 4H, J = 4.5 Hz, -ArH_β). As lit.[2]

Zinc 5,15-bis-(3,5-bis-octyloxy-phenyl)-10-ethynyl-20-trihexylsilanylethynyl-porphyrin 6a[2]
Zinc 5,15-bis-(3,5-bis-octyloxy-phenyl)-10,20-bis-ethynyl-porphyrin *l*-dP1$_{C8}$[2]

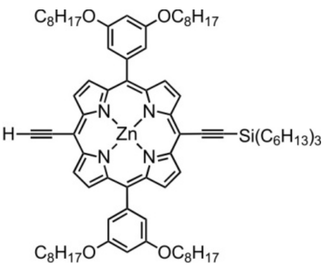

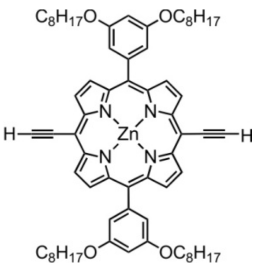

Tetra-*n*-butylammonium fluoride (1 M solution in THF, 1.27 mL, 1.27 mmol) was added to a solution of porphyrin monomer ***l*-P1$_{C8}$** (1.41 g, 0.85 mmol) in 1:1 solvent mixture of CH_2Cl_2 and $CHCl_3$ (180 mL) and the reaction mixture stirred for 30 minutes before CH_3COOH (150 µL, 2.55 mmol) was added. The volume was reduced and the reaction mixture passed through a short silica gel column (CH_2Cl_2). Chromatography on silica gel (100:1:1, 40-60 °C petroleum ether : Ethyl acetate : pyridine) and recrystallization by layer addition (CH_2Cl_2/methanol) yielded:

Zinc 5,15-bis-(3,5-bis-octyloxy-phenyl)-10-ethynyl-20-trihexylsilanylethynyl-porphyrin **6a**
(371 mg, 32%). ^{1}H NMR (400 MHz, CDCl$_3$/1% d_5-pyridine): δ_H 0.86–0.95 (m, 21H, -CH_3), 0.97–1.10 (m, 6H, -CH_2),1.39–1.62 (m, 58H, -CH_2), 1.75–1.83 (m, 6H, -CH_2), 1.85–1.92 (m, 8H, -CH_2), 4.14 (s, 1H, ≡CH), 4.15 (t, 8H, J = 6.5 Hz, -OCH_2), 6.90 (t, 2H, J = 2.0 Hz, -ArH_{para}), 7.35 (d, 4H, J = 2.0 Hz, -ArH_{ortho}), 8.99 (t, 4H, J = 4.5 Hz, -ArH_β), 9.65 (m, 4H, -ArH_β). As lit.[2]

Zinc 5,15-bis-(3,5-bis-octyloxy-phenyl)-10,20-bis-ethynyl-porphyrin ***l*-dP1$_{C8}$**
(267 mg, 29%). ^{1}H NMR (400 MHz, CDCl$_3$/1% d_5-pyridine): δ_H 0.87 (t, 12H, J = 6.5 Hz , -CH_3), 1.22–1.55 (m, 40H, -CH_2), 1.83–1.91 (m, 8H, -CH_2), 4.14 (t, 8H, J = 5.5 Hz, -OCH_2; s, 2H, ≡CH), 6.89 (t, 2H, J = 2.0 Hz, -ArH_{para}), 7.33 (d, 4H, J = 2.0 Hz, -ArH_{ortho}), 8.99 (m, 4H, -ArH_β), 9.65 (m, 4H, -ArH_β). As lit.[2]

Zinc 5,15-bis-(3,5-bis-octyloxy-phenyl)-10,20-trihexylsilanylethynyl-porphyrin dimer *l*-P2$_{C8}$[2]

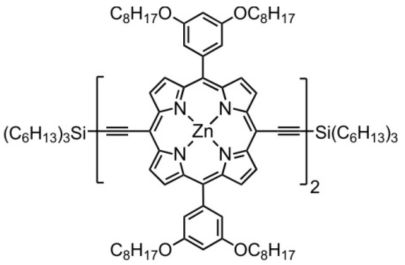

CuCl (1.18 g, 11.9 mmol) and *N,N,N',N'*-tetramethyl-ethylenediamine (1.35 mL, 11.1 mmol) were added to a vigorously stirred solution of monodeprotected porphyrin monomer **6a** (272 mg, 0.200 mmol) in dry CH$_2$Cl$_2$ (80 mL), in a 5 L round bottom flask, and the reaction mixture stirred 10 minutes. The reaction mixture was passed through a short plug of silica gel using CH$_2$Cl$_2$. Recrystallization by layer addition (CH$_2$Cl$_2$/methanol) gave the product as a green solid (231 mg, 85%).

^{1}H NMR (400 MHz, CDCl$_3$/1% d_5-pyridine): δ_H 0.93–1.01 (m, 42H, -CH_3), 1.03–1.17 (m, 12H, -CH_2), 1.35–1.67 (m, 116H, -CH_2), 1.82–1.98 (m, 28H, -CH_2), 4.20 (t, 16H, J = 6.5 Hz, -OCH_2), 6.93 (s, 4H, -ArH_{para}), 7.43 (d, 8H, J = 2.0 Hz, -ArH_{ortho}), 9.06 (d, 4H, J = 4.5 Hz, -ArH_β), 9.17 (d, 4H, J = 4.5 Hz, -ArH_β), 9.74 (d, 4H, J = 4.5 Hz, -ArH_β), 9.98 (d, 4H, J = 4.5 Hz, -ArH_β). As lit.[2]

Zinc 5,15-bis-(3,5-bis-octyloxy-phenyl)-10-ethynyl-20-trihexylsilanylethynyl-porphyrin dimer 7a[2]

Zinc 5,15-bis-(3,5-bis-octyloxy-phenyl)-10,20-bis-ethynyl-porphyrin dimer *l*-dP2$_{C8}$[2]

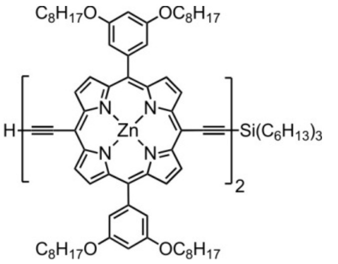

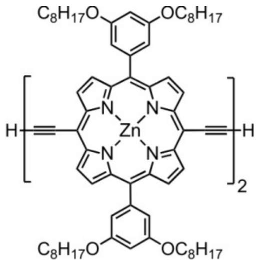

Tetra-*n*-butylammonium fluoride (1 M solution in THF, 0.29 mL, 0.29 mol) was added to a solution of porphyrin dimer ***l*-P2$_{C8}$** (524 mg, 0.19 mmol) in a 1:1 solvent mixture of CH_2Cl_2 and $CHCl_3$ (34 mL) and the reaction mixture stirred for 40 minutes before CH_3COOH (34 μL, 0.60 mmol) was added. The volume was reduced and the reaction mixture passed through a short silica gel column (CH_2Cl_2). Chromatography on silica gel (18:1:1, 40-60 °C petroleum ether : ethyl acetate : pyridine) and recrystallization by layer addition (CH_2Cl_2/methanol) yielded:

Zinc 5,15-Bis-(3,5-bis-octyloxy-phenyl)-10-ethynyl-20-trihexylsilanylethynyl-porphyrin dimer **7a** (142 mg, 31%). ^{1}H NMR (400 MHz, $CDCl_3$/1% *d*$_5$-pyridine): δ_H 0.96–1.04 (m, 33H, -CH_3), 1.12–1.33 (m, 6H, -CH_2), 1.42–1.70 (m, 98H, -CH_2), 1.86–2.03 (m, 22H, -CH_2), 4.25–4.29 (m, 17H, -OCH_2, ≡C*H*), 7.02 (s, 4H, -ArH_{para}), 7.49 (d, 8H, *J* = 2.5 Hz, -ArH_{ortho}), 9.08 (d, 4H, *J* = 4.5 Hz, -ArH_β), 9.19 (d, 4H, *J* = 4.5 Hz, -ArH_β), 9.74 (m, 4H, -ArH_β), 10.00 (m, 4H, -ArH_β). As lit.[2]

Zinc 5,15-Bis-(3,5-bis-octyloxy-phenyl)-10,20-bis-ethynyl-porphyrin dimer ***l*-dP2$_{C8}$** (110 mg, 27%). ^{1}H NMR (400 MHz, $CDCl_3$/1% *d*$_5$-pyridine): δ_H 0.87 (t, 24H, *J* = 6.5 Hz, -CH_3), 1.29–1.57 (m, 80H, -CH_2), 1.90 (m, 16H, -CH_2), 4.17 (t, 16H, *J* = 6.5 Hz, -OCH_2), 4.18 (s, 2H, ≡C*H*), 6.92 (d, 4H, *J* = 2.0 Hz, -ArH_{para}), 7.38 (d, 8H, *J* = 2.0 Hz, -ArH_{ortho}), 9.03 (m, 4H, -ArH_β), 9.10 (m, 4H, -ArH_β), 9.67 (m, 4H, -ArH_β), 9.91 (m, 4H, -ArH_β). As lit.[2]

Zinc 5,15-bis-(3,5-bis-octyloxy-phenyl)-10,20-trihexylsilanylethynyl-porphyrin trimer *l*-P3$_{C8}$[4]

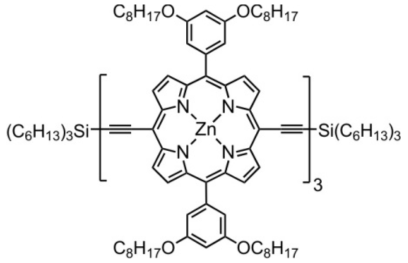

Monodeprotected porphyrin monomer ***l*-dP1$_{C8}$** (128 mg, 93.7 μmol) and monodeprotected porphyrin dimer ***l*-dP2$_{C8}$** (230 mg, 93.7 μmol) were dissolved in dry CH_2Cl_2 (73 mL). The mixture was vigorously stirred in a flame dried flask equipped with a $CaCl_2$ drying tube for 25 min. Copper(I) chloride (556 mg, 5.62 mmol) and *N,N,N',N'*-tetramethylethylenediamine (650 µL, 5.62 mmol) were added and vigorous stirring was continued for 1 hour. The reaction mixture was filtered over a short plug of silica using CH_2Cl_2 and solvents were removed under vacuum. Size exclusion chromatography on Biobeads SX–1 using tetrahydrofuran gave the trimer as a brown solid (109 mg, 30%); porphyrin dimer (20%) and porphyrin tetramer (20%) were isolated as byproducts.

^{1}H NMR (400 MHz, $CDCl_3$/1% d_5-pyridine): δ_H 0.86–0.94 (m, 54H, -CH_3), 1.01–1.06 (m, 12H, -CH_2), 1.29–1.45 (m, 120H, -CH_2), 1.50–1.58 (m, 36H, -CH_2), 1.75–1.81 (m, 12H, -CH_2), 1.87–1.94 (m, 24H, -CH_2), 4.16–4.21 (m, 24H, -OCH_2), 6.91–6.94 (m, 6H, -ArH_{para}), 7.39 (d, J = 2.0 Hz, 8H, -ArH_{ortho}), 7.42 (d, J = 2.0 Hz, 4H, -ArH_{ortho}), 8.97 (d, J = 4.5 Hz, 4H, -ArH_β), 9.07–9.08 (m, 8H, -ArH_β), 9.65 (d, J = 4.5 Hz, 4H, -ArH_β), 9.87–9.89 (m, 8H, -ArH_β). As lit.[4]

Zinc 5,15-Bis-(3,5-bis-octyloxy-phenyl)-10-ethynyl-20-trihexylsilanylethynyl-porphyrin trimer 9a[4]

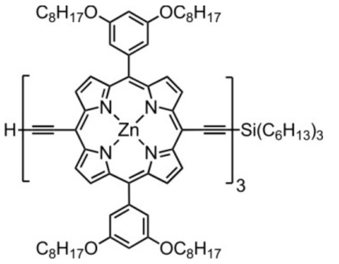

Tetra-*n*-butylammonium fluoride (1M in THF, 39.0 µL, 39.0 µmol) was added to a deoxygenated solution of Porphyrin-Trimer ***l*-P3$_{C8}$** (100 mg, 26.2 µmol) in CH_2Cl_2 (2.3 mL) and $CHCl_3$ (2.3 mL). The progress of the reaction was followed by TLC (15% pyridine in petrol 40-60 as eluent). The reaction was quenched with acetic acid (40 µL) and passed through a short plug of silica using dichloromethane. Chromatography on flash silica gel using 15% pyridine / petrol 40-60 as eluent afforded the desired product as a brown solid (36.1 mg, 39%).

^{1}H NMR (400 MHz, $CDCl_3$/1% d_5-pyridine): δ_H 0.83–0.93 (m, 45H, -CH_3), 1.00–1.05 (m, 6H, -CH_2), 1.28–1.44 (m, 108H, -CH_2), 1.49–1.59 (m, 30H, -CH_2), 1.74–1.82 (m, 6H, -CH_2), 1.86–1.94 (m, 24H, -CH_2), 4.15–4.20 (m, 24H, -OCH_2), 6.91–6.93 (m, 6H, -ArH_{para}), 7.37–7.41 (m, 12H, -ArH_{ortho}), 8.96–8.99 (m, 4H, -ArH_β), 9.06–9.08 (m, 8H, -ArH_β), 9.63–9.66 (m, 4H, -ArH_β), 9.86–9.90 (m, 8H, -ArH_β). As lit.[4]

Zinc 5,15-bis-(3,5-bis-octyloxy-phenyl)-10,20-trihexylsilanylethynyl-porphyrin tetramer *l*-P4$_{\mathrm{C8}}$[2]

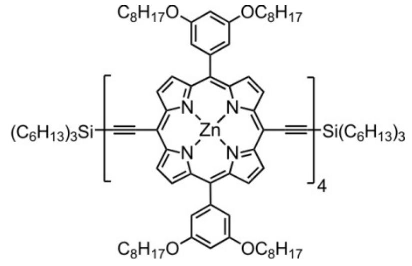

CuCl (306 mg, 3.09 mmol) and *N,N,N',N'*-tetramethylethylenediamine (360 µL, 3.09 mmol) were added to a vigorously stirred solution of monodeprotected porphyrin dimer **7a** (253 mg, 0.103 mmol) in dry CH_2Cl_2 (40 mL). The reaction mixture was stirred for 10 minutes and then passed through a short plug of silica gel (100:1, CH_2Cl_2 : pyridine) and recrystallized by layer addition (CH_2Cl_2/methanol) gave the product as a brown solid (175 mg, 69%).

^{1}H NMR (400 MHz, $CDCl_3$/1% d_5-pyridine): δ_H 0.85–1.08 (m, 78H, -C*H*$_3$), 1.30–1.56 (m, 196H, -C*H*$_2$), 1.72–1.93 (m, 44H, -C*H*$_2$), 4.20 (m, 32H, -OC*H*$_2$), 6.93 (m, 8H, -Ar*H*$_{\mathrm{para}}$), 7.39 (d, 8H, *J* = 2.0 Hz, -Ar*H*$_{\mathrm{ortho}}$), 7.44 (d, 8H, *J* = 2.0 Hz, -Ar*H*$_{\mathrm{ortho}}$), 8.98 (d, 4H, *J* = 4.5 Hz, -Ar*H*$_\beta$), 9.08 (m, 12H, -Ar*H*$_\beta$), 9.65 (d, 4H, *J* = 4.5 Hz, -Ar*H*$_\beta$), 9.90 (m, 12H, -Ar*H*$_\beta$). As lit.[2]

Zinc 5,15-Bis-(3,5-bis-octyloxy-phenyl)-10-ethynyl-20-trihexylsilanylethynyl-porphyrin tetramer 8a[2]

Zinc 5,15-Bis-(3,5-bis-octyloxy-phenyl)-10,20-bis-ethynyl-porphyrin tetramer *l*-dP4$_{\mathrm{C8}}$[2]

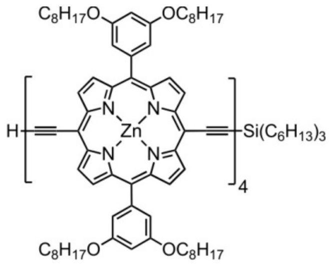

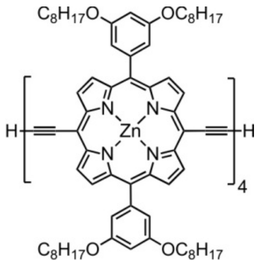

Tetra-*n*-butylammonium fluoride (1 M solution in THF, 71 µL, 0.071 mmol) was added to a solution of porphyrin tetramer ***l*-P4$_{\mathrm{C8}}$** (230 mg, 0.047 mmol) in CH_2Cl_2 (4 mL) and $CHCl_3$ (4 mL) and the reaction mixture stirred for 30 minutes before CH_3COOH (8 µL, 0.142 mmol) was added. The volume was reduced and the reaction mixture passed through a short plug of silica gel (CH_2Cl_2). Chromatography on silica gel (85:15, 40-60 °C petroleum ether : pyridine) and recrystallization by layer addition (CH_2Cl_2/methanol) gave:

Zinc 5,15-Bis-(3,5-bis-octyloxy-phenyl)-10-ethynyl-20-trihexylsilanylethynyl-porphyrin tetramer **8a** (81 mg, 37%). ^{1}H NMR (400 MHz, $CDCl_3$/1% d_5-pyridine): δ_H 0.91–1.11 (m, 63H, -C*H*$_3$), 1.35–1.67 (m, 178H, -C*H*$_2$), 1.81–1.88 (m, 6H, -C*H*$_2$), 1.93–2.02 (m, 32H, -C*H*$_2$), 4.24 (m, 33H, -OC*H*$_2$, ≡C*H*), 6.98 (s, 4H, -Ar*H*$_{para}$), 7.00 (s, 4H, -Ar*H*$_{para}$), 7.45 (s, 8H, -Ar*H*$_{ortho}$), 7.49 (d, 8H, *J* = 2.0 Hz, -Ar*H*$_{ortho}$), 9.04 (m, 4H, -Ar*H*$_{\beta}$), 9.15 (m, 12H, -Ar*H*$_{\beta}$), 9.70 (m, 4H, -Ar*H*$_{\beta}$), 9.95 (m, 12H, -Ar*H*$_{\beta}$). As lit.[2]

Zinc 5,15-Bis-(3,5-bis-octyloxy-phenyl)-10,20-bis-ethynyl-porphyrin tetramer ***l*-dP4$_{C8}$**

(48 mg, 21%). ^{1}H NMR (400 MHz, CDCl$_3$/1% d_5-pyridine): δ_H 0.87 (m, 48H, C*H*$_3$), 1.29–1.53 (m, 160H, C*H*$_2$), 1.90 (m, 32H, C*H*$_2$), 4.18 (m, 32H, OC*H*$_2$), 6.92 (m, 8H, Ar-*H*^{para}), 7.38 (s, 8H, Ar-*H*^{ortho}), 7.42 (s, 8H, Ar-*H*^{ortho}), 8.98 (d, 4H, *J* = 4.5 Hz, -Ar*H*$_{\beta}$), 9.08 (m, 12H, -Ar*H*$_{\beta}$), 9.63 (d, 4H, *J* = 4.5 Hz, -Ar*H*$_{\beta}$), 9.89 (m, 12H, -Ar*H*$_{\beta}$). As lit.[2]

Zinc 5,15-bis-(3,5-bis-octyloxy-phenyl)-10,20-trihexylsilanylethynyl-porphyrin hexamer *l*-P6$_{C8}$[4]

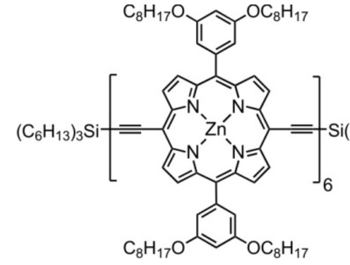

Porphyrin trimer **9a** (30.0 mg, 8.48 µmol) was dissolved in dry CH$_2$Cl$_2$ (5.2 mL). The mixture was vigorously stirred in a flame dried flask equipped with a CaCl$_2$ drying tube for 15 min. Copper(I) chloride (25.2 mg, 254 µmol) and *N*,*N*,*N*’,*N*’-tetramethylethylenediamine (29 µL, 254 µmol) were added and vigorous stirring was continued for 2.5 hours. The reaction mixture was filtered over a short plug of silica using CH$_2$Cl$_2$ and solvents were removed under vacuum. Size exclusion chromatography on Biobeads SX–1 using tetrahydrofuran afforded porphyrin hexamer as a brown solid (24.3 mg, 81%).

^{1}H NMR (400 MHz, CDCl$_3$ / 1% d_5-pyridine): δ_H 0.86–0.94 (m, 90H, -C*H*$_3$), 1.01–1.05 (m, 12H, -C*H*$_2$), 1.26–1.42 (m, 192H, -C*H*$_2$), 1.50–1.58 (m, 72H, -C*H*$_2$), 1.75–1.81 (m, 12H, -C*H*$_2$), 1.89–1.94 (m, 60H, -C*H*$_2$), 4.16–4.20 (m, 48H, -OC*H*$_2$), 6.91–6.92 (m, 4H, -Ar*H*$_{para}$), 6.94–6.95 (m, 8H, -Ar*H*$_{para}$), 7.38–7.39 (m, 8H, -Ar*H*$_{ortho}$), 7.42–7.44 (m, 16H, -Ar*H*$_{ortho}$), 8.97 (d, *J* = 4.5 Hz, 4H, -Ar*H*$_{\beta}$), 9.07–9.10 (m, 20H, -Ar*H*$_{\beta}$), 9.65 (d, *J* = 4.5 Hz, 4H, -Ar*H*$_{\beta}$), 9.87–9.91 (m, 20H, -Ar*H*$_{\beta}$). As lit.**[4]**

Zinc 5,15-Bis-(3,5-bis-octyloxy-phenyl)-10,20-trihexylsilanylethynyl-porphyrin octamer *l*-P8$_{C8}$[2]

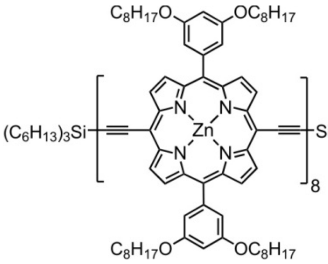

CuCl (40 mg, 0.40 mmol) and *N,N,N',N'*-tetramethylethylenediamine (46 µL, 0.40 mmol) were added to a vigorously stirred solution of monodeprotected porphyrin tetramer **8a** (192 mg, 0.042 mmol) in dry CH_2Cl_2 (8 mL) and stirred for 10 minutes. The reaction mixture was passed through a short plug of silica gel (10:1, 40-60 °C petroleum ether : pyridine) and recrystallization by layer addition (CH_2Cl_2/methanol) gave the product as a brown solid (165 mg, 86%).

^{1}H NMR (400 MHz, $CDCl_3$/1% d_5-pyridine): δ_H 0.86–0.94 (m, 114H, -CH_3), 1.00–1.07 (m, 6H, -CH_2), 1.25–1.61 (m, 372H, -CH_2), 1.75–1.82 (m, 6H, -CH_2), 1.87–1.96 (m, 60H, -CH_2), 4.21 (m, 64H, -OCH_2), 6.91–6.95 (m, 32H, -ArH_{para}), 7.38–7.44 (m, 32H, -ArH_{ortho}), 8.97 (d, 4H, J = 4.5 Hz, -ArH_β), 9.08 (m, 30H, -ArH_β), 9.64 (d, 4H, J = 4.5 Hz, -ArH_β), 9.89 (m, 30H, -ArH_β). As lit.[2]

Zinc 5,15-Bis-(3,5-bis-octyloxy-phenyl)-10,20-trihexylsilanylethynyl-porphyrin octamer *l*-P*n*$_{C8}$[5]

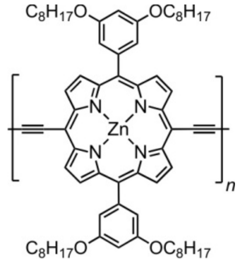

1,4-Benzoquinone (15 mg, 0.13 mmol), copper(I) iodide (7.2 mg, 0.038 mmol) and $Pd(PPh_3)_4$ (4.8 mg, 0.004 mmol) were placed in a flask. The vessel was evacuated and refilled with argon. Toluene (10 mL) and diisopropylamine (4.8 mL) were added to the flask. A solution of fully deprotected porphyrin monomer ***l*-dP1$_{C8}$** (100 mg, 0.092 mmol) in toluene (5 mL) was added. The flask was closed and heated to 60°C overnight. Then, a small amount of tetrahydofuran was added and the mixture was precipitated into methanol and centrifuged (1500 rpm, 10 min). The polymer was purified by washing and subsequent centrifugation in methanol, 40-60 petroleum ether and then dichloromethane.

^{1}H NMR (400 MHz, $CDCl_3$/1% d_5-pyridine) δ_H 0.85–0.88 (m, 12H,-CH_3) 1.25–1.41 (m, 16H, -CH_2), 1.52–1.56 (m, 8H, -CH_2), 4.20 (br s, 8H, -OCH_2), 6.95 (br s, 2H, -ArH_{para}), 7.43 (br s, 4H, -ArH_{ortho}), 9.09 (d, J=3.8 Hz, 4H, -ArH_β), 9.90 (d, J=3.9 Hz, 4H, -ArH_β); GPC (THF, Polymer Laboratories PLgel 5 µm MIXED-D column, calibrated using monodisperse porphyrin oligomers): M_n = 43,000 (corresponds to an average of about 40 porphyrin units); λ_{max} (THF) / nm (log ε) 470 (4.87), 587 (3.77), 787 (4.61) [extinction coefficients per repeat unit]. As lit.[5]

Hexakis(4-bromophenyl) benzene[6]

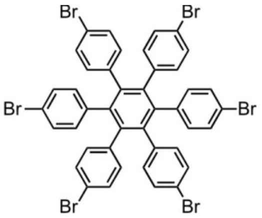

Neat bromine (8.24 g, 51.6 mmol) was dropped very slowly to hexaphenylbenzene (2.00 g, 3.74 mmol). Stirring of the dark orange slurry was continued after the addition for 45 minutes. Ethanol (40 mL) was carefully added, while cooling the reaction flask in a dry-ice/acetone bath. The precipitate was collected by filtration and washed with an aqueous $Na_2S_2O_3$ solution. The crude product was dissolved in $CHCl_3$ and washed with aq. $Na_2S_2O_3$ and water. Solvents were removed under vacuum and the residue was recrystallized from hot CH_2Cl_2/methanol to give the product as a white solid (3.52 g, 93%).

^{1}H NMR (400 MHz, $CDCl_3$): δ_H 6.61 (d, J = 8.5 Hz, 12H), 7.07 (d, J = 8.5 Hz, 12H). As lit.[6]

Hexadentate template T6[4]

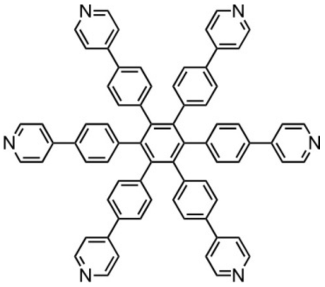

To a solution of hexakis-(4-bromophenyl)benzene (300.0 mg, 297 µmol) in dimethyleneglycol (9.0 mL) and tetrahydrofuran (21 mL) was added dichlorobis(triphenylphosphine)-palladium(II) (40.0 mg, 57.0 µmol). After addition of water (12 mL), $NaHCO_3$ (450 mg, 5.36 mmol) and 4-pyridineboronic acid (882 mg, 7.18 mmol), the mixture was deoxygenated and stirred at 70 °C for 5 days. Solvents were removed and the crude product was purified by column chromatography on flash silica gel (dichloromethane : methanol : triethylamine = 10 : 1 : 0.05) to give the template as a white solid (148 mg, 50%).

^{1}H–NMR (400 MHz, $CDCl_3$): δ_H ppm 6.96 (d, J = 8.5 Hz, 12H), 7.18 (d, J = 8.5 Hz, 12H), 7.29 (d, J = 5.5 Hz, 12H), 8.36 (d, J = 5.5 Hz, 12H). As lit.[4]

Zinc (3,5-bis-octyloxy-phenyl)-porphyrin[6] nanoring–template complex ***c*-P6$_{C8}$·T6**[4]

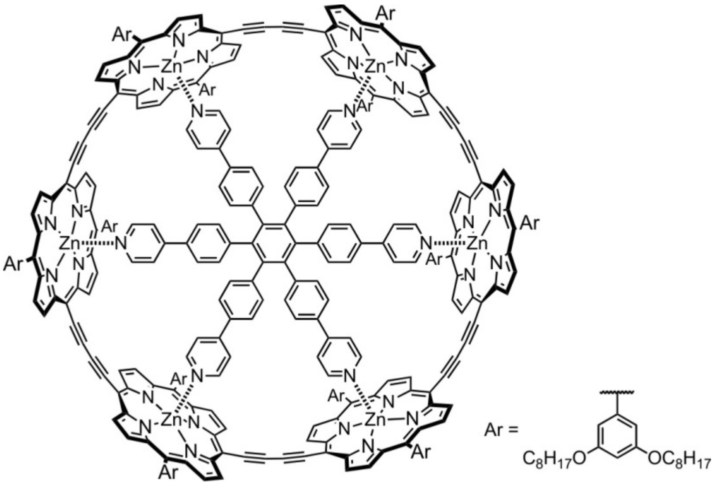

Hexadentate template **T6** (12 mg, 12 µmol) and porphyrin monomer ***l*-dP1$_{C8}$** (50 mg, 46 µmol) were dissolved in toluene (40 mL) and sonicated for 30 min (bath sonicator). A catalyst solution was prepared by dissolving $Pd(PPh_3)_2Cl_2$ (2 mg, 3 µmol), copper(I) iodide (3 mg, 15 µmol) and 1,4-benzoquinone (10 mg, 92 µmol) in toluene (10 mL) and freshly distilled di*iso*propylamine (0.3 mL). The catalyst solution was added to the porphyrin solution, and the mixture was stirred at room temperature for 2 h, and then for 1 h at 50 °C (under air). The mixture was passed through a plug of alumina using $CHCl_3$ as eluent, and purified by size exclusion chromatography on Biobeads SX-1 in toluene. The second band was isolated and recrystallized by layer addition (CH_2Cl_2/methanol) to give ***c*-P6$_{C8}$·T6** as a dark brown solid (18 mg, 31%).

^{1}H NMR (400 MHz, $CDCl_3$): δ_H 0.85–0.90 (m, 72H, -C*H*$_3$), 1.26–1.56 (m, 240H, -C*H*$_2$), 1.83–1.94 (m, 48H, -C*H*$_2$), 2.26 (d, *J* = 6.5 Hz, 12H, -pyridyl*H*$_\alpha$), 4.09 (t, *J* = 6.5 Hz, 24H, -C*H*$_2$), 4.20 (t, *J* = 6.5 Hz, 24H, -C*H*$_2$), 5.00 (d, *J* = 6.5 Hz, 12H, -pyridyl*H*$_\beta$), 5.47 (d, *J* = 8.5 Hz, 12H, -Ar*H*), 5.55 (d, *J* = 8.5 Hz, 12H, -Ar*H*), 6.89 (s, 12H, -Ar*H*$_{para}$), 7.11 (s, 12H, -Ar*H*$_{ortho}$), 7.38 (s, 12H, -Ar*H*$_{ortho}$), 8.85 (d, *J* = 4.5 Hz, 24H, -Ar*H*$_\beta$), 9.54 (d, *J* = 4.5 Hz, 24H, -Ar*H*$_\beta$). As lit.[4]

Zinc (3,5-bis-octyloxy-phenyl)-porphyrin[6] nanoring $\mathbf{cP6_{C8}}$[4]

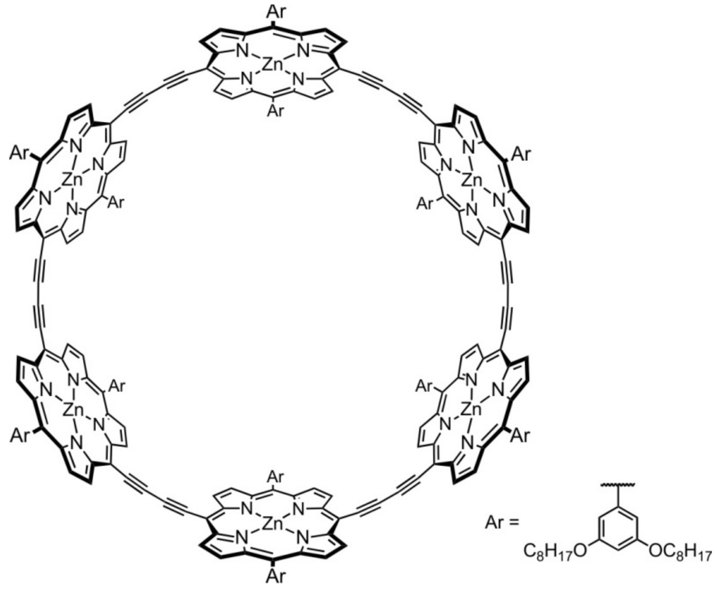

Cyclic hexamer–template complex $\mathbf{cP6_{C8}{\cdot}T6}$ (2.7 mg, 0.36 μmol) was passed through a size exclusion column (Biobeads SX-1) containing a (40 mg mL^{-1}) solution of recrystallized DABCO in freshly distilled tetrahydrofuran. The crude product was dissolved in chloroform and recrystallized by layer addition with methanol to afford the template-free nanoring as a brownish solid (2.1 mg, 89%).

^{1}H NMR (400 MHz, $CDCl_3$/1% d_5–pyridine): δ_H 0.85–0.90 (m, 72H, -CH_3), 1.26–1.56 (m, 240H, -CH_2), 1.83–1.94 (m, 48H, -CH_2), 4.08 (t, J = 6.5 Hz, 48H, -OCH_2), 6.84 (s, 12H, -ArH_{para}), 7.22 (s, 24H, -ArH_{ortho}), 8.87 (d, J = 4.5 Hz, 24H, -ArH_β), 9.59 (d, J = 4.5 Hz, 24H, -ArH_β); As lit.[4]

Free Base 5,15-bis-(3,5-bis-*tert*-butyl-phenyl)-porphyrin **3b**[7]

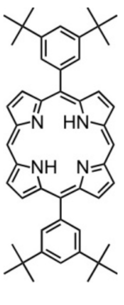

3,5-Bis(*tert*-butyl)benzaldehyde **2b**[8] (1.79 g, 8.21 mmol) and dipyrromethane **1** (1.20 g, 8.21 mmol) were placed in a dry flask under N_2 and dissolved in CH_2Cl_2 (1600 mL). The solution was degassed three times by repeated evacuation and purging with nitrogen. Trifluoroacetic acid (0.37 mL, 4.9 mmol) was added and the reaction mixture stirred in the dark for 3 h. DDQ (2.42 g, 10.7 mmol) was added and stirring continued for 0.5 h. After quenching of the acid by addition of triethylamine (8.0 mL) the mixture was passed over a short silica plug (CH_2Cl_2). Recrystallization from CH_2Cl_2/methanol gave porphyrin **3b** as a red solid (1.73 g, 56%).

^{1}H NMR (400 MHz, $CDCl_3$): δ_H -3.10 (br. s, 2H, N*H*), 1.58 (s, 36H, -*t*Bu*H*), 7.85 (t, 2H, *J* = 2.0 Hz, -ArH_{para}), 8.16 (d, 4H, *J* = 2.0 Hz, -ArH_{ortho}), 9.15 (d, 4H, *J* = 4.5 Hz, -ArH_β), 9.42 (d, 4H, *J* = 4.5 Hz, -ArH_β), 10.33 (s, 2H, -ArH_{meso}). As lit.[7]

Zinc 5,15-bis-(3,5-bis-*tert*-butyl-phenyl)-porphyrin 4b[7]

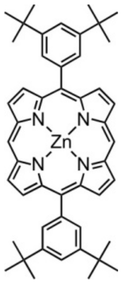

$Zn(OAc)_2$•$2H_2O$ (1.67 g, 7.63 mmol) was dissolved in methanol (15 mL) and added to a solution of free-base porphyrin **3b** (1.02 g, 1.48 mmol) in $CHCl_3$ (150 mL). The reaction was stirred at room temperature for 1 hour. The mixture was passed through a short plug of silica gel using CH_2Cl_2. The crude product was recrystallized by layer addition (CH_2Cl_2/methanol) to give a purple powder (1.17 g, 95 %).

^{1}H NMR (400 MHz, $CDCl_3$): δ_H 1.59 (s, 36H, -*t*Bu*H*), 7.86 (t, 2H, *J* = 2.0 Hz, -ArH_{ortho}), 8.17 (d, 4H, *J* = 2.0 Hz, -ArH_{ortho}), 9.23 (d, 4H, *J* = 4.5 Hz, -ArH_β), 9.45 (d, 4H, *J* = 4.5 Hz, -ArH_β), 10.36 (s, 2H, -ArH_{meso}). As lit.[7]

Zinc 5,15-bis-(3,5-bis-*tert*-butyl-phenyl)-10,20-dibromo-porphyrin 5b[7]

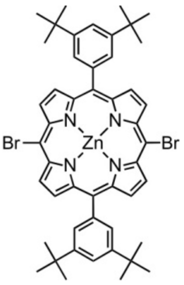

To a solution of zinc porphyrin **4b** (1.2 g, 8.2 mmol) in $CHCl_3$ (190 mL) and pyridine (0.8 mL) was added dropwise *N*-bromosuccinimide (0.61 g, 3.4 mmol) dissolved in $CHCl_3$ (30 mL). After stirring in the dark for 15 minutes, the reaction was quenched with acetone (1.0 mL). The solvent was removed and the crude product recrystallized by layer addition from CH_2Cl_2/methanol to give dibromoporphyrin **5b** as a purple solid (1.36 g, 92%).

^{1}H NMR (400 MHz, $CDCl_3$): δ_H 1.50 (s, 36H, -*t*Bu*H*),7.80 (t, *J* = 2.0 Hz, -ArH_{para}), 7.99 (d, *J* = 2.0 Hz, 4H, -ArH_{ortho}), 8.91 (d, *J* = 4.5 Hz, 4H, -ArH_β), 9.66 (d, *J* = 4.5 Hz, 4H, -ArH_{meso}). As lit.[7]

Zinc 5,15-bis-(3,5-bis-*tert*-butyl-phenyl)-10,20-bis-trihexylsilanylethynyl-porphyrin *l*-P1[7]

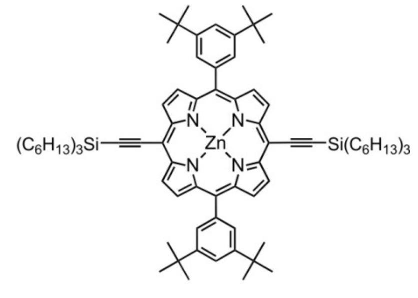

tris-(Dibenzylideneacetone)-di-palladium(0) (64 mg, 70 µmol), copper(I) iodide (28 mg, 0.14 mmol), triphenylphosphine (36 mg, 0.14 mmol) and dibromoporphyrin **5b** (0.64 g, 0.7 mmol) were placed in a dried Schlenk tube under argon. Toluene (45 mL), *i*Pr_2NH (24 mL) and pyridine (1.27 mL) were added and the reaction mixture deoxygenated. Trihexylsilyl acetylene (0.81 mL, 2.1 mmol) was added by syringe. The reaction mixture was stirred at 80 °C for 3 hours, solvents removed and the residue passed through a short silica gel column using CH_2Cl_2. Recrystallization by layer addition (CH_2Cl_2/methanol) gave the product ***l*-P1** as a green solid (0.96 g, 99 %).

^{1}H NMR (400 MHz, $CDCl_3$): δ_H 0.90 (t, 18H, J = 7.0 Hz, -CH_3), 1.02 (m, 12H, -CH_2), 1.39 (m, 24H, -CH_2), 1.58–1.51 (m, 48H, -CH_2, -*t*Bu*H*), 1.77 (m, 12H, -CH_2), 7.83 (t, 2H, J = 1.5 Hz, -ArH_{para}), 8.06 (d, 4H, J = 1.5 Hz, -ArH_{ortho}), 8.98 (d, 4H, J = 4.5 Hz, -ArH_β), 9.74 (d, 4H, J = 4.5 Hz, -ArH_β). As lit.[7]

Zinc 5,15-bis-(3,5-bis-*tert*-butyl-phenyl)-10-ethynyl-20-trihexylsilanylethynyl-porphyrin 6b[7]
Zinc 5,15-bis-(3,5-bis-*tert*-butyl-phenyl)-10,20-bis-ethynyl-porphyrin *l*-dP1[7]

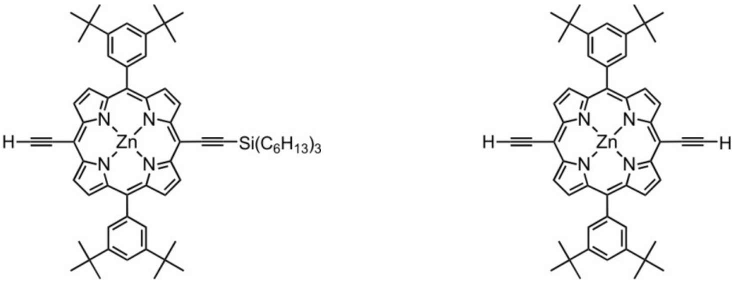

Protected porphyrin monomer ***l*-P1** (1.54 g, 1.13 mmol) was dissolved in CH_2Cl_2 (280 mL) and $CHCl_3$ (280 mL). Tetra-*n*-butylammonium fluoride (1.7 mL, 1.0 M solution in THF, 1.7 mmol) was added to the stirred solution. The progress of the reaction was monitored by TLC until an optimal product mixture was reached and the reaction then quenched with CH_3COOH (0.2 mL, 3.4 mmol). The volume was reduced and the mixture passed through a short plug of silica gel (CH_2Cl_2). Column chromatography (100:1:1, 40-60 petroleum ether : Ethyl acetate : pyridine) gave:

Zinc 5,15-bis-(3,5-bis-*tert*-butyl-phenyl)-10-ethynyl-20-trihexylsilanylethynyl-porphyrin **6b** (474 mg, 37 %). ^{1}H NMR (400 MHz, $CDCl_3$): δ_H 0.91 (t, 9H, J = 7.0 Hz, -CH_3), 1.01–1.05 (m, 6H, -CH_2), 1.37–1.44 (m, 12H, -CH_2), 1.52–1.57 (m, 42H, -CH_2, -*t*Bu*H*), 1.76–1.81 (m, 6H, -CH_2), 4.15 (s, 1H, ≡C*H*), 7.81 (t, 2H, *J* = 2.0 Hz, -ArH_{para}), 8.03 (d, 4H, *J* = 2.0 Hz, -ArH_{ortho}), 8.92 (m, 4H, -ArH_{β}), 9.68 (m, 4H, -ArH_{β}). As lit.[7]

Zinc 5,15-bis-(3,5-bis-*tert*-butyl-phenyl)-10,20-bis-ethynyl-porphyrin ***l*-dP1**

(312 mg, 33 %). ^{1}H NMR (400 MHz, $CDCl_3$): δ_H 1.55 (s, 36H, -*t*Bu*H*), 4.15 (s, 2H, ≡C*H*), 7.79 (t, 2H, *J* = 1.5 Hz, -ArH_{para}), 8.01 (d, 4H, *J* = 1.5 Hz, -ArH_{ortho}), 8.91 (d, 4H, *J* = 4.5 Hz, -ArH_{β}), 9.67 (d, 4H, *J* = 4.5 Hz, -ArH_{β}). As lit.[7]

Zinc 5,15-bis-(3,5-bis-*tert*-butyl-phenyl)-10,20-bis-ethynyl-porphyrin *l*-dP1[7]

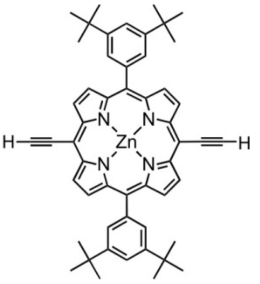

THS-protected porphyrin monomer ***l*-P1** (100 mg, 73.3 μmol) was dissolved in CH_2Cl_2 (10 mL) and tetra-*n*-butylammonium fluoride (0.70 mL, 1.0 M solution in THF, 70 mmol) was added. After stirring at room temperature for 15 minutes the mixture was immediately passed through a short plug of silica gel (CH_2Cl_2). Recrystallization by layer addition (CH_2Cl_2/methanol) gave the product ***l*-dP1** as a dark green solid (54 mg, 92 %).

^{1}H NMR (400 MHz, $CDCl_3$): δ_H 1.55 (s, 36H, -*t*Bu*H*), 4.15 (s, 2H, ≡C*H*), 7.79 (t, 2H, *J* = 1.5 Hz, -ArH_{para}), 8.01 (d, 4H, *J* = 1.5 Hz, -ArH_{ortho}), 8.91 (d, 4H, *J* = 4.5 Hz, -ArH_{β}), 9.67 (d, 4H, *J* = 4.5 Hz, -ArH_{β}). As lit.[7]

Zinc 5,15-bis-(3,5-*tert*-butyl-phenyl)-10,20-trihexylsilanylethynyl-porphyrin dimer *l*-P2[9]

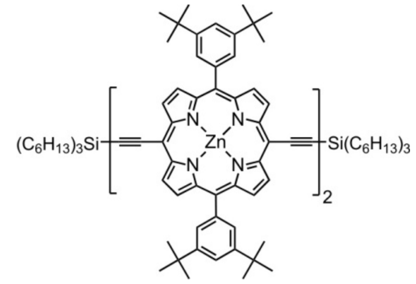

CuCl (205 mg, 2.07 mmol) and *N,N,N',N'*-tetramethyl-ethylenediamine (239 μL, 2.07 mmol) were added to a vigorously stirred solution of monodeprotected porphyrin monomer **6b** (74.5 mg, 68.9 μmol) in dry CH_2Cl_2 (17 mL), in a 1 L round bottom flask, and the reaction mixture stirred 30 minutes. The reaction mixture was passed through a short plug of silica gel (CH_2Cl_2).

Recrystallization by layer addition (CH_2Cl_2/methanol) gave the product as a dark green solid (68.9 mg, 93%).

^{1}H NMR (400 MHz, $CDCl_3$/1% d_5-pyridine): δ_H 0.91 (t, 18H, J = 7.0 Hz, -CH_3), 1.00–1.04 (m, 12H, -CH_2), 1.35–1.45 (m, 24H, -CH_2), 1.51–1.61 (m, 72H, -*t*Bu*H*, -CH_2), 1.73–1.82 (m, 12H, -CH_2), 7.81–7.82 (m, 4H, -ArH_{para}), 8.05 (d, 8H, J = 1.5 Hz, -ArH_{ortho}), 8.89 (d, 4H, J = 4.5 Hz, -ArH_β), 8.99 (d, 4H, J = 4.5 Hz, -ArH_β), 9.66 (d, 4H, J = 4.5 Hz, -ArH_β), 9.89 (d, 4H, J = 4.5 Hz, -ArH_β). As lit.[9]

Zinc 5,15-bis-(3,5-*tert*-butyl-phenyl)-10-ethynyl-20-trihexylsilanylethynyl-porphyrin dimer 7b[9]

Zinc 5,15-bis-(3,5-bis-octyloxy-phenyl)-10,20-bis-ethynyl-porphyrin dimer *l*-dP2[9]

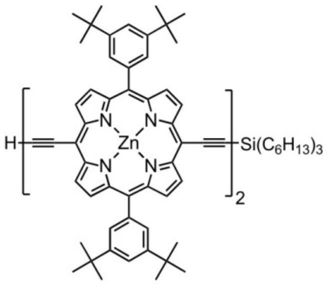

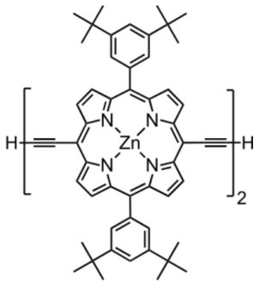

Tetra-*n*-butylammonium fluoride (10.5 µL, 1 M solution in THF) was added to a solution of porphyrin dimer ***l*-P2** (68 mg, 31 µmol) in a mixture of CH_2Cl_2 (7 mL) and $CHCl_3$ (7 mL). The reaction was monitored by TLC and quenched after 30 minutes with CH_3COOH (0.19 mL, 3.4 mmol). The volume was reduced and the reaction mixture passed through a short silica gel column (CH_2Cl_2/1% pyridine). Chromatography on silica gel (10:1:1, 40-60 °C petroleum ether : Ethyl acetate : pyridine) and recrystallization by layer addition (CH_2Cl_2/methanol) yielded:

Zinc 5,15-Bis-(3,5-bis-*tert*-butyl-phenyl)-10-ethynyl-20-trihexylsilanylethynyl-porphyrin dimer **7b**
(24 mg, 41%). ^{1}H NMR (500 MHz, $CDCl_3$/1% d_5-pyridine): δ_H 0.91 (t, 9H, J = 6.5 Hz, -CH_3), 1.03 (m, 6H, -CH_2), 1.40 (m, 12H, -CH_2), 1.56 (m, 6H, -CH_2), 1.58 (s, 72H, -*t*Bu*H*), 1.76 (m, 6H, -CH_2), 4.18 (s, 1H, ≡C*H*), 7.82 (t, 2H, J =2.0 Hz, -ArH_{para}), 7.83 (t, 2H, J =2.0 Hz, -ArH_{para}), 8.06 (d, 4H, J = 2.0 Hz, -ArH_{ortho}), 8.07 (d, 4H, J = 2.0 Hz, -ArH_{ortho}), 8.90 (d, 2H, J = 5.0 Hz, -ArH_β), 8.94 (d, 2H, J = 5.0 Hz, -ArH_β), 9.00 (d, 2H, J = 5.0 Hz, -ArH_β), 9.01 (d, 2H, J = 5.0 Hz, -ArH_β), 9.68 (d, 2H, J = 5.0 Hz, -ArH_β), 9.69 (d, 2H, J = 5.0 Hz, -ArH_β), 9.90 (d, 2H, J = 5.0 Hz, -ArH_β), 9.92 (d, 2H, J = 5.0 Hz, -ArH_β). As lit.[9]

Zinc 5,15-Bis-(3,5-bis-*tert*-butyl-phenyl)-10,20-bis-ethynyl-porphyrin dimer ***l*-dP2**
(5 mg, 10%). ^{1}H NMR (400 MHz, $CDCl_3$/1% d_5-pyridine): δ_H 1.56 (s, 72H, -*t*Bu*H*), 4.17 (s, 2H, ≡C*H*), 7.82 (br. s, 4H, -ArH_{para}), 8.05 (br. s, 8H, -ArH_{ortho}), 8.92 (d, 4H, J = 4.5 Hz, -ArH_β), 9.00 (d, 4H, J = 4.5 Hz, -ArH_β), 9.67 (d, 4H, J = 4.5 Hz, -ArH_β), 9.90 (d, 4H, J = 4.5 Hz, -ArH_β). As lit.[9]

Zinc 5,15-bis-(3,5-*tert*-butyl-phenyl)-10,20-trihexylsilanylethynyl-porphyrin dimer ***l*-P4**[9]

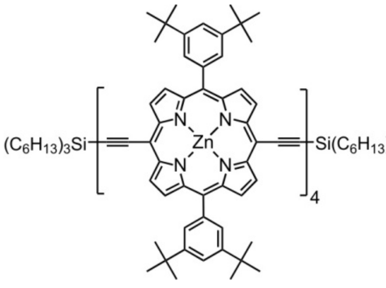

CuCl (76 mg, 0.77 mmol) and *N,N,N',N'*-tetramethylethylenediamine (112 µL, 0.74 mmol) were added to a vigorously stirred solution of monodeprotected porphyrin dimer **7b** (24 mg, 13 µmol) in dry CH_2Cl_2/1% pyridine (32 mL). The reaction mixture was stirred for 10 minutes and then passed through a short plug of silica gel (CH_2Cl_2/1% pyridine) and recrystallized by layer addition (CH_2Cl_2/methanol) gave the product as a brown solid (18 mg, 75%).

^{1}H NMR (500 MHz, $CDCl_3$/1% d_5-pyridine): δ_H 0.92 (t, 18H, J = 7.0 Hz, -CH_3), 1.05 (m, 12H, -CH_2), 1.42 (m, 24H, -CH_2), 1.56 (m, 12H, -CH_2), 1.59 (s, 72H, -*t*Bu*H*), 1.61 (s, 72H, -*t*Bu*H*), 1.81 (m, 12H, -CH_2), 7.85 (t, 4H,J = 2.0 Hz, -ArH_{para}), 7.87 (t, 4H,J = 2.0 Hz, -ArH_{para}), 8.07 (d, 8H, J = 2.0 Hz, -ArH_{ortho}), 8.11 (d, 8H, J = 2.0 Hz, -ArH_{ortho}), 8.88 (d, 4H, J = 5.0 Hz, -ArH_β), 8.98 (d, 4H, J = 5.0 Hz, -ArH_β), 8.99 (d, 4H, J = 5.0 Hz, -ArH_β), 9.00 (d, 4H, J = 5.0 Hz, -ArH_β), 9.67 (d, 4H, J = 5.0 Hz, -ArH_β), 9.90 (d, 4H, J = 5.0 Hz, -ArH_β), 9.91 (d, 4H, J = 5.0 Hz, -ArH_β), 9.92 (d, 4H, J = 5.0 Hz, -ArH_β). As lit.[9]

Zinc (3,5-bis-*tert*-butyl-phenyl)-porphyrin[6] nanoring–template complex ***c*-P6·T6**[4]

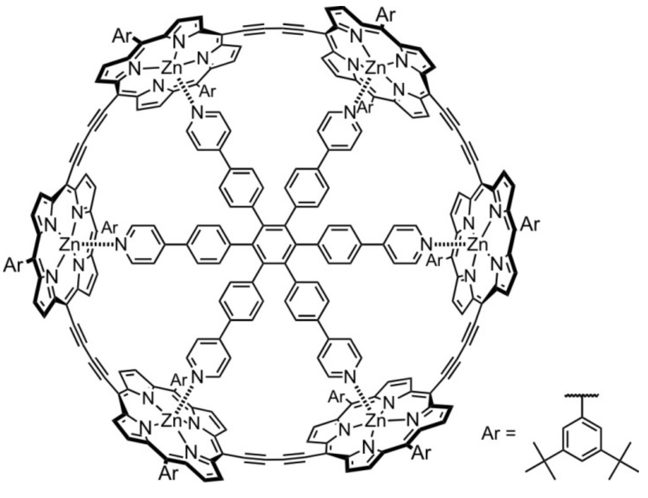

Hexadentate template **T6** (100 mg, 0.100 mmol) and porphyrin monomer ***l*-P1** (370 mg, 0.463 mmol) were dissolved in $CHCl_3$ (500 mL) and sonicated for 30 min (bath sonicator). A catalyst solution was prepared by dissolving $Pd(PPh_3)_2Cl_2$ (108 mg, 0.154 mmol), copper(I) iodide (147 mg, 0.772 mmol) and 1,4-benzoquinone (334 mg, 3.09 mmol) in $CHCl_3$ (90 mL) and freshly distilled di*iso*propylamine

(3.7 mL). The catalyst solution was added to the porphyrin solution, and the mixture was stirred at room temperature for 2 h, and then for 1 h at 50 °C. The mixture was passed through a plug of alumina using $CHCl_3$ as eluent, and purified by size exclusion chromatography on Biobeads SX-1 in toluene. The second band was isolated and recrystallized by layer addition (CH_2Cl_2/methanol) to give ***c*-P6·T6** as a dark brown solid (93 mg, 21%).

^{1}H NMR (400 MHz, $CDCl_3$): δ_H 1.54 (s, 108H, -*t*Bu*H*), 1.58 (s, 108H, -*t*Bu*H*), 2.33 (d, *J* = 7.0 Hz, 12H, -pyridylH_α), 5.00 (d, *J* = 7.0 Hz, 12H, -pyridylH_β), 5.48 (d, *J* = 9.0 Hz, 12H, -Ar*H*), 5.52 (d, *J* = 9.0 Hz, 12H, -Ar*H*), 7.81 (s, 12H, -ArH_{para}), 7.86 (s, 12H, -ArH_{ortho}), 8.05 (s, 12H, -ArH_{ortho}), 8.81 (d, *J* = 4.5 Hz, 24H, -ArH_β), 9.59 (d, *J* = 4.5 Hz, 24H, -ArH_β). As lit.[4]

Zinc (3,5-bis-*tert*-butyl-phenyl)-porphyrin[6] nanoring *c*-P6[4]

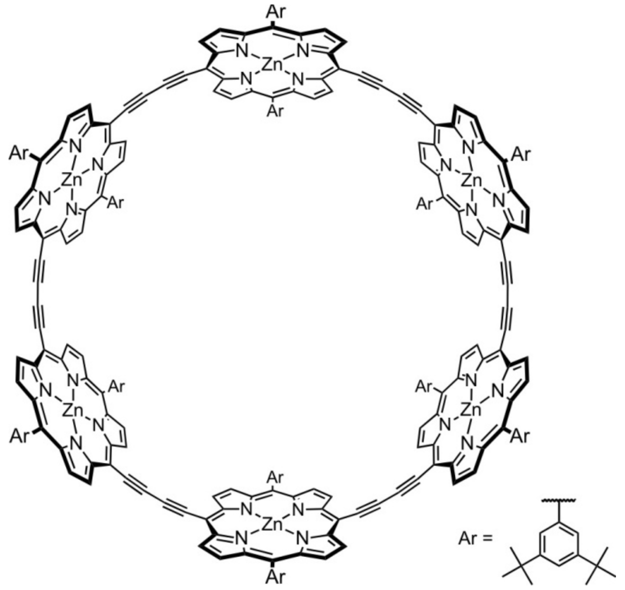

Cyclic hexamer–template complex ***c*-P6·T6** (3.7 mg, 0.64 μmol) was passed through a size exclusion column (Biobeads SX–1) containing a (50 mg mL^{-1}) solution of recrystallized DABCO in freshly distilled tetrahydrofuran. The crude product was recrystallized by layer addition (CH_2Cl_2/methanol) to afford the template-free nanoring as a brownish solid (2.5 mg, 81%).

^{1}H NMR (400 MHz, $CDCl_3$/1% d_5-pyridine): δ_H 1.49 (s, 216 H, -*t*Bu*H*), 7.75 (d, *J* = 1.5 Hz, 12 H, -ArH_{para}), 7.90 (d, *J* = 1.5 Hz, 24 H, -ArH_{ortho}), 8.79 (d, *J* = 4.5 Hz, 24 H, -ArH_β), 9.62 (d, *J* = 4.5 Hz, 24 H, -ArH_β). As lit.[4]

Octyl-4-formylbenzoate 60[10]

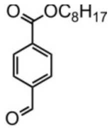

4-Formylbenzoic acid (5 g, 33.3 mmol) and 1-bromooctane (6.3 g, 33.3 mmol) were dissolved in dimethylformamide (120 mL) and K_2CO_3 (9.2 g, 66.6 mmol) added. After stirring at 70 °C for 12 hours the solvent was removed and the residue dissolved in CH_2Cl_2 (100 mL). The solution was washed three times with H_2O (30 mL) and purified by column chromatography on silica gel to give the product as an oily yellowish solid (7.7 g, 88%).

^{1}H NMR (400 MHz, $CDCl_3$) δ_H 0.89 (t, J = 7.0 Hz, 3H, -CH_3), 1.16–1.54 (m, 10H, -CH_2), 1.72–1.87 (m, 2H, -CH_2), 4.36 (t, 2H, J = 7.0 Hz, -OCH_2), 7.96 (d, 2H, J = 8.0 Hz, -Ar*H*), 8.20 (d, 2H, J = 8.0 Hz, -Ar*H*), 10.11 (s, 1H, -CO*H*). As lit.[10]

1,4-Benzenebis(*N*,*N*’-dicyclohexylamidine) BA[11]

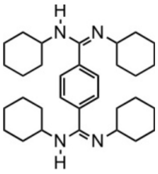

1,4-Dibromobenzene (0.50 g, 2.1 mmol) was dissolved in tetrahydrofuran (10 mL) under inert atmosphere and the solution cooled to -78° C. A solution of *n*-butyllithium (8.0 mL, 1.6 M in hexane, 13 mmol) was added and after stirring for 30 minutes the solution was allowed to warm up to room temperature and was stirred for 1 h. The reaction mixture was cooled to 0° C and a solution of 1,3-dicyclohexylcarbodiimide (2.6 g, 13 mmol) in tetrahydrofuran (5 mL) was added and the reaction mixture was stirred for 12 h. After addition of H_2O (0.25 mL) the mixture was stirred for 10 minutes and the reaction mixture then washed twice with H_2O. The aqueous phases were extracted with diethylether and then the organic phases combined. The solvent was removed and the resulting orange oil dried under high vacuum (190° C, 8×10^{-2} mbar) to remove volatile side-products. The residue was crystallized from diethylether to afford the target compound as white crystals (0.47 g, 45%).

^{1}H NMR (400 MHz, $CDCl_3$) δ_H 1.11–1.25 (m, 40H, -CH_2), 2.98–3.15 (m, 4H, -NC*H*), 7.20 (d, 0.8H, J = 6.0 Hz, -Ar*H*), 7.23 (s, 2H, -Ar*H*), 7.48 (s, 0.4H, -Ar*H*), 7.51 (d, 0.8H, J = 6.0 Hz, -Ar*H*). [comment: at room temperature the compound exists in three conformations that lead to the three sets of signals observed in the aromatic region (see ref. 11): E–E (singlet), Z–Z (singlet), E–Z (two doublets). Addition of a carboxylic acid (e.g. benzoic acid) results in only one singlet from the bisamidine in the aromatic region.] *m/z* (ESI) 491.4098 ($C_{32}H_{51}N_4$, $[M+H]^+$ requires 491.4108, 100%). As lit.**[11]**

8.3 Synthetic Procedures for Novel Compounds

Figure-of-eight complex c-P12·(T6)$_2$

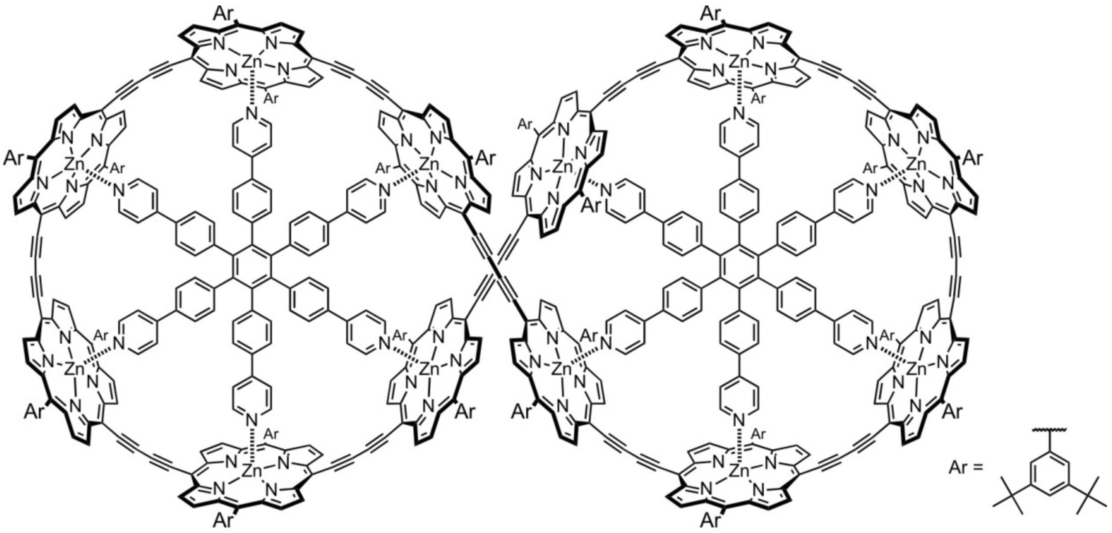

Hexadentate template **T6** (19.5 mg, 19.6 μmol) and deprotected porphyrin tetramer ***l*-dP4** (61.0 mg, 19.1 μmol) were dissolved in $CHCl_3$ (88 mL) and sonicated for 1 h (bath sonicator). A catalyst solution was prepared by dissolving $Pd(PPh_3)_2Cl_2$ (17.7 mg, 25.2 μmol), copper(I) iodide (24.2 mg, 0.127 mmol) and 1,4-benzoquinone (56.1 mg, 0.52 mmol) in $CHCl_3$ (12 mL) and freshly distilled di*iso*propylamine (610 μL). The catalyst solution was added to the template and porphyrin tetramer mixture. The reaction mixture was stirred at room temperature for 1 h and then for 1.5 h at 50 °C under air. The mixture was passed through a plug of alumina using $CHCl_3$ as eluent, and purified by size exclusion chromatography on Biobeads SX-1 in toluene. Recrystallization by layer addition ($CHCl_3$) gave the product as a dark brown solid (29.0 mg, 39%).

^{1}H NMR (700 MHz, $CDCl_3$): δ_H -0.64 (s, 36H, -*t*Bu*H*), 1.14 (s, 36H, -*t*Bu*H*), 1.46 (s, 36H, -*t*Bu*H*), 1.51–1.53 (m, 144H, -*t*Bu*H*), 1.54–1.55 (m, 72H, -*t*Bu*H*), 1.58 (m, 72H, -*t*Bu*H*), 1.70 (s, 36H, -*t*Bu*H*), 2.19–2.22 (m, 24H, -pyridylH_α), 4.81 (d, 8H, J = 9.5 Hz, -pyridylH_β), 4.94–4.97 (m, 16H, -pyridylH_β), 5.22 (d, 4H, J = 9.5 Hz, -Ar*H*), 5.27 (d, 4H, J = 10.0 Hz, -Ar*H*), 5.39 (d, 4H, J = 9.0 Hz, -Ar*H*), 5.42–5.49 (m, 32H, -Ar*H*), 5.53 (d, 4H, J = 10.0 Hz, -Ar*H*), 6.40 (s, 4H, Ar-*H*), 6.98 (s, 4H, -Ar*H*), 7.37 (s, 4H, -Ar*H*), 7.74–7.83 (m, 36H, -Ar*H*), 7.89 (s, 4H, -Ar*H*), 8.02–8.06 (m, 16H, -Ar*H*), 8.08 (d, 4H, J = 4.0 Hz, -ArH_β), 8.11 (s, 4H, -Ar*H*), 8.32 (d, 4H, J = 3.5 Hz, -ArH_β), 8.72 (d, 4H, J = 4.0 Hz, -ArH_β), 8.75–8.80 (m, 28H, -ArH_β), 8.86 (d, 4H, J = 4.5 Hz, -ArH_β), 9.03 (d, 4H, J = 3.5 Hz, -ArH_β), 9.30 (d, 4H, J = 3.5 Hz, -ArH_β), 9.48 (d, 4H, J = 4.0 Hz, -ArH_β), 9.53–9.57 (m, 32H, -ArH_β), 10.16 (d, 4H, J = 3.5 Hz, -ArH_β), 10.92 (d, 4H, J = 4.5 Hz, -ArH_β); *m/z* (MALDI-TOF) 11554 ($C_{768}H_{696}N_{60}Zn_{12}$, M^+ requires 11551, 100%); λ_{max} ($CHCl_3$) / nm (log ε) 497 (5.88), 766 (5.45), 803 (5.54), 882 (5.85), 840 (5.59).

Zinc (3,5-bis-*tert*-butyl-phenyl)-porphyrin[12] nanoring *c*-P12

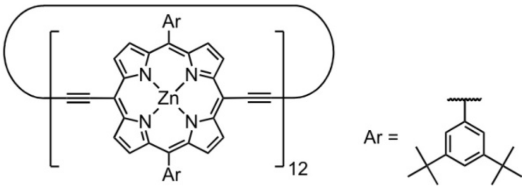

The figure-of-eight complex ***c*-P12·(T6)₂** (3.0 mg, 0.26 mmol) was dissolved in toluene (2 mL) and pyridine (0.2 mL) and passed over a size exclusion column (Biobeads SX-1) using a mixture of toluene and pyridine (10/1 *v/v*) as eluent. Recrystallization by layer addition ($CHCl_3$/methanol) gave the product as a dark brown solid (2.4 mg, 96%).

^{1}H NMR (500 MHz, $CDCl_3$/1% d_5-pyridine): δ_H 1.56 (s, 432H, -*t*Bu*H*), 7.81 (t, 24H, J = 1.5 Hz, -ArH_{para}), 8.05 (d, 48H, J = 1.5 Hz, -ArH_{ortho}), 8.95 (d, 48H, J = 4.5 Hz, -ArH_β), 9.84 (d, 48H, J = 4.5 Hz, -ArH_β); ^{13}C NMR (126 MHz, $CDCl_3$/1% d_5-pyridine): δ_C 32.1, 35.4, 84.3, 100.5, 121.3, 124.0, 125.3, 128.6, 129.4, 131.0, 133.6, 136.3, 141.8, 148.9, 150.0, 150.8, 153.0; *m/z* (MALDI-TOF) 9563 ($C_{624}H_{600}N_{48}Zn_{12}$, M^+ requires 9556, 100%); λ_{max} (toluene/1% pyridine) / nm (log ε) 472 (5.89), 488 (shoulder, 5.86), 816 (5.69).

Zinc (3,5-bis-octyloxy-phenyl)-porphyrin[12] nanoring *c*-P12$_{C8}$

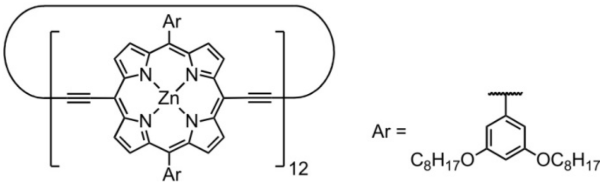

Hexadentate template **T6** (2.5 mg, 2.5 μmol) and deprotected porphyrin tetramer ***l*-dP4$_{C8}$** (10.0 mg, 2.3 μmol) were dissolved in dichloromethane (5 mL) and sonicated for 15 min. The solvent was removed and the residue redissolved in toluene (11 mL). A catalyst solution was prepared by dissolving $Pd(PPh_3)_2Cl_2$ (2.0 mg, 2.8 μmol), copper(I) iodide (2.0 mg, 11 μmol) and 1,4-benzoquinone (7.0 mg, 65 μmol) in toluene (2 mL) and freshly distilled diisopropylamine (80 μL). The catalyst solution was added to the reaction mixture. The reaction mixture was stirred at room temperature for 2 h and then refluxed for 6 h under air. The mixture was passed through a plug of alumina using toluene as eluent, and passed over a size exclusion column on Biobeads SX-1 in toluene. The first band was isolated and passed over a short size exclusion column (toluene/pyridine = 10/1) to remove the template from figure-of-eight. After drying under high vacuum for 1 h, the crude product was redissolved in CH_2Cl_2 and passed over a silica plug (eluent: CH_2Cl_2). Recrystallization by layer addition (CH_2Cl_2/methanol) gave the product as a dark brown solid (3.0 mg, 30%).

^{1}H NMR (400 MHz, $CDCl_3$/1% d_5-pyridine): δ_H 0.84 (t, 144H, *J* = 6.5 Hz, -C*H*$_3$), 1.41–1.25 (m, 384H, -C*H*$_2$), 1.56–1.48 (m, 96H, -C*H*$_2$), 1.93–1.86 (m, 96H, -C*H*$_2$), 4.17 (s br, 96H, -OC*H*$_2$), 6.91 (t, 24H, *J* = 2.0 Hz, -Ar*H*$_{para}$), 7.38 (d, 48H, *J* = 2.0 Hz, -Ar*H*$_{ortho}$), 9.03 (d, 48H, *J* = 4.5 Hz, -Ar*H*$_\beta$), 9.82 (d, 48H, *J* = 4.5 Hz, -Ar*H*$_\beta$); λ_{max} (toluene/1% pyridine) / nm (log ε) 473 (6.02), 491 (6.02), 810 (5.85).

Triethylenegycol-monomethyl-ether-4-formylbenzoate 53

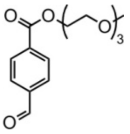

4-Formylbenzoic acid (1.84 g, 12.4 mmol), *N*-(3-Dimethylaminopropyl)-*N*′-ethylcarbodiimide hydrochloride (2.86 g, 14.9 mmol) and 4-(dimethylamino)pyridine (1.82 g, 14.9 mmol) were dried under high vacuum with gentle heating (40–50 °C). Triethylene glycol monomethyl ether (2.45 g, 14.9 mmol) and dry CH_2Cl_2 (120 mL) were added under N_2 atmosphere and the reaction mixture stirred for 14 h. The solvent was removed and the residue dissolved in ethyl acetate (150 mL) and washed twice with 1.0 M HCl (50 mL), twice with saturated aqueous $NaHCO_3$ (50 mL) and once with brine (50 mL). The organic phase was dried with Na_2SO_4 and the solvent removed. The crude product was purified by column chromatography on silica (CH_2Cl_2/ethylacetate = 6/1) to yield the product as a colourless oil (3.76 g, 95%).

R_f = 0.25 in CH_2Cl_2/ethyl acetate = 4/1. ^{1}H NMR (400 MHz, $CDCl_3$) δ_H 3.37 (s, 3H, -OC*H*$_3$), 3.49–3.59 (m, 2H, -OC*H*$_2$), 3.60–3.77 (m, 6H, -OC*H*$_2$), 3.80–3.91 (m, 2H, -OC*H*$_2$), 4.45–4.57 (m, 2H, -OC*H*$_2$), 7.95 (d, *J* = 8.5 Hz, 2H, -Ar*H*), 8.22 (d, *J* = 8.5 Hz, 2H, -Ar*H*), 10.11 (s, 1H, -C*H*O). ^{13}C NMR (101 MHz, $CDCl_3$) δ_C 59.0, 64.9, 69.0, 70.6, 70.6, 70.7, 71.9, 129.4, 130.3, 135.1, 139.1, 165.5, 191.6. *m/z* (ESI) 319.1156 ($C_{15}H_{20}NaO_6$, $[M+Na]^+$ requires 319.1152, 100%).

Free Base 5-(3,5-bis-octyloxy-phenyl)-15-(4-triethylenegycol monomethyl ether benzoate) porphyrin 54

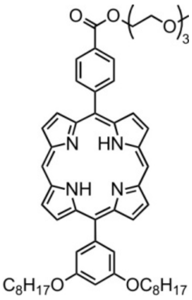

Triethylenegycol monomethyl ether 4-formylbenzoate **53** (2.74 g, 9.25 mmol), 3,5-bis-octyloxy benzaldehyde **2a** (3.05 g, 8.41 mmol) and dipyrromethane **1** (2.46 g, 16.8 mmol) were placed in a dry flask under N_2 and then dissolved in CH_2Cl_2 (1700 mL). The solution was degassed three times by repeated evacuation and purging with nitrogen. Trifluoroacetic acid (0.75 mL, 10.1 mmol) was added and the reaction mixture stirred in the dark for 3 h. DDQ (5.72 g, 25.2 mmol) was added and stirring continued for 0.5 h. After quenching of the acid by addition of triethylamine (10 mL) the solvent was removed and the residue redissolved in CH_2Cl_2 and passed over a short silica plug (CH_2Cl_2/ethyl acetate = 2/1). The crude product was purified by column chromatography on silica gel (CH_2Cl_2/ethyl acetate = 10/1 to 2/1) and subsequent recrystallization from CH_2Cl_2/methanol by layer addition to give the pure product as a pink powder (1.84 g, 23%).

R_f = 0.46 in CH_2Cl_2/EtOAc = 6/1; mp > 250 °C; ^{1}H NMR (400 MHz, $CDCl_3$) δ_H -3.11 (br. s., 2H, -N*H*), 0.84–0.95 (t, *J* = 6.5 Hz, 6H, -CH_3) 1.21–1.46 (m, 16H, -CH_2), 1.48–1.61 (m, 4H,-CH_2), 1.83–1.99 (m, 4H, -CH_2), 3.43 (s, 3H, -OCH_3), 3.57–3.67 (m, 2H, -OCH_2), 3.71–3.93 (m, 6H, -OCH_2), 3.98–4.06 (m, 2H, -OCH_2), 4.18 (t, *J* = 6.5 Hz, 4H, -ArOCH_2), 4.67–4.78 (m, 2H, -COOCH_2), 6.96 (t, *J* = 2.0 Hz, 1H, -ArH_{para}), 7.46 (d, *J* = 2.0 Hz, 2H, -ArH_{ortho}), 8.38 (d, *J* = 8.0 Hz, 2H, -Ar*H*), 8.54 (d, *J* = 8.0 Hz, 2H, -Ar*H*), 9.05 (d, *J* = 4.5 Hz, 2H, -ArH_β), 9.23 (d, *J* = 4.5 Hz, 2H, -ArH_β), 9.41 (m, 4H, -ArH_β), 10.33 (s, 2H, -ArH_{meso}); ^{13}C NMR (126 MHz, $CDCl_3$) δ_C 14.1, 22.6, 26.1, 29.2, 29.4, 31.8, 59.1, 64.5, 68.4, 69.4, 70.7, 70.8, 70.8, 72.0, 101.0, 105.4, 114.6, 117.5, 119.4, 127.8, 128.3, 129.5, 130.1, 130.5, 131.3, 131.6, 131.9, 134.8, 142.9, 145.2, 145.4, 146.4, 146.5, 147.1, 158.6, 166.8; *m/z* (MALDI-TOF) 909.82 ($C_{56}H_{68}N_4O_7$, M+ requires 909.52, 100%); λ_{max} ($CHCl_3$) / nm (log ε) 410 (5.58), 504 (4.25), 540 (3.83), 576 (3.81).

Zinc 5-(3,5-bis-octyloxy-phenyl)-15-(4-triethylenegycol monomethyl ether benzoate) porphyrin 55

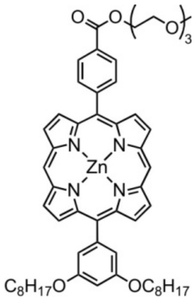

$Zn(OAc)_2{\cdot}2H_2O$ (388 mg, 1.77 mmol) in MeOH (5 mL) was added to a stirred solution of free base porphyrin **54** (805 mg, 0.884 mmol) in $CHCl_3$ (70 mL) and the solution stirred for 1 h at room temperature. The volume was reduced and the reaction mixture passed over a silica plug ($CHCl_3$/pyridine = 10/1) to remove excess $Zn(OAc)_2$. Recrystallization from CH_2Cl_2/methanol gave the product as a red solid (857 mg, 99%).

R_f = 0.10 in PE 40-60/EtOAc/pyridine = 10/1/1; mp > 250 °C; ^{1}H NMR (400 MHz, $CDCl_3$) δ_H 0.89 (t, *J* = 6.5 Hz, 6H, -CH_3), 1.17–1.46 (m, 16H, -CH_2), 1.46–1.61 (m, 4H, -CH_2), 1.81–1.97 (m, 4H, -CH_2), 3.21 (s, 3H, -OC*H*$_3$), 3.34–3.43 (m, 2H, -OC*H*$_2$), 3.47–3.55 (m, 2H, -OC*H*$_2$), 3.56–3.64 (m, 2H, -OC*H*$_2$), 3.66–3.78 (m, 2H, -OC*H*$_2$), 3.82–3.94 (m, 2H, -OC*H*$_2$), 4.16 (t, *J* = 6.5 Hz, 4H, -ArOC*H*$_2$), 4.46–4.65 (m, 2H, -COOC*H*$_2$), 6.92 (t, *J* = 2.0 Hz, 1H, -Ar*H*$_{para}$), 7.45 (d, *J* = 2.0 Hz, 2H, -Ar*H*$_{ortho}$), 8.33 (d, *J* = 8.0 Hz, 2H, -Ar*H*), 8.39 (d, *J* = 8.0 Hz, 2H, -Ar*H*), 9.03 (d, *J* = 4.5 Hz, 2H, -Ar*H*$_β$), 9.25 (d, *J* = 4.5 Hz, 2H, -Ar*H*$_β$), 9.40 (d, *J* = 4.5 Hz, 4H, -Ar*H*$_β$), 10.25 (s, 2H, -Ar*H*$_{meso}$); ^{13}C NMR (126 MHz, CDCl$_3$) δ_C 14.1, 22.6, 26.1, 29.2, 29.4, 29.4, 31.8, 58.9, 64.3, 68.3, 69.3, 70.5, 70.5, 70.5, 70.6, 70.7, 71.8, 71.8, 100.5, 106.0, 114.7, 118.0, 119.9, 121.9, 127.7, 128.9, 130.1, 131.5, 131.7, 131.7, 132.5, 134.7, 135.5, 142.8, 144.7, 148.2, 149.3, 149.3, 149.6, 149.9, 158.2, 166.9; *m/z* (MALDI-TOF) 971.86 ($C_{56}H_{66}N_4O_7Zn$, M+ requires 971.43, 100%); λ_{max} (CHCl$_3$) / nm (log ε) 411 (5.53), 504 (4.24).

Zinc 5-(3,5-bis-octyloxy-phenyl)-15-(4-triethylenegycol monomethyl ether benzoate)-10,20-dibromo porphyrin 56

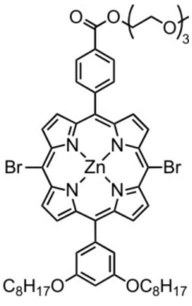

To a solution of zinc porphyrin **55** (840 mg, 0.865 mmol) in CHCl$_3$ (90 mL) and pyridine (0.5 mL) was added dropwise *N*-bromosuccinimide (307 mg, 1.73 mmol) dissolved in CHCl$_3$ (36 mL). After stirring in the dark for 15 minutes, the reaction was quenched by addition of acetone (1 mL). The solvent was removed and the crude product recrystallized from CH$_2$Cl$_2$/methanol to give the title compound as a purple solid (944 mg, 97%).

R$_f$ = 0.19 in PE 40-60/EtOAc/pyridine = 10/1/1; mp > 250 °C; ^{1}H NMR (400 MHz, CDCl$_3$) δ_H 0.88 (t, *J* = 6.5 Hz, 6H, -C*H*$_3$), 1.20–1.45 (m, 16H, -C*H*$_2$), 1.45–1.60 (m, 4H, -C*H*$_2$), 1.81–1.91 (m, 4H, -C*H*$_2$), 3.41 (s, 3H, -OC*H*$_3$), 3.56–3.65 (m, 2H, -OC*H*$_2$), 3.70–3.76 (m, 2H, -OC*H*$_2$), 3.76–3.81 (m, 2H, -OC*H*$_2$), 3.82–3.89 (m, 2H, -OC*H*$_2$), 3.97–4.04 (m, 2H, -OC*H*$_2$), 4.14 (t, *J* = 6.5 Hz, 4H, -ArOC*H*$_2$), 4.61–4.77 (m, 2H, -COOC*H*$_2$), 6.89 (t, *J* = 2.0 Hz, 1H, -Ar*H*$_{para}$), 7.31 (d, *J* = 2.0 Hz, 2H, -Ar*H*$_{ortho}$), 8.23 (d, *J* = 8.0 Hz, 2H, -Ar*H*), 8.45 (d, *J* = 8.0 Hz, 2H, -Ar*H*), 8.80 (d, *J* = 4.5 Hz, 2H, -Ar*H*$_β$), 9.00 (d, *J* = 4.5 Hz, 2H, -Ar*H*$_β$), 9.60 - 9.73 (m, 4H, -Ar*H*$_β$); ^{13}C NMR (126 MHz, CDCl$_3$) δ_C 14.1, 22.7, 26.1, 29.2, 29.4, 31.8, 58.9, 64.3, 68.4, 69.3, 70.5, 70.6, 70.7, 71.8, 100.7, 105.0, 114.6, 120.3, 122.2, 122.5, 127.7, 127.8, 129.2, 130.1, 132.8, 133.0, 133.2, 133.6, 134.5, 136.1, 142.9, 144.1, 147.5, 150.0, 150.1, 150.3, 150.7, 158.1, 166.7; *m/z* (MALDI-TOF) 1130.11 ($C_{56}H_{64}Br_2N_4O_7Zn$, M+ requires 1129.25, 100%); λ_{max} (CHCl$_3$) / nm (log ε) 431 (5.55), 436 (5.53), 572 (4.19), 612 (3.99).

Zinc 5-(3,5-bis-octyloxy-phenyl)-15-(4-triethylenegycol monomethyl ether benzoate)-10,20-bistri*iso*propylsilanylethynyl porphyrin 57

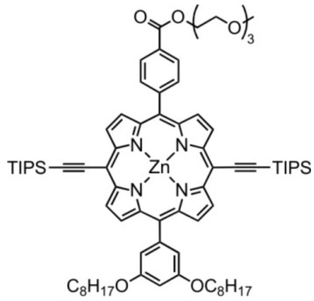

Bromoporphyrin **56** (2.05 g, 1.81 mmol), $Pd(OAc)_2$ (50 mg, 0.22 mmol), PPh_3 (0.12 g, 0.44 mmol) and CuI (35 mg, 0.18 mmol) were placed in a dry flask under N_2 atmosphere and dry tetrahydrofuran (100 mL) was added. After three cycles of degassing by evacuation followed by purging with N_2, (tri*iso*propylsilyl) acetylene (1.20 mL, 5.44 mmol) and dry triethylamine (4.3 mL) were added and the reaction mixture again degassed (3x). After stirring for 3 h at 40 °C TLC confirmed completion of the reaction. The solvent was removed and the crude passed over a silica gel column (PE 40-60/EtOAc/pyridine = 5/1/1). Recrystallization from CH_2Cl_2/methanol gave the product (2.19 g, 91%) as a purple solid.

R_f = 0.6 in PE 40-60/EtOAc/pyridine = 4/1/1; mp > 250 °C; ^{1}H NMR (400 MHz, $CDCl_3$) δ_H 0.87 (t, 6H, J = 6.5 Hz, -CH_2CH_3), 1.27–1.53 (m, 62H, -SiCH, -CHCH_3, -CH_2), 1.84–1.91 (m, 4H, -CH_2), 3.24 (s, 3H, -OCH_3), 3.43–3.46 (m, 2H, -OCH_2), 3.53–3.55 (m, 2H, -OCH_2), 3.59–3.62 (m, 2H, -OCH_2), 3.72–3.74 (m, 2H, -OCH_2), 3.87–3.89 (m, 2H, -OCH_2), 4.13 (t, J = 6.5 Hz, 4H, -ArOCH_2), 4.54–4.56 (m, 2H, -COOCH_2), 6.88 (t, J = 2.0 Hz, 1H, -ArH_{para}), 7.33 (d, J = 2.0 Hz, 2H, -ArH_{ortho}), 8.21 (d, J = 8.0 Hz, 2H, -ArH), 8.31 (d, J = 8.0 Hz, 2H, -ArH), 8.83 (d, J = 4.5 Hz, 2H, -ArH_β), 9.05 (d, J = 4.5 Hz, 2H, -ArH_β), 9.71 (m, 4H, -ArH_β); ^{13}C NMR (126 MHz, $CDCl_3$) δ_C 12.0, 14.2, 19.2, 22.8, 26.3, 29.4, 29.5, 29.6, 32.0, 58.6, 64.0, 68.5, 69.2, 70.0, 70.2, 70.5, 71.5, 98.8, 101.0, 102.0, 109.4, 114.4, 121.2, 122.9, 127.9, 129.1, 131.4, 132.4, 133.2, 134.3, 144.1, 147.2, 149.6, 150.2, 152.6, 152.7, 158.4, 166.6; *m/z* (MALDI-TOF) 1332.35 ($C_{78}H_{106}N_4O_7Si_2Zn$, M+ requires 1333.70, 100%).

Zinc 5-(3,5-bis-octyloxy-phenyl)-15-(4-carboxy-phenyl)-10,20-bistri*iso*propylsilanylethynyl porphyrin ***l*-P1ac**

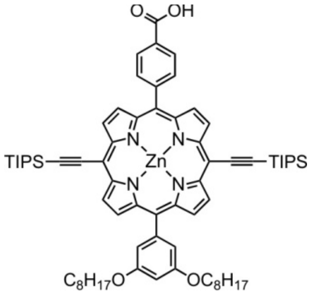

TIPS-protected porphyrin **57** (100 mg, 75.0 μmol) was dissolved in tetrahydrofuran (18 mL) and methanol (9 mL) followed by the addition of 8M NaOH (aqueous solution, 4.5 mL, 36 mmol). The reaction mixture was stirred 3 h. $CHCl_3$ was added to form two phases and the organic phase was separated, then washed twice with 1 M HCl (30 mL) and once with H_2O (30 mL). The crude was passed over a short size-exclusion column (tetrahydrofuran, Biobeads SX-1) and then recrystallized from CH_2Cl_2/methanol to afford the product as a green solid (76 mg, 86%).

mp > 250 °C; ^{1}H NMR (400 MHz, $CDCl_3$) δ_H 0.88 (t, 6H, J = 6.5 Hz, -CH_2CH_3), 1.26–1.55 (m, 62H, -SiCH, -CHCH_3, -CH_2), 1.85–1.92 (m, 4H, -CH_2), 4.14 (t, J = 6.5 Hz, 4H, -ArOCH_2), 6.89 (t, J = 2.0 Hz, 1H, -ArH_{para}), 7.34 (d, J = 2.0 Hz, 2H, -ArH_{ortho}), 8.34 (d, J = 8.0 Hz, 2H, -ArH), 8.54 (d, J = 8.0 Hz, 2H, -ArH), 8.92 (d, J = 4.5 Hz, 2H, -ArH_β), 9.09 (d, J = 4.5 Hz, 2H, -ArH_β), 9.78 (d, J = 4.5 Hz, 2H, -ArH_β), 9.81 (d, J = 4.5 Hz, 2H, -ArH_β); ^{13}C NMR (126 MHz, $CDCl_3$) δ_C 11.0, 13.2, 18.3, 21.8, 25.3, 28.4, 28.5, 28.6, 31.0, 67.6, 98.2, 100.2, 101.3, 108.1, 113.4, 120.1, 122.1, 127.6, 127.7, 130.6, 130.8, 131.5, 132.3, 133.6, 142.8, 147.2, 148.5, 149.3, 151.6, 151.9, 157.5, 169.9; *m/z* (MALDI-TOF) 1186.35 ($C_{71}H_{92}N_4O_4Si_2Zn$, M+ requires 1187.60, 100%); λ_{max} ($CHCl_3$) / nm (log ε) 438 (5.67), 576 (4.28), 618 (4.57).

Zinc 5-(3,5-bis-octyloxy-phenyl)-15-(4-triethylenegycol monomethyl ether benzoate)-10-ethynyl-20-tri*iso*propylsilanylethynyl porphyrin **58**

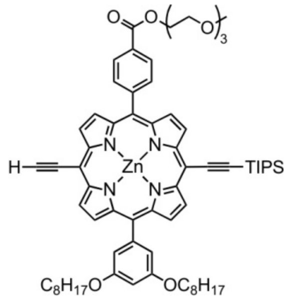

TIPS-protected porphyrin **57** (0.53 g, 0.40 mmol) under N_2 was dissolved in dry CH_2Cl_2 (150 mL). Tetra-*n*-butylammonium fluoride (1M in THF, 0.59 mL, 0.59 mmol) was added and stirred for 50 min when TLC showed a good ratio of products. The reaction was quenched with CH_3COOH (60 µL) and the solvent removed. The crude was passed over a silica gel column (PE 40-60/EtOAc/pyridine = 6/1/1 to 4/1/1) and the second band recrystallized (CH_2Cl_2/methanol) to give the target compound as a green solid (182 mg, 39%).

R_f = 0.4 in PE 40-60/EtOAc/pyridine = 4/1/1; mp > 250 °C; ^{1}H NMR (500 MHz, $CDCl_3$/1% d_5-pyridine) δ_H 0.86 (t, 6H, J = 6.5 Hz, -CH$_2$C*H*$_3$), 1.25–1.53 (m, 41H, -SiC*H*, -CHC*H*$_3$, -C*H*$_2$), 1.84–1.89 (m, 4H, -C*H*$_2$), 3.40 (s, 3H, -OC*H*$_3$), 3.59–3.60 (m, 2H, -OC*H*$_2$), 3.72–3.73 (m, 2H, -OC*H*$_2$), 3.76–3.78 (m, 2H, -OC*H*$_2$), 3.83–3.85 (m, 2H, -OC*H*$_2$), 3.99–4.01 (m, 2H, -OC*H*$_2$), 4.11–4.14 (m, 5H, ≡C*H*, -ArOC*H*$_2$), 4.67–4.69 (m, 2H, -COOC*H*$_2$), 6.87 (br. s, 1H, -ArH_{para}), 7.31 (br. s, 2H, -ArH_{ortho}), 8.23 (d, J = 8.0 Hz, 2H, -Ar*H*), 8.43 (d, J = 8.0 Hz, 2H, -Ar*H*), 8.78–8.79 (m, 2H, -ArH_β), 8.97–8.98 (m, 2H, -ArH_β), 9.63–9.66 (m, 2H, -ArH_β), 9.68–9.70 (m, 2H, -ArH_β); ^{13}C NMR (126 MHz, $CDCl_3$) δ_C 12.0, 14.2, 19.2, 22.8, 26.2, 29.3, 29.5, 29.8, 31.9, 59.2, 64.5, 68.5, 69.5, 70.8, 70.9, 70.9, 72.1, 83.4, 86.8, 97.9, 99.2, 100.7, 101.6, 110.1, 114.6, 120.8, 122.1, 122.6, 127.9, 129.3, 131.0, 131.2, 131.3, 131.8, 132.2, 132.9, 133.0, 134.6, 136.1, 144.4, 147.9, 149.5, 150.2, 150.3, 152.3, 152.4, 152.4, 152.6, 158.2, 158.3, 167.0; *m/z* (MALDI-TOF) 1776.62 ($C_{69}H_{86}N_4O_7SiZn$, M+ requires 1175.56, 100%).

Zinc 5-(3,5-bis-octyloxy-phenyl)-15-(4-triethylenegycol monomethyl ether benzoate)-10,20-tri*iso*propylsilanylethynyl dimer 59

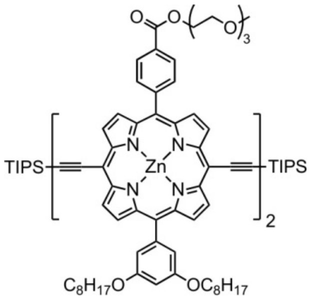

Mono-deprotected porphyrin **58** (0.18 g, 0.16 mmol) was placed in a dry flask equipped with a dry tube, dissolved in dry CH_2Cl_2 (60 mL) and stirred vigorously for 20 minutes. *N,N,N',N'*-tetramethylethylenediamine (0.69 mL, 4.6 mmol) and CuCl (0.46 g, 4.6 mmol) were added and the reaction mixture stirred for 30 minutes when TLC confirmed completion. The reaction mixture was passed over a short silica plug (CH_2Cl_2/1% pyridine) and purified by size-exclusion chromatography (toluene/1% pyridine, Biobeads, SX-1). Recrystallization from CH_2Cl_2/methanol gave the product as a dark green solid (137 mg, 75%).

R_f = 0.35 in PE 40-60/EtOAc/pyridine = 4/1/1; mp > 250 °C; ^{1}H NMR (400 MHz, $CDCl_3$/1% d_5-pyridine) δ_H 0.85 (t, 12H, J = 6.5 Hz, -CH$_2$C*H*$_3$), 1.25–1.54 (m, 82H, -SiC*H*, -CHC*H*$_3$, -C*H*$_2$), 1.84–1.91 (m, 8H, -C*H*$_2$), 3.39 (s, 6H, -OC*H*$_3$), 3.58–3.60 (m, 4H, -OC*H*$_2$), 3.71–3.73 (m, 4H, -OC*H*$_2$), 3.75–3.78 (m, 4H, -OC*H*$_2$), 3.84–3.85 (m, 4H, -OC*H*$_2$), 3.98–4.01 (m, 4H, -OC*H*$_2$), 4.14 (t, 8H, J = 6.5

Hz, -ArOCH_2), 4.67–4.69 (m, 4H, -COOCH_2), 6.89 (t, 2H, *J* = 2.0 Hz, -ArH_{para}), 7.34 (d, 4H, *J* = 2.0 Hz, -ArH_{ortho}), 8.27 (d, 4H, *J* = 8.0 Hz, -Ar*H*), 8.46 (d, 4H, *J* = 8.0 Hz, -Ar*H*), 8.78 (d, 2H, *J* = 4.5 Hz, -ArH_β), 8.86 (d, 2H, *J* = 4.5 Hz, -ArH_β), 8.97 (d,2H, *J* = 4.5 Hz, -ArH_β), 9.06 (d,2H, *J* = 4.4 Hz, -ArH_β), 9.67–9.70 (m, 4H, -ArH_β), 9.85–9.88 (m, 4H, -ArH_β); ^{13}C NMR (126 MHz, $CDCl_3$/1% d_5-pyridine) δ_C 12.0, 14.2, 19.2, 22.7, 26.2, 29.3, 29.5, 31.9, 59.2, 64.5, 68.5, 69.5, 70.8, 70.9, 70.9, 72.1, 82.4, 88.4, 98.3, 99.6, 100.7, 102.2, 110.0, 114.6, 121.4, 123.2, 127.9, 130.9, 131.1, 131.2, 131.4, 132.1, 132.5, 132.9, 133.3, 134.6, 135.8, 136.0, 144.4, 147.8, 149.7, 149.9, 150.5, 152.4, 152.7, 153.1, 153.4, 158.3, 167.0; *m/z* (MALDI-TOF) 2357.87 ($C_{138}H_{170}N_8O_{14}Si_2Zn_2$, M+ requires 2352.10, 100%).

Zinc 5-(3,5-bis-octyloxy-phenyl)-15-(4-triethylenegycol monomethyl ether benzoate)-10,20-ethynyl dimer *l*-P2ac

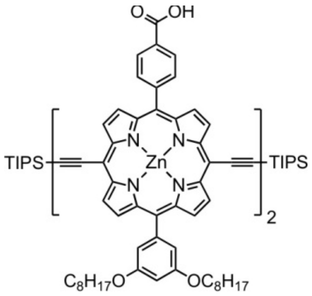

TIPS-protected porphyrin dimer **58** (40 mg, 17.0 μmol) was dissolved in tetrahydrofuran (8 mL) and methanol (4 mL) followed by the addition of 8M NaOH (aqueous solution, 2 mL, 17 mmol). The reaction mixture was stirred 3 h when MALDI confirmed completion. $CHCl_3$ was added to form two phases and the organic phase was separated, then washed twice with 1 M HCl (20 mL) and once with H_2O (20 mL). The crude was passed over a short size-exclusion column (tetrahydrofuran, Biobeads SX-1) and then recrystallized from CH_2Cl_2/methanol to afford the product as a green solid (27 mg, 78%).

mp > 250 °C; ^{1}H NMR (400 MHz, $CDCl_3$/1% d_5-pyridine) δ_H 0.85 (t, 12H, *J* = 6.5 Hz, -CH$_2$CH_3), 1.25–1.54 (m, 82H, -SiC*H*, -CHCH_3, -CH_2), 1.84–1.91 (m, 8H, -CH_2), 4.14 (t, 8H, *J* = 6.5 Hz, -ArOCH_2), 6.89 (t, 2H, *J* = 2.0 Hz, -ArH_{para}), 7.35 (d, 4H, *J* = 2.0 Hz, -ArH_{ortho}), 8.29 (d, 4H, *J* = 8.0 Hz, -Ar*H*), 8.53 (d, 4H, *J* = 8.0 Hz, -Ar*H*), 8.84 (d, 2H, *J* = 4.5 Hz, -ArH_β), 8.91 (d, 2H, *J* = 4.5 Hz, -ArH_β), 8.97 (d,2H, *J* = 4.5 Hz, -ArH_β), 9.06 (d,2H, *J* = 4.4 Hz, -ArH_β), 9.68–9.70 (m, 4H, -ArH_β), 9.86–9.89 (m, 4H, -ArH_β); ^{13}C NMR (126 MHz, $CDCl_3$/1% d_5-pyridine) δ_C 12.0, 14.2, 19.2, 22.7, 26.2, 29.3, 29.5, 29.5, 31.9, 68.5, 82.4, 88.5, 98.1, 99.5, 100.8, 102.1, 110.1, 114.6, 121.9, 123.8, 128.0, 130.9, 131.1, 131.2, 131.3, 132.3, 132.7, 132.8, 133.2, 134.5, 144.4, 147.0, 149.5, 150.4, 152.4, 152.6, 153. 1, 153.3, 158.3, 169.7; *m/z* (MALDI-TOF) 2057.86 ($C_{124}H_{142}N_8O_8Si_2Zn_2$, M+ requires 2059.92, 100%); λ_{max} ($CHCl_3$) / nm (log ε) 461 (5.63), 496 (5.37), 589 (4.37), 670 (4.92), 737 (5.07).

Zinc 5-(3,5-bis-octyloxy-phenyl)-15-(4-triethylenegycol monomethyl ether benzoate)-10,20-bistrihexylsilanylethynyl porphyrin 65a

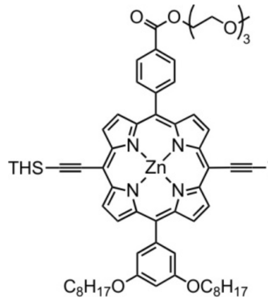

Bromoporphyrin **56** (622 mg, 0.550 mmol), $Pd(OAc)_2$ (7.5 mg, 0.033 mmol), PPh_3 (17.3 mg, 0.067 mmol) and CuI (5.2 mg, 0.028 mmol) were placed in a dry flask under N_2 atmosphere and dry tetrahydrofuran (30 mL) was added. After three cycles of degassing by evacuation followed by purging with N_2, ethynyltrihexylsilane (0.64 mL, 1.65 mmol) and dry triethylamine (1.3 mL) were added and the reaction mixture again degassed (3x). After stirring for 3 h at 40°C TLC confirmed completion of the reaction. The solvent was removed and the crude passed over a silica gel column (PE 40-60/EtOAc/pyridine = 5/1/1). Recrystallization from CH_2Cl_2/methanol gave the product (672 mg, 77%) as a green solid.

R_f = 0.52 in PE 40-60/EtOAc/pyridine = 10/1/1; mp > 250 °C; ^{1}H NMR (400 MHz, $CDCl_3$) δ_H 0.78–0.97 (m, 24H, -CH_3), 0.97–1.10 (m, 12H, -SiCH_2), 1.16–1.63 (m, 56H, -CH_2), 1.66–1.83 (m, 12H, -CH_2), 1.83–1.99 (m, 4H, -CH_2), 3.31 (s, 3H, -OCH_3), 3.47–3.56 (m, 2H, -OCH_2), 3.58–3.66 (m, 2H, -OCH_2), 3.67–3.73 (m, 2H, -OCH_2), 3.75–3.82 (m, 2H, -OCH_2), 3.90–3.99 (m, 2H, -OCH_2), 4.14 (t, *J* = 6.5 Hz, 4H, -ArOCH_2), 4.54–4.70 (m, 2H, -COOCH_2), 6.90 (t, *J* = 2.0 Hz, 1H, -ArH_{para}), 7.34 (d, *J* = 2.0 Hz, 2H, -ArH_{ortho}), 8.25 (d, *J* = 8.0 Hz, 2H, -Ar*H*), 8.41 (d, *J* = 8.0 Hz, 2H, -Ar*H*), 8.84 (d, *J* = 4.5 Hz, 2H, -ArH_β), 9.05 (d, *J* = 4.5 Hz, 2H, -ArH_β), 9.71 (m, 4H, -ArH_β); ^{13}C NMR (126 MHz, $CDCl_3$) δ_C 12.3, 12.8, 13.6, 13.8, 13.9, 14.1, 14.2, 22.1, 22.6, 22.7, 22.8, 23.2, 24.1, 24.4, 26.1, 29.2, 29.4, 30.9, 31.7, 31.7, 31.8, 32.5, 33.3, 33.7, 58.7, 64.2, 68.4, 68.4, 69.2, 70.2, 70.4, 70.5, 71.5, 100.4, 100.9, 101.7, 108.5, 114.2, 114.3, 121.0, 122.3, 122.7, 127.8, 129.2, 131.3, 131.5, 132.1, 132.8, 134.3, 143.1, 143.9, 147.3, 149.4, 150.1, 152.3, 152.5, 158.3, 166.6; *m/z* (MALDI-TOF) 1587.33 ($C_{96}H_{142}N_4O_7Si_2Zn$, M+ requires 1585.91, 100%); λ_{max} ($CHCl_3$) / nm (log ε) 444 (5.53), 456 (5.25), 626 (sh, 4.15), 643 (4.50).

Zinc 5-(3,5-bis-octyloxy-phenyl)-15-(4-triethylenegycol monomethyl ether benzoate)-10-ethynyl-20-trihexylsilanylethynyl porphyrin 66a

Zinc 5-(3,5-bis-octyloxy-phenyl)-15-(4-triethylenegycol monomethyl ether benzoate)-10,20-bisethynyl porphyrin d65a

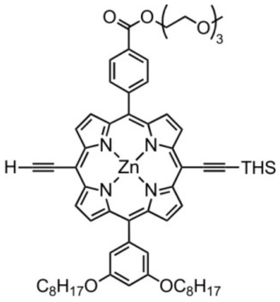

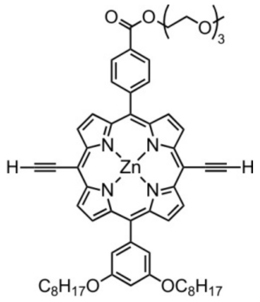

THS-acetylene porphyrin **65a** (1.16 g, 0.728 mmol) under N_2 in a dry flask was dissolved in CH_2Cl_2 (90 mL) and $CHCl_3$ (90 mL). Tetra-*n*-butylammonium fluoride (1M in THF, 1.24 mL, 1.24 mmol) was added and stirred for 30 min when TLC showed a good ratio of products. The reaction was quenched with CH_3COOH (80 μL) and the solvent removed. The crude was passed over a silica gel column (PE 40-60/EtOAc/pyridine = 10/1/1 to 5/1/1) and the three fractions recrystallized from CH_2Cl_2/methanol to give:

Recovered starting porphyrin **65a**: 256 mg, 22%.

Zinc 5-(3,5-bis-octyloxy-phenyl)-15-(4-triethylenegycol monomethyl ether benzoate)-10-ethynyl-20-trihexylsilanylethynyl porphyrin **66a** (361 mg, 38%): R_f = 0.49 in PE 40-60/EtOAc/pyridine = 5/1/1; mp > 250 °C^{1}H NMR (400 MHz, $CDCl_3$) δ_H 0.80–0.97 (m, 15H, -CH_3), 0.97–1.09 (m, 6H, -SiCH_2), 1.20–1.47 (m, 28H, -CH_2), 1.47–1.64 (m, 10H, -CH_2), 1.70–1.83 (m, 6H, -CH_2), 1.83–1.96 (m, 4H, -CH_2), 3.41 (s, 3H, -OCH_3), 3.55–3.64 (m, 2H, -OCH_2), 3.70–3.76 (m, 2H, -OCH_2), 3.76–3.82 (m, 2H, -OCH_2), 3.82–3.91 (m, 2H, -OCH_2), 3.96–4.06 (m, 2H, -OCH_2), 4.13 (s, 1H, ≡C*H*), 4.14–4.20 (m, 4H, -ArOCH_2), 4.63–4.75 (m, 2H, -COOCH_2), 6.89 (t, *J* = 2.0 Hz, 1H, -ArH_{para}), 7.33 (d, *J* = 2.0 Hz, 2H, -ArH_{ortho}), 8.25 (d, *J* = 8.0 Hz, 2H, -Ar*H*), 8.45 (d, *J* = 8.0 Hz, 2H, -Ar*H*), 8.79 (m, 2H, -ArH_β), 8.94–9.02 (m, 2H, -ArH_β), 9.60–9.73 (m, 4H, -ArH_β); ^{13}C NMR (126 MHz, $CDCl_3$) δ_C 13.8, 14.1, 14.2, 22.7, 22.7, 24.4, 26.1, 29.2, 29.4, 30.9, 31.7, 31.8, 33.3, 59.1, 64.4, 68.4, 69.4, 70.7, 70.8, 70.8, 72.0, 83.3, 86.7, 99.1, 99.7, 100.6, 101.4, 109.2, 114.5, 120.7, 122.5, 122.8, 127.8, 129.2, 130.9, 131.0, 131.1, 131.3, 131.8, 132.1, 132.6, 132.8, 134.5, 135.9, 144.3, 145.3, 147.8, 149.4, 150.1, 150.1, 152.2, 152.2, 152.4, 152.5, 158.2, 166.9; *m/z* (MALDI-TOF) 1305.61 ($C_{78}H_{104}N_4O_7SiZn$, M+ requires 1303.71, 100%); λ_{max} ($CHCl_3$) / nm (log ε) 441 (5.35), 578 (4.07), 637 (4.26).

Zinc 5-(3,5-bis-octyloxy-phenyl)-15-(4-triethylenegycol monomethyl ether benzoate)-10,20-bisethynyl porphyrin **d65a** (132 mg, 18%): R_f = 0.29 in PE 40-60/EtOAc/pyridine = 5/1/1; mp > 250 °C; ^{1}H NMR (400 MHz, $CDCl_3$) δ_H 0.79–0.97 (m, 6H, -CH_3), 1.19–1.43 (m, 16H, -CH_2), 1.43–1.70 (m, 4H, -CH_2), 1.83–1.98 (m, 4H, -CH_2), 3.41 (s, 3H, -OCH_3), 3.57–3.66 (m, 2H, -OCH_2), 3.70–3.76

(m, 2H, -OCH_2), 3.76–3.82 (m, 2H, -OCH_2), 3.83–3.90 (m, 2H, -OCH_2), 3.97–4.06 (m, 2H, -OCH_2), 4.16 (s, 2H, ≡CH), 4.16 (t, J = 8.0 Hz, 4H, -ArOCH_2), 4.63–4.75 (m, 2H, -COOCH_2), 6.89 (s, 1H, -ArH_{para}), 7.33 (d, J = 2.0 Hz, 2H, -ArH_{ortho}), 8.26 (d, J = 8.0 Hz, 2H, -ArH), 8.45 (d, J = 8.0 Hz, 2H, -ArH), 8.81 (d, J = 4.5 Hz, 2H, -ArH_β), 9.00 (d, J = 4.5 Hz, 2H, -ArH_β), 9.61–9.74 (m, 4H, -ArH_β); ^{13}C NMR (126 MHz, $CDCl_3$) δ_C 14.1, 22.6, 26.1, 29.2, 29.4, 31.8, 59.1, 64.4, 68.4, 69.4, 70.7, 70.7, 70.8, 72.0, 83.4, 86.6, 99.4, 100.6, 114.5, 120.7, 122.4, 122.5, 127.8, 129.2, 130.1, 131.0, 131.2, 132.1, 132.9, 134.5, 135.9, 143.9, 144.3, 147.7, 149.5, 150.2, 152.2, 152.4, 158.1, 166.8; m/z (MALDI-TOF) 1020.06 ($C_{60}H_{66}N_4O_7Zn$, M+ requires 1019.43, 100%); λ_{max} ($CHCl_3$) / nm (log ε) 438 (5.27), 572 (4.15), 631 (4.12).

Zinc 5-(3,5-bis-octyloxy-phenyl)-15-(4-triethylenegycol monomethyl ether benzoate)-10,20-trihexylsilanylethynyl porphyrin dimer 67a

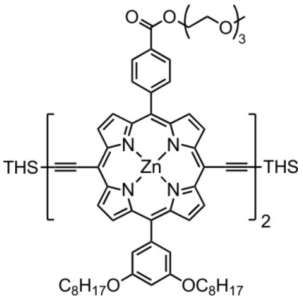

Mono-deprotected porphyrin **66a** (85 mg, 0.0652 mmol) was placed in a dry flask equipped with a dry tube, dissolved in dry CH_2Cl_2 (25 mL) and stirred vigorously for 15 minutes. *N,N,N',N'*-tetramethylethylenediamine (0.29 mL, 1.96 mmol) and CuCl (194 mg, 1.96 mmol) were added and the reaction mixture stirred for 15 minutes when TLC confirmed completion. The solvent was removed and the product isolated by column chromatography on silica gel (PE 40-60/EtOAc/pyridine = 7/1/1). Recrystallization from CH_2Cl_2/methanol gave the product as a dark green solid (62 mg, 73%).

R_f = 0.40 in PE 40-60/EtOAc/pyridine = 5/1/1; mp > 250 °C; ^{1}H NMR (400 MHz, $CDCl_3$/1% d_5-pyridine) δ_H 0.77–0.98 (m, 30H, -CH_3), 0.98–1.11 (m, 12H, -SiCH_2), 1.25–1.47 (m, 56H, -CH_2), 1.48–1.63 (m, 20H, -CH_2), 1.68–1.84 (m, 12H, -CH_2), 1.84–1.98 (m, 8H, -CH_2), 3.40 (s, 6H, -OCH_3), 3.55–3.65 (m, 4H, -OCH_2), 3.69–3.75 (m, 4H, -OCH_2), 3.75–3.82 (m, 4H, -OCH_2), 3.82–3.90 (m, 4H, -OCH_2), 3.97–4.05 (m, 4H, -OCH_2), 4.16 (t, J = 6.5 Hz, 8H, -ArOCH_2), 4.64–4.77 (m, 4H, -COOCH_2), 6.91 (t, J = 2.0 Hz, 2H, -ArH_{para}), 7.37 (d, J = 2.0 Hz, 4H, -ArH_{ortho}), 8.30 (d, J = 8.0 Hz, 4H, -ArH), 8.48 (d, J = 8.0 Hz, 4H, -ArH), 8.79 (d, J = 4.5 Hz, 2H, -ArH_β), 8.88 (d, J = 4.5 Hz, 2H, -ArH_β), 8.98 (d, J = 4.5 Hz, 2H, -ArH_β), 9.08 (d, J = 4.4 Hz, 2H, -ArH_β), 9.63–9.70 (m, 4H, -ArH_β), 9.85–9.93 (m, 4H, -ArH_β); ^{13}C NMR (126 MHz, $CDCl_3$/1% d_5-pyridine) δ_C 8.9, 11.4, 13.8, 13.9, 14.1, 14.1, 14.2, 14.3, 15.1, 18.8, 19.4, 20.4, 22.2, 22.3, 22.6, 22.7, 22.7, 24.4, 25.8, 26.1, 27.7, 28.9, 29.1, 29.2, 29.4, 29.7, 30.3, 31.7, 31.8, 33.4, 33.7, 34.1, 36.1, 36.3, 41.3, 44.7, 59.0, 64.3, 64.4, 68.4, 69.3, 70.6, 70.7, 70.8, 71.9, 82.3, 88.2, 99.6, 100.3, 100.7, 102.1, 103.6, 109.0, 114.5, 121.4, 122.5, 123.1, 127.9, 129.2, 130.9, 131.0, 131.3, 131.4, 132.0, 132.5, 132.7, 133.2, 134.4, 136.1, 143.2, 144.1, 147.6, 149.2, 149.6, 149.9, 150.4, 152.3, 152.5, 153.0, 153.2, 158.2, 166.8; *m/z* (MALDI-TOF) 2607.95 ($C_{156}H_{206}N_8O_{14}Si_2Zn_2$, M+ requires 2604.39, 100%); λ_{max} ($CHCl_3$) / nm (log ε) 461 (5.56), 495 (5.18), 585 (4.28), 669 (4.84), 722 (4.85).

Zinc 5-(3,5-bis-octyloxy-phenyl)-15-(4-triethylenegycol monomethyl ether benzoate)-10,20-bisethynyl porphyrin dimer 68a

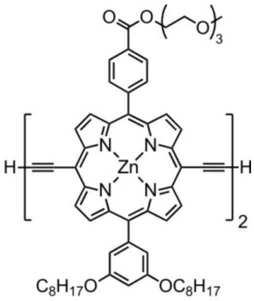

Porphyrin dimer **67a** (110 mg, 42.2 μmol) under N_2 was dissolved in dry CH_2Cl_2 (20 mL) and tetra-*n*-butylammonium fluoride (1M in THF, 85 μL, 85 μmol) added. After stirring at 30°C for 30 minutes the reaction was quenched by adding $CaCl_2$. The volume was reduced and the reaction mixture passed over a short silica plug (CH_2Cl_2/pyridine = 50/1). Recrystallization from CH_2Cl_2/methanol gave the title compound as a dark green solid (69 mg, 80%).

R_f = 0.30 in PE 40-60/EtOAc/pyridine = 3/1/1; mp > 250 °C; λ_{max} ($CHCl_3$) / nm (log ε) 458 (5.39), 492 (5.07), 582 (4.17), 661 (4.72), 712 (4.74); ^{1}H NMR (400 MHz, $CDCl_3$) δ_H 0.87 (t, *J* = 7.0, 12H, -C*H*$_3$), 1.19–1.42 (m, 32H, -C*H*$_2$), 1.47–1.58 (m, 8H, -C*H*$_2$), 1.83–1.94 (m, 8H, -C*H*$_2$), 3.40 (s, 6H, -OC*H*$_3$), 3.57–3.64 (m, 4H, -OC*H*$_2$), 3.69–3.75 (m, 4H, -OC*H*$_2$), 3.75–3.81 (m, 4H, -OC*H*$_2$), 3.81–3.89 (m, 4H, -OC*H*$_2$), 3.97–4.05 (m, 4H, -OC*H*$_2$), 4.16 (t, *J* = 6.5 Hz, 8H, -ArOC*H*$_2$), 4.18 (s, 2H, ≡C*H*), 4.65–4.74 (m, 4H, -COOC*H*$_2$), 6.91 (d, *J* = 2.0 Hz, 2H, -ArH_{para}), 7.36 (d, *J* = 2.0 Hz, 4H, -ArH_{ortho}), 8.29 (d, *J* = 8.0 Hz, 4H, -Ar*H*), 8.48 (d, *J* = 8.0 Hz, 4H, -Ar*H*), 8.80 (d, *J* = 4.5 Hz, 2H, -ArH_β), 8.89 (d, *J* = 4.5 Hz, 2H, -ArH_β), 8.99 (d, *J* = 4.5 Hz, 2H, -ArH_β), 9.08 (d, *J* = 4.5 Hz, 2H, -ArH_β), 9.67 (m, 4H, -ArH_β), 9.87–9.94 (m, 4H, -ArH_β); ^{13}C NMR (126 MHz, $CDCl_3$) δ_C 14.1, 22.6, 26.1, 29.2, 29.4, 31.8, 59.1, 64.4, 68.4, 69.4, 70.6, 70.7, 70.8, 72.0, 82.3, 83.6, 86.5, 88.2, 99.7, 100.0, 100.6, 114.5, 121.3, 123.0, 127.8, 129.3, 130.9, 131.0, 131.2, 132.1, 132.4, 132.9, 133.2, 134.5, 144.2, 147.6, 149.7, 150.0, 150.4, 152.2, 152.5, 152.9, 153.2, 158.2, 166.8; *m/z* (MALDI-TOF) 2041.70 ($C_{120}H_{128}N_8O_{14}Zn_2$, M+ requires 2037.82, 100%); λ_{max} ($CHCl_3$) / nm (log ε) 458 (5.39), 492 (5.07), 582 (4.17), 661 (4.72), 712 (4.74).

Zinc 5-(3,5-bisoctyloxy phenyl)-15-(4-triethylenegycol monomethyl ether benzoate)-porphyrin[6] nanoring–template complex **69a·T6**

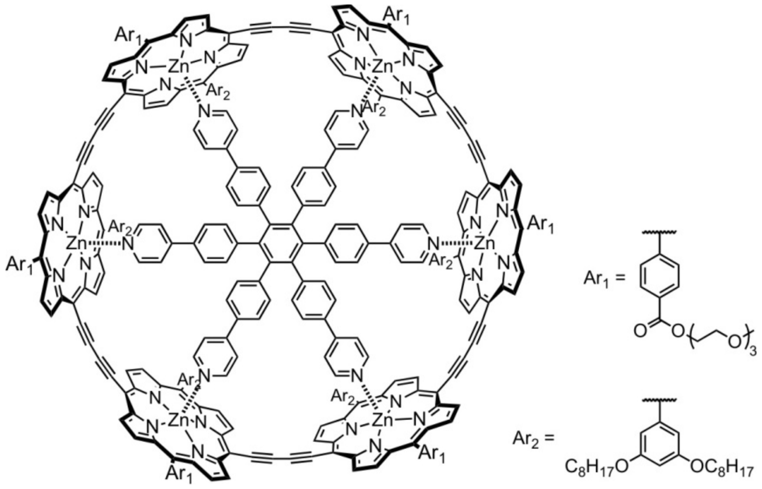

Deprotected porphyrin dimer **68a** (69 mg, 33.8 μmol) and hexadentate template **T6** (11 mg, μmol) were dissolved in dry CH_2Cl_2 (10 mL) and sonicated for 20 minutes. The solvent was removed and the residue dried under high vacuum. $Pd(PPh_3)_2Cl_2$ (11 mg, 15 μmol), CuI (5.0 mg, 28 μmol) and I_2 (33 mg, 0.13 mmol) were dissolved in dry toluene (16 mL) and $^{i}Pr_2NH$ (1.2 mL) added. The resulting orange solution was added to the dried reactants (under air) and the mixture sonicated for 15 minutes. The reaction mixture (in a flask with dry tube) was stirred at 60 °C for 2 h. The solvent was removed and the crude passed over a short silica plug (toluene/triethylamine = 10/1). After purification by size exclusion chromatography (tetrahydrofuran, Biobeads SX-1) and recrystallization from CH_2Cl_2/methanol the pure product was obtained as a brown solid (25 mg, 32%).

R_f = 0.30 in PE 40-60/EtOAc/pyridine = 3/1/1; mp > 250 °C; ^1H NMR (500 MHz, $CDCl_3$) δ_H 0.78–0.95 (m, 36H, -C*H*$_3$), 1.20–1.52 (m, 120H, -C*H*$_2$), 1.78–1.98 (m, 24H, -C*H*$_2$), 2.26 (d, *J* = 7.0 Hz, 12H, -pyridylH_α), 3.43 (m, 18H, -OC*H*$_3$), 3.59–3.68 (m, 12H, -OC*H*$_2$), 3.72–3.79 (m, 12H, -OC*H*$_2$), 3.79–3.84 (m, 12H, -OC*H*$_2$), 3.86–3.91 (m, 12H, -OC*H*$_2$), 4.00–4.06 (m, 12H, -OC*H*$_2$), 4.09 (t, *J* = 6.5 Hz, 12H, -ArOC*H*$_2$), 4.21 (t, *J* = 6.5 Hz, 12H, -ArOC*H*$_2$), 4.69–4.76 (m, 12H, -COOC*H*$_2$), 5.02 (d, *J* = 7.0 Hz, 12H, -pyrdiylH_β), 5.48 (d, *J* = 8.5 Hz, 12H, -Ar*H*), 5.55 (d, *J* = 7.5 Hz, 12H, -Ar*H*), 6.90 (s, 6H, -Ar*H*), 7.11 (s, 6H, -Ar*H*), 7.38 (t, *J* = 4.5 Hz, 6H, -Ar*H*), 8.08 (d, *J* = 6.5 Hz, 6H, -Ar*H*), 8.28 (d, *J* = 6.5 Hz, 6H, -Ar*H*), 8.40–8.50 (m, 12H, -Ar*H*), 8.68 (d, *J* = 4.0 Hz, 12H, -ArH_β), 8.86 (d, *J* = 2.5 Hz, 12H, -ArH_β), 9.55 (d, *J* = 4.5 Hz, 12H, -ArH_β), 9.57 (d, *J* = 4.5 Hz, 12H, -ArH_β). ^{13}C NMR (126 MHz, $CDCl_3$) δ_C 12.3, 12.8, 13.6, 13.8, 13.9, 14.1, 14.2, 22.1, 22.6, 22.7, 22.8, 23.2, 24.1, 24.4, 26.1, 29.2, 29.4, 30.9, 31.7, 31.7, 31.8, 32.5, 33.3, 33.7, 58.7, 58.8, 64.2, 64.3, 68.4, 68.4, 69.2, 69.3, 70.2, 70.4, 70.5, 70.7, 71.5, 71.7, 99.8, 100.1, 100.4, 100.6, 100.9, 101.7, 108.5, 114.3, 120.1, 121.0, 121.9, 122.3, 122.7, 127.8, 129.2, 131.2, 131.3, 131.5, 132.1, 132.8, 134.3, 135.9, 143.1, 143.9, 147.3, 149.4, 150.1, 152.3, 152.5, 158.3, 166.6; *m/z* (MALDI-TOF) 7107.9 ($C_{432}H_{432}N_{30}O_{42}Zn_6$, M+ requires

7107.8, 100%); λ_{max} ($CHCl_3$) / nm (log ε) 485 (5.74), 432 (sh, 5.46), 612 (4.61), 719 (sh, 4.97), 762 (5.56), 798 (5.69), 839 (5.62), 891 (sh, 4.65).

Zinc 5-(3,5-bisoctyloxy phenyl)-15-(4-triethylenegycol monomethyl ether benzoate)-porphyrin[6] nanoring–template complex **69a**

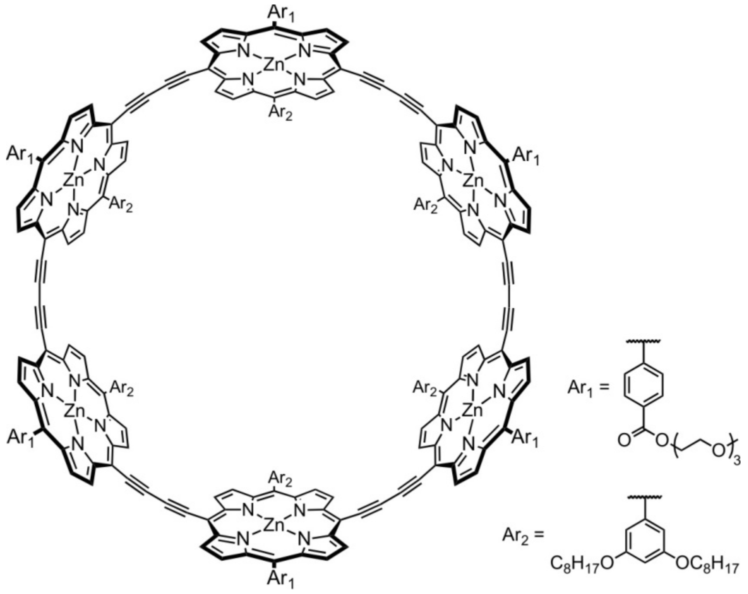

Cyclic hexamer–template complex **69a·T6** (4.0 mg, 0.56 µmol) was passed through a size exclusion column (Biobeads SX–1) containing a (50 mg mL^{-1}) solution of recrystallized DABCO in freshly distilled tetrahydrofuran. The crude product was recrystallized by layer addition (CH_2Cl_2/methanol) to afford the template-free nanoring as a brownish solid (3.0 mg, 87%).

mp > 250 °C; ^1H NMR (500 MHz, $CDCl_3$/1% d_5-pyridine) δ_H 0.76 (t, 36H, J = 6.5 Hz, -CH_3), 1.16–1.32 (m, 96H, -CH_2), 1.39–1.45 (m, 24H, -CH_2), 1.76–1.83 (m, 24H, -CH_2), 3.35 (s, 18H, -OCH_3), 3.55–3.57 (m, 12H, -OCH_2), 3.68–3.70 (m, 12H, -OCH_2), 3.73–3.75 (m, 12H, -OCH_2), 3.80–3.82 (m, 12H, -OCH_2), 3.96–3.97 (m, 12H, -OCH_2), 4.05 (t, 24H, J = 6.5 Hz, -ArOCH_2), 4.64–4.66 (m, 12H, -COOCH_2), 6.83 (t, 6H, J = 2.0 Hz, -ArH_{para}), 7.19 (d, 12H, J = 2.0 Hz, -ArH_{ortho}), 8.12 (d, 12H, J = 5.0 Hz, -ArH), 8.38 (d, 12H, J = 5.0 Hz, -ArH), 8.67 (d, 12H, J = 4.0 Hz, -ArH_β), 8.86 (d, 12H, J = 4.0 Hz, -ArH_β), 9.59 (d, 12H, J = 4.5 Hz, -ArH_β), 9.62 (d, 12H, J = 4.5 Hz, -ArH_β). ^{13}C NMR (126 MHz, $CDCl_3$/1% d_5-pyridine) δ_C 14.1, 22.6, 25.7, 26.1, 29.2, 29.4, 29.7, 31.8, 46.6, 59.1, 64.5, 68.0, 68.4, 69.4, 70.6, 70.7, 70.8, 70.9, 72.0, 88.5, 94.5, 100.8, 114.3, 122.2, 122.8, 123.5, 127.9, 129.4, 130.8, 130.9, 132.5, 133.3, 134.3, 135.1, 135.8, 143.9, 147.3, 149.1, 152.1, 152.3, 158.3, 166.8; *m/z* (MALDI-TOF) 6116 ($C_{360}H_{384}N_{24}O_{42}Zn_6$, M+ requires 6111, 100%).

Free Base 5,15-bis(4-octyl benzoate) porphyrin 62b

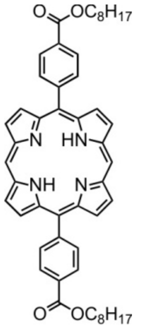

Octyl 4-formylbenzoate **60** (2.33 g, 8.89 mmol) and dipyrromethane **1** (1.30 g, 8.89 mmol) were placed in a dry flask under N_2 and then dissolved in CH_2Cl_2 (1500 mL). The solution was degassed three times by repeated evacuation and purging with nitrogen. Trifluoroacetic acid (0.4 mL, 5.34 mmol) was added and the reaction mixture stirred in the dark for 3 h. DDQ (2.62 g, 11.6 mmol) was added and stirring continued for 0.5 h. After quenching of the acid by addition of triethylamine (4 mL) the solvent was removed and the residue redissolved in CH_2Cl_2 and passed over a silica plug (CH_2Cl_2). Recrystallization from CH_2Cl_2/methanol by layer addition gave the pure product as a pink powder (1.13 g, 33%).

R_f = 0.5 in CH_2Cl_2; mp > 250 °C; ^{1}H NMR (400 MHz, $CDCl_3$) δ_H -3.13 (br. s., 2H, -N*H*), 0.95 (t, 6H, *J* = 6.5 Hz, -C*H*$_3$), 1.25–1.54 (m, 16H, -C*H*$_2$), 1.54–1.70 (m, 4H, -C*H*$_2$), 1.89–2.04 (m, 4H, -C*H*$_2$), 4.56 (t, 4H, *J* = 6.5 Hz, -COOC*H*$_2$), 8.37 (d, 4H, *J* = 8.0 Hz, -Ar*H*), 8.52 (d, 4H, *J* = 8.5 Hz, -Ar*H*), 9.06 (d, 4H, *J* = 4.5 Hz, 4H, -Ar*H*$_\beta$), 9.42 (d, 4H, *J* = 4.5 Hz, -Ar*H*$_\beta$), 10.35 (s, 2H, -Ar*H*$_{meso}$); ^{13}C NMR (126 MHz, $CDCl_3$) δ_C 14.1, 22.7, 26.2, 28.9, 29.3, 29.4, 31.9, 65.5, 105.7, 118.0, 128.1, 129.9, 130.8, 132.0, 134.8, 145.3, 146.0, 146.7, 166.9; *m/z* (MALDI-TOF) 775.61 ($C_{50}H_{54}N_4O_4$, M+ requires 775.42, 100%); λ_{max} ($CHCl_3$) / nm (log ε) 410 (5.57), 504 (4.23), 539 (3.87), 578 (3.75).

Zinc 5,15-bis(4-octyl benzoate) porphyrin 63b

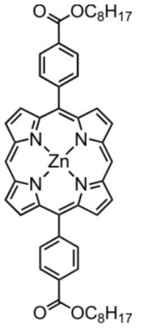

$Zn(OAc)_2 \cdot 2H_2O$ (0.8 g, 3.65 mmol) in methanol (11 mL) was added to a stirred solution of free base porphyrin **62b** (1.13 g, 1.46 mmol) in $CHCl_3$ (110 mL) and the solution stirred for 1 h at room temperature. The volume was reduced and the reaction mixture passed over a silica plug

(CH_2Cl_2/pyridine = 10/1) to remove excess $Zn(OAc)_2$. Recrystallization from CH_2Cl_2/methanol gave the product as a red solid (1.23 g, 99%).

R_f = 0.24 in PE 40-60/EtOAc/pyridine = 10/1/1; mp > 250 °C; ^{1}H NMR (400 MHz, $CDCl_3$) δ_H 0.95 (t, 6H, J = 6.5 Hz, -CH_3), 1.26–1.54 (m, 16H, -CH_2), 1.61 (m, 4H, -CH_2), 1.88–2.01 (m, 4H, -CH_2), 4.53 (t, 4H, J = 6.5 Hz, -COOCH_2), 8.35 (d, 4H, J = 8.0 Hz, -ArH), 8.46 (d, 4H, J = 8.0 Hz, -ArH), 9.05 (d, 4H, J = 4.5 Hz, -ArH_β), 9.41 (d, 4H, J = 4.5 Hz, -ArH_β), 10.27 (s, 2H, -ArH_{meso}). ^{13}C NMR (126 MHz, $CDCl_3$) δ_C 14.1, 22.7, 26.2, 28.9, 29.3, 29.4, 31.9, 65.4, 106.2, 118.4, 127.6, 129.4, 131.9, 131.9, 134.8, 148.0, 149.5, 149.5, 167.1; *m/z* (MALDI-TOF) 837.74 ($C_{50}H_{52}N_4O_4Zn$, M+ requires 837.34, 100 %); λ_{max} ($CHCl_3$) / nm (log ε) 411 (5.35), 538 (4.07).

Zinc 5,15-bis(4-octyl benzoate)-10,20-dibromo porphyrin 64b

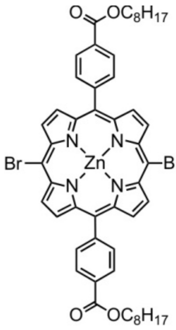

To a solution of zinc porphyrin **63b** (1.22 g, 1.46 mmol) in $CHCl_3$ (160 mL) and pyridine (1 mL) was added dropwise *N*-bromosuccinimide (518 mg, 2.91 mmol) dissolved in $CHCl_3$ (65 mL). After stirring in the dark for 15 minutes, the reaction was quenched by addition of acetone (1 mL). The solvent was removed and the crude product recrystallized from CH_2Cl_2/methanol to give the title compound as a purple solid (1.43 g, 98%).

R_f = 0.31 in PE 40-60/EtOAc/pyridine = 10/1/1. ; mp > 250 °C; ^{1}H NMR (400 MHz, $CDCl_3$/1% d_5-pyridine) δ_H 0.92 (t,6H, J = 7.0 Hz, 6H, -CH_3), 1.26–1.52 (m, 16H, -CH_2), 1.53–1.66 (m, 4H, -CH_2), 1.86–2.01 (m, 4H, -CH_2), 4.52 (t, 4H, J = 6.5 Hz, -COOCH_2), 8.22 (d, 4H, J = 8.0 Hz, -ArH), 8.43 (d, 4H, J = 8.5 Hz, -ArH), 8.81 (d, 4H, J = 5.0 Hz, -ArH_β), 9.66 (d, 4H, J = 4.5 Hz, -ArH_β); ^{13}C NMR (126 MHz, $CDCl_3$/1% d_5-pyridine) δ_C 14.1, 22.7, 26.2, 28.9, 29.2, 29.3, 31.8, 65.5, 105.1, 120.6, 127.6, 129.7, 132.9, 133.2, 134.5, 147.3, 150.2, 150.2, 166.9; *m/z* (MALDI-TOF) 997.86 ($C_{50}H_{50}Br_2N_4O_4Zn$, M+ requires 997.15, 100 %); λ_{max} ($CHCl_3$/1% pyridine) / nm (log ε) 436 (5.61), 572 (4.28), 619 (4.12).

Zinc 5,15-bis(4-octyl benzoate)-10,20-bistrihexylsilanylethynyl porphyrin 65b

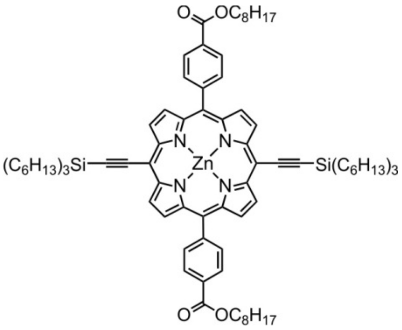

Bromoporphyrin **64b** (713 mg, 0.716 mmol), $Pd(OAc)_2$ (10 mg, 0.043 mmol), PPh_3 (23 mg, 0.086 mmol) and CuI (7 mg, 0.036 mmol) were placed in a dry flask under N_2 atmosphere and dry tetrahydrofuran (40 mL) was added. After three cycles of degassing by evacuation followed by purging with N_2, trihexylsilyl acetylene (552 mg, 1.79 mmol) and dry triethylamine (1.7 mL) were added and the reaction mixture again degassed (3x). After 2 h at 40°C TLC confirmed completion of the reaction. The solvent was removed and the crude passed over a silica gel column (PE 40-60/EtOAc/pyridine = 10/1/1). Recrystallization from CH_2Cl_2/methanol gave the product (814 mg, 78%) as a green solid.

$R_f = 0.58$ in PE 40-60/EtOAc/pyridine = 10/1/1 ; mp > 250 °C; ^1H NMR (400 MHz, $CDCl_3$) δ_H 0.78–0.97 (m, 24H, -CH_3), 0.97–1.10 (m, 12H, -SiCH_2), 1.16–1.63 (m, 56H, -CH_2), 1.66–1.83 (m, 12H, -CH_2), 1.83–1.99 (m, 4H, -CH_2), 3.31 (s, 3H, -OCH_3), 4.53 (t, 4H, $J = 6.5$ Hz, -COOCH_2), 8.26 (d, 4H, $J = 8.0$ Hz, -ArH), 8.44 (d, 4H, $J = 8.0$ Hz, -ArH), 8.80 (d, 4H, $J = 4.5$ Hz, -ArH_β), 9.67 (d, 4H, $J = 4.5$ Hz, -ArH_β); ^{13}C NMR (126 MHz, $CDCl_3$) δ_C 13.8, 14.1, 14.2, 22.7, 22.7, 24.4, 26.2, 28.9, 29.3, 29.4, 31.6, 31.9, 33.3, 65.5, 100.3, 101.6, 108.8, 121.2, 122.4, 127.7, 129.7, 131.5, 132.1, 134.4, 136.0, 143.1, 147.3, 149.6, 152.4, 167.0; *m/z* (MALDI-TOF) 1453.11 ($C_{90}H_{128}N_4O_4SiZn$, M+ requires 1451.89, 100 %); λ_{max} ($CHCl_3$) / nm (log ε) 444 (5.38), 456 (5.35), 590 (4.13), 619 (sh, 4.18), 642 (4.60).

Zinc 5,15-bis(4-octyl benzoate)-10-ethynyl-20-trihexylsilanylethynyl porphyrin 66b

Zinc 5,15-bis(4-octyl benzoate)-10,20-bisethynyl porphyrin d65b

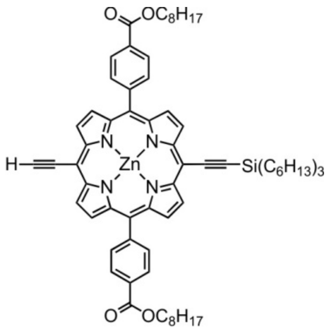

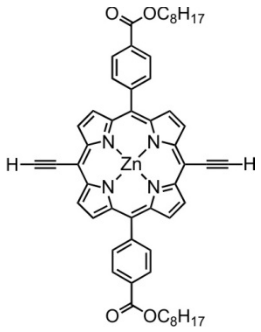

THS-acetylene porphyrin **65b** (1.60 g, 1.104 mmol) under N_2 in a dry flask was dissolved in CH_2Cl_2 (140 mL) and $CHCl_3$ (140 mL). Tetra-*n*-butylammonium fluoride (1M in THF, 1.8 mL, 1.767 mmol) was added and stirred for 30 min when TLC showed a good ratio of products. The reaction was quenched with CH_3COOH (0.13 mL) and the solvent removed. The crude was passed over a silica gel column (PE 40-60/EtOAc/pyridine = 10/1/1 to 5/1/1) and the three fractions recrystallized from CH_2Cl_2/methanol to give:

Recovered starting porphyrin **65b**: 323 mg, 20%

Zinc 5,15-bis(4-octyl benzoate)-10-ethynyl-20-trihexylsilanylethynyl porphyrin **66b**: 543 mg, 42%

R_f = 0.34 in PE 40-60/EtOAc/pyridine = 10/1/1; mp > 250 °C; ^1H NMR (400 MHz, $CDCl_3$) δ_H 0.85–0.98 (m, 15H, -CH_3), 0.98–1.08 (m, 6H, -SiCH_2), 1.32–1.61 (m, 38H, -CH_2), 1.70–1.84 (m, 6H, -CH_2), 1.89–2.02 (m, 4H, -CH_2), 4.17 (s, 1H, ≡C*H*), 4.53 (t, 4H, *J* = 6.5 Hz, -COOCH_2), 8.26 (d, 4H, *J* = 8.0 Hz, -Ar*H*), 8.44 (d, 4H, *J* = 8.0 Hz, -Ar*H*), 8.74–8.89 (m, 4H, -ArH_β), 9.68 (d, 4H, *J* = 4.0 Hz, -ArH_β); ^{13}C NMR (126 MHz, $CDCl_3$) δ_C 13.8, 14.1, 14.2, 22.7, 22.7, 24.4, 26.2, 28.9, 29.3, 29.4, 31.6, 31.9, 33.3, 65.5, 83.5, 86.5, 99.5, 100.1, 101.7, 109.0, 121.1, 127.6, 129.7, 131.2, 131.5, 132.1, 132.3, 134.5, 147.4, 149.6, 149.7, 152.4, 152.4, 167.0; *m/z* (MALDI-TOF) 1171.45 ($C_{72}H_{90}N_4O_4SiZn$, M+ requires 1169.61, 100 %); λ_{max} ($CHCl_3$) / nm (log ε) 441 (5.19), 582 (4.07), 636 (4.17).

Zinc 5,15-bis(4-octyl benzoate)-10,20-bisethynyl porphyrin **d65b**: 290 mg, 30%

R_f = 0.23 in PE 40-60/EtOAc/pyridine = 10/1/1; mp > 250 °C; ^1H NMR (400 MHz, $CHCl_3$/1% d_5-pyridine) δ_H 0.93 (t, 6H, *J* = 6.5 Hz, -CH_3), 1.30–1.53 (m, 16H, -CH_2), 1.55–1.67 (m, 4H, -CH_2), 1.89–2.00 (m, 4H, -CH_2), 4.17 (s, 2H, ≡C*H*), 4.53 (t, 4H, *J* = 6.5 Hz, -COOCH_2), 8.25 (d, 4H, *J* = 8.0 Hz, -Ar*H*), 8.44 (d, 4H, *J* = 8.0 Hz, -Ar*H*), 8.83 (d, 4H, *J* = 4.5 Hz, -ArH_β), 9.69 (d, 4H, *J* = 4.5 Hz, -ArH_β); ^{13}C NMR (126 MHz, $CHCl_3$/1% d_5-pyridine) δ_C 14.1, 22.7, 26.2, 28.9, 29.3, 29.3, 31.8, 65.5, 83.6, 86.5, 99.7, 121.1, 127.6, 129.7, 131.3, 132.3, 134.5, 147.4, 149.7, 152.4, 166.9; *m/z* (MALDI-TOF) 885.78 ($C_{54}H_{52}N_4O_4Zn$, M+ requires 885.34, 100 %); λ_{max} ($CHCl_3$/pyridine 1%) / nm (log ε) 437 (5.51), 450 (5.45), 5.83 (4.25), 631 (4.42).

Zinc 5,15-bis(4-octyl benzoate)-10,20-trihexylsilanylethynyl porphyrin dimer 67b

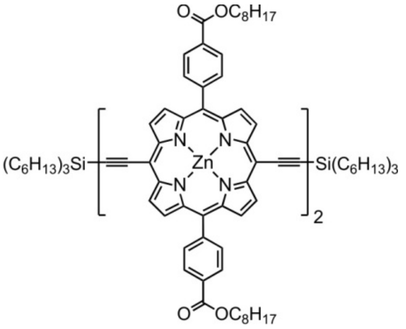

Mono deprotected porphyrin **66b** (62 mg, 0.053 mmol) was placed in a dry flask equipped with a dry tube, dissolved in dry CH_2Cl_2 (20 mL) and stirred vigorously for 15 minutes. *N,N,N',N'*-tetramethylethylenediamine (0.24 mL, 1.59 mmol) and CuCl (158 mg, 1.59 mmol) were added and the reaction mixture stirred for 15 minutes when TLC confirmed completion. The reaction was quenched by addition of water and the solution passed over a short plug of silica (PE 40-60/EtOAc/pyridine = 10/1/1) and the crude product isolated by size-exclusion chromatography (tetrahydrofuran). The obtained dark green solid was recrystallised from CH_2Cl_2/methanol to give the pure product (49 mg, 79%).

R_f = 0.22 in PE 40-60/EtOAc/pyridine = 10/1/1; mp > 250 °C; ^1H NMR (400 MHz, $CDCl_3$/1% d_5-pyridine) δ_H 0.83–0.97 (m, 30H, -CH_3), 0.99–1.09 (m, 12H, -SiCH_2), 1.21–1.67 (m, 76H, -CH_2), 1.70–1.85 (m, 12H, -CH_2), 1.89–2.02 (m, 8H, -CH_2), 4.54 (t, 8H, J = 6.5 Hz, -COOCH_2), 8.29 (d, 8H, J = 8.0 Hz, -Ar*H*), 8.47 (d, 8H, J = 8.0 Hz, -Ar*H*), 8.80 (d, 4H, J = 4.5 Hz, -ArH_β), 8.89 (d, 4H, J = 4.5 Hz, -ArH_β), 9.67 (d, 4H, J = 4.5 Hz, -ArH_β), 9.90 (d, 4H, J = 4.5 Hz, -ArH_β); ^{13}C NMR (126 MHz, $CDCl_3$/1% d_5-pyridine) δ_C 13.8, 14.1, 14.2, 22.7, 24.4, 26.2, 28.9, 29.3, 29.3, 31.6, 31.8, 33.3, 33.3, 65.5, 82.3, 88.3, 99.6, 100.4, 102.3, 109.0, 121.7, 127.7, 129.7, 131.1, 131.5, 132.1, 132.6, 134.5, 135.2, 135.6, 147.3, 148.6, 149.4, 149.8, 152.4, 153.1, 167.0; *m/z* (MALDI-TOF) 2337.01 ($C_{174}H_{178}N_8O_8Si_2Zn_2$, M+ requires 2337.20, 100 %); λ_{max} ($CHCl_3$) / nm (log ε) 461 (5.47), 495 (5.11), 585 (4.39), 668 (4.74), 721 (4.74).

Zinc 5,15-bis(4-octyl benzoate)-10,20-bisethynyl porphyrin dimer **68b**

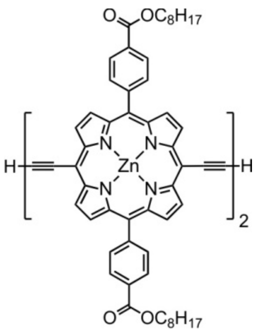

Porphyrin dimer **67b** (132 mg, 56.5 μmol) under N_2 was dissolved in dry CH_2Cl_2 (20 mL) and tetra-*n*-butylammonium fluoride (1M in THF, 120 μL, 118.7 μmol) added. After stirring at room temperature for 30 minutes, the reaction was quenched with CH_3COOH (50 μL). The volume was reduced and the reaction mixture passed over a short silica plug (CH_2Cl_2/pyridine = 50/1). Recrystallization from CH_2Cl_2/methanol gave the title compound as a dark green solid (80 mg, 80%).

R_f = 0.05 in PE 40-60/EtOAc/pyridine = 10/1/1; mp > 250 °C; ^1H NMR (400 MHz, $CDCl_3$/1% d_5-pyridine) δ_H 0.89–0.98 (m, 12H, -CH_3), 1.24–1.52 (m, 32H, -CH_2), 1.52–1.66 (m, 8H, -CH_2), 1.88–1.99 (m, 8H, -CH_2), 4.53 (t, 8H, J = 6.5 Hz, -COOCH_2), 8.29 (d, 8H, J = 8.0 Hz, -Ar*H*), 8.47 (d, 8H, J = 8.0 Hz, -Ar*H*), 8.82 (d, 4H, J = 4.5 Hz, -ArH_β), 8.91 (d, 4H, J = 4.5 Hz, -ArH_β), 9.69 (d, 4H, J = 4.5 Hz, -ArH_β), 9.92 (d, 4H, J = 4.5 Hz, -ArH_β); ^{13}C NMR (126 MHz, $CDCl_3$/1% d_5-pyridine) δ_C 14.1, 22.7, 26.2, 28.9, 29.2, 29.3, 29.4, 31.8, 65.5, 67.9, 82.4, 83.9, 86.4, 88.2, 99.9, 100.4, 121.7, 127.7, 129.7, 131.2, 131.4, 132.4, 132.7, 134.5, 147.2, 149.5, 149.9, 152.4, 153.1, 166.9; *m/z* (MALDI-TOF) 1772.88 ($C_{108}H_{102}N_8O_8Zn_2$, M+ requires 1771.65, 100 %); λ_{max} ($CHCl_3$) / nm (log ε) 458 (5.31), 492 (5.04), 579 (4.33), 661 (4.59), 710 (4.62).

2-Hexyldecyl 4-formylbenzoate **61**

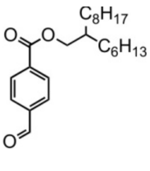

4-Formylbenzoic acid (6.00 g, 40.0 mmol), *N*-(3-dimethylaminopropyl)-*N'*-ethylcarbodiimide hydrochloride (9.20 g, 48.0 mmol) and 4-(dimethylamino)pyridine (5.86 g, 48.0 mmol) were dried under high vacuum with gentle heating. 2-Hexyl-1-decanol (11.6 g, 48.0 mmol) and dry CH_2Cl_2 (390 mL) were added under N_2 atmosphere. The reaction mixture was stirred for 14 h at room temperature. The mixture was washed twice with 1M HCl (50 mL), once with H_2O (50 mL) and once with brine (50 mL). The solvent was removed and the crude product purified by column chromatography on silica (PE 40-60/EtOAc = 20/1) to yield the product as a colorless oil (11.7 g, 78%).

R$_f$ = 0.35 in PE 40-60/EtOAc = 20/1; ^{1}H NMR (400 MHz, CDCl$_3$) δ_H 0.85–0.89 (m, 6H, -C*H*$_3$), 1.28–1.43 (m, 24H, -C*H*$_2$), 1.75–1.83 (m, 1H, -C*H*), 4.26 (d, 2H, *J* = 5.5 Hz, -OC*H*$_2$), 7.96 (d, 2H, *J* = 8.0 Hz, -Ar*H*), 8.19 (d, 2H, *J* = 8.0 Hz, -Ar*H*), 10.11 (s, 1H, -CO*H*); ^{13}C-NMR (126 MHz, CDCl$_3$) δ_C 14.4, 14.5, 23.0, 23.0, 27.1, 27.1, 29.6, 29.9, 29.9, 30.3, 31.8, 32.2, 32.2, 37.8, 68.8, 129.9, 130.5, 135.9, 139.4, 166.1, 192.0; *m/z* (ESI) 397.2707 ($C_{24}H_{38}NaO_3$, [M+Na]$^+$ requires 397.2713, 100%).

Free Base 5,15-bis(4-(2-hexyldecyl) benzoate) porphyrin 62c

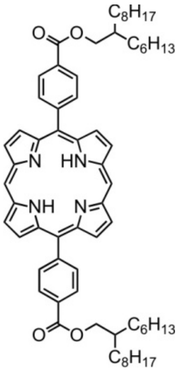

2-Hexyldecyl 4-formylbenzoate **61** (5.56 g, 14.8 mmol) and and dipyrromethane **1** (2.17 g, 14.8 mmol) were placed in a dry flask under N$_2$ and then dissolved in CH$_2$Cl$_2$ (2.5 L). The solution was degassed three times by repeated evacuation and purging with nitrogen. Trifluoroacetic acid (0.66 mL, 8.9 mmol) was added and the reaction mixture stirred in the dark for 3 h. DDQ (5.05 g, 22.2 mmol) was added and stirring continued for 30 minutes. After quenching of the acid by addition of triethylamine (6.7 mL) the solvent was removed and the crude passed over a silica plug (CH$_2$Cl$_2$). Recrystallization from CHCl$_3$/methanol by layer addition yielded the pure product as a pink solid (3.0 g, 41%).

R$_f$ = 0.87 in DCM; ^{1}H NMR (400 MHz, CDCl$_3$) δ_H -3.13 (s, 2H, -N*H*), 0.88–0.96 (m, 12H, -C*H*$_3$), 1.32–1.64 (m, 48H, -C*H*$_2$), 1.91–2.00 (m, 2H, -C*H*), 4.46 (d, 4H, *J* = 5.5 Hz, -OC*H*$_2$), 8.37 (d, 4H, *J* = 8.0 Hz, -Ar*H*), 8.50 (d, 4H, *J* = 8.0 Hz, -Ar*H*), 9.06 (d, 4H, *J* = 4.5 Hz, -ArH_β), 9.43 (d, 4H, *J* = 4.5 Hz, -ArH_β), 10.36 (s, 2H, -ArH_{meso}); ^{13}C NMR (126 MHz, CDCl$_3$) δ_C 14.5, 14.5, 27.2, 27.3, 29.7, 30.0, 30.1, 30.4, 31.9, 32.3, 32.3, 38.0, 68.5, 106.0, 118.4, 128.5, 130.4, 131.2, 132.4, 135.2, 145.7, 146.4, 147.1, 167.4; *m/z* (MALDI-TOF) 999.04 ($C_{66}H_{86}N_4O_4$, M+ requires 999.66, 100 %).

Zinc 5,15-bis(4-(2-hexyldecyl) benzoate) porphyrin **63c**

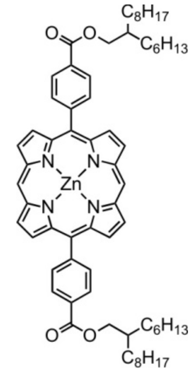

$Zn(OAc)_2 \cdot 2H_2O$ (6.35 g, 29.0 mmol) in methanol (76 mL) was added to a solution of free base porphyrin **62c** (5.79 g, 5.79 mmol) in $CHCl_3$ (760 mL). The solution was stirred for 30 min when TLC confirmed completion. The solvent was removed and the crude product passed over a silica plug (CH_2Cl_2/pyridine = 20/1) to remove excess $Zn(OAc)_2$. Recrystallization from $CHCl_3$/methanol by layer addition yielded the product as a red solid. (6,00 g, 98%).

R_f = 0.67 in DCM; ^{1}H NMR (400 MHz, $CDCl_3$) δ_H 0.87–0.95 (m, 12H, -CH_3), 1.31–1.63 (m, 48H, -CH_2), 1.90–1.99 (m, 2H, -C*H*), 4.44 (d, 4H, *J* = 5.5 Hz, -OCH_2), 8.35 (d, 4H, *J* = 8.0 Hz, -Ar*H*), 8.45 (d, 4H, *J* = 8.0 Hz, -Ar*H*), 9.05 (d, 4H, *J* = 4.5 Hz, -ArH_β), 9.40 (d, 4H, *J* = 4.5 Hz, -ArH_β), 10.26 (s, 2H, -ArH_{meso}); ^{13}C NMR (126 MHz, $CDCl_3$) δ_C 14.5, 14.5, 23.1, 27.2, 27.3, 29.7, 30.0, 30.1, 30.4, 32.0, 32.3, 32.3, 38.0, 68.4, 106.5, 118.7, 127.9, 129.8, 132.2, 132.3, 136.2, 143.7, 148.4, 149.8, 167.6; *m/z* (MALDI-TOF) 1060.05 ($C_{66}H_{84}N_4O_4Zn$, M+ requires 1060.58, 100 %).

Zinc 5,15-bis(4-(2-hexyldecyl) benzoate) 10,20-dibromo porphyrin **64c**

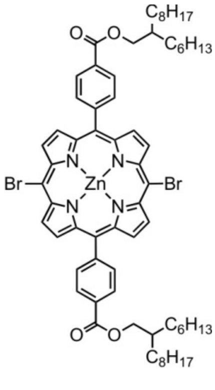

To a solution of zinc porphyrin **63c** (1.50 g, 1.41 mmol) in $CHCl_3$ (150 mL) and pyridine (1 mL) was added dropwise *N*-bromosuccinimide (505 mg, 2.84 mmol) dissolved in $CHCl_3$ (60 mL). After stirring in the dark for 20 minutes, the reaction was quenched by addition of acetone (10 mL). The solvent was removed and the crude product recrystallized from CH_2Cl_2/methanol to give the pure compound as a green solid (6.75 g, 98%).

R_f = 0.4 in PE 40-60/EtOAc/pyridine = 10/1/1; ^{1}H NMR (400 MHz, $CDCl_3$) δ_H 0.86–0.94 (m, 12H, -CH_3), 1.30–1.62 (m, 48H, -CH_2), 1.89–1.98 (m, 2H, -C*H*), 4.43 (d, 4H, *J* = 5.5 Hz, -OCH_2), 8.23 (d, 4H, *J* = 8.0 Hz, -Ar*H*), 8.42 (d, 4H, *J* = 8.0 Hz, -Ar*H*), 8.82 (d, 4H, *J* = 4.5 Hz, -ArH_β), 9.67 (d, 4H, *J* = 4.5 Hz, -ArH_β); ^{13}C NMR (126 MHz, $CDCl_3$) δ_C 14.5, 14.5, 23.0, 27.2, 27.2, 29.7, 30.0, 30.0, 30.4, 31.9, 32.2, 32.3, 38.0, 68.4, 105.5, 121.0, 127.9, 130.1, 133.3, 133.6, 134.9, 147.7, 150.6, 150.6, 167.4; *m/z* (MALDI-TOF) 1222.15 ($C_{66}H_{82}Br_2N_4O_4Zn$, M+ requires 1220.40, 100 %).

Zinc 5,15-bis(4-(2-hexyldecyl) benzoate)-10,20-trihexylsilanylethynyl porphyrin 65c

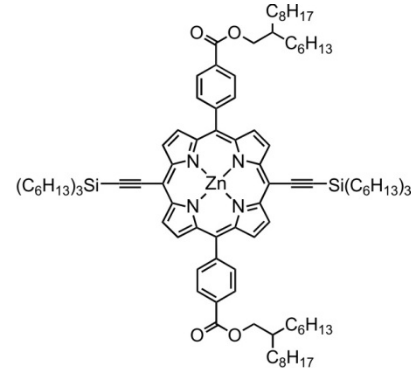

Dibromo porphyrin **64c** (800 mg, 0.655 mmol), $Pd_2(dba)_3$ (60 mg, 66 μmol), PPh_3 (68 mg, 0.26 mmol) and CuI (25 mg, 0.13 mmol) were placed in a dry flask under N_2 atmosphere and dry toluene (38 mL), freshly distilled trietylamine (38 mL) and pyridine (1.8 mL) were added. After three cycles of degassing by evacuation followed by purging with N_2, ethynyltrihexylsilane (0.51 g, 1.6 mmol) was added and the reaction mixture again degassed (3x). After stirring for 3 h at 80°C the solvent was removed and the crude passed over a silica gel column (PE 40-60/EtOAc/pyridine = 20/1/1). Recrystallization from $CHCl_3$/methanol gave the product (989 mg, 90%) as a green solid.

R_f = 0.38 in PE 40-60/EtOAc/pyridine = 10/1/1; ^{1}H NMR (400 MHz, $CDCl_3$) δ_H 0.87–0.94 (m, 30H, -CH_3), 0.98–1.02 (m, 12H, -SiCH_2), 1.29–1.57 (m, 84H, -CH_2), 1.71–1.79 (m, 12H, -CH_2), 1.90–1.97 (m, 2H, -C*H*), 4.43 (d, 4H, *J* = 5.5 Hz, -OCH_2), 8.25 (d, 4H, *J* = 8.0 Hz, -Ar*H*), 8.42 (d, 4H, *J* = 8.0 Hz, -Ar*H*), 8.80 (d, 4H, *J* = 4.5 Hz, -ArH_β), 9.66 (d, 4H, *J* = 4.5 Hz, -ArH_β); ^{13}C NMR (126 MHz, $CDCl_3$) δ_C 14.2, 14.5, 14.5, 23.0, 23.1, 24.7, 27.2, 27.3, 29.7, 30.0, 30.1, 30.4, 31.9, 32.0, 32.3, 32.3, 33.7, 38.0, 68.4, 100.6, 102.0, 109.2, 121.5, 128.0, 130.1, 131.8, 132.5, 134.8, 147.1, 149.9, 152.8, 167.4; *m/z* (MALDI-TOF) 1673.56 ($C_{106}H_{160}N_4O_4Si_2Zn$, M+ requires 1675.13, 100 %).

Zinc 5,15-bis(4-(2-hexyldecyl) benzoate)-10-trihexylsilanylethynyl-20-ethynyl porphyrin **66c**

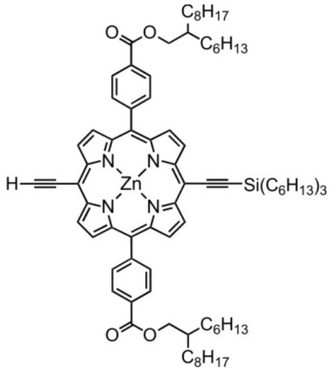

THS-protected porphyrin **65c** (0.98 g, 0.59 mmol) was placed in a dry flask under N_2 and dissolved in CH_2Cl_2 (75 mL) and $CHCl_3$ (75 mL). Tetra-*n*-butylammonium fluoride (1M in THF, 0.88 mL, 0.88 mmol) was added and the reaction mixture was stirred for 30 min when TLC showed a good ratio of products. The reaction was quenched with CH_3COOH (0.1 mL) and the solvent removed. The crude product was passed over a silica column (PE 40-60/EtOAc/pyridine = 15/1/1). Recrystallization from $CHCl_3$/methanol gave the product (180 mg, 22%) as a green solid.

R_f = 0.30 in PE 40-60/EtOAc/pyridine = 10/1/1; ^{1}H NMR (400 MHz, $CDCl_3$) δ_H 0.87–0.94 (m, 21H, -C*H*$_3$), 0.99–1.04 (m, 6H, -SiC*H*$_2$), 1.31–1.62 (m, 66H, -C*H*$_2$), 1.72–1.80 (m, 6H, -C*H*$_2$), 1.89–1.98 (m, 2H, -C*H*), 4.18 (s, 1H, ≡C*H*), 4.42 (d,4H, *J* = 5.5 Hz, -OC*H*$_2$), 8.27 (d, 4H, *J* = 8.5 Hz, -Ar*H*), 8.43 (d, 4H, *J* = 8.0 Hz, -Ar*H*), 8.86–8.88 (m, 4H, -ArH_β), 9.73 (d, 4H, *J* = 4.5 Hz, -ArH_β); ^{13}C NMR (126 MHz, $CDCl_3$) δ_C 14.2, 14.5, 14.5, 23.0, 23.1, 24.7, 27.2, 27.2, 29.7, 30.0, 30.1, 30.4, 31.9, 32.0, 32.3, 32.3, 33.7, 38.0, 68.4, 84.5, 86.5, 100.2, 101.0, 102.5, 108.9, 121.6, 128.1, 130.2, 131.8, 132.0, 132.6, 132.9, 134.8, 147.5, 150.1, 150.1, 152.8, 152.8, 167.4; *m/z* (MALDI-TOF) 1391.61 ($C_{88}H_{122}N_4O_4SiZn$, M+ requires 1392.85, 100 %).

Zinc 5,15-bis(4-(2-hexyldecyl) benzoate)-10,20-trihexylsilanylethynyl porphyrin dimer **67c**

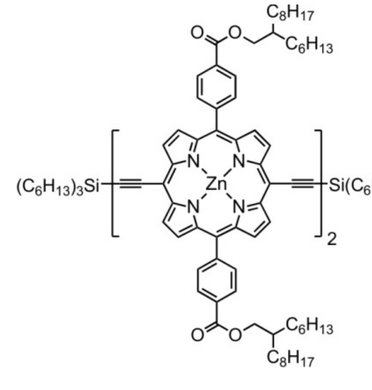

Mono-deprotected porphyrin **66c** (180 mg, 0.129 mmol) was placed in a dry flask under inert atmosphere. $Pd(PPh_3)_2Cl_2$ (4.5 mg, 6.5 μmol), CuI (12.3 mg, 64.6 μmol) and 1,4-benzoquinone (27.9

mg, 0.258 mmol) were dissolved in dry toluene (11 mL) and di*iso*propylamine (4.2 mL). The catalyst solution was added to the porphyrin with a syringe under N_2 and the reaction mixture was stirred for 30 minutes. The solvent was removed and the crude passed over a short silica plug (CH_2Cl_2/1% pyridine) and a size-exclusion column (tetrahydrofuran). Recrystallization from $CHCl_3$/methanol gave the product as a dark green solid (140 mg, 73%).

The dimer **67c** was also synthesized by the following route:

Porphyrin dimer **67b** (1.16 g, 0.497 mmol) was dissolved in 2-hexyl-1-decanol (24.0 mL, 82.8 mmol) under inert atmosphere and titanium(IV) isopropoxide (110 μL, 0.373 mmol) was added. The reaction mixture was stirred for 15 min at 120 °C and 20 mbar and then for 1 h at 120° C and 0.05 mbar. Then the 2-hexyl-1-decanol was distilled off (160 °C, 0.05 mbar) and the residue dissolved in petroleum ether 40-60 passed over a plug of silica (PE 40-60 then PE 40-60/EtOAc/pyridine = 10/1/1). The crude product was recrystallized from CH_2Cl_2/methanol to give the target compound as a dark green solid. (1.35 g, 97%).

$R_f = 0.24$ in PE 40-60/EtOAc/pyridine = 10/1/1; ^1H NMR (400 MHz, $CDCl_3$/1% d_5-pyridine) δ_H 0.84–0.93 (m, 42H, -CH_3), 1.00–1.04 (m, 12H, -SiCH_2), 1.30–1.58 (m, 132H, -CH_2), 1.73–1.80 (m, 12H, -CH_2), 1.90–1.98 (m, 4H, -C*H*), 4.44 (d, 8H, J = 5.5 Hz, -OCH_2), 8.28 (d, 8H, J = 8.0 Hz, -Ar*H*), 8.45 (d, 8H, J = 8.0 Hz, -Ar*H*), 8.79 (d, 4H, J = 4.5, -ArH_β), 8.89 (d, 4H, J = 4.5 Hz, -ArH_β), 9.66 (d, 4H, J = 4.5, -ArH_β), 9.88 (d, 4H, J = 4.5 Hz, -ArH_β); ^{13}C NMR (126 MHz, $CDCl_3$/1% d_5-pyridine) δ_C 13.9, 14.2, 14.3, 14.3, 22.8, 22.8, 24.5, 27.0, 27.0, 29.5, 29.7, 29.8, 30.1, 31.7, 31.8, 32.0, 32.0, 33.4, 37.7, 69.2, 82.5, 88.4, 99.8, 100.5, 102.4, 109.1, 121.8, 123.8, 127.8, 129.9, 131.2, 131.6, 132.3, 132.7, 134.6, 147.5, 150.0, 152.6, 153.3, 167.2: *m/z* (MALDI-TOF) 2782.07 ($C_{176}H_{242}N_8O_8Si_2Zn_2$, M+ requires 2784.69, 100 %).

Zinc 5,15-bis(4-(2-hexyldecyl) benzoate)-10,20-ethynyl porphyrin dimer 68c

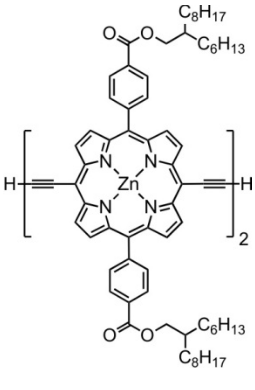

Porphyrin dimer **67c** (100 mg, 35.9 μmol) under N_2 was dissolved in dry CH_2Cl_2 (18 mL) and tetra-*n*-butylammonium fluoride (1M in THF, 75 μL, 75 μmol) added. After stirring at room temperature for 30 minutes, the reaction was quenched with CH_3COOH (50 μL). The reaction mixture was passed over a short silica plug (CH_2Cl_2/pyridine = 50/1). Recrystallization from CH_2Cl_2/methanol gave the title compound as a dark green solid (78 mg, 98%).

^{1}H NMR (250 MHz, $CDCl_3$/1% d_5-pyridine) δ_H 0.84–0.94 (m, 24H, -CH_3), 1, 1.25–1.57 (m, 96H, -CH_2), 1.87–1.98 (m, 4H, -C*H*), 4.19 (s, 2H, ≡C*H*), 4.43 (d, 8H, *J* = 5.5 Hz, -OCH_2), 8.27 (d, 8H, *J* = 8.0 Hz, -Ar*H*), 8.45 (d, 8H, *J* = 8.0 Hz, -Ar*H*), 8.81 (d, 4H, *J* = 4.5, -ArH_β), 8.90 (d, 4H, *J* = 4.5 Hz, -ArH_β), 9.68 (d, 4H, *J* = 4.5, -ArH_β), 9.90 (d, 4H, *J* = 4.5 Hz, -ArH_β); ^{13}C NMR (126 MHz, $CDCl_3$/1% d_5-pyridine) δ_C 14.2, 14.2, 22.8, 26.9, 27.0, 29.4, 29.7, 29.8, 30.1, 31.6, 32.0, 32.0, 37.7, 68.2, 82.5, 84.0, 86.5, 88.3, 100.0, 100.5, 121.8, 123.8, 127.8, 129.9, 131.3, 131.5, 132.5, 132.8, 134.6, 147.3, 150.1, 152.5, 153.2, 167.1; *m/z* (MALDI-TOF) 2220.10 ($C_{140}H_{166}N_8O_8Zn_2$, M+ requires 2220.15, 100 %).

Zinc 5,15-bis(4-(2-hexyldecyl) benzoate)-porphyrin[6] nanoring–template complex 69c·T6

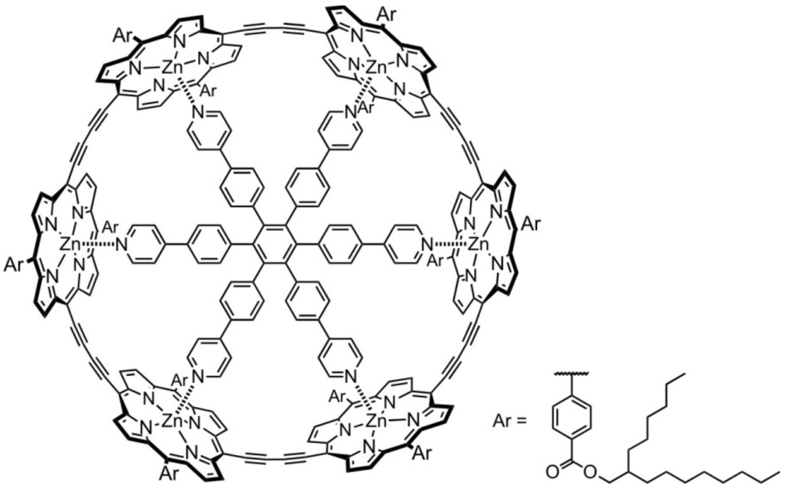

Hexadentate template **T6** (4.2 mg, 4.2 μmol) and porphyrin dimer **68c** (28 mg, 12.6 μmol) were dissolved in CH_2Cl_2 (5 mL) and sonicated for 30 min. The solvent was removed, the residue dried under high vacuum and dissolved in toluene (4 mL). A catalyst solution was prepared by dissolving $Pd(PPh_3)_2Cl_2$ (2.7 mg, 3.8 μmol), copper(I) iodide (7.2 mg, 38 μmol) and 1,4-benzoquinone (5.5 mg, 50 μmol) in toluene (2 mL) and freshly distilled di*iso*propylamine (0.45 mL). The catalyst solution was added to the porphyrin solution, and the mixture was stirred at room temperature for 2 h, and then for 1 h at 50 °C. The mixture was passed through a plug of alumina using toluene as eluent, and purified by size exclusion chromatography on Biobeads SX-1 in toluene. The second band was isolated and recrystallized by layer addition (CH_2Cl_2/methanol) to give **69c·T6** as a dark brown solid (15.0 mg, 47%).

^{1}H NMR (400 MHz, $CDCl_3$) δ_H 0.89–0.97 (m, 72H, -CH_3), 1.31–1.61 (m, 288H, -CH_2), 1.95–2.01 (m, 12H, -C*H*), 2.27 (d, 12H, *J* = 5.5 Hz, -pyridylH_α), 4.47 (d, 24H, *J* = 5.0 Hz, -OCH_2), 5.02 (d, 12H, *J* = 5.5 Hz, -pyridylH_β), 5.48 (d, 12H, *J* = 8.5 Hz, -Ar*H*), 5.54 (d, 12H, *J* = 8.5 Hz, -Ar*H*), 8.07 (d, 12H, *J*

= 7.5 Hz, -Ar*H*), 8.28 (d, 12H, *J* = 7.5 Hz, -Ar*H*), 8.41 (d, 12H, *J* = 7.5 Hz, -Ar*H*), 8.45 (d, 12H, *J* = 7.5 Hz, -Ar*H*), 8.70 (d, 24H, *J* = 4.5 Hz, -ArH_β), 9.58 (d, 24H, *J* = 4.5 Hz, -ArH_β); ^{13}C NMR (126 MHz, $CDCl_3$) δ_C 14.3, 14.3, 22.9, 27.0, 27.0, 29.5, 29.8, 30.2, 31.7, 32.1, 32.1, 37.8, 68.3, 89.8, 96.4, 100.7, 119.3, 122.8, 123.9, 127.8, 128.1, 130.0, 130.4, 131.2, 132.1, 132.4, 134.3, 134.8, 138.8, 140.1, 142.9, 146.5, 147.0, 149.4, 151.8, 167.1; *m/z* (MALDI-TOF) 7652 ($C_{492}H_{540}N_{30}O_{24}Zn_6$, M+ requires 7650, 100 %).

Zinc 5,15-bis(4-(2-hexyldecyl) benzoate)-porphyrin[6] nanoring 69c

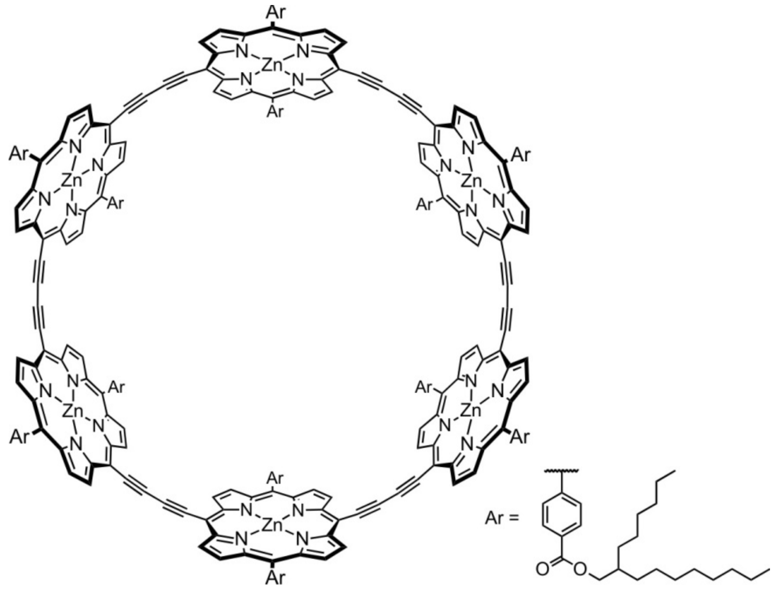

Cyclic hexamer–template complex **69c·T6** (2.0 mg, 0.26 μmol) was passed through a size exclusion column (Biobeads SX–1) containing a (50 mg mL^{-1}) solution of recrystallized DABCO in freshly distilled tetrahydrofuran. The crude product was recrystallized by layer addition (CH_2Cl_2/methanol) to afford the template-free nanoring as a brownish solid (1.5 mg, 87%).

^{1}H NMR (400 MHz, $CDCl_3$/1% d_5-pyridine) δ_H 0.84–0.93 (m, 72H, -CH_3), 1.28–1.61 (m, 288H, -CH_2), 1.95–2.01 (m, 12H, -C*H*), 4.42 (d, 24H, *J* = 5.0 Hz, -OCH_2), 8.15 (d, 24H, *J* = 8.0 Hz, -Ar*H*), 8.38 (d, 24H, *J* = 8.0 Hz, -Ar*H*), 8.71 (d, 24H, *J* = 4.5 Hz, -ArH_β), 9.63 (d, 24H, *J* = 4.5 Hz, -ArH_β); ^{13}C NMR (126 MHz, $CDCl_3$/1% d_5-pyridine) δ_C 14.2, 14.3, 22.8, 26.9, 29.5, 29.7, 29.8, 30.1, 31.7, 32.0, 32.0, 37.7, 44.9, 68.2, 88.7, 94.5, 101.0, 122.6, 127.8, 129.9, 131.1, 132.8, 134.4, 147.0, 152.3, 167.1; *m/z* (MALDI-TOF) 6654 ($C_{420}H_{492}N_{24}O_{24}Zn_6$, M+ requires 6653, 100 %).

8.4 References

[1] B. J. Littler, M. A. Miller, C.-H. Hung, R. W. Wagner, D. F. O’Shea, P. D. Boyle, J. S. Lindsey, *J. Org. Chem.* **1999**, *64*, 1391–1396.

[2] C. J. Wilson, *Large Porphyrin Based π-Systems*, DPhil Thesis, University of Oxford, Oxford, **2006**.

[3] A. Krivokapic, *Meso-Alkynyl Porphyrins and Porphyrinoids for Nonlinear Optics*, DPhil Thesis, University of Oxford, Oxford, **2003**.

[4] M. Hoffmann, J. Kärnbratt, M.-H. Chang, L. M. Herz, B. Albinsson, H. L. Anderson, *Angew. Chem. Int. Ed.* **2008**, *47*, 4993–4996.

[5] A. Saywell, J. K. Sprafke, L. J. Esdaile, A. J. Britton, A. Rienzo, H. L. Anderson, J. N. O'Shea, P. H. Beton, *Angew. Chem. Int. Ed.* **2010**, *49*, 9236–9139.

[6] R. Rathore, C. L. Burns, I. A. Guzei, *J. Org. Chem.* **2004**, *69*, 1524–1530.

[7] M. Hoffmann, *Nanosized Porphyrin Molecular Wires and Rings*, D.Phil. Thesis, University of Oxford, Oxford, **2008**.

[8] M. S. Newman, L. F. Lee, *J. Org. Chem.* **1972**, *37*, 4468–4469.

[9] P. N. Taylor, H. L. Anderson, *J. Am. Chem. Soc.* **1999**, *121*, 11538–11545.

[10] X.-B. Shao, X.-K. Jiang, X.-Z. Wang, Z.-T. Li and S.-Z. Zhu, *Tetrahedron* **2003**, *59*, 4881–4889.

[11] J. Grundy, M. P. Coles, P. B. Hitchcock, *J. Organomet. Chem.* **2002**, *662*, 178–187.

Appendix

SAXS analysis: Porphyrin tetramer (***l*-P4**$_{\mathbf{C8}}$) aggregate

In the absence of coordinating ligands ***l*-P4**$_{\mathbf{C8}}$ forms aggregates which, according to NMR analysis, seem to consist of three tetramer units. This structure can be confirmed by SAXS.

Linearity in the Guinier region confirms monodispersity of the sample and gives a radius of gyration R_g = 15.1 Å (from both Primus and Gnom analysis) which matches the value obtained from the model (R_g = 15.8 Å). The extrapolated scattering intensity at $q = 0$ was used to calculate the molecular weight of the aggregate using cyclic hexamer as a standard. The molecular weight MW = 15.6 ± 0.3 kDa matches very well the expected weight for an aggregate consisting of three tetramer units (MW = 15.5 kDa). The pair distribution function matches the one calculated for the model (Figure 1c) well. All features are reproduced and the two peaks at longest distance can be confidently assigned as the distance along one tetramer and diagonally across the aggregate.

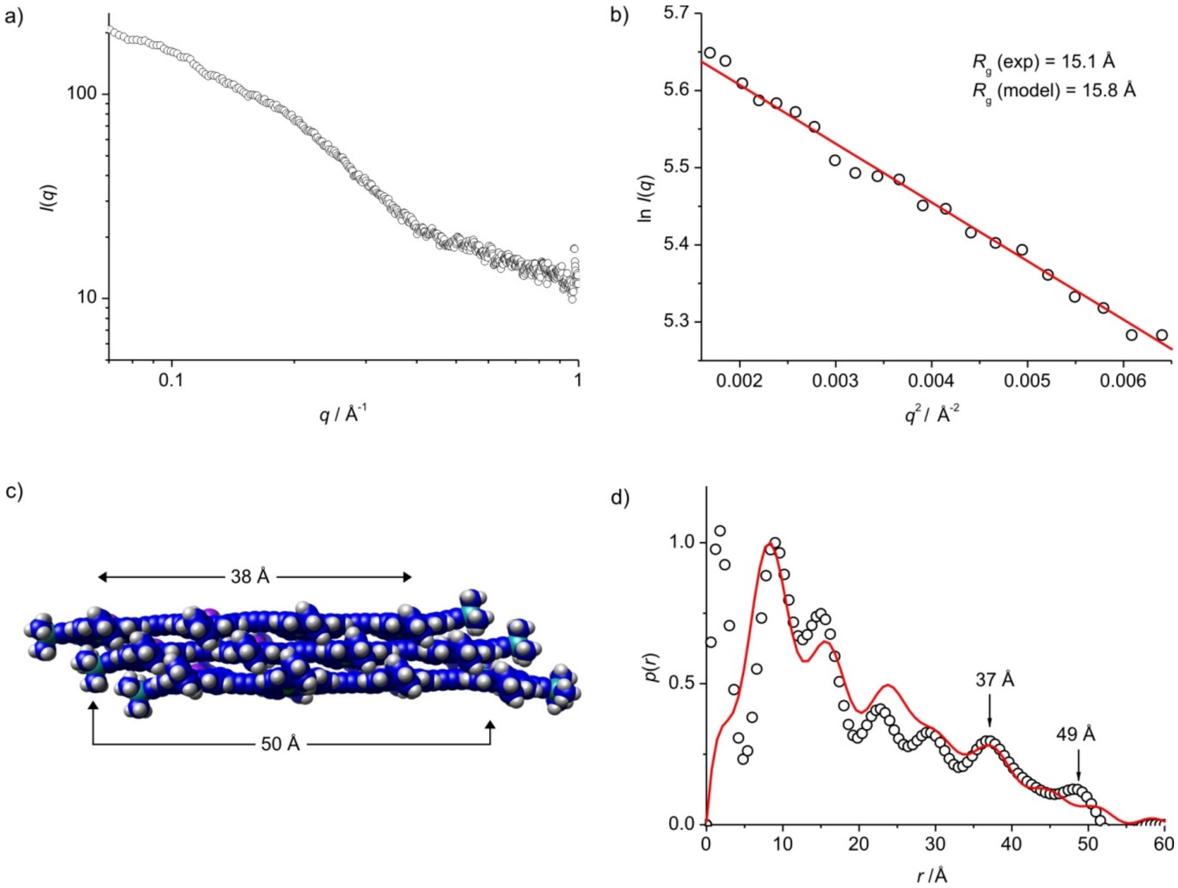

Figure 1. *a) Experimental scattering curve (black circles) of **l-P4**$_{\mathbf{C8}}$ in toluene (3.0 mg/L). b) Experimental scattering (black circles) and Guinier fit (red line). c) MM+ minimized structure of the tetramer aggregate used for data fitting. d) Pair distribution function of the experimental scattering data (black circles) and the model (red line). The peaks at 37 and 49 Å correspond to the calculated longest Zn-Zn distances along one molecule (38 Å) and diagonally across the aggregate (50 Å).*

SAXS analysis: NDI Assemblies

The group of Professor Jeremy Sanders (Cambridge) synthesized chiral naphthalene diimide (NDI) derivatives that assemble into helical tubes, as demonstrated by crystal structure analysis. In order to show that these tubes also form in solution SAXS analysis was carried out. The data suggest that only very short tubes form in solution.

The radius of gyration (R_g) of the NDI assembly was determined to be 10.8 Å (Figure 1b).

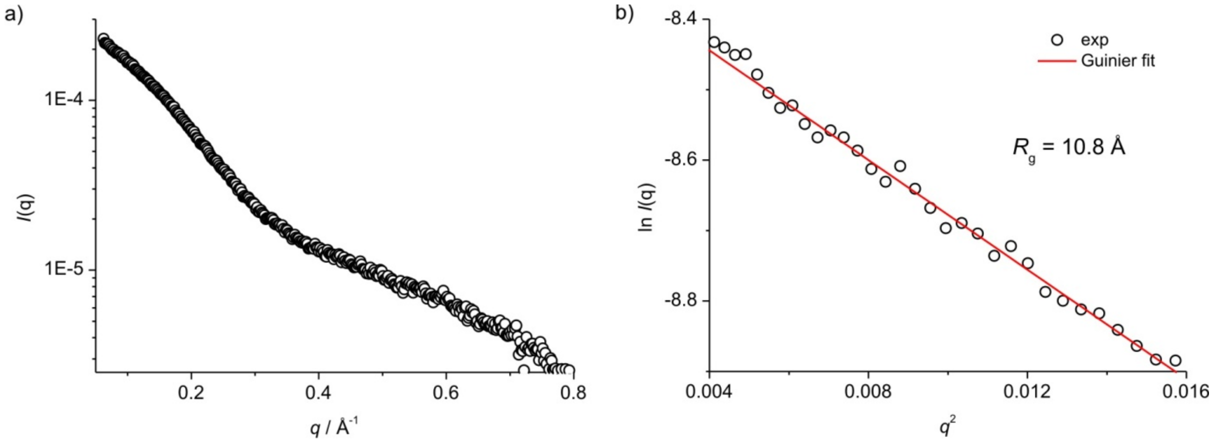

***Figure 1.** a) Experimental scattering curve. b) Guinier plot and fit of experimental scattering data.*

Scattering data of four models, all based on the crystal structure of NDI, were simulated and the R_g values determined using the Guinier plot. The four models are shown in Figure 2b. Model "4tube" consists of a helix with 4 turns (each turn has 3 NDI units), "3tube" has 3 turns and "2tube" has 2 turns. Model "1tube" consists of one turn plus one more NDI unit to form a closed loop by interaction between two adjacent NDIs. The R_g values deduced from these models are listed in the table below.

	NDI exp	**1tube**	**2tube**	**3tube**	**4tube**
R_g in Å	**10.8**	10.2	10.8	12.2	14.1

The best agreement is obtained for the model "2tube".

The absence of significant probability for an electron-electron distance beyond 30 Å in the pair distribution function is a first indication that the length of the tubes is relatively small. When simulating PDFs for the models we find the best agreement for "1tube" and "2tube", whereas the models for longer tubes clearly fail to reproduce the experimental curve (Figure 2a).

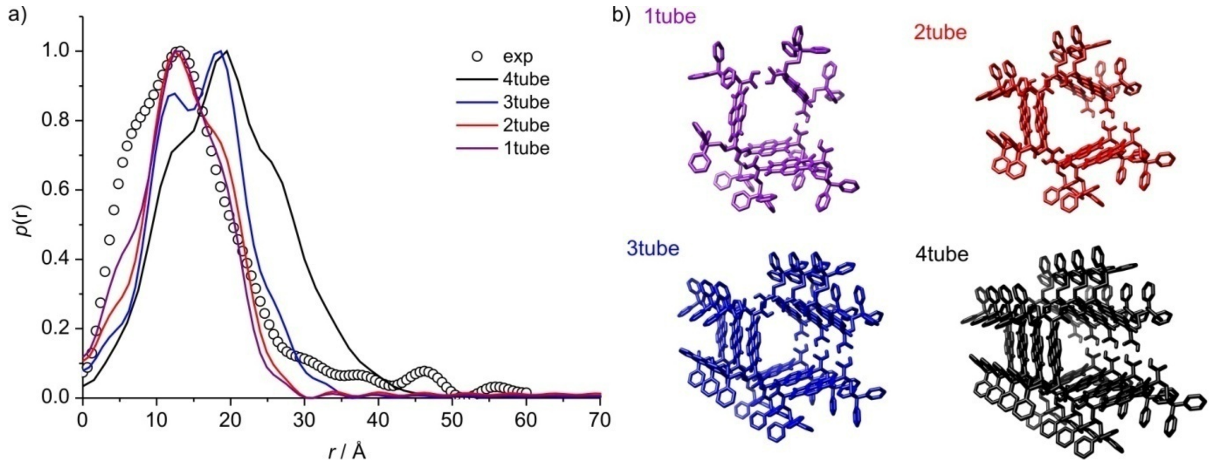

Figure 2. *a) Pair distribution functions from experimental data (black circles), 1tube (purple line), 2tube (red line), 3tube (blue line) and 4tube (black line). b) Models used for simulation of SAXS data.*

The results of the SAXS experiments strongly suggest that under the chosen experimental conditions (in toluene, mM concentration) the length of self-assembled helical tubes does not exceed two turns. This conclusion is supported by the excellent agreement of experimental data with simulations for R_g and PDF based on the corresponding models.

SAXS analysis: Porphyrin Bowtie

The “bowtie” is a porphyrin-based receptor that can bind two fullerene molecules. The compound was characterized by NMR and MS but SAXS analysis can give additional information about the shape of the molecule. The distance between the two receptor sites may be of particular importance in regard of planned experiments on spin entanglement between two molecules of N@C_{60}.

Both, the experimental scattering data and the pair distribution function, cannot be reproduced satisfactorily by using a rigid model (Figure 1c, top). It is well known, that the butadiyne linker that connects the two receptor sites is not highly rigid and thus we used a combination of six molecular models with different bending angles (Figure 1c, bottom) to fit the experimental data. The simulated scattering curve fits the experimental scattering very well at small scattering angles. The slight deviation at higher *q*-values may be associated with the background subtraction since the shape is generally well reproduced. The radii of gyration calculated for the models are spread over 3 Å and are slightly smaller than the experimental value determined using Gnom. The averaged pair distribution function, based on the six models, reproduces the features of the experimental PDF well.

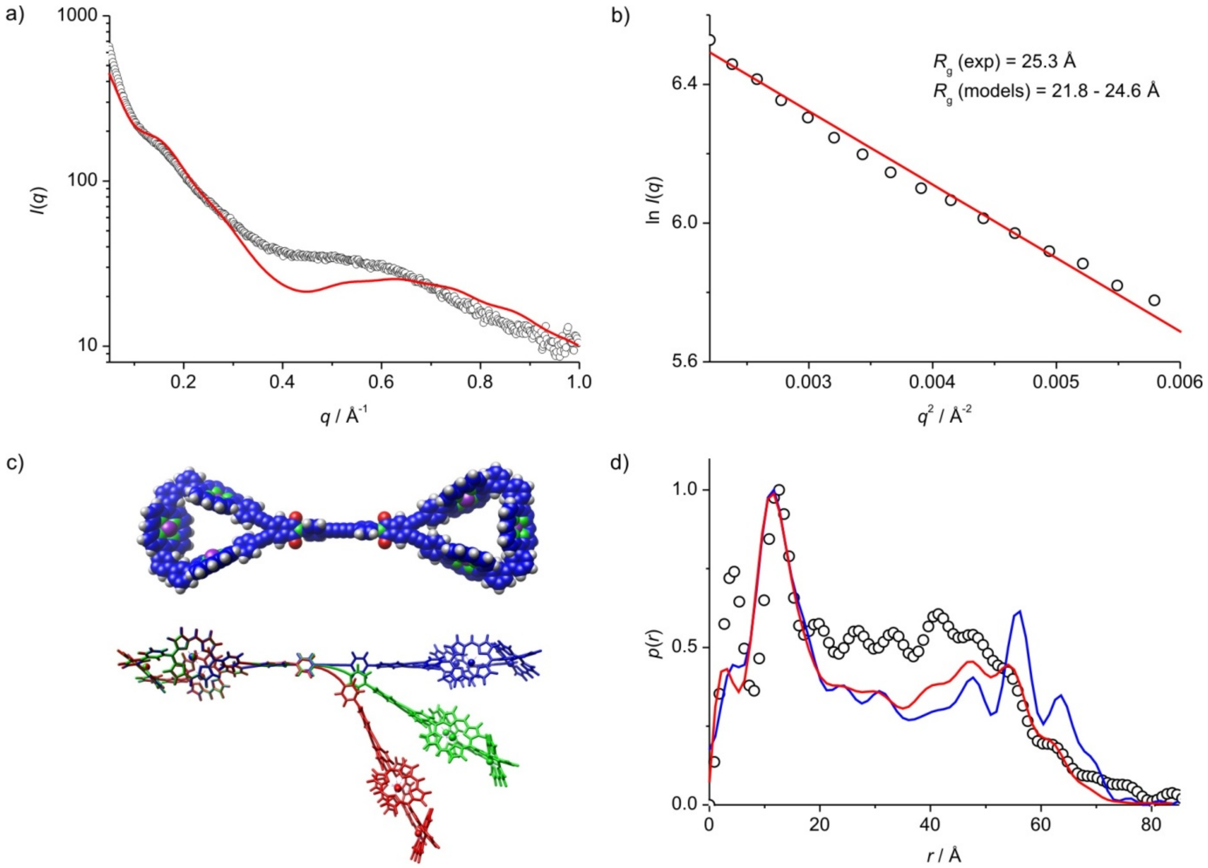

Figure 1. *a) Experimental scattering curve (black circles) in toluene/1% pyridine (1.7 mg/L) and simulated curve (red line). b) Experimental scattering (black circles) and Guinier fit (red line). c) MM+ minimized structure of the bowtie (top) and structures constrained to a smaller bending angle (bottom),d) Pair distribution function from the experimental scattering data (black circles), the rigid model (blue line) and a combination of bent models (red line).*

SAXS analysis: Triphenyl amine functionalized β-cyclodextrin (**TPA-CD**)

β-Cyclodextrin is a commonly used macrocyle in the synthesis of conjugated polyrotaxanes. Giuseppe Sforazzini functionalized this macrocycle with 21 triphenyl amine groups that should act as hole transport groups in such polyrotaxanes. SAXS analysis was carried out to acquire information on the solution structure of the macrocycle, particularly to determine its diameter. This parameter can then be used to determine the structure of the polyrotaxane using SAXS.

Linearity over a wide range in the Guinier region confirms monodispersity of the sample and gives a radius of gyration R_g = 11.9 Å (Figure 1b, from Gnom analysis) which matches the value obtained from the MD minimized structure (Figure 1c, R_g = 12.1 Å). We also found prefect matches of the experimental scattering data (Figure 1a) as well as the pair distribution function (Figure 1d) with data based on a MD simulation (10 000 frames). From the model and the pair distribution function we can deduce the longest intramolecular distance (d = 35 Å) which corresponds to the diameter of **TPA-CD**.

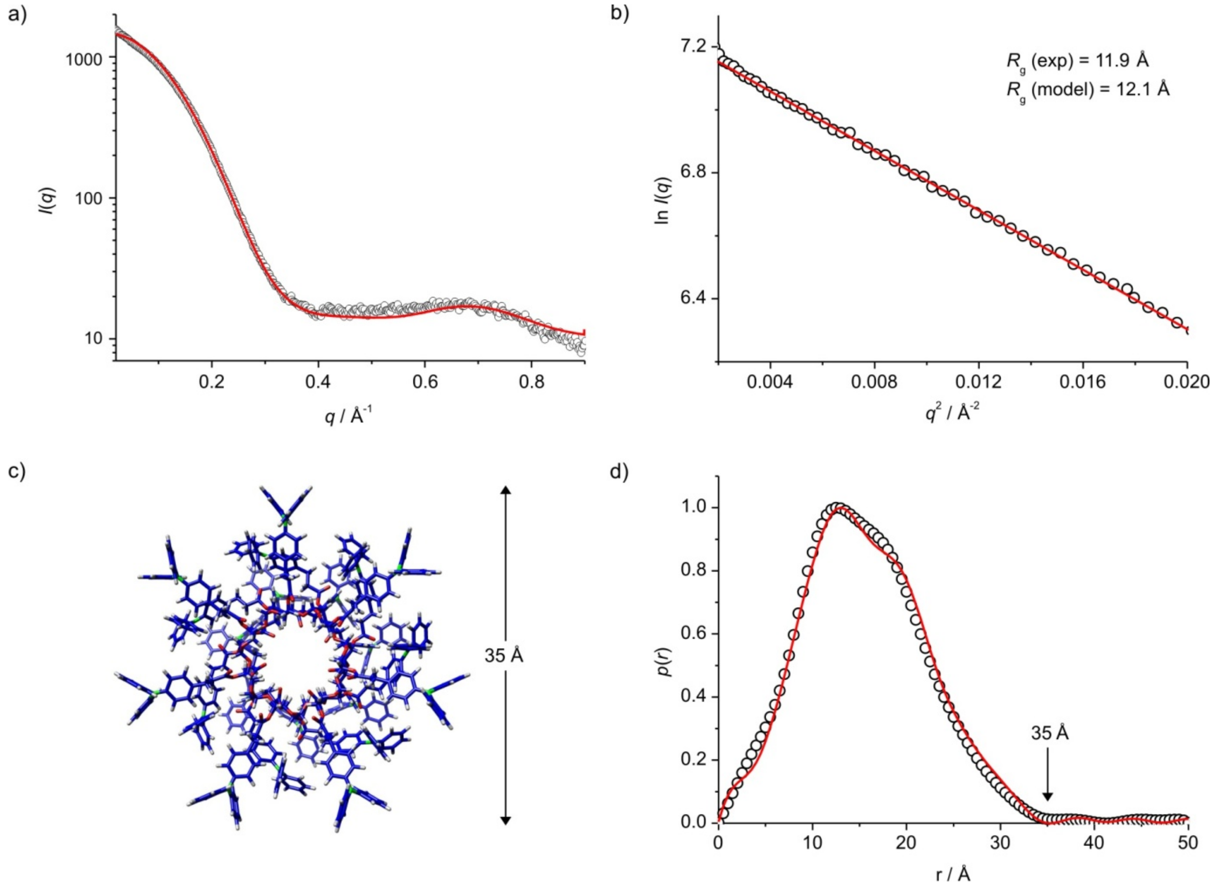

Figure 1. *a) Experimental scattering curve (black circles) of **TPA-CD** in toluene (14.6 mg/L) and simulated scattering from MD (red line). b) Experimental scattering (black circles) and Guinier fit (red line). c) Snapshot of **TPA-CD** from MD simulation. d) Pair distribution function of the experimental scattering data (black circles) and the model (red line).*

SAXS analysis: Polyfluorenebiphenylene rotaxane functionalized with triphenyl amine **(PFBP-TPA)**

Triphenyl amine functionalized polyrotaxanes were designed to act as coaxial molecular wires with an electron transporting conjugated polymer in the center surrounded by a hole transporting TPA layer. Knowledge of the average length of this wire is crucial to understand its charge transport behavior. Gel permeation chromatography, the standard technique to determine MW of polymers, fails here because of the high rigidity. Length determination by SAXS is challenging because the polymer is polydisperse, so no indirect Fourier transformation can be carried out to obtain the pair distribution function. The rigid structure of the polyrotaxane in Figure 1c is slightly misleading. The dynamics in solution result in a more uniform distribution of TPA units around the polymer backbone. Our attempt to analyze the data is thus based on simulating scattering data for a generic cylindrical object using the program "scatter" (Professor Stephan Förster, Universität Hamburg). The polyrotaxane is best represented by a cylinder with a homogenous core (polymer backbone) and an inhomogenous shell (TPA) since the electron density ϕ decreases at larger distances from the core (R), as observed in cylindrical polymer brushes (Figure 1b). We chose the radius of the inner core (R_c = 4 Å) according to the inner radius of cyclodextrin and the outer radius (R_m = 17 Å) according to the radius of **TPA-CD** determined by SAXS (see previous sample). For the standard deviation of the radius $\sigma(R)$ we used the default setting of the program and ρ, the ratio of electron densities of the core ϕ_c and at the interface to the shell ϕ_{cs} were assumed to be 1. We then varied the length of the cylinder (L) and the decay factor for the electron density in the shell α ($\phi \sim r^{-\alpha}$) to obtain the best fit with the experimental scattering data. This leads to a cylinder length of 150 Å which is slightly shorter than expected from the polymerization conditions (180 Å). The fit of the model to the experimental scattering data is only good up to $q = 0.5$ Å^{-1} corresponding to a distance of 12.6 Å. This distance is by about a factor of three smaller than the diameter of the cylinder and thus most of the scattering intensity in this area must be due to short range interactions for example distances between individual TPA units. Such distances are not incorporated in the coarse model of an inhomogenous cylinder which may explain the poor fit in this area.

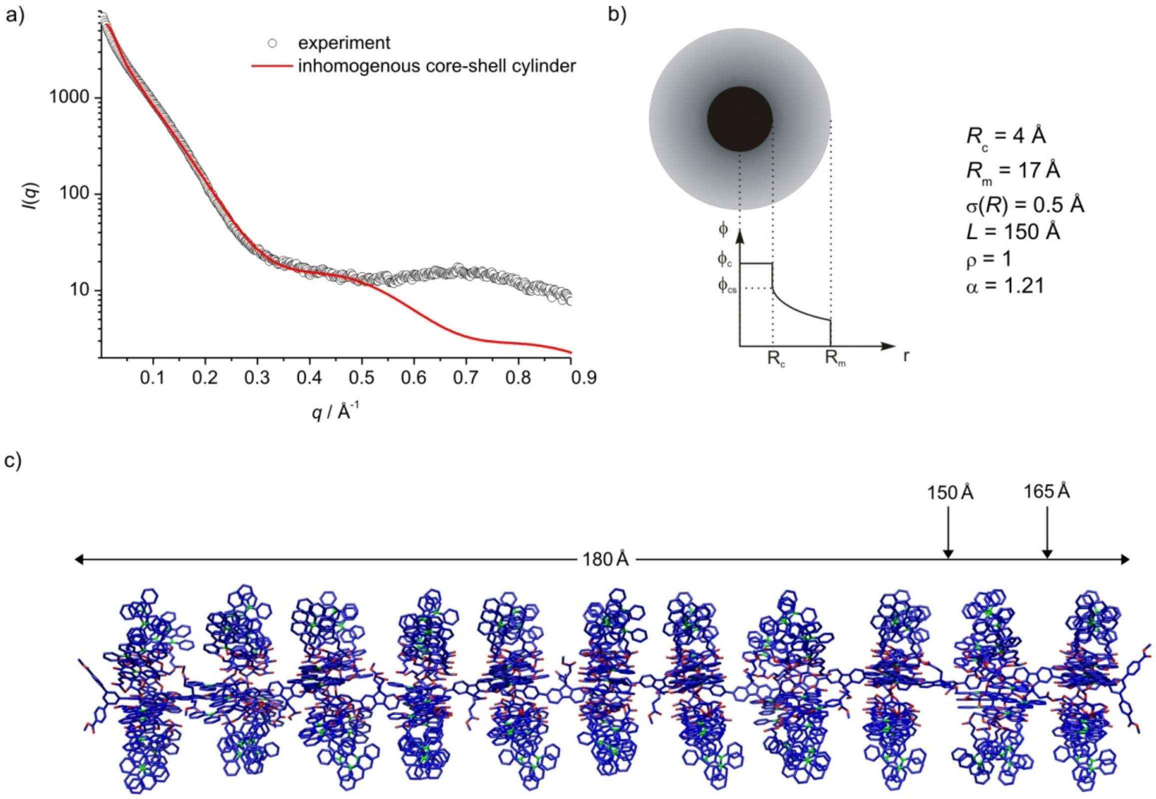

Figure 1. *a) Experimental scattering curve (black circles) of* ***PFBP-TPA*** *in toluene (12.4 mg/L) and scattering data simulated for a cylinder with core and inhomogenous shell using the program "scatter". b) Model and parameters used to fit the experimental data. c) MM minimized structure of* ***PFBP-TPA*** *to illustrate its dimensions. The determined length of 150 Å corresponds to 9 repeat units.*